

# **Foam glass production from vitrified municipal waste fly ashes**

PROEFSCHRIFT

ter verkrijging van de graad van doctor aan de  
Technische Universiteit Eindhoven, op gezag van de  
Rector Magnificus, prof.dr.ir. C.J. van Duijn, voor een  
commissie aangewezen door het College voor  
Promoties in het openbaar te verdedigen  
op maandag 28 augustus 2006 om 16.00 uur

door

**Arjen Christian Steiner**

geboren te Düsseldorf, Duitsland

Dit proefschrift is goedgekeurd door de promotoren:

prof.dr.ir. R.G.C. Beerkens

en

prof.dr.ir. A.G. Buekens

Copromotor:

dr.ir. J. van der Schaaf

A catalogue record is available from the Library Eindhoven University of Technology

ISBN-10: 90-386-2748-3

ISBN-13: 978-90-386-2748-9

Printed by Eindhoven University Press, Eindhoven, The Netherlands

Cover design: Paul Verspaget, Grafische Vormgeving - Communicatie, Nuenen, The Netherlands

voor mijn ouders

Samenstelling promotiecommissie:

Kerncommissie:

Eerste promotor:     prof.dr.ir. R.G.C. Beerkens,     Technische Universiteit Eindhoven

Tweede promotor:    prof.dr.ir. A.G. Buekens,     Vrije Universiteit Brussel, België

Copromotor:          dr.ir. J. van der Schaaf,     Technische Universiteit Eindhoven

prof.dr.ir. J.C. Schouten,             Technische Universiteit Eindhoven

dr.ir. J. Meuldijk,                    Technische Universiteit Eindhoven

Leden aangevulde commissie:

prof.dr.ir. A.C.P.M. Backx,           Technische Universiteit Eindhoven

prof.dr.ir. J.W. Niemantsverdriet,   Technische Universiteit Eindhoven

prof.dr. S. Persson,                  Växjö University, Zweden

prof.dr.-ing. H. Hessenkemper,       Technische Universität Bergakademie Freiberg,  
Duitsland

# Summary

The production of foam glass from municipal solid waste (MSW) fly ash is a promising approach to increase the value of this waste material. MSW fly ash, a waste product emerging from MSW incineration facilities, contains environmental harmful components like heavy metals, salts and organic toxins and shows strong variations of composition. Foam glass is a material that contains a high volume fraction of small, homogeneously distributed gas bubbles, which are sealed and separated from each other by very thin glass lamellae. It is a lightweight construction material suitable for both heat and sound insulation. It is a glass with strict specifications on desired resistance to heat conductivity, mechanical strength and corrosion resistance. It also has a high additional value after manufacturing. Foam glass, used as construction material, however, is subject to legal requirements in terms of environmental sustainability, which is not critical when using standard glass raw materials for its production, but can constitute a problem when using glasses from MSW fly ashes or other waste glasses. Hereby, leaching of environmentally harmful components, such as heavy metals or salts from the glass towards the environment, is a critical issue.

The objective of this study is the establishment of basic understanding (process steps, physics and chemistry involved) and development of technological tools to be able to safely transform fly ash originating from MSW incineration facilities into a high quality foam glass. This process is subdivided into four main parts:

1. Detoxification of the fly ash;
2. Salt phase separation;
3. Glass preparation by melting of the detoxified;
4. Foaming of the glass powder obtained from melting process and subsequent grinding and mixing with a reduced foaming agent.

Controlling the different process steps in a way that the product of one process step results in an adequate starting material for the subsequent step, is hereby of major importance. The two main technological tools, developed in this study are first a thermodynamic model to predict chemical activities in multicomponent glass melts and secondly a physicochemical model to predict transient bubble growth in foam glass.

Today, many detoxification processes for MSW fly ash are already available, resulting in different non-toxic products, which are not necessarily suitable for foam glass production. An effective removal of the heavy metals (Pb, Cu, Zn, etc.) and the organic toxins

(dioxins and furans) from the fly ash melt can be achieved very efficiently by chlorination of the fly ash in packed bed installations with humidified HCl or Cl<sub>2</sub> gas. The effectiveness of such a first detoxification step is shown in this study based on thermodynamic calculations and results of chlorination experiments from different literature sources. Literature reports that removal rates of 98.5% for Zn, 99.5% for Cu, 99.8% for Cd, and 99.8% for Pb could be achieved using hydrochlorination. In addition to that, salt roasting using solid MgCl<sub>2</sub> below the melting range of the fly ash, also showed removal rates above 90 % for Pb, Zn, Cu and Cd. The disadvantage of relatively large additional salt fractions after chlorination can be overcome by a liquid-liquid separation process forming a glass and molten salt phase during melting of the chlorinated fly ash. This separation can be achieved by heating the melt up to 1473 K. Experiments conducted in the framework of this thesis have shown, that the silicate melt phase is completely liquid at this temperature and that a salt phase separates from the silicate phase, floating on top of the glassy phase. A glass, used as raw material for foam glass production must be free of environmentally harmful components. It should be homogeneous and showing distinct physicochemical properties (e.g., distinct viscosity-temperature relation, surface tension, oxidation state). To produce a homogeneous glass from the chlorinated fly ash, free of remaining salts, it must then be heated to higher temperatures, around 1673 K.

Because of the, e.g., high CaO concentrations in the vitrified fly ash (CaO > 25 wt.%) the glass melt is prone to crystallization either during cooling from the melting process after detoxification or during the foaming process, which is usually conducted between 923 and 1173 K. Crystals in the glass influence the apparent viscosity of the glass melt and thereby the foaming behavior. The crystals also influence the structural integrity of the foam due to differences of the thermal expansion between the glass and the crystals. This can result in open or cracked lamellae between adjacent bubbles, which reduces the insulation behavior and strength of the foam glass. Additions to the vitrified fly ash to control the composition and thus the main important glass properties can reduce the liquidus temperature and the crystallization tendency. In order to optimize the preparation of glass melts from fly ash, applicable for foam glass production, a general and fundamental model to predict the chemical activity of the glass melt components has been developed. The here developed ideal mixture compound model (IMCM), calculates the chemical activities in a glass melt considered as an ideal mixture of single oxides (e.g., Na<sub>2</sub>O or SiO<sub>2</sub>) and structural compounds (e.g., Na<sub>2</sub>O · SiO<sub>2</sub> or CaO · SiO<sub>2</sub>). The application of the Lagrange method of undetermined multipliers, as a minimization routine, enables the extension of present compound models for binary or ternary to multicomponent glass systems. Comparison between calculated and experimentally determined sodium oxide activity values found in literature show very good agreement for multicomponent soda-lime-silica based clear float glass. The maximum deviation in activity values ( $a_{\text{Na}_2\text{O}}$ ) between the modeled values and the experimental ones for a float glass was 24% at 1368 K. The IMCM has been used to estimate the activities of some single oxides and structural compounds in a glass melt derived from vitrified fly ash. It is shown that the model can estimate the crystallization tendency by comparing chemical activity values. As an application of the IMCM, parts of the liquidus temperature curve of the binary sodium-silicate system are modeled in good agreement with phase diagrams reported in literature, using a modification factor. This modification was necessary, to correlate the different reference states

of the applied activity values. Because of the lack of thermodynamic data, calculations of the liquidus temperature of multicomponent glasses or even glasses with compositions similar to MSW vitrification materials, did not show satisfactory results. It seems that the simple modification of the activity, which shows good results in the binary  $\text{Na}_2\text{O-SiO}_2$  system is not simply transferable to multicomponent systems. Small differences in  $\Delta G$  values influence the activity and also the course of the liquidus lines and can produce significant deviations in calculated liquidus temperatures compared to experimentally determined liquidus temperatures.

A detailed analysis of the foaming process and especially the foaming gas reactions is necessary to produce foam glass from the detoxified, vitrified fly ash glass, which is adjusted in composition to obtain distinct glass properties. Inside the closed bubbles of the developing foam, a reduced agent, e.g., carbon, reacts with oxygen, originating from oxygen release of the polyvalent ions in the glass, to form CO and  $\text{CO}_2$ , the typical foaming gases. The bubble will grow when the pressure increases, due to the foaming gas formation and exceeds a force, which can stretch the bubble surface against viscosity and the surface tension of the glass, surrounding the bubble. Experiments using glasses with only iron as polyvalent ions have shown that CO is the prevalent foaming gas. The amount of CO gas formed during foaming depends on the oxidation state of the glass.

For quantitative description of bubble growth during the foaming process a first principle model is developed, which describes the transient (time dependent) bubble growth in foam glass as a function of physical, chemical and process parameters. The model also respects local thermodynamic equilibrium between the polyvalent ions in the glass. The validation of the model, using controlled laboratory foaming experiments shows, that the model can be used to estimate the bubble growth of foam glass in the initial stages. The model strongly overestimates the final foam height. The effect of the heating rate on the transient bubble growth is in good agreement with the measured real foam expansion rate at the start. The parameter study, focussing on the two main process parameters, i.e. the initial bubble size (depending on the size of the glass powder particles) and the heating rate has shown, that these parameters significantly influence the bubble growth rate. Despite the deviations between the modeled and experimental foam expansion rates and because of the fundamental basis of the model, it can provide a tool to optimize process conditions and glass properties for obtaining required glass foams. In addition to that, the model can provide, with some modifications, a considerable improvement to existing bubble models, describing fining in industrial glass melting processes.

In this thesis, a path for the detoxification and transformation of MSW fly ash into an added-value foam glass has been presented. The major process steps, (heavy metal and salt phase removal) have been identified and described with experiments and results from model simulations with the models developed in this study. Based on this, practical solutions for the described problems are presented and suggestions for future research are given.





# Contents

<b>Summary</b>	<b>5</b>
<b>1 Introduction</b>	<b>13</b>
1.1 Incineration of Municipal Solid Waste (MSW)	14
1.2 Fly ash disposal or treatment	17
1.3 Conventional foam glass production processes	20
1.4 Objective and outline of this study	21
1.5 Bibliography	24
<b>2 Detoxification of MSW fly ash</b>	<b>25</b>
2.1 Introduction	26
2.2 Thermal detoxification of fly ash	30
2.2.1 Experimental procedures	32
2.2.2 Results and discussion	34
2.3 Thermodynamics for heavy metal removal by use of chlorination reactions	39
2.4 Concluding remarks	45
2.5 Bibliography	47
<b>3 Prediction of chemical activities and liquidus temperatures in multicomponent oxide glass melts</b>	<b>51</b>
3.1 Introduction	53
3.2 Chemical activity models for multicomponent oxide glass melts	55
3.2.1 The compound model approach applied to oxide glasses	57
3.2.2 Model for chemical activities in oxide glass melts "Ideal Mixture Compound Model" (IMCM)	62
3.2.3 Validation of activity model (IMCM) for glass melts	63
3.3 Prediction of liquidus temperatures	73
3.3.1 Validation of the liquidus temperature calculations	76
3.4 Concluding remarks	78
3.5 Nomenclature	81
3.6 Bibliography	83
3.7 Appendix: Gibbs energy minimization procedure used in IMCM	86
3.7.1 Governing equations	86
3.7.2 Minimization routine	87

---

<b>4</b>	<b>Gas forming reactions during heating of mixtures of powdered glass and foaming agent</b>	<b>91</b>
4.1	Introduction . . . . .	93
4.2	Gas forming reactions during foaming . . . . .	99
4.3	Foaming gas identification: experiments, results and discussion . . . . .	101
4.3.1	Foaming gas identification experiments . . . . .	101
4.3.2	Quantitative determination of foaming gas evolution . . . . .	103
4.3.3	Influence of oxidation state and glass particle size on foam gas evolution . . . . .	105
4.4	Concluding remarks . . . . .	112
4.5	Bibliography . . . . .	114
4.6	Appendix . . . . .	116
4.6.1	The partial oxygen pressure in the glass . . . . .	116
4.6.2	Experimental results of CO release at T=1173 K . . . . .	116
<b>5</b>	<b>Physicochemical model for bubble growth in foam glass</b>	<b>119</b>
5.1	Introduction . . . . .	120
5.2	Governing equations for bubble growth model . . . . .	126
5.2.1	Model assumptions . . . . .	126
5.2.2	Equation of continuity . . . . .	127
5.2.3	Momentum equation . . . . .	128
5.2.4	Force balance at bubble shell . . . . .	129
5.2.5	Mass transport in the glass melt shell . . . . .	131
5.2.6	Thermodynamic equilibrium in the glass . . . . .	133
5.2.7	Chemical reaction in the gas phase and mass conservation at glass-bubble interface . . . . .	139
5.2.8	Pressure inside bubble . . . . .	141
5.2.9	Heating rate . . . . .	142
5.3	Numerical solution of the model equations . . . . .	143
5.3.1	Spatial variable in diffusion domain . . . . .	144
5.3.2	Dimensionless groups . . . . .	144
5.3.3	Formulation of transformed equations . . . . .	146
5.3.4	Analytical solution . . . . .	147
5.4	Experimental validation of the simulation model for foam glass . . . . .	148
5.4.1	Determination of model input parameters . . . . .	149
5.4.2	Foaming experiments . . . . .	154
5.4.3	Comparison of experimental and modeled glass foam volume expansion . . . . .	159
5.5	Process Parameter study . . . . .	166
5.5.1	Influence of initial bubble size on bubble growth . . . . .	166
5.5.2	Influence of heating rate on bubble growth rate . . . . .	169
5.6	Model calculations, results and discussion . . . . .	169
5.7	Concluding remarks . . . . .	176
5.8	Nomenclature . . . . .	178
5.9	Bibliography . . . . .	181
5.10	Appendix . . . . .	186

---

5.10.1	Integration of momentum equation . . . . .	186
5.10.2	Lagrangian coordinate transformation . . . . .	187
5.10.3	Physicochemical glass melt properties . . . . .	188
5.10.4	Numerical implementation . . . . .	195
5.10.5	Experimental determination of $\Delta H^{*r}$ and $\Delta S^{*r}$ values of iron oxide redox reactions in the glass melt . . . . .	197
5.10.6	Image analysis of sintered powder and foam samples and volume expansion determination . . . . .	200
<b>6</b>	<b>Conclusions and outlook</b>	<b>205</b>
6.1	Process steps . . . . .	205
6.2	Optimization tools for fly ash melting and foaming process . . . . .	207
6.3	Recommendations for future research . . . . .	211
	<b>Samenvatting</b>	<b>213</b>
	<b>Zusammenfassung</b>	<b>217</b>
	<b>Acknowledgments</b>	<b>221</b>
	<b>Curriculum Vitae</b>	<b>223</b>



# Chapter 1

## Introduction

---

<b>1.1</b>	<b>Incineration of Municipal Solid Waste (MSW)</b>	<b>14</b>
<b>1.2</b>	<b>Fly ash disposal or treatment</b>	<b>17</b>
<b>1.3</b>	<b>Conventional foam glass production processes</b>	<b>20</b>
<b>1.4</b>	<b>Objective and outline of this study</b>	<b>21</b>
<b>1.5</b>	<b>Bibliography</b>	<b>24</b>

---

The large volumes of municipal solid waste (MSW) generated by our society's consumption behavior become more and more a problem of today's modern civilization. The incineration of waste reduces these large quantities, but creates other relatively useless and partly toxic waste volumes. Fly ash is one of them. In a sustainable society, attempts should be made to convert the generated waste streams in ecologically compliant and economically valuable products. Many processes are available to convert fly ash into harmless fractions, but only few attempts have been made to develop products from these harmless fractions. This thesis shows a route of an environmentally compliant conversion process of the most problematic waste stream from MSW incineration: fly ash. In this process, the fly ash is converted into an ecologically harmless high, added-value construction material: foam glass. The thesis discusses the chemistry and physicochemical processes during the conversion of fly ash into an inert foam glass.

The first section of this introduction discusses MSW incineration as practised in The Netherlands. It describes the different incineration residues and their reuse or storage (disposal) strategies. The disposal of fly ash, according to the Dutch legislation on waste storage, requires a detoxification and/or immobilization treatment of environmentally harmful fly ash components prior to permanent storage, to prevent leakage or leaching of environmentally harmful components from fly ash to the environment. Fly ash disposal is discussed in the second section of this introduction. The immobilized incineration products and especially the immobilized, silica rich fly ash material, can potentially be reused as raw material for foam glass production. However, such a production process requires different, well defined process steps to obtain a final product with required and constant properties. Foam glass is a high performance construction material often applied for heat

*Table 1.1: Overview of produced MSW incineration residues in The Netherlands in 2001 [2]. The second column stands for the number of incineration plants in which the indicated incineration product is generated.*

Residue	Number of incineration plants	Mass (Mg)	Fraction (wt.%)
Bottom ash	11	1,100,000	81.3
Fly ash	11	79,000	0.3
Boiler ash	4	4,700	5.8
Ferrous metals	11	121,000	8.9
Non-ferrous metals	11	8,500	0.6
Flue gas cleaning residues:			
Filter cake	8	8,000	0.6
Flue gas cleaning salts	5	25,500	1.9
Sludge	2	4,300	0.3
Gypsum	1	1,800	0.1
Total	11	1,352,800	100

and sound insulation [1]. The technology of the foam glass production process is briefly discussed in the third section of this chapter. Finally, in the fourth section, the objectives of this thesis are stated and a guideline for reading through this work is presented.

## 1.1 Incineration of Municipal Solid Waste (MSW)

In 1995, the Dutch government issued a decree to reduce the amount of waste to be sent to landfills: "Prohibition on Landfilling Wastes Decree". According to this decree, only waste that cannot be cleaned in an economically feasible way or treated in another way, is allowed to be stored in landfills. This applies to contaminated soil, non-reusable building and demolition waste, waste from incinerators, ash from incinerated sludge and contaminated building materials. In 2010 only 4% of the total waste collected is allowed to be stored in Dutch landfills. As a result of the decree, waste incineration is supported to fulfill the decree requirements.

In 2001, 4.8 million metric tons of MSW were incinerated in 11 Dutch incineration plants. The incineration is nowadays optimized to maximum use. It reduces the waste volume by approximately 90% and the mass by approximately 70%, but this is not the only benefit. In 2000, nearly one million Dutch households could be supplied with electricity from waste incineration [2]. Despite these advantages, incineration leads to various by-products with different environmental impacts. These products are, in order of the sequence of separation inside the incineration plant: bottom ash or clinker, ferrous and non-ferrous metal fraction, boiler ash, fly ash and flue gas cleaning products. An overview of the amounts of generated Dutch MSW incineration products in 2001 is given in table 1.1. The bottom ash constitutes the largest mass fraction of the incineration products. It is the residue which remains on the incineration grate after combustion. At this time, 9

out of 11 Dutch incineration plants produce bottom ash which fulfills the requirements of a category 2 building material according to the Dutch Building Materials Decree<sup>1</sup>. It can for example be used as a road construction material. The fly ash denotes the particles which leave the incineration grate together with the flue gases and are usually separated in the Netherlands by electrostatical precipitator (ESP) filters, see figure 1.1. They contain, in addition to an inorganic matrix (e.g. silicates), heavy metals (e.g. Cd, Pb, Hg, Zn), salts (e.g. chlorides, fluorides and sulfates) and also organic components (e.g. dioxins and furans). These components are harmful to the environment in different ways. According to a resolution of the Dutch Ministry of Housing, Spatial Planning, and the Environment (VROM), which came into force in January 1998, MSW fly ash is not allowed to be stored in landfills unless it has the Dutch class 3 (c3) waste quality [3]. This usually requires an immobilization process of the harmful components.

The boiler ash is the residue, which condenses and thus forms deposits on the surface of the flue gas side of the boiler tubes, in which the water is transformed into steam for electricity production. It is sometimes collected separately, but most of the time it is added to the bottom ash or the fly ash, depending on the incineration plant technology. The ferrous and non-ferrous metal scrap is recovered and usually recycled in the metal industry. Flue gas cleaning residues are generated after the fly ash has been separated from the flue gases. Depending on the cleaning procedure (wet, quasi-dry or dry) the products of the flue gas cleaning process may differ. Gypsum, one of the cleaning products, can be reused in the construction industry, while other flue gas cleaning products, e.g. sludge or salts, are usually deposited on landfills.

Figure 1.1 gives an overview of the mass flow through an incineration plant for two different methods of flue gas cleaning, designated by route A and B in the figure. The amount of bottom ash accounts for approximately 25-35 wt.% compared to the initial amount of waste charged to the incineration chamber. The amount of boiler ash is very low (0.1-1.2 wt.%). Taking the wet flue gas cleaning route (route A) in figure 1.1, between 2.5 and 6.5 wt.% of solid dry residue is produced by the flue gas cleaning process, where between 0.5 and 1.5 wt.% (dry) come from the wet flue gas cleaning stage. Between 4 and 8 wt.% of residue are produced when cleaning the flue gases by a dry method (route B). The differences in residue production between the two routes can be explained by the type of absorbents or amount of adsorbents applied. The amount of residue from waste incineration, besides the bottom ash, for which reuse applications are available, seems little compared to the initial mass charged to the incineration. However, given the total

---

<sup>1</sup>Excerpt from the Dutch Building Materials Decree: "Category 2 building materials are building materials whose composition values do not exceed those stipulated in the Building Materials Decree but whose immission values would if additional isolation measures were not taken. The immission value depends on two factors: the leaching behavior of a material and its proposed use. The leaching (emission) is a fixed value; the immission depends each time on the circumstances, e.g., the temperature, degree of contact with water, presence of isolation measures and the height (thickness of the layer) at which the building material is used. The immission value expresses how much of a substance will in practice actually end up in the soil. The immission value is established in two stages. First, the leaching from a building material (emission value) is measured in a laboratory using standard leaching tests. The emission values obtained in the laboratory are then converted with the aid of formulae into expected immission values in practice."

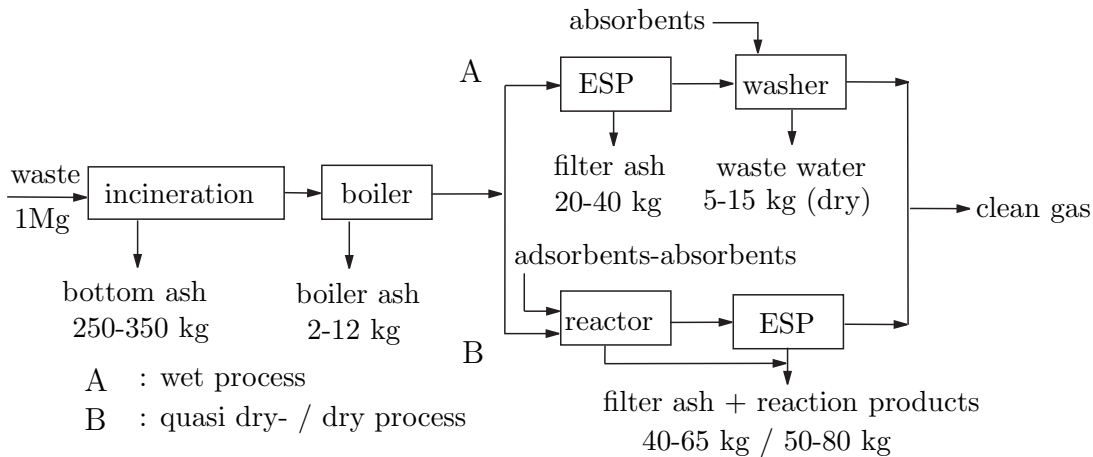


Figure 1.1: Mass stream and specific amounts of residues of MSW waste incineration according to [4]. The flue gas cleaning by ESP filters and the subsequent wet cleaning of the flue gases is given by route A. The use of additives for chemical neutralization reactions of the flue gases and fly ash and subsequent filtering of the solid reaction products is schematically shown in route B.

mass of MSW generated, the amount of fly ash and flue gas cleaning products is certainly not negligible.

The genesis of fly ash and its chemical composition in MSW incinerators is influenced by three main factors [5]:

1. The type of waste;
2. The type of incinerator;
3. The operating parameters of the combustion, mainly the amount of primary combustion air.

The type of waste (waste composition) determines the calorific value of the waste and the composition of the fly ash. Waste composed, for example, of a lot of plastic material, has a higher calorific value and less co-firing by, e.g., gas burners is necessary, but more chlorine will be found in the fly ash. The type of incinerator or more specific the design of the combustion chamber with the grate influences the combustion and thus the generation of fly ash. In the combustion chamber the waste is dried, ignited and combusted. The gases and vapors formed are carefully burned, to control air pollution [5]. The grate supports, conveys and stirs the waste and distributes the primary combustion air to achieve a uniform and complete combustion. The amount of primary air is partially (65-85 vol.%) determined by the amount of air necessary for cooling the grate and by the calorific value of the waste, presupposing a constant partial oxygen pressure in the combustion gases. The flame temperatures, which are also influenced by the amount of combustion air, influence the evaporation of salts and heavy metals, which occurs between 1070 and 1270 K. The more salts and heavy metals evaporate from the waste on the grate, the more will be found in the fly ash. The primary combustion air flow and high combustion gas turbulences and increases, among other things, the amount of fly ash generated. From the



view of an incineration plant, fly ash is seen as a waste product during incineration and electricity production [5].

The residues of MSW incineration are either reused (bottom ash) or stored in landfills (flue gas cleaning products). Disposal solutions for fly ash and boiler ash fractions are going to be discussed in the next section. The expression fly ash itself is not well defined and usually designates solid particles in the flue gases from combustion processes, e.g., waste incineration, coal power plants, glass melting furnaces etc.. The expression fly ash in the context of this thesis designates fly ash from MSW incineration, taking into account that sometimes boiler ash and flue gas cleaning residues are added to the fly ash, which is not necessarily mentioned in literature references.

## 1.2 Fly ash disposal or treatment

Fly ash is not allowed to be disposed in Dutch landfills unless it meets the c3 waste quality. This classification is determined by leaching values for environmental harmful components. In order to meet the c3 waste quality requirements, an immobilization procedure for the harmful fly ash components must be applied. The criterion for disposal or usage of fly ash is based on the immission values for critical components in the environment where the materials are going to be applied. The processing of fly ash in construction materials, e.g., as asphalt filler or concrete additive, is critical because of the environmental regulations for construction materials regarding leaching. Fly ash contains heavy metals, which typically accounts, on an elemental basis, for 1-4 wt.% of the total fly ash composition. In addition to salts and the organic components, fly ash contains large amounts of  $\text{SiO}_2$ ,  $\text{Al}_2\text{O}_3$  and  $\text{CaO}$ . Additional components are alkaline and alkaline earth oxides as well as halogenides and sulfides. A compositional overview on an elemental basis of fly ash from different incineration plants is given in table 1.2. Principally, the leaching of the harmful components from fly ash into the environment depends strongly on the chemical composition and the structure of the fly ash material. However, the way in which harmful components are incorporated into fly ash also determines their leaching rate. The harmful components can, for example, be bound into the silicate matrix of fly ash or deposited on the surfaces of the fly ash particles because of condensation during cooling. This will be discussed in more detail in section 2.2 on page 30.

Based on the composition of fly ash containing mainly  $\text{SiO}_2$ ,  $\text{Al}_2\text{O}_3$ ,  $\text{CaO}$ , two main detoxification treatments are usually applied. One is to separate and remove harmful components (organic toxins, heavy metals and salts) from the fly ash and dispose them in special landfills. The harmless (inorganic) part is also either stored (disposed) in landfills or reused. The other way is to immobilize the harmful components by inclusion in a glass or glassy matrix. This, however, has major limitations. Organic components cannot be incorporated into a glass or glassy matrix. The incorporation of salts depends on their solubility in, e.g., a glass. Heavy metals can in general be dissolved in glasses easily as heavy metal oxides. This can however be limited by their vapor pressure during melting of the glass. An essential requirement of this immobilization is that the resulting material has immission values of toxic components below the values stated in the regu-

Table 1.2: Overview of non-treated fly ash composition ranges (g/(kg fly ash)) from MSW incineration, derived from literature references. Only the most important elements are given here. The composition is given per element, n.g.=not given.

Literature reference		[6]	[7]	[4] <sup>a</sup>	[8]	[9]	[10] <sup>b</sup>
Element		g/kg	g/kg	g/kg	g/kg	g/kg	g/kg
Si	min	30	30	102.8	140	167	146.81
	max	159	160	168.2			
Al	min	14.4	2	63.9	70	82	86.29
	max	111	110	95			
Ca	min	30	30	27	136	89	137.86
	max	230	230	117			
Na	min	6	6	12	32	20	25.23
	max	120	120	75			
K	min	7.8	8	19	38	33	38.17
	max	120	120	78			
Fe	min	4.5	5	25	30	30	18.88
	max	39	40	46			
Cu	min	0.3	0.3	0.96	1.2	1.1	0.67
	max	2.7	3	2			
Cr	min	0.09	0.1	0.2	0.8	0.81	0.45
	max	1.2	1.2	3.2			
Ni	min	0.04	0.05	0.05	0.12	0.17	0.04
	max	0.45	0.5	0.46			
Zn	min	5.3	5	6.2	33	16	10.39
	max	70	70	55			
Pb	min	0.4	1	2.4	8.8	5.3	3.21
	max	30	30	54			
Sn	min	0.006	0.01	0.5	3.3	1.8	1.1
	max	5	5	6.2			
Cd	min	0.03	0.03	0.06	0.57	0.28	0.13
	max	1.9	30	1			
Hg	min	0.001	0.001	0.0002	0.019	0.2	0.2
	max	0.043	0.05	20			
Cl	min	36	30	6	56	30	44
	max	323	320	82			
P	min	0.06	0.1	0.2	8.9	n.g.	1.31
	max	9	8	30			
S	min	3	3	6	26	n.g.	11.62
	max	50	50	29.7			
F	min	0.004	0.004	0.03	6	12	1.5
	max	4.3	4.3	12			
C	min	9	10	1.6	38	n.g.	76
	max	54	60	42			

<sup>a</sup> Range of fly ash compositions from 20 different MSW incinerators

<sup>b</sup> Average fly ash composition from German MSW incineration plants

lations for building materials. The detoxification and/or treatment of the different waste streams emerging from MSW incineration and fly ash in particular, will be discussed in more detail in the next chapter.

Most of the established fly ash treatment processes<sup>2</sup> produce an inert material plus other waste streams (evaporation products), of which the latter are usually stored in special landfills. The inert material can be used as raw material for different applications, e.g., as a blasting abrasive or a filler material for road construction. These applications, however, have a low economic value. Alternatively, foam glass, a high value construction material, can be made out of this inert material. The main aspect to be investigated throughout this thesis is the transforation of fly ash from MSW incinerators into foam glass. The production process for foam glass requires distinct physicochemical glass properties and thus specific raw material properties, from which the glass is made of [13]. With controlled modifications to the inert glass composition produced from fly ash, the required

<sup>2</sup>An overview of different detoxification and immobilization processes is given in the next chapter.

*Table 1.3: Typical composition range of vitrified MSW fly ash and existing and foamable glass compositions [8, 11, 12].*

oxide / Element	Fly ash wt. %	Foam glass wt. %
SiO <sub>2</sub>	35 - 50	66 - 72
Al <sub>2</sub> O <sub>3</sub>	10 - 20	2 - 5
CaO	10 - 30	5.5 - 11
Fe <sub>2</sub> O <sub>3</sub>	2 - 8	0.01 - 3
Na <sub>2</sub> O K <sub>2</sub> O	2 - 13	12 - 15
Pb, Hg, Cd, Zn, Sn	1 - 9	~0
S, Cl, F	0 - 5	0.5 (SO <sub>3</sub> )

raw material and consequently glass properties can be obtained. An important aspect is the crystallization sensitivity of fly ash melts, which is an important subject of this thesis.

Silicate glasses made from fly ash are prone to crystallization during too slow cooling because of their relatively high calcium oxide concentrations (see table 1.3). Crystals in the glass influence the apparent viscosity of the glass melt and thus the foaming behavior [14]. They also influence the structural integrity of the foam due to differences in thermal expansion between the glass and the crystals. This can result in open or cracked lamellae between adjacent bubbles, which reduces the insulation behavior of the foam and enhances further coalescence of bubbles during foaming [14]. Certain additions to the melt phase can reduce the crystallization tendency of fly ash melts. Due to the strongly altering composition of fly ash, the composition of fly ash melt also varies. This makes it difficult to determine the required compositional modifications. Crystallization thermodynamics in silicate glasses are strongly determined by the glass composition. Thermodynamic modeling of multicomponent silicate systems with the prediction of chemical activities of the constitutional components and the crystallization tendency can be used to find conditions (compositions) to avoid or minimize the crystallization during cooling.

In addition to the compositional modifications required to reduce the crystallization tendency during the cooling of the glass melt, other distinct glass melt properties are required to produce a high quality foam glass. Thus a predictive fundamental physicochemical model is required, which determines the impact of composition on relevant foam glass properties. This is also an important aspect studied in this thesis. Such a model also makes it possible to study alternative glass compositions for foam glass production. The typical composition of fly ash melts and the compositional range of which glasses are foamed in industrial practise is given in table 1.3. The differences in required composition show the complexity of required compositional modifications to transform variable fly ash compositions into a constant foamable glass composition.

However, because of national (Dutch) and international regulations for the storage or reuse of fly ash and because of the large fraction of vitrifiable components in fly ash, the use of the inert waste fraction of fly ash as raw material for added value foam glass

*Table 1.4: Some material properties of industrially produced foam glass for insulation purposes.*

Property	Value
Volumetric mass	110 - 175 kg · m <sup>-3</sup>
Heat transfer coefficient	0.04 - 0.045 W · m <sup>-1</sup> · K <sup>-1</sup>
Compressive strength	0.5 - 1.6 N · mm <sup>-2</sup>
Heat capacity	0.84 kJ · kg <sup>-1</sup> · K <sup>-1</sup>

production, appears to be a promising and sustainable solution. The industrial production technology of foam glass and the required foam glass material properties are briefly discussed in the next section. It is beyond the scope of this thesis to discuss all these processes in greater detail.

### 1.3 Conventional foam glass production processes

Foam glass is a material that contains a high volume fraction of small, homogeneously distributed gas bubbles, which are sealed and separated from each other by very thin glass lamellae. It is a lightweight construction material suitable for both heat and sound insulation. As a heat insulating material, it has superior properties compared to glass wool or rock wool or organic insulating materials, e.g., styrofoam. Foam glass is water and vapor proof and does not burn. It is dimensionally stable, has superior compressive strength and is resistant to vermin and microbes. It is also CFC (chlorofluorocarbon) and HCFC (hydrogen chlorofluorocarbon) free and resistant to most industrial reagents. These properties qualify foam glass for its potential use in several industrial and domestic environments. For the latter case, under ecological and economical aspects, it is considered one of the best insulating materials [1]. Some specific foam glass properties are given in table 1.4.

The properties of foam glass and the possible application strongly depend on the structure of the glass foam, e.g., average bubble size and bubble size distribution, gas content inside the bubble and also on the shape of the material, i.e., brick shape, plates or granulate material. Different production methods for foam glass are discussed in literature [11, 15–17]:

- a. Insertion and mechanical distribution of gases in a low viscosity melt;
- b. Release and expansion of dissolved gases in a low viscosity melt under vacuum
- c. Insertion of foaming agents to a melt, which produces gas by dissociation or chemical reaction (e.g. carbonates, sulfates or nitrates);
- d. Mixing of a glass powder with a foaming agent and subsequent heating.

An example of a recent development in the production of glassy foam from vitrified waste material is a patented process developed by Rüegg [17]. In this process, a powdered foaming agent is added to a molten slag or glass inside a rotary kiln. Because the foaming

takes place inside the rotary kiln the extracted foam unfortunately disqualifies for the production of foam boards and bricks, because the foam exits the kiln as a foam cake. A general quality aspect of foam glass, in terms of insulation behavior, is its bubble size uniformity. This requirement disqualifies all mentioned methods except method d., which produces the highest quality foam glass [11], with respect to its properties as given in table 1.4. This is the reason to choose this method as the basis method in this thesis. More details to this method are given in chapter 5.

## 1.4 Objective and outline of this study

The objective of this study is the establishment of basic understanding (process steps, physics and chemistry involved) and development of technological tools to be able to safely transform fly ash originating from MSW incineration facilities into a high quality foam glass. This process is subdivided into four main parts:

1. Detoxification of the fly ash;
2. Salt phase separation;
3. Glass preparation by melting of the detoxified fly ash;
4. Foaming of the glass powder obtained from the melting process and subsequent grinding and mixing with a reduced foaming agent.

The detoxification of fly ash includes a destruction/decomposition of the organic components and a removal of the heavy metals. This occurs below the melting range of the fly ash. A subsequent step is the separation of the salt components from the silicate phase during heating at melting temperatures of the glass. Rather simple laboratory experiments have been performed to investigate the mass loss and the salt layer formation of a specific MSW fly ash from an existing MSW incineration plant during heating and to determine the oxidation state of the obtained glasses from fly ash, compared to the oxidation state of common glasses. Generally, because of the strongly altering composition of fly ash, fundamental tools to control the composition and properties of the obtained melt and to optimize the transformation processes (melting and foaming) are required. These tools are provided by two simulation models, which have been developed in this thesis. First, a thermodynamic model to predict thermodynamic properties and crystallization tendency of the vitrified fly ash melt depending on the temperature and the glass composition and secondly, a physicochemical model to predict bubble growth during the foaming process of the glass, are presented. The models are essential for the design of the transformation process of fly ash into an added-value glass product, foam glass.

The proposed transformation process of fly ash into foam glass is schematically given in figure 1.2. The structure of this thesis follows directly from this scheme. The first step (A) is the detoxification and vitrification of fly ash. This process step will be discussed in *Chapter 2*. Many detoxification and vitrification processes have been developed in the time period from 1985 to 2000. However, not every detoxification process is suitable to use its final product as raw material for foam glass production. The combination of

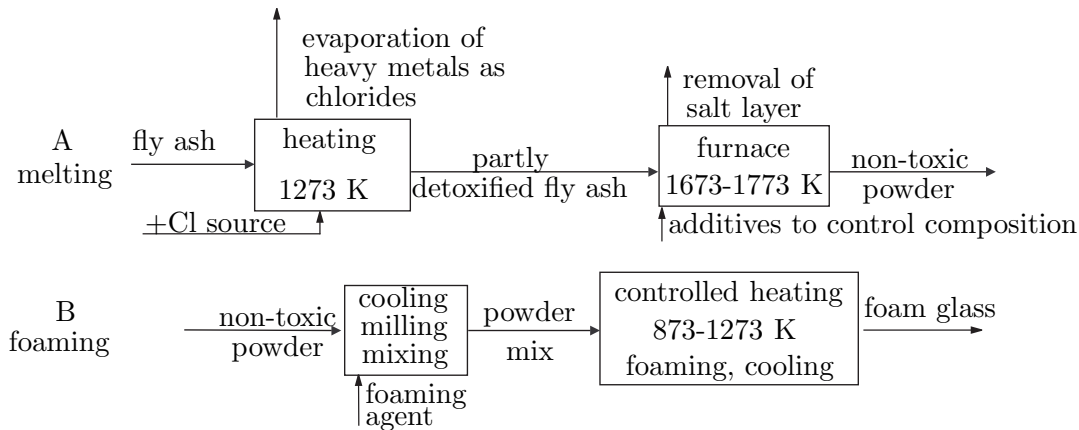


Figure 1.2: Schematic representation of transformation process of fly ash into foam glass.

different processes or parts thereof can lead to a glass composition with adequate properties suitable for foam glass production. In *Chapter 2*, literature data and information is predominantly used, supported by some selected melting experiments carried out in this thesis, to propose a detoxification route for fly ash into a silicate glass. First, vitrification techniques and thermodynamic aspects of fly ash detoxification and heavy metal removal will be discussed in *Chapter 2*. A three-step procedure for the detoxification and vitrification of the fly ash is proposed and discussed using literature data. In a first step, the procedure consists of the heavy metal removal using chlorinating agents. In the subsequent second step, the salt phase is extracted by separating it from the silicate glass melt at temperatures, typically above 1473 K. In the third and last step, the glass is heated to temperatures above 1650 K to obtain a sufficient low viscosity to produce a homogeneous glass melt.

The detoxified and salt-free molten glass phase or glassy material may be sensitive to crystallization during cooling and in the stages of foam formation, due to its relatively high calcium oxide concentration. Crystals in the glass influence the apparent viscosity during foaming and affect the structural integrity of the final foam. Crystallization of minerals, e.g. Wollastonite ( $\text{CaO} \cdot \text{SiO}_2$ ), from the glass melt can be prevented or limited by adjusting the glass composition and cooling rate. Thermodynamic modeling of multi-component silicate systems with the prediction of chemical activities of the components in the melt and the crystallization tendency can be used to find conditions (compositions) to reduce the crystallization tendency during cooling. Such a thermodynamic model for silicate systems is presented in *Chapter 3*. First, a model for the prediction of chemical activities of the constitutional glass components is developed. The calculated activities are then used to estimate liquidus temperatures. The complete model was supposed to predict the onset temperature of crystallization during cooling of the glass melt as a function of glass composition. This is successfully shown for parts of the sodium-silicate system. Unfortunately, the reliable prediction of the liquidus temperature of multicomponent systems is not achieved, but trends of the crystallization tendency as a function of changes to the glass composition can be estimated from calculated chemical activity values. The results of the calculated chemical activities and liquidus temperatures are

---

validated using available literature data for soda-lime-silicate glasses.

To use the vitrified fly ash as raw material for foam glass production, its foaming behavior in terms of gas release potential in contact with the reduced foaming agent is essential for bubble growth in the pre-sintered glass powder mass. The gas release from the glass powder in contact with a powdered reduced forming agent involves reduction-oxidation (redox) reactions in the molten glass. Until recently, not much has been known about the influence of polyvalent ions and the oxidation state of the glass on the reaction with a reduced foaming agent during the foaming process. Modeling of the gas forming reactions during foaming of glass has probably hardly been performed so far, because literature on this issue seems to be very rare. Gas formation during heating of powder mixtures of glass and a reduced foaming agent is studied experimentally and described in *Chapter 4*. These studies aim to identify the relevant chemical gas forming reactions during the foaming process in a glass mass with a reduced foaming agent. A relationship between the gas release potential and the oxidation state of the glass (oxidation state, presence of polyvalent ions) is also derived by experiments.

The use of waste glasses or ash as raw materials for stable and reproducible foam glass production requires compositional corrections and specific process parameters during melting and foaming. In order to optimize the foaming process for different types of glasses, a fundamental physicochemical model for bubble growth in foam glass is derived and presented in *Chapter 5*. The model predicts the bubble growth and foam height of a mixture of powdered glass and a reducing foaming agent. During the foaming process, the foaming behavior as a function of the main physicochemical glass properties (composition, gas release potential (oxidation state), glass melt viscosity, surface tension) and the applied process parameters can be estimated. The mathematical simulation model will be validated experimentally, and the influence of the different process parameters on the bubble growth rates during foaming are investigated by means of a parameter study. This model is the basis to find the optimum glass composition and process settings for the production of foam glass with required properties (see table 1.4).

Based on the findings of this thesis the complete process to transform MSW fly ash into a foam glass and the most important aspects to control the process steps are discussed in *chapter 6*. It is shown how the detoxification route and the developed models have to be applied to optimize the preparation of a harmless glass from the MSW fly ash and to derive a foam glass product from this glass.

## 1.5 Bibliography

- [1] B. Strebel and M. Welter. Schaumglas-Dämmstoffe. *Schweizer Ing. und Architekt*, 47:1128–1131, 1991.
- [2] Dutch waste processing association (VVAV). <http://www.vvav.nl>, August 2002.
- [3] Besluit stortverbod afvalstoffen. Staatsblad van het Koninkrijk der Nederlanden 665, 1997.
- [4] M. Faulstich. *Inertisierung von Rückständen aus der Abfallverbrennung durch reduzierendes Schmelzen*. PhD thesis, TU Berlin, Germany, 1992.
- [5] A. Buekens and J. Schoeters. Thermal methods in waste disposal (final report), Part 1: Pyrohydrolysis and gasification. EEC Report, contract number: ECI 1011 / B 7210 / 83 / B, 1983.
- [6] R. Gutmann. Thermal technologies to convert solid waste residuals into technical glass products. *Glastechn. Ber. Glass Sci. Technol.*, 69(9):285–299, 1996.
- [7] R. Gutmann and H. Vonmont. Elektrofilterasche aus Müllverbrennungsanlagen - Quantitative Zusammensetzung. *Z. Umweltchem. Ökotox.*, 6(5):257–263, 1994.
- [8] R. Gutmann, C. Wieckert, and H. Vonmont. Verglaste Filterstäube aus Müllverbrennungsanlagen - Schmelzverfahren, Prozeßführung und chemische Analyse. *UWSF-Z. Umweltchem. Ökotox.*, 8(4):187–196, 1996.
- [9] M. Hirth, J. Jochum, H. Jodeit, and C. Wieckert. A thermal process for the detoxification of filter ash from waste incinerators. In *Envirotech Proc. Vienna 20-23 February 1989*, pages 267–281. Elsevier Press, 1989.
- [10] M. Krauß. Vitrification of waste materials. *Glastechn. Ber. Glass Sci. Technol.*, 70(12):375–381, 1997.
- [11] B. K. Demidovich. *Foam Glass*. Nauki i Teknika, Minsk, 1975. In Russian.
- [12] S. Köse. *Untersuchungen zur Blähdynamik des Schaumglases*. PhD thesis, Eidgenössische Technische Hochschule (ETH) Zürich, Switzerland, 1981.
- [13] H. Scholze. *Glas Natur, Struktur und Eigenschaften*. Springer-Verlag, Berlin Heidelberg New York, 1988.
- [14] F. Schill. Über die Kristallisation im Schaumglas. *Silikattechnik*, 15(1):10–13, 1964.
- [15] M. Hübscher. Schaumglas, Teil I: Eigenschaften und Anwendung. *Silikattechnik*, 5(6):243–247, 1954.
- [16] E. O. Schulz. Schaumglas, Teil II: Zur Verfahrenstechnik bei der Herstellung von Schaumglas. *Silikattechnik*, 5(8):343–346, 1954.
- [17] H. Rüegg. Verfahren zum Schäumen von Material, insbesondere Schlacken oder Glas. European Patent EP0 922 679 A1, 1999.



# Chapter 2

## Detoxification of MSW fly ash

---

<b>2.1</b>	<b>Introduction . . . . .</b>	<b>26</b>
<b>2.2</b>	<b>Thermal detoxification of fly ash . . . . .</b>	<b>30</b>
<b>2.3</b>	<b>Thermodynamics for heavy metal removal by use of chlorination reactions . . . . .</b>	<b>39</b>
<b>2.4</b>	<b>Concluding remarks . . . . .</b>	<b>45</b>
<b>2.5</b>	<b>Bibliography . . . . .</b>	<b>47</b>

---

The first chapter of this thesis has shown that several waste streams emerge from municipal solid waste (MSW) incineration. Because of their chemical composition, fly ash represents the most troublesome fraction to be disposed or reused. Most countries have issued regulations, implying that fly ash is not allowed to be stored on landfills without prior stabilization, further separation or detoxification processes to prevent leaching of harmful components into the environment. These regulations initiated the development of many processes to transform fly ash into harmless materials to be stored or reused as raw material for other applications, e.g., the fabrication of concrete, ceramics or glass [1–4].

Most of the building materials or products using fly ash as raw material must be harmless to the environment in which they are going to be applied. The leaching of, e.g., heavy metals or salts under the different conditions of application (dry, wet, acidic etc.) are of great importance. The expression "harmful" in the course of the text should be understood as harmful according to the specific regulations, which have to be met by fly ash and products derived. Most of the time, these are the regulations for the application of fly ash or materials thereof as construction material.

In order to use fly ash as raw material for, e.g., foam glasses, the potentially harmful components, according to the environmental regulations (toxic organic components, heavy metals and salts), must be separated from the harmless mineral or glassy silicate fraction. Many very effective processes to separate the harmful components from fly ash have been developed in the last years [5–10]. Unfortunately, not every detoxification process is suitable to transform its final inert product into a foam glass. However, most

of the developed processes contain useful process steps, which, combined in a controlled way, can be incorporated into a detoxification route to transform MSW fly ash into a suitable foam glass raw material. This is why this chapter is not intended to develop another detoxification process, but to show a useful detoxification route for later use of the "cleaned" fly ash as raw material for foam glass production. The detoxification route, which is presented here, is based on findings of literature references. For some cases, however, own experiments have been performed to investigate the melting behavior of the particular fly ash (from a Dutch MSW incineration plant) used in this thesis, because fly ash compositions may vary a lot.

First, in the introduction, a brief overview of detoxification techniques is presented, focussing on thermal processes suitable to transform fly ash finally into a harmless silicate melt, necessary for foam glass production. In the second section, the behavior of fly ash during heating is discussed presenting also some simple experiments. Thermodynamic modeling of chemical reactions can be used to evaluate and discuss important process steps for fly ash detoxification. This is presented in the third section of this chapter. Finally a possible detoxification route is presented.

## 2.1 Introduction

As briefly described in the first chapter, MSW fly ash is not allowed to be stored in Dutch landfills, unless it has the Dutch class 3 (c3) waste quality [11]. In order to meet with the requirements of this regulation, many different processes to detoxify and/or immobilize fly ash have been developed. Most processes were designed to detoxify fly ash to be able to comply with the required waste quality (c3) and to be stored on landfills. The extracted heavy metals are usually stored as special waste. The quality of fly ash regarding its application as raw material was rarely considered, as long as it fulfilled the regulations for storage on landfills. Depending on the detoxification method, the non-toxic final product is not necessarily suitable to be used as raw material for foam glass production.

Fly ash contains considerable amounts of heavy metals, salts, and toxic organic components such as dioxins and furans [9, 12]. All these components are harmful to the environment. The toxic organic components are usually destroyed within one second by 99.99% at  $T > 1273$  K [13]. However, studies on dioxin emissions in MSW incinerators have shown that the de novo synthesis<sup>1</sup> is probably the major mechanism of dioxin formation in MSW incinerators [16]. The de novo synthesis can occur during the cooling at around 573 K of the flue gases and the carbon or ash particles leaving the incineration grating. With dioxins already present in fly ash, the formation of organic toxins can also occur during the cooling and cleaning of the flue gases produced during the heating or vitrification of fly ash. According to Huang et al. [17], the following five factors were determined in laboratory scale experiments to be the major influencing factors for the de novo synthesis of dioxins during waste incineration:

---

<sup>1</sup>Oxidative degradation of solid carbon structures and partial transformation to chloroaromatic compounds [14, 15].

1. Gaseous oxygen;
2. Solid carbon of certain degenerated graphitic structures;
3. Chlorine in the solid phase (either organic or inorganic);
4. Copper as a strong catalyst;
5. Temperature (573 K is the optimal temperature for the de novo synthesis).

Adequate cooling and treatment of the flue gases produced during heat treatment of fly ash vitrification process can avoid the formation of dioxins and the pollution of the environment. The treatment of the flue gases released during fly ash vitrification and/or the treatment or formation of organic components during fly ash vitrification is out of the scope of this thesis.

The concentrations of heavy metals and salts in MSW fly ash show large variations comparing reported compositions in literature references. The halogenides (F, Cl, Br) are found in fly ash at levels of more than 10 wt %, with Cl being the largest fraction. The heavy metals (Cu, Cr, Ni, Zn, Pb, Sn, Cd, Hg) represent between 1 and 4 wt % of fly ash, with Zn generally being the largest fraction. An overview of fly ash compositions, derived from literature references is given in table 1.2 on page 18.

Developed processes, treating fly ash, either immobilize the toxic components or separate them from the fly ash [18, 19]. The separated fractions can either be recycled (metal fraction) or have to be stored on landfills as special waste, because no recycling procedure or re-use application exists today (salts). A schematic overview of the different processes for fly ash and/or slags (bottom ash) is given in figure 2.1. The scheme was partially adopted from [19], where descriptions of the different processes and literature references for more detailed information of the processes can be found. The different processes can be subdivided in two main groups: physicochemical and thermal processes.

The physicochemical processes are primarily washing processes, using either acidic or neutral liquids for heavy metal extraction and their subsequent recycling. Additives such as clay, concrete or gypsum are used to bind the fly ash residue after extraction. In some of these processes the bound fly ash is returned into the waste combustion chamber of the MSW incinerator to separate its volatile components and to dispose the residue together with the bottom ash. The volatile compounds are then separated (as dust or scrubber) during the cleaning of the flue gases, together with the flue gases from the waste incineration. Other processes store the bound fly ash directly on landfills. The drawback of wet extraction processes, e.g., by use of chelating agents [20], is the difficult recovery of the metals from the leachate because of its complex matrix.

The thermal treatment processes can be subdivided into sinter processes and melting processes. The sintering processes operate below the melting temperature range of fly ash, typically between 1273 and 1473 K. The harmful components are either evaporated or bound in the sintered material, depending on the process. In addition to the processes, schematically given in figure 2.1, the separation of heavy metals from fly ash using the

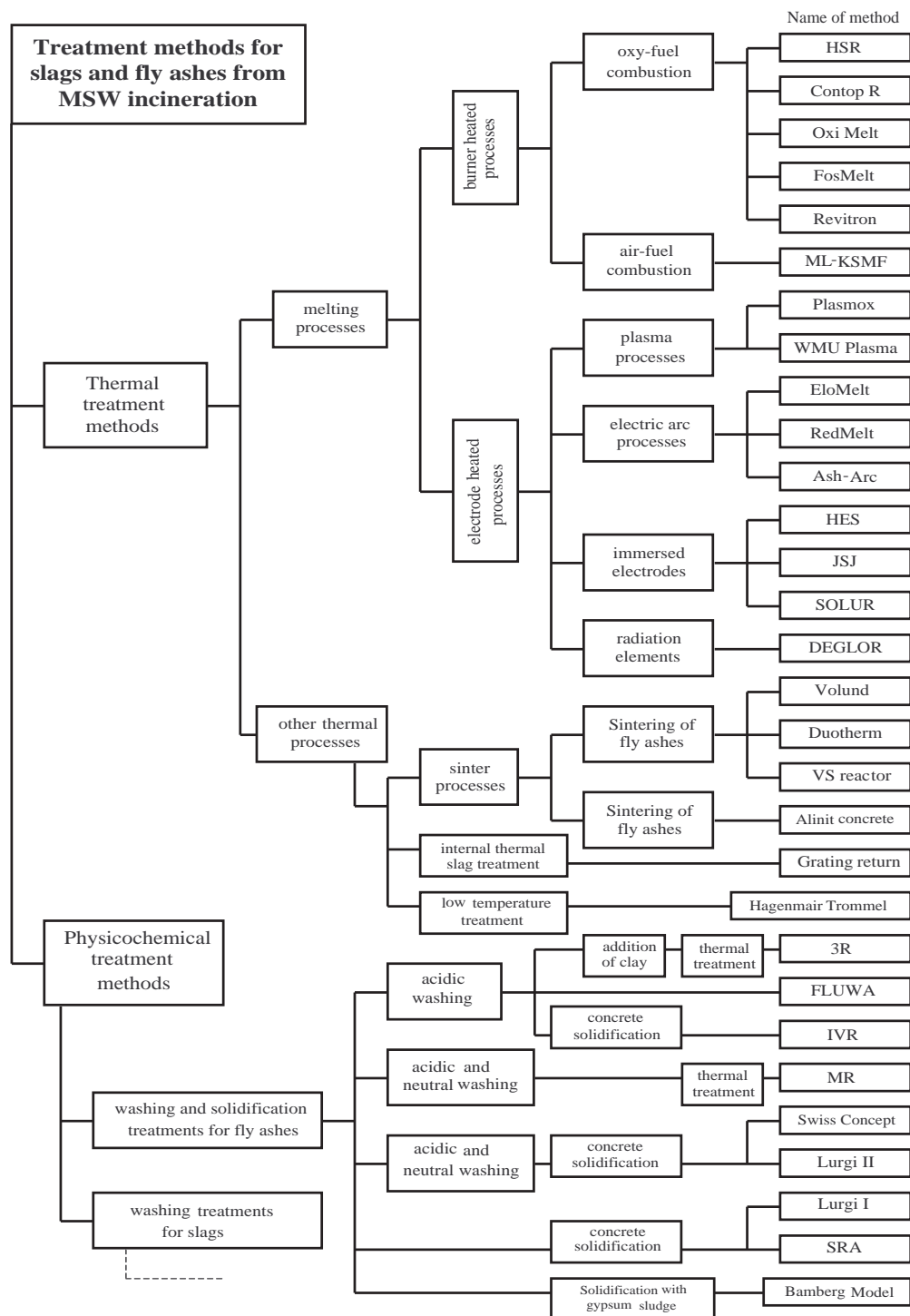


Figure 2.1: Treatment methods for fly ash or slags. The overview was partially adopted from [19]. For detailed description of the different processes, see also [19]. Fly ash detoxification methods, using chlorination agents are not included, but will be discussed in more detail in section 2.3 on page 39.

volatile nature of heavy metal chlorides is very effective [21–23]. This is discussed in more detail in the next section. The majority of the treatment processes for fly ash are melting processes. During the different melting processes, fly ash is heated up to levels above its melting temperature by either electrodes or burners. These processes operate almost as regular glass melting processes and evaporated heavy metals or salts must be recuperated or separated from the flue gases by either condensation, filtering or washing steps. Burner-heated melting furnaces have the disadvantage of high evaporation rates and carry-over due to the high combustion gas velocities that occur in the combustion chamber. Furthermore, the flames of the burners emit radiation in the near Infrared (IR) spectrum (800-1400 nm). Especially  $\text{Fe}^{2+}$  in the melt has a strong absorption in this spectrum ( $\pm 1050$  nm) [24]. The glass will therefore be strongly heated at the surface and heat penetration by radiation into the glass is limited. This supports the evaporation of, e.g., heavy metals at the glass/atmosphere interface in term of "cleaning the glass" from harmful components, but has a negative effect on the heat distribution in the glass melt, which is important to obtain a homogeneous melt. Colder glass surfaces and more homogeneous heat distributions compared to burner heated melting technologies for fly ash melts can be obtained by electrode heated processes. Plasma or electric arc processes, or processes where electrodes heat the melt either from the top or submerged in the melt, were developed. Evaporation of either salts or heavy metals can also be suppressed by continuous coverage of the submerged electrode heated melt with freshly charged cold ash (cold-top). The heavy metals are then bound into the glassy matrix. Products from such a process would not be suitable for, e.g., foam glass production, because of the risk of leaching of heavy metals from the glass into the environment. An extensive overview and description of the different processes as well as their implication for the environment is given in [18,19].

The use of fly ash as raw material for foam glass production requires, that the fly ash must first be transformed into a glass. As already mentioned, fly ash contains large salt quantities. Processes that operate at temperatures above the onset melting temperature of fly ash, forming mineral melts, have the disadvantage of high evaporation rates of the heavy metal and salts. Depending on the melting process and the nature of the fly ash, a salt phase floating on top of the molten silicate phase (glass) after fusion can occur by segregation. This salt phase evaporates easily at temperatures above 1473 K, where the evaporation depends more or less on temperature and residence time [25]. This was also observed for the particular fly ash originating from the MSW incineration facility in Amsterdam, The Netherlands, which has been used in this study. The evaporation of large salt quantities in glass melting aggregates at temperatures above 1473 K has an adverse effect on the refractory lifetime. Liquid salt phases are very corrosive to the refractories of the melting aggregate. For foam glass production, first a homogeneous melt, which is free of harmful components must be prepared and thus temperatures higher than 1573 K are needed. As a consequence, a combination of both thermal procedures seems to be most suitable: first a thermal treatment below and then above the melting temperature ( $T \sim 1473$  K). This treatment will be discussed in more detail in the next section.

Detoxification processes, that result in a glass suitable as construction material, thus not showing the leaching of harmful components, are not necessarily suitable for producing a

raw material for foam glass production. One example is the required oxidation state of the vitrified material, from which the foam is supposed to be formed. The oxidation state of an  $\text{Fe}_2\text{O}_3$  containing soda-lime-silicate glass is usually characterized in the cold state by the  $\text{Fe}^{2+}/\text{Fe}^{3+}$  ratio and in the liquid state by the partial oxygen pressure in the silicate melt in equilibrium with the chemically dissolved oxygen. This is discussed in more detail in subsection 5.10.5 on page 197. The oxidation state of a silicate glass determines, among other things, the availability of chemically dissolved oxygen in the glass, which is an important factor for the foaming gas formation during foam glass production. The influence of the oxidation state of silicate glass on the foaming potential of glass powder after sintering will be discussed in more detail in chapters 4 and 5. A detailed view on the typical oxidation states of harmless glasses obtained from detoxification processes is required, which will be discussed in more detail in the next section.

A general (overall) detoxification treatment is difficult to be realized, because of the complex and permanently changing composition of fly ash. As shown in chapter 1, foam glass production needs distinct and well controlled glass melt properties. The present section has shown that many different detoxification processes were developed in the past, but not all are suitable for generating a residue suitable as raw material for foam glass production. However, the combination of different processes or detoxification steps can lead to a feasible process to obtain a residue suitable as raw material for foam glass production. The next section will describe thermal processes, operating below and above the melting temperature range of the fly ash. Some simple experiments were also conducted to gain some basic information on the melting behavior of the particular fly ash used in this study and on the oxidation state of the obtained glass after vitrification of the ash. The thermal processes can be applied to separate first the harmful components from fly ash and then to transform the treated and purified fly ash into a glass, suitable for foam glass production.

## 2.2 Thermal detoxification of fly ash

The last section has suggested, that a thermal pretreatment and vitrification process of fly ash is needed to use it as harmless raw material for foam glass production. It has also been shown that thermal processes can be used to separate the harmful fly ash components from the reusable ones.

In order to optimize the detoxification of fly ash, a closer look into the mineralogy and the association of the heavy metals in the fly ash and the salts is required. Studies, that mineralogically characterize fly ash from electrostatic precipitators (ESP) and fly ash from flue gas cleaning systems show, that fly ash consists mainly of gypsum, anhydrite, quartz, hematite, rutil, wüstite, halite, sylvite, calcite and ettringite [26,27]. The ash studied by Kirby et al. [27], contained (wt.%) 18% crystalline minerals, 9% structural and absorbed water, 72% vitreous material and less than 1% of organic material. Eighmy et al. [28] analyzed the element and compound speciation of Canadian MSW fly ash. The major salt components, which are also highly soluble in water, were identified to be  $\text{NaCl}$ ,  $\text{K}_2\text{ZnCl}_4$  and  $\text{KClO}_4$ . The mineral phases contained calcium-, sodium- and potassium- aluminosil-

icates, lead silicates ( $\text{Pb}_2\text{SiO}_4$ ) and spinels ( $\text{TiO}_2$ ). Summarizing, the main components of fly ash are mineral components in crystalline and vitreous state, together with heavy metal and salt contaminations. This means, that there is a mineral basis containing different silicates, from which an inert material, e.g., a glass can be formed, presupposing the extraction and separation of all harmful components. Important for the formation of an oxide glass from fly ash is the amount of so called network formers<sup>2</sup>.

During cooling of the flue gases of the MSW incineration process, the heavy metal components with sufficient high vapor pressure, e.g., As, Cd, Zn, Pb, deposit on the surface of the ash particles instead of penetrating into the bulk of the ash particle [30,31]. Depending on the flue gas composition, with or without chlorine, reduced or oxidized etc., the heavy metals undergo different combinations with components in the atmosphere prior to condensation [32]. For example, reactions with chlorine in the flue gas atmosphere, which comes, e.g., from the combustion of chlorinated plastic materials or Cl containing organic substances: first, there is a competition for chlorine between hydrogen (from the combustion) and the metals. Secondly, there is competition among the metals, because of differences in the chlorine affinity. The differences in MSW compositions, combustion and flue gas cleaning techniques make it virtually impossible to foresee fly ash compositions and, which is more important, the association of the metals. The heavy metals are present on the surface of the ash particles in a relatively pure state, as a pure metal or metal oxide, but one generally does not know the association of the heavy metals with the salts and the silicates. The relatively pure state of, e.g., the heavy metal oxides, is advantageous for their removal by chlorination reactions. This will be discussed in more detail in the next section.

Up to 10 wt.% of fly ash consists of salt components with chlorine being the largest fraction. The solubility of salts in water is very high, so that the salt fraction must be separated from the fly ash. The solubility of salts in silicate glass melts is limited, so that during heating of fly ash above its fusion temperature, a salt layer, generally with a lower density than the silicate melt, floating on top of the melt can be formed [25].

In order to study the melting behavior of the particular fly ash, used in this study, some simple heating experiments and partial pressure measurements in a fly ash melt were performed. The heating experiments were performed to determine the onset temperature of melting (the temperature range in which first melt phases appear) and the weight loss as a function of temperature to get a first impression on the behavior of the fly ash when heated. The partial oxygen pressure measurements in the obtained melt were performed in order to compare the oxidation state of the fly ash melt with typical oxidation state values for technical glasses, e.g, glasses used for industrial foam glass production. The procedures of the different experiments will be presented in the next subsection.

---

<sup>2</sup>Expression in glass structure theory. They denote elements (Si, B, P), corresponding to an apparent coordination of oxygen surrounding these elements in the glass of 3 or 4. Network formers are responsible for the establishment of a glass structure (network). In addition to the network formers there are the so called network modifiers, breaking up the network forming covalent bonds, forming ionic bonds (coordination of 6 and higher (Na, K, Ca, Ba)), and the so called intermediates (Al, Mg, Zn), with a coordination between 4 and 6 [29].

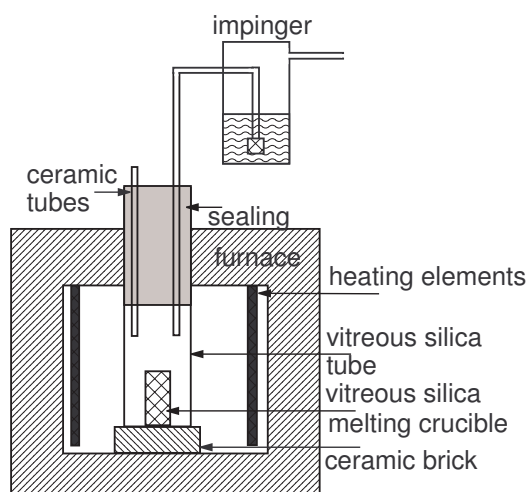


Figure 2.2: Schematics of experimental setup for fly ash melting experiments.

### 2.2.1 Experimental procedures

To obtain information on the behavior of the fly ash when heated, to determine the temperature range at which first melt phases appear and to determine the oxidation state of the glass after melting of the ash, simple, but controlled heating and melting experiments were performed. First, the thermal treatment procedure for the fly ash and secondly the partial oxygen pressure measurements are described in the next section.

#### Thermal treatment of fly ash into a silicate melt

For the thermal treatment of the fly ash from the AVI in Amsterdam, The Netherlands<sup>3</sup>, a vitreous silica or aluminum oxide crucible was filled with the ash and placed in a large vitreous silica tube (diameter: 650 mm). The gases evolved during the thermal treatment and melting are ducted through and cleaned in impingers (gas washing bottles), which were filled with 1 M  $\text{HNO}_3$  aqueous solution. In order to study the weight loss of the fly ash during thermal treatment, the samples in vitreous silica crucibles were isothermally treated for 1 and 5 hours (the samples were directly inserted in the preheated furnace) at different temperature levels. However, for the thermal treatment during 5h at 1573 K and during 1h at 1673 K, aluminum oxide crucibles were used, because of the higher corrosion resistance at higher temperatures. Because of the limited thermal shock resistance of the dense alumina crucibles, the crucible had to be heated up more slowly from room temperature to the final melting temperature. After the isothermal treatment, the samples were cooled and analyzed. The schematics of the experimental setup is given in figure 2.2. In these experiments, 12 g of fly ash (as received) was used per experiment and air as carrier gas of  $1 \text{ Nl} \cdot \text{min}^{-1}$  was applied to purge the system (i.e. the space above the melting fly ash). After the experiment and cooling, the residue in the melting crucible (fly ash or glass, and salt layer) was collected and weighed.

<sup>3</sup>For reasons of confidentiality, the origin, but not the exact chemical composition of the used fly ash is allowed to disclose.



### Oxygen gas activity measurements of different silicate melts

The measurement of the partial oxygen pressure ( $p_{O_2}$ ), in equilibrium with the molecular oxygen dissolved in the melt, of the different fly ash glass melts was performed by the use of a commercial iridium - (Ni-NiO) electrochemical sensor (Rapidox). The partial oxygen pressure in silicate glass melts depends on temperature and is used to characterize the oxidation state of the glasses. The use of electrochemical sensors to determine the partial oxygen pressure in glass melts is a standard technique (Thonthat et al. [33], Beerkens et al. [34]). The electromotive force (EMF) between the reference electrode in equilibrium with NiO-Ni and the measuring electrode in the glass melt was measured during cooling of the melts. The temperature dependent EMF-value is directly determined by the oxygen activity in the glass melt, according to the Nernst equation:

$$EMF(T) = \frac{RT}{nF} \ln \left[ \frac{a_{O_2}(m)}{a_{O_2}(ref)} \right] \quad (2.1)$$

where  $R$  is the ideal gas constant ( $8.314 \text{ J} \cdot \text{mol}^{-1} \cdot \text{K}^{-1}$ ),  $T$  the absolute temperature (K), assuming the same temperature for the reference cell and the glass melt,  $n$  the number of electrons transferred (here 2),  $F$  the Faraday constant ( $96485,33 \text{ C} \cdot \text{mol}^{-1}$ ),  $a_{O_2}(m)$  the oxygen activity in the glass melt (-) and  $a_{O_2}(ref)$  the oxygen activity in the reference gas ( $a_{O_2}(ref) = 1$  for pure oxygen and 0.21 for air). The oxygen gas activity  $a_{O_2}(m)$  in equilibrium with the dissolved oxygen in the glass can directly be calculated from equation (2.1).

Because the preparation of the glass melts was different for the different measurements, the procedures are given as follows:

**Glass melt from Fly ash:** Prior to the partial oxygen measurement, about 1 kg of the fly ash, as it was received from the MSW incineration plant, was vitrified at 1673 K for 30 minutes in a Nabertherm HT16/17 Muffle furnace in an  $Al_2O_3$  crucible in a normal (1 bar) air atmosphere. The heating rate from room temperature to 1023 K was  $300 \text{ K} \cdot \text{h}^{-1}$  and from 1023 K to 1673 K it was  $600 \text{ K} \cdot \text{h}^{-1}$ . After quenching, the salt layer on top of the glass was removed and the glass was re-melted. The temperature during re-melting was not higher than the temperature during vitrification. It is thus assumed that during re-melting oxygen exchange with the environment is limited. Therefore it was assumed that the oxygen equilibrium at high temperature did not change significantly. The oxygen gas activity of the glass melt was measured during a stepwise cooling procedure between 1673 and 1523 K in steps of 50 K. The chemical composition of the recovered glass is given in table 2.2 on page 38, the composition of the recovered salt layer after the first melting step is given in table 2.1 on page 35.

**Foam Glass:** The oxygen gas activity measurement was done from base glass cullet of the original Pittsburgh Corning soda-lime-silicate glass<sup>4</sup>, which is used for the production of foam glass. 700 g of cullet was molten at 1473 K for 1 hour in a silica crucible. The oxygen gas activity has been determined during stepwise cooling between 1673 K to 1523 K in steps of 50 K.

---

<sup>4</sup>For reasons of confidentiality, the exact chemical composition of the base glass is not allowed to disclose.

**Reference glasses (dark amber, green and colorless):** In order to compare the oxidation state of waste glass melts with typical oxidation states of glasses used in glass industries, the partial oxygen pressures of glass melts reported by Beerkens et al. [35] were used. They studied the chemistry of sulfur in soda-lime-silica glass melts with different oxidation states. The glasses were of the composition: (wt.%):  $\pm 74\%$   $\text{SiO}_2$  -  $\pm 16\%$   $\text{Na}_2\text{O}$  -  $\pm 10\%$   $\text{CaO}$  and were molten from reagent grade chemicals, except the sand (99.8 wt.%  $\text{SiO}_2$ ,  $<0.006$  wt.%  $\text{Fe}_2\text{O}_3$ ). Active coal was used as reducing agent to vary glass melt oxidation states. The glass batch of approximately 700 g was inserted into a furnace at 1373 K and then melted for 16h at 1473 K under an air atmosphere prior to the partial oxygen pressure measurements at different temperatures.

**Glasses from vitrified fly ash (DEGLOR and AshArc):** The glasses from the DEGLOR<sup>5</sup> and AshArc process [6, 36–38] were received in cullet form. Approximately 700 g of cullet was inserted into a pre-heated furnace at 1373 K and the glass melts were then heated to 1573 K in air with a heating rate of  $35 \text{ K} \cdot \text{min}^{-1}$ , where it was kept for 90 minutes. Afterwards the temperature was increased to 1673 K, at which the glass melt was kept for one hour prior to the beginning of the measurement. The partial oxygen pressure was then measured during cooling between 1673 K and 1473 K in steps of 50 K. A short description of both, DEGLOR and the AshArc process, is given with the discussion of the results.

## 2.2.2 Results and discussion

The weight losses of the original fly ash, during 1 hour and 5 hours lasting isothermal treatments as a function of temperature are given in figure 2.3. Visual observation showed, that the fly ash did not show any melt phases below 1173 K. At 1173 K, the total weight loss for the 1 hour treatment was 8.3 wt.% and 13.5 wt.% for the 5 hour treatment. At temperatures above 1473 K the formation of a salt layer was observed. A sharp increase of the slope between 1473 and 1573 K is observed for the 5 hour curve, due to the complete evaporation of the salt layer. The chemical composition of the salt layer is given in table 2.1. The chemical composition of the glass phase is given in table 2.2 on page 38.

The phase distribution for the two different experimental times is shown in figure 2.4. As observed from figure 2.4(b), at 1473 K, 19 wt.% of the fly ash evaporates, and 14 wt.% of the fly ash is transformed into the salt layer after 5 hours. At 1573 K, no salt layer was present after 5 hours and in total 44 wt % has been evaporated from the fly ash. The difference in weight loss, comparing the 5 hours curve to the curve for 1 hour isothermal treatments, increases with increasing temperature. The large difference at 1573 K may be caused by the complete evaporation of the salt layer and subsequently by some evaporation from the glass melt itself during the 5 hours treatment whereas after the 1 hour treatment, 17 wt.% of the original fly ash is still present as a salt layer. The phase distribution after the 1 hour isothermal treatment as a function of temperature is shown in figure 2.4(a). The difference in weight loss between 1473 and 1573 K seems to be mainly due to the increasing evaporation of the salt layer as temperature goes up. The

---

<sup>5</sup>Decontamination and Glassification of Residue

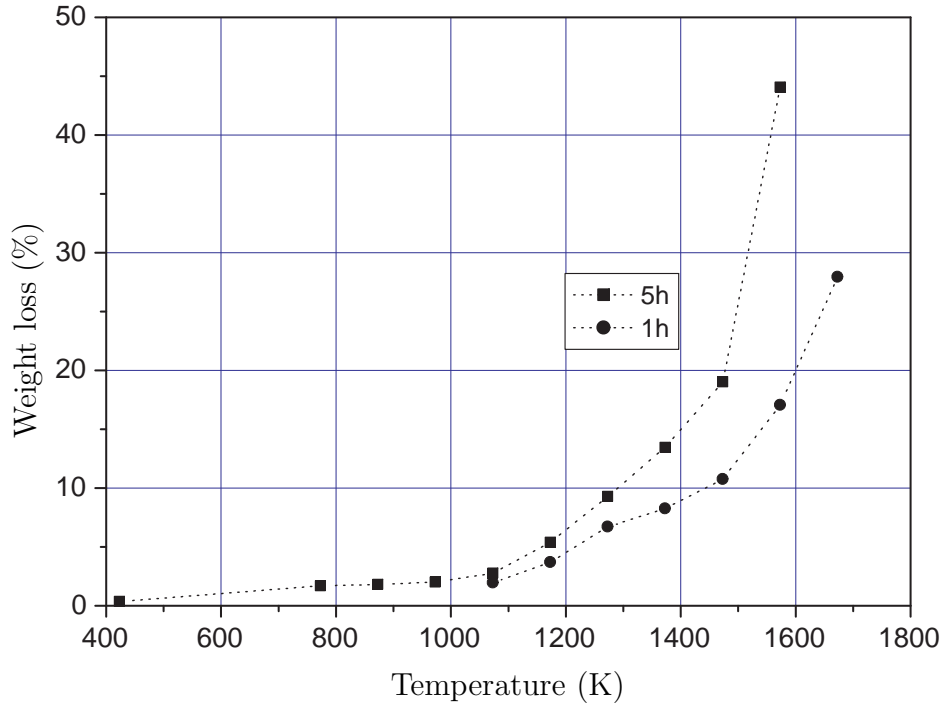


Figure 2.3: Weight loss (%) of fly ash after 1 hour and 5 hours of iso-thermal treatment (new fresh samples were used for each temperature and time period).

Table 2.1: Chemical composition of the salt layer after first melting step of fly ash (30 minutes at 1673 K). The composition was obtained from XRF analysis.

Element	Salt layer (wt.%)	Element	Salt layer (wt.%)
Na	16.38	Mn	0.02
Mg	30.18	Fe	0.04
Si	0.14	Cu	0.12
P	0.83	Zn	0.24
S	18.87	Br	0.29
Cl	23.56	Sr	0.12
K	17.11	Sb	0.02
CaO	21.05	Ba	0.66
Ti	0.03	Pb	0.14
Cr	0.2		

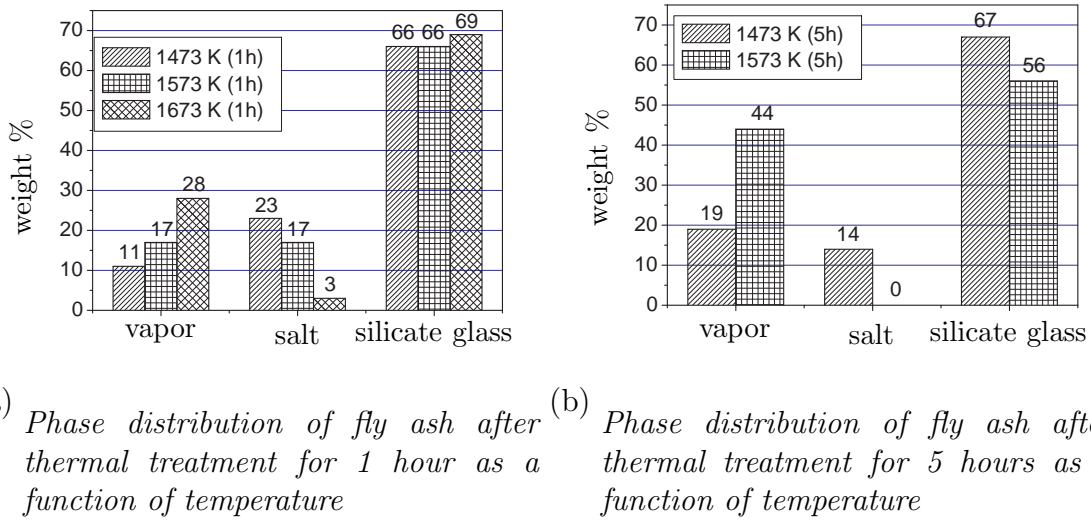


Figure 2.4: Phase distribution in wt.% of initial amount of fly ash after thermal treatment as a function of temperature.

amount of the glass phase is nearly the same (66 wt.%) for the 1 hours treatment at 1473 or 1573 K. The amount of the silicate glass phase at 1673 K of the 1 h experiments is 3 wt.% higher than at lower temperatures, and still higher than, e.g., at 1473 K for the 5 hours isothermal experiment. This difference is most probably caused by experimental errors. Compared to the 5 hours experiment at 1573 K, a salt phase was still found, which could inhibit the evaporation from the melt. The volatile salts, can cause severe corrosion to the refractory material of the melting aggregate. However, the formation of such a salt phase layer at lower temperatures, allows to extract the salt phase prior to its complete evaporation, which is technically realized by Pieper et al. [39]. It should be noted that evaporation of the salts in the fly ash cannot be prevented, but reduced when separation of the liquid salt phase during heating is applied.

As mentioned above, silicate melts, resulting from fly ash vitrification are not necessarily suitable for foam glass production. Two fly ash or waste residue vitrification processes resulting in a silicate glass were developed by ABB Switzerland, the DEGLOR and the Ash-Arc process [6, 36–38].

The DEGLOR process converts waste materials, including filter dust, bottom ash and also flue gas cleaning residues into two different parts, an inert glassy part, which can be deposited or reused, and a concentrate of heavy metals, which can be divided into reusable metal compositions and salts. The DEGLOR process is described as follows: The waste materials are melted at approximately 1573 K without any additions in an air atmosphere using an electrically heated furnace with continuous input (100 kg/h, plant in Hinwil, Switzerland). The electrodes are located above the melt covered with ceramic tubes to prevent corrosion. Most heavy metals as well as the toxic organic compounds evaporate during the process. Compositions with high boiling points stay in the glass matrix. The flue gases are suddenly cooled to temperatures between 423 and 473 K to avoid a reformation of dioxins (de novo synthesis). The resulting condensable gases are

separated and filled into big bags, whereas the other gas components are resent into the flue gas cleaning system of the incineration facility. The choice of a hot top resistor, electric heating minimizes the amount of flue gases, avoids gas turbulence (no fossil fuel combustion) inside the melting chamber and prevents the output of non-treated filter dust (carry-over). The radiated heat from the ceiling of the melter keeps the bath surface hot and the evaporation at a high level. The DEGLOR process was applied to an incineration plant in Kobe (Japan). The DEGLOR process generally produces a glass fulfilling the strict Swiss regulations for glasses from waste residues to be reused as construction material.

The Ash-Arc process [6, 38] uses a plasma to melt MSW fly ash and bottom ash. These residues, e.g. bottom ash, are separated from the metallic materials prior to the Ash-Arc process. The part, which has a size between 0 and 2 mm is transferred into the melting chamber via hollow electrodes. The direct current (DC) arc furnace develops temperatures up to 1773 K and strongly reducing conditions which reduces the metals in the residues to their elemental state. The metals sink to the bottom and form an alloy phase which can then be separated from the glassy phase. Because of the strongly reducing conditions, the glass from this process is strongly reducing (low  $p_{O_2}$  values in the glass melt).

A comparison of the measured oxidation state (during cooling of the melts) of different glasses obtained from different fly ash vitrification processes and reference glasses is given in figure 2.5. The glasses denoted with DEGLOR and AshArc were produced according to the previously described processes<sup>6</sup> [6, 36–38]. The colorless, green and dark amber glass were glasses prepared for sulfur chemistry studies of soda-lime-silica glasses by Beerkens et al. [35]. The  $p_{O_2}$  measurements of the glasses were used for comparative reasons. The glass from Dutch fly ash, as received, was melted in our laboratory in air and the partial oxygen pressure of the obtained silicate melt was measured. It should be noted that this glass was not suitable for any reuse because of the possible leaching of heavy metals. The chemical composition of this glass is given in table 2.2. The Pittsburgh Corning glass is the starting glass from which the commercially available foam glass is made<sup>7</sup>.

It can be seen from figure 2.5, that the vitrification procedure has a significant influence on the oxidation state of the obtained glass. A more reduced melting environment during the vitrification process, leads to a more reduced glass. The oxidation state values of the DEGLOR glass are close to the values found for normal green soda-lime-silicate container glass, which would probably also be suitable for foam glass production [40]. The oxidation state values of the glass from the Dutch fly ash, prepared in a laboratory furnace in an air atmosphere are close to the one of the foam glass. This shows that vitrifying the fly ash adequately, can probably form a glass being suitable as raw material for foam

---

<sup>6</sup>The author is grateful to Dr. Christian Wieckert, ABB Switzerland research laboratory, Baden, Switzerland, who kindly provided me with the glasses from the DEGLOR and Ash-Arc process for oxidation state measurements.

<sup>7</sup>The author is grateful to Dr. Hans Strauven from Pittsburgh Corning, Tessenderloo, Belgium, who kindly provided me with the glasses for oxidation state measurements.

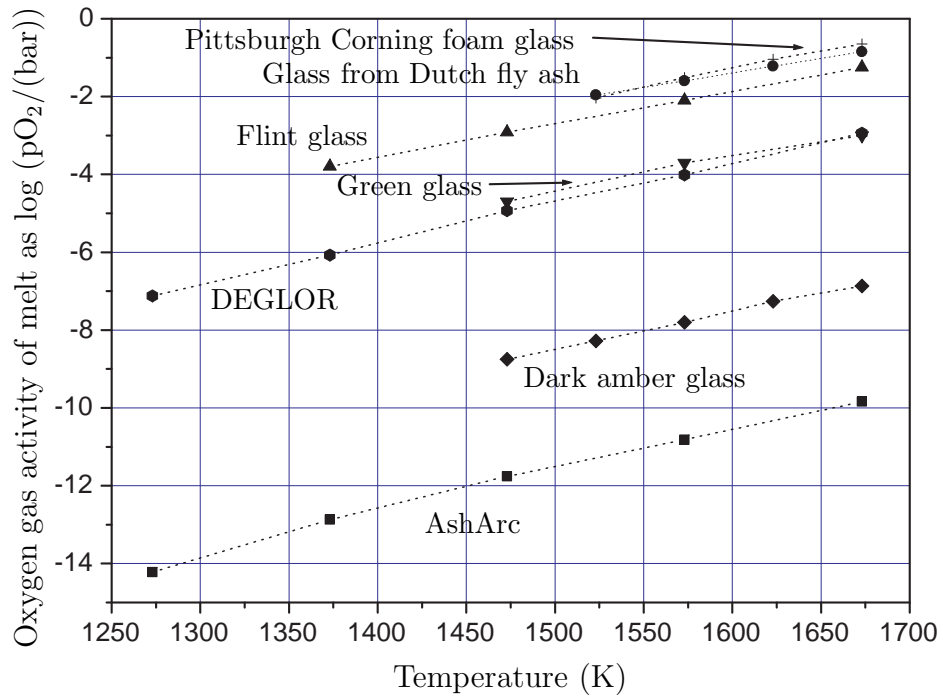


Figure 2.5: Oxygen gas activity in different soda lime silicate glasses melts, measured during cooling of the melts.

Table 2.2: Chemical composition (oxidic) of the vitrified fly ash used in this study (glass phase), after separation of the salt phase, obtained from XRF analysis.

Oxide	Glass phase (wt.%)	Oxide	Glass phase (wt.%)
Na <sub>2</sub> O	1.1	Fe <sub>2</sub> O <sub>3</sub>	3.44
MgO	3.59	NiO	0.03
Al <sub>2</sub> O <sub>3</sub>	16.4	CuO	0.1
SiO <sub>2</sub>	32	ZnO	4.38
P <sub>2</sub> O <sub>5</sub>	2.09	As <sub>2</sub> O <sub>3</sub>	0.02
SO <sub>3</sub>	0.5	Br	<0.01
Cl	0.9	SrO	0.04
K <sub>2</sub> O	0.43	ZrO <sub>2</sub>	0.11
CaO	30	CdO	0.03
TiO <sub>2</sub>	3.03	SnO <sub>2</sub>	0.6
V <sub>2</sub> O <sub>5</sub>	0.06	Sb <sub>2</sub> O <sub>3</sub>	0.27
Cr <sub>2</sub> O <sub>3</sub>	0.2	BaO	0.14
MnO	0.14	PbO	0.39

glass, with respect to the required oxidation state. The influence of the oxidation state on the foaming behavior of a glass melt will be presented in more detail in chapters 4 and 5.

During melting of fly ash at temperatures above 1473 K, the silicate melt and salt phase are in the liquid state. Most of the heavy metals are dissolved in the silicate melt and the salt phase starts to evaporate. The extraction of the heavy metals can only occur by evaporation from the melt. However, more effective methods exist to separate heavy metals from fly ash, making use of the volatile nature of heavy metal chlorides, also used in extractive metallurgy [41]. The heavy metal removal using chlorination agents will be discussed in the next section. Thermodynamic calculations and experimental results from literature references are used to present and discuss the potential to remove metals from fly ash using this extraction method.

## 2.3 Thermodynamics for heavy metal removal by use of chlorination reactions

As mentioned in the last chapter, the heavy metals precipitate from the vapor phase on the surface of the ash particles during cooling of the flue gases after the MSW incineration. As a result, the different heavy metal compounds are mainly present in a relatively pure state as oxides or salts [30, 31]. If a species is in its pure state, its chemical activity is defined to be unity. This allows a basic thermodynamic analysis as first estimate for the evaluation of possible chlorination reactions. This can be done using the standard Gibbs free energy change of a chemical reaction. This type of consideration is only allowed under distinct conditions, which will be discussed in the following.

The standard Gibbs free energy change of a chemical reaction ( $\Delta G^r$ ) is defined as [42]:

$$\Delta G^r \equiv \sum_i \nu_i G_i^r = -RT \ln K_r = -RT \ln \left( \prod_i (a_i)^{\nu_i} \right) \quad (2.2)$$

where  $\nu_i$  denotes the stoichiometric number of species  $i$  in the reaction,  $R$  is the ideal gas constant,  $T$  the absolute temperature,  $K_r$  the chemical equilibrium constant of the considered reaction and  $a_i$  the activity of reacting species  $i$ . The chemical activity of a species  $i$  is defined as:

$$a_i = \gamma_i x_i \quad (2.3)$$

where  $\gamma_i$  denotes the activity coefficient and  $x_i$  the mole fraction of species  $i$ .  $\Delta G^r$  is the difference of the Gibbs free energies of the products and reactants weighed by their stoichiometric coefficients. An analysis based on equation (2.2) can be carried out, assuming pure phases for the solids ( $a_i(\text{solid})=1$ ) and ideal gases ( $(\gamma_i(\text{gases})=1)$ ). This view requires that the temperature of the system is constant and equal for all species and that the pressure of the system is fixed. The pressure for the following calculations was set to  $10^5$  Pa (1 bar).

Under the mentioned conditions,  $\Delta G^r$  can be used as a measure for the reactivity or the probability that a reaction between pure substances forming pure substances takes

Table 2.3: Melting and boiling points of some selected metal and heavy metal compounds [43].

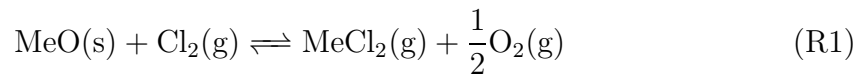
Heavy metal compound	Melting point (K)	Boiling point (K)	Heavy metal compound	Melting point (K)	Boiling point (K)
NaCl	1074	1757	ZnO	2243	–
CaCl <sub>2</sub>	1045	2279	ZnCl <sub>2</sub>	591	1004
MgCl <sub>2</sub>	980	1634	CuO	1609	–
PbO	1159	1897	Cu <sub>2</sub> O	1517	–
PbCl <sub>2</sub>	774	1223	CuCl	709	1485
CdO	–	1755 <sup>a</sup>	CuCl <sub>2</sub>	903	1266 <sup>a</sup>
CdCl <sub>2</sub>	842	1236			

<sup>a</sup> Dissociation

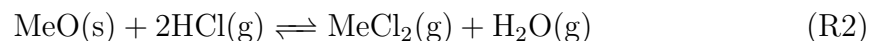
place. This means that, in this case, reactions with negative  $\Delta G^r$  can take place and that comparing reactions, the more negative  $\Delta G^r$ , the more probable a reaction will take place.

As a starting point for the thermodynamic calculations, pure heavy metal compounds, either oxides or salts, are considered. To study the evaporation and melting of different heavy metal compounds, the melting and boiling points of some selected heavy metal compounds are shown in table 2.3. The melting points of the heavy metal chlorides are below 1000 K and the boiling points are below 1300 K (except for CuCl). These temperatures are most of the time below the temperature ranges at which fly ash melts. Figure 2.6 shows the vapor pressure of some selected heavy metal oxides and chlorides as a function of temperature. From the vapor pressure values of the heavy metal chlorides below 1373 K, it is expected that heavy metal chloride evaporation is more favorable than the evaporation of the heavy metal oxides. As shown experimentally, the fly ash shows primary melt phases between 1173 and 1273 K. A transformation of heavy metal oxides into chlorides below the melting range of the fly ash in order to support their evaporation seems to be an advantageous approach to completely separate and extract the heavy metals from fly ash. This even offers the possibility of re-utilization of the heavy metals after extraction of the metals from the condensed chlorides [45]. Generally, four chlorination reactions for the heavy metal oxides deposited on fly ash particle surfaces, using different chlorine sources can be distinguished. It should be noted that for the following consideration, pure substance thermodynamics and  $10^5$  Pa (1 bar) pressure is applied here respecting the above mentioned conditions.

1. Chlorination reaction:



2. Hydro chlorination:





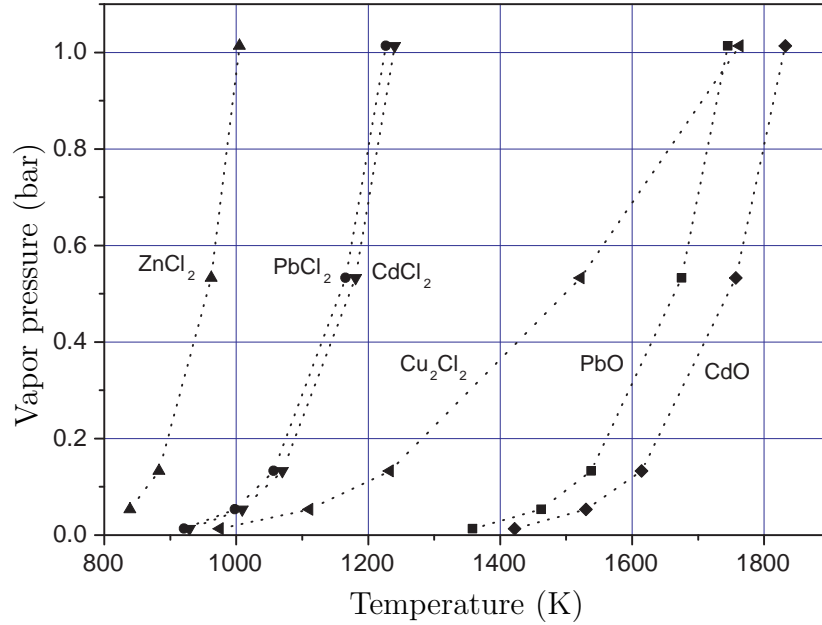
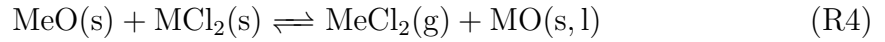
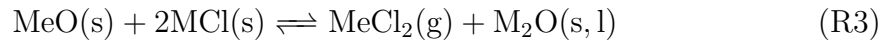


Figure 2.6: Vapor pressure of some pure metal oxides and pure metal chlorides as a function of temperature. Data taken from Barin et al. [44].

3. Salt roasting for mono- and bivalent metal reagents:

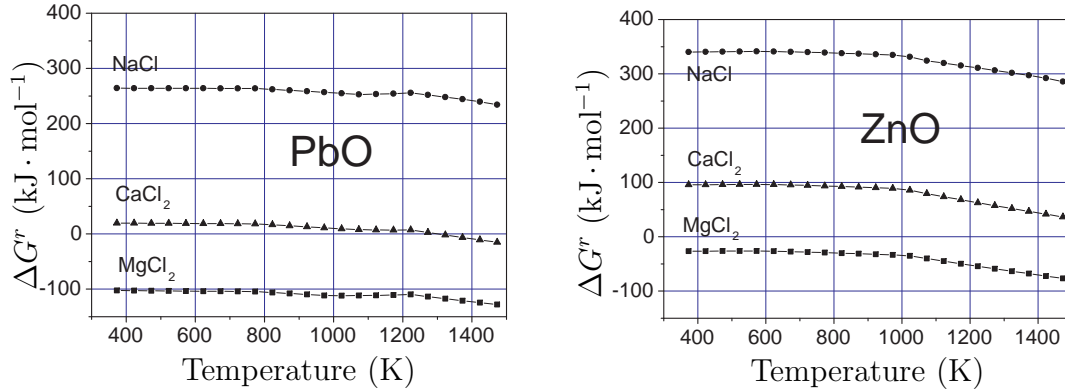


4. Salt and silica additions using mono- and bivalent metal reagents:



where Me denotes the heavy metals, e.g., Pb, Cd, Zn etc. and M denotes the metal in the reagent, e.g., Na, Mg or Ca.

The four different chemical chlorination reactions will be discussed in terms of reactivity ( $\Delta G^r$  values) using PbO and ZnO as exemplary heavy metals. It should be noted that for reactions (R5) and (R6) also other reaction products can be formed, when the amount of, e.g., added  $\text{SiO}_2$  does not represent the stoichiometric quantity for in this case ( $2\text{SiO}_2 \cdot \text{Na}_2\text{O}$ ), which of course would then give other  $\Delta G^r$  values. For exemplary reasons only the exact reaction as given by reactions (R5) and (R6) are considered. The thermodynamic calculations were performed using the computer program FactSage 5.0 (Reaction Module) [46]. The calculated  $\Delta G^r$  values are presented as function of temperature between 373 and 1473 K, whereas always the most stable phase of the different species at a temperature was chosen (solid, liquid or gaseous). The changes in aggregate state (of one or more of the reactants or products) can be seen in the graphs when the



(a)  $\Delta G^r$  as a function of temperature for PbO chlorination according to reaction (R3) or (R4), respectively. (b)  $\Delta G^r$  as a function of temperature for ZnO chlorination according to reaction (R3) or (R4), respectively.

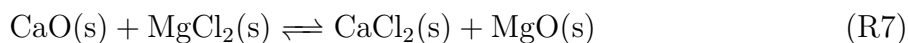
Figure 2.7: Gibbs free energy of reaction,  $\Delta G^r$ , for the reactions (R3) or (R4), respectively for the two heavy metal oxides PbO and ZnO with pure NaCl,  $\text{CaCl}_2$  and  $\text{MgCl}_2$  as reactants.

slopes of the curves suddenly change. All calculations were performed at a pressure of  $10^5$  Pa, assuming reaction of pure reactants forming pure products and ideal gases or gases at  $10^5$  Pa partial pressure.

Figure 2.7 shows the calculated result of the Gibbs free energy of reactions (R3) and (R4) for the heavy metal oxides PbO and ZnO reacting with pure NaCl,  $\text{CaCl}_2$  and  $\text{MgCl}_2$  as reactants. From a thermodynamic point of view, sodium chloride is the less effective reactant, and  $\text{MgCl}_2$  the most effective. However, the formation of pure  $\text{Na}_2\text{O}$  is not very probable as single oxide, compared to CaO or MgO. In the fly ash environment, sodium oxide more probably forms silicates in the form of, e.g.,  $\text{Na}_2\text{O} \cdot \text{SiO}_2$  rather than existing alone as  $\text{Na}_2\text{O}$ . This would then result in lower  $\Delta G^r$  values. This can be seen in figure 2.9, which will be discussed later.  $\text{CaCl}_2$  is also less favorable to react with the heavy metals than  $\text{MgCl}_2$  forming heavy metal chlorides.

Jakob et al. [21, 22] experimentally studied the evaporation of heavy metals (Zn, Pb, Cd and Cu) from untreated, fine grained MSW fly ash in the temperature range between 943 and 1573 K. At 1373 K, the total evaporation loss of Pb, Cd and Cu in an air atmosphere was between 98 - 100% and 50% for Zn, compared to the initial heavy metal content in the fly ash. In an Argon atmosphere, the evaporation loss of Pb, Cd and Zn was 98 - 100% and 10% for Cu. The weak evaporation of Zn in the air atmosphere was related to the formation of  $\text{Zn}_2\text{SiO}_4$  and  $\text{ZnAl}_2\text{O}_4$ , whereas the low evaporation rate of Cu in the argon atmosphere was related to the reduction of Cu- compounds to elemental Cu by  $\text{H}_2$  or C in the studied temperature range [21]. In a later study [22], the evaporation (loss and rate of evaporation) of the selected heavy metals was related to the chlorine content in the fly ash. Chan et al. [47] showed experimentally, that approximately 90%

of Pb, Zn, Cu and Cd can be removed from fly ash by adding solid chlorination agents such as: NaCl, AlCl<sub>3</sub>, MgCl<sub>2</sub>, FeCl<sub>2</sub> and CaCl<sub>2</sub>. For the evaporation of Pb, Cu, and Cd, the choice of chlorination agent showed hardly an influence on the maximum evaporation, except for Zn and for larger additions of chlorination agent. With NaCl and AlCl<sub>3</sub>, the evaporation of Zn was about 20% less than with the other three chlorination agents. A study by Buekens et al. [48] on the chlorination of heavy metals using molten salts (NaCl, CaCl<sub>2</sub> and MgCl<sub>2</sub>), showed, that a mixture of 30 wt.% MgCl<sub>2</sub> and 70 wt.% of CaCl<sub>2</sub> is efficient in ecological and economical terms: From the three salt reactants, MgCl<sub>2</sub> is the most expensive, but the most efficient. Pure MgCl<sub>2</sub> was experimentally found to be the most efficient salt in terms of heavy metal evaporation, even for ZnO entrapped in a silicate matrix. The fact that ZnO can be entrapped in a silicate matrix, was also found by Jakob et al. [21]. The efficiency of MgCl<sub>2</sub> in the removal of heavy metals from the fly ash decreases from 99% to 88% with the addition of 24 wt.% of CaO to the fly ash. This decrease in MgCl<sub>2</sub> efficiency was related to the competitive reaction [48]:



However, to select the type of salt species for the heavy metal evaporation, the efficiency or reactivity is not the only criterion. From the salt roasting reactions (reactions (R3), (R4), (R5) and (R6)), it can be seen, that the oxide of the metal reagent will stay in the fly ash and thus later on in the glass. Fly ash already contains large amounts of calcium oxide, which decreases the vitrifiability of the fly ash, because it increases for example the liquidus temperature of a silicate glass melt. This may lead to crystallization during the cooling or forming (foaming) process of the silicate melt. Thus further additions of Ca-containing components are not preferable. The addition of MgCl<sub>2</sub> is limited by the final MgO content in the glass, which is usually about 4-5 wt.%.

The chlorination by application of gaseous chlorination agents according to reactions (R1) and (R2), does not show the disadvantage of unwanted reaction products as with the addition of solid or molten salts. Figure 2.8 shows  $\Delta G^r$  as a function of temperature for the two different chlorination reactions (R1) and (R2), respectively for pure PbO and pure ZnO with either HCl or Cl<sub>2</sub> at 10<sup>5</sup> Pa partial pressure. It can be seen, from a thermodynamic point of view, that below 873 K, HCl is a better reagent for the formation of the pure heavy metal chloride than Cl<sub>2</sub>, which seems to be better above that temperature. Comparing the  $\Delta G^r$  values for the reactions, using the solid or molten salts with reactions using the gaseous chlorine species as presented in figures 2.7 and 2.8, the chlorination and thus the evaporation, using the gaseous chlorination agents seems to be more efficient. This is because the  $\Delta G^r$  values for the chlorination with HCl or Cl<sub>2</sub> (at 10<sup>5</sup> Pa), are lower than using the pure solid chlorides. In technical applications, the above reactions also depend on the partial pressures of O<sub>2</sub> and H<sub>2</sub>O in the furnace or reactor atmosphere.

All four types of chlorination reactions are shown in figure 2.9 for comparative reasons, where ZnO was used as exemplary heavy metal oxide. This is because, as seen from the experimental results from [21, 22, 47], the evaporation of ZnO from fly ash is one of the most difficult to realize technically. In terms of heavy metal chlorination, NaCl is the worst reactant, even with SiO<sub>2</sub> present, forming Na<sub>2</sub>O · SiO<sub>2</sub>, because Na<sub>2</sub>O is usually not very stable. Salt roasting with pure MgCl<sub>2</sub>, seems to be very favorable for the chlorination

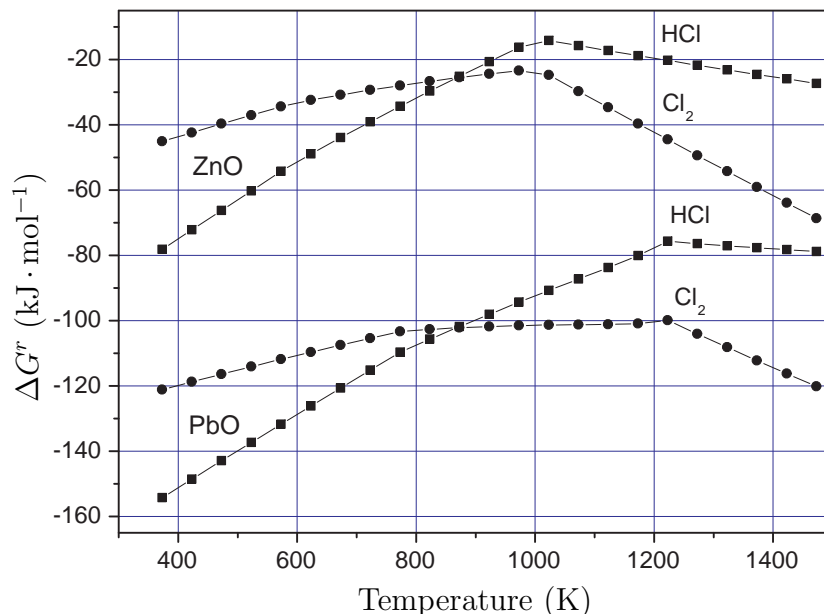


Figure 2.8: Gibbs free energy of reaction ( $\Delta G^r$ ) as a function of temperature for the different chlorination reactions (R1) and (R2), respectively for pure PbO and ZnO. Gases are at  $10^5$  Pa pressure.

of ZnO, even better at the presence of  $\text{SiO}_2$  and better than the treatment with  $\text{Cl}_2$  or HCl, at temperatures above 523 K.

An extensive experimental study by Wedemeyer [10] on the recovery of heavy metals from fly ash of MSW incinerators by chloridizing volatilization also showed, that the evaporation of heavy metals is significantly enhanced by addition of chlorine, either gaseous or solid. This results in a fly ash material residue, which meets the Swiss regulations for inert material<sup>8</sup> [49]. Packed bed experiments at 1073 K for 240 minutes showed an evaporation of (wt.%) 98.6% for Zn, 97.7% for Pb, >90% for Cd (below detection limit) and 73.7% for Cu (below the regulation limit of 0.05 wt.%). However, it was found, that gaseous chlorine gas ( $\text{Cl}_2$ ) was not more favorable, than solid chlorides, especially  $\text{MgCl}_2$ . This was also observed from the thermodynamic calculations as shown in figure 2.9, where the differences in  $\Delta G^r$  values are not large. Because of the high amount of  $\text{SiO}_2$  in fly ash, the formation of  $\text{MgO} \cdot \text{SiO}_2$  is also very probable. A major disadvantage of the use of gaseous chlorine is the chlorine content of the fly ash after the treatment, which was about 25-30 wt.%.

The hydro-chlorination, as represented by reaction (R2), uses HCl as chlorination agent. The effectiveness of this method was also shown by [45,50]. The use of HCl as chlorination agent was studied in the European project UPCYCLE - "Treatment of fly ash for sound material utilization" [48]. The highest removal rates of 99.2% for Zn, 99.7% for Pb and 99.8% for Cd were achieved at a HCl concentration in the carrier gas of 15 vol.% (10

<sup>8</sup>Limits for inert material in Switzerland (wt.%): Zn: 0.1, Pb: 0.05, Cd: 0.001, Cu: 0.05

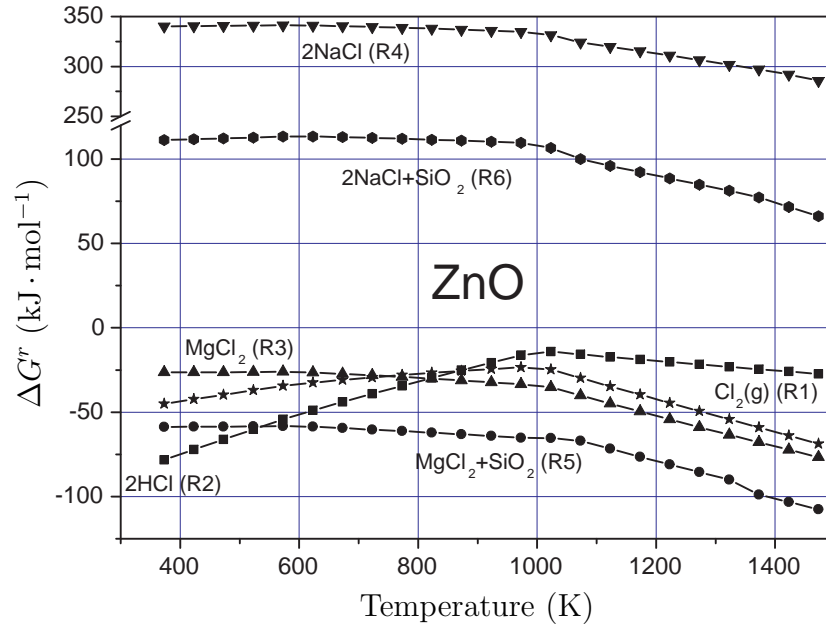


Figure 2.9: Gibbs free energy of reaction ( $\Delta G^r$ ) as a function of temperature for the different chlorination reactions ((R1)- (R6)) for pure ZnO with different chlorination agents. The reaction products (pure substances) follow directly from the reaction equations, indicated in parentheses. Gases are at  $10^5$  Pa pressure.

vol.% H<sub>2</sub>O and 65 vol.% N<sub>2</sub>), at 1200 K for 90 minutes residence time in a horizontal tube furnace. Because of the good heavy metal removal efficiency, the HCl chlorination was applied to a pilot plant fluidized bed setup and later to the so called CT-Fluapur process [23], which was integrated into a conventional MSW incinerator. With this industrially applied process, the following removal rates at 1173 K for 4 hours with a HCl concentration of 10 vol.% were achieved: Zn: 98.5%, Cu: 99.5%, Cd: 99.8%, and Pb: 99.8%. A schematic representation of the CT-Fluapur process is given in figure 2.10. With the CT-Fluapur process, the detoxification can be carried out with a low energy consumption. Bottom ash can also be treated optionally. A small part of the incineration flue gases is transferred into the detoxification reactor and an additional burner is installed to stabilize the temperature. The HCl from the flue gas scrubber system is used to create the necessary 10 vol.% HCl atmosphere necessary for the chlorination reactions. The heavy metal chlorides are recuperated in a filter system as recyclable heavy metal condensate. The flue gases from the detoxification are cleaned together with the incineration flue gases. As final product, an inert material, which fulfills, e.g., the Swiss guideline for the reuse as cement or concrete addition, is obtained.

## 2.4 Concluding remarks

Many detoxification techniques resulting in an almost inert material, i.e., a material which does not show leaching of environmental harmful components, have been developed in the

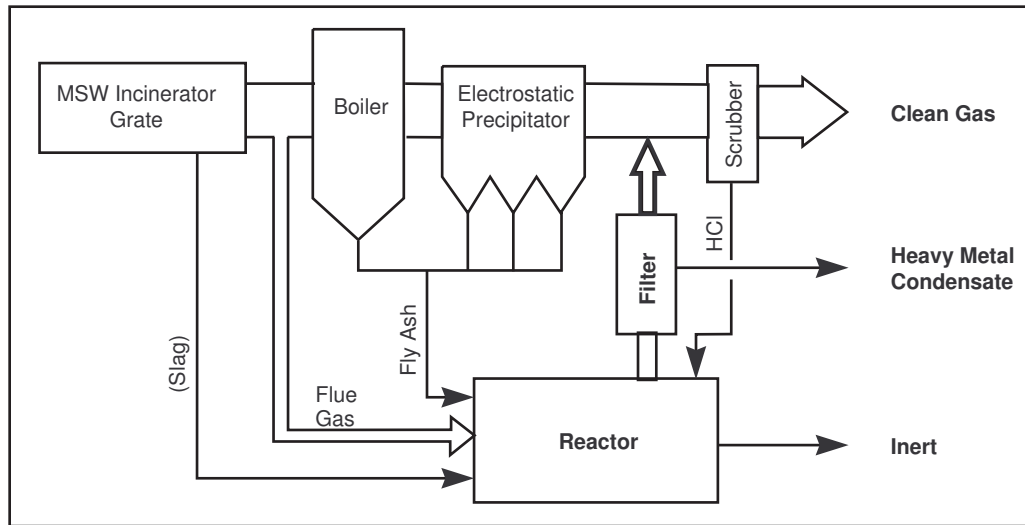


Figure 2.10: Schematic representation of the CT-Fluapur process. The scheme was adopted from [23].

past. Not every process is suitable to use its treated (final) product as raw material for foam glass production. Some of these processes result directly in an inert glass, e.g., DEGLOR or AshArc, where, e.g., the oxidation state of the glass determines whether the glass can be used for foam glass production. The detoxification of fly ash by use of chlorination agents has shown to be very effective for the separation of heavy metals below the melting range of the fly ash. Especially hydrochlorination is very effective and industrially applicable. The disadvantage of residual chlorine in fly ash after the chlorination, risking its evaporation during melting of fly ash and refractory corrosion, can be avoided by already present techniques of salt layer removal [39].

A three step treatment, meaning first the heavy metal removal by use of chlorination agents, secondly further heating and subsequent separating of the salt layer after its formation and finally melting to obtain a homogeneous silicate melt can lead to a glass product harmless to the environment. The temperature ranges for these three process steps are as follows:

- **$T < 1200 \text{ K}$** : Heavy metal separation and extraction by evaporation using gaseous or solid chlorination agents, preferably  $\text{HCl}$  or  $\text{MgCl}_2$ .
- **$1200 \text{ K} < T < 1500 \text{ K}$** : Melting of fly ash and separation of the salt layer.
- **$T > 1500 \text{ K}$** : Complete melting of the fly ash melt into a silicate melt.

Compositional additions to fly ash prior or during the thermal process can be applied to adopt the final glass composition, e.g., sand or soda or the addition of  $\text{MgCl}_2$  to adopt the  $\text{MgO}$  content in the final silicate melt, for foam glass production. The selection and the combination of the different techniques is determined by the required heavy metal removal efficiency and the requested final glass properties for foam glass production, e.g., oxidation state, viscosity, iron content etc..

## 2.5 Bibliography

- [1] E.W. Haltinger and J. Jochum. Filterstaub entgiften und verwerten. *Energie*, 43(1/2):28–33, 1991.
- [2] A.R. Boccaccini, M. Köpf, and W. Stumpfe. Glass-ceramics from filter dusts from waste incinerators. *Ceramics International*, 21:231–235, 1994.
- [3] A. R. Boccaccini, M. Petitmermet, and E. Wintermantel. Glass-ceramics from municipal incinerator fly ash. *Am. Cer. Soc. Bul.*, 76(11):75–78, 1997.
- [4] R. Gutmann. Recycling of municipal solid waste incinerator ash by thermal separation and vitrification. *Proc. R25 Conference, Geneva*, 4:9–13, 1995.
- [5] W. Wenzel and M. Schingnitz. Die Verglasung von Filterstäuben nach dem NOELL-Verfahren. In *Einschmelzen von Filteraschen und Verwertung der Produkte*. Institut für Umwelttechnologie und Umweltanalytik e.V., 1994. Proc. IUTA Workshop Duisburg-Rheinhausen, Germany.
- [6] F. G. Simon and J. Millard. AshArc<sup>TM</sup>, Ein Schmelzprozeß für Aschen aus der Abfallverbrennung. *Glas-Ingenieur*, (3):53–56, 1997.
- [7] A. Selinger, C. Wieckert, V. Schmidt, B. Carcer, H. Rüegg, and G. Mechtersheimer. Inrec<sup>plus</sup> The next step in waste incineration ash recycling. Internal ABB report, 2000.
- [8] H. Pieper, H. Zschocher, G. Mayer-Schwinning, and H. Merlet. SOLUR-Glasschmelzverfahren. *Müll und Abfall*, pages 116–118, 1990. Beihefte 29, Reststoffe aus der Rauchgasreinigung.
- [9] R. Gutmann. Thermal technologies to convert solid waste residuals into technical glass products. *Glastechn. Ber. Glass Sci. Technol.*, 69(9):285–299, 1996.
- [10] S. Wedemeyer. *Recovery of heavy metals from fly ash of municipal solid waste incinerators by chloridizing volatilization*. PhD thesis, Clausthal, Techn. Univ., Germany, 2003.
- [11] Besluit stortverbod afvalstoffen. Staatsblad van het Koninkrijk der Nederlanden 665, 1997.
- [12] R. Gutmann and H. Vonmont. Elektrofilterasche aus Müllverbrennungsanlagen - Quantitative Zusammensetzung. *Z. Umweltchem. Ökotox.*, 6(5):257–263, 1994.
- [13] R. Gutmann. Charakterisierung von verglaster Elektrofilterasche aus Müllverbrennungsanlagen. *Abfallwirtschaftsjournal (Sonderdruck)*, 6:2–11, 1994.
- [14] H. Vogg and L. Stieglitz. Thermal behavior of PCDD/PCDF in fly ash from municipal incinerators. *Chemosphere*, 15:1373–1378, 1986.

- [15] R. Ishikawa, A. G. Buekens, H. Huang, and K. Watanabe. The relationship between flue gas/fly ash compositions and dioxin level in fluidized bed incinerators. *Chem. Eng. Technol.*, 23(4):313–315, 2000.
- [16] H. Huang and A. Buekens. On the mechanisms of dioxin formation in combustion processes. *Chemosphere*, 31:4099–4117, 1995.
- [17] H. Huang and A. Buekens. De novo synthesis of polychlorinated dibenzo-p-dioxins and dibenzofurans. Proposal of a mechanistic scheme. *Sci. Total Environment*, 193(2):121–141, 1996.
- [18] K. G. Schmidt and T. Leclaire. Ökologischer Vergleich verschiedener Behandlungsverfahren zur Inertisierung und Verwertung von HVM-Rückständen/Abfällen (Teil A). Abschlußbericht zum Forschungsvorhaben 103 10 902 des Bundesministeriums für Umwelt, Naturschutz und Reaktorsicherheit, Germany, June 1996.
- [19] K. G. Schmidt and T. Leclaire. Ökologischer Vergleich verschiedener Behandlungsverfahren zur Inertisierung und Verwertung von HVM-Rückständen/Abfällen, Teil B: Verfahrensbeschreibungen, June 1996. Abschlußbericht zum Forschungsvorhaben 103 10 902 des Bundesministeriums für Umwelt, Naturschutz und Reaktorsicherheit, Germany.
- [20] Kyung-Jin Hong, Shuzo Tokunaga, and Toshio Kajiuchi. Extraction of heavy metals from MSW incinerator fly ashes by chelating agents. *J. Hazard. Mater.*, B 75:57–73, 2000.
- [21] A. Jakob, S. Stucki, and P. Kuhn. Evaporation of heavy metals during the heat treatment of municipal solid waste incinerator fly ash. *Environ. Sci. Technol.*, 29(9):2429–2436, 1995.
- [22] A. Jakob, S. Stucki, and S. P. W. J. Struis. Complete heavy metal removal from fly ash by heat treatment: Influence of chlorides on evaporation rates. *Environ. Sci. Technol.*, 30(11):3275–3283, 1996.
- [23] A. Jakob and R. Moergeli. Detoxification of municipal solid waste incinerator fly ash: the CT-fluapur process. In I. Gaballah, J. Hager, and R. Soloabal, editors, *Proc. REWAS'99, San Sebastian, Spain*, pages 1737–1744, September 1999.
- [24] H. Scholze. *Glas Natur, Struktur und Eigenschaften*. Springer-Verlag, Berlin Heidelberg New York, 1988.
- [25] M. Krauß. Vitrification of waste materials. *Glastechn. Ber. Glass Sci. Technol.*, 70(12):375–381, 1997.
- [26] A. Plüss and Jr. R. E. Ferrell. Characterization of lead and other heavy metals in fly ash from municipal waste incinerators. *Hazard. Waste Hazard. Mater.*, 8(4):275–292, 1991.
- [27] C. S. Kirby and J. D. Rimstidt. Mineralogy and surface properties of municipal solid waste ash. *Environ. Sci. Technol.*, 27(4):652–660, 1993.



- 
- [28] T. T. Eighmy, T. D. Eusden Jr., J. E. Krzanowski, D. S. Domingo, D. Stämpfli, J. R. Martin, and P. M. Erickson. Comprehensive Approach towards understanding element speciation and leaching behavior in municipal solid waste incineration electrostatic precipitator ash. *Environ. Sci. Technol.*, 29(3):629–646, 1995.
- [29] W. Vogel. *Glaschemie*. Springer-Verlag, Berlin, Heidelberg, New York, 3 edition, 1992.
- [30] H. Brunner and H. Mönch. The flux of metals through municipal solid waste incineration. *Waste Management Res.*, 4:105–119, 1986.
- [31] L. Morselli, S. Zappoli, and S. Militerno. The presence and distribution of heavy metals in municipal solid waste incinerators. *Toxicol. Environ. Chem.*, 37:139–145, 1993.
- [32] W. P. Linak and J. O. L. Wendt. Toxic metal emission from incineration: Mechanisms and control. *Prog. Energy Sci.*, 19:145–185, 1993.
- [33] T. Thonthat and G. Odon. Redox des calcins de recyclage. *Verre*, 3(5), 1997.
- [34] R. G. C. Beerkens, A. Faber, J. Plessers, and T. Thontat. Methods for the characterization of redox state of cullet and batches in glass manufacturing. *Glass International*, pages 371–375, 1997.
- [35] R. G. C. Beerkens and K. Kahl. Chemistry of sulfur in soda-lime-silica glass melts. *Phys. Chem. Glasses*, 43(4):189–198, 2002.
- [36] R. Gutmann, C. Wieckert, and H. Vonmont. Verglaste Filterstäube aus Müllverbrennungsanlagen - Schmelzverfahren, Prozeßführung und chemische Analyse. *UWSF-Z. Umweltchem. Ökotox.*, 8(4):187–196, 1996.
- [37] M. Hirth, J. Jochum, H. Jodeit, and C. Wieckert. A thermal process for the detoxification of filter ash from waste incinerators. In *Envirotech Proc. Vienna 20-23 February 1989*, pages 267–281. Elsevier Press, 1989.
- [38] D. Traber, U. Mäder, U. Eggenberger, F.-G. Simon, and C. Wieckert. Phase chemistry study of products from the vitrification processes Ash Arc and Deglor. *Glastechn. Ber. Glass Sci. Technol.*, 72(3):91–98, 1999.
- [39] H. Pieper, L. Rott, and M. Bucar. Process and apparatus for separating gall in glass-melting processes in electrically heated furnaces for vitrifying asbestos, fly ashes, and filter ashes. Eur. Pat. Appl. EP 718242 A2, 1996.
- [40] S. Köse and G. Bayer. Schaumbildung im System Altglas-SiC und die Eigenschaften derartiger Schaumgläser. *Glastechn. Ber. Glass Sci. Technol.*, 55(7):151–160, 1982.
- [41] O. Kubaschewski and C. B. Alcock. *Metallurgical Thermochemistry*. Pergamon Press, 5 edition, 1979.

- [42] J. M. Smith, H. C. Van Ness, and M. M. Abbott. *Introduction to Chemical Engineering Thermodynamics*. Chemical Engineering Series. McGraw-Hill International, fifth edition, 1996.
- [43] O. Knacke, O. Kubaschewski, and K. Hesselman. *Thermochemical properties of inorganic substances*. Springer Verlag, Berlin, 2 edition, 1991.
- [44] I. Barin, F. Sauert, E. Schultze-Rhonhof, and Wang Shu Sheng. *Thermochemical data of pure substances*, volume 1+2. Weinheim, VCH, second edition, 1993.
- [45] E. M. L. Peek. *Chloride pyrohydrolysis - lixiviant regeneration and metal separation*. PhD thesis, Technical University Delft, The Netherlands, 1995.
- [46] C. W. Bale, A. D. Pelton, and W. T. Thompson. *FactSage 5.0 User Manual*, 2001. Ecole Polytechnique de Montréal, Royal Military College, Canada.
- [47] C. Chan, C. Q. Jia, W. Graydon, and D. W. Kirk. The behavior of selected heavy metals in MSW incineration electrostatic precipitator ash during roasting with chlorination agents. *J. Hazard. Mater.*, 50:1–13, 1996.
- [48] UPCYCLE - Treatment of fly ash for sound material utilization. European Union Research Project ENV4-CT95-0085.
- [49] Schweizerischer Bundesrat. Technische Verordnung für Abfälle (TVA), 1990.
- [50] H. J. Luggenhorst and C. L. Deelen. Metal separation through pyrohydrolysis. Proceedings R'25 Meeting, Geneva, Switzerland, 1995.

## Chapter 3

# Prediction of chemical activities and liquidus temperatures in multicomponent oxide glass melts

---

3.1	Introduction . . . . .	53
3.2	Chemical activity models for multicomponent oxide glass melts . . . . .	55
3.3	Prediction of liquidus temperatures . . . . .	73
3.4	Concluding remarks . . . . .	78
3.5	Nomenclature . . . . .	81
3.6	Bibliography . . . . .	83
3.7	Appendix: Gibbs energy minimization procedure used in IMCM . . . . .	86

---

The experimental results presented in the second chapter of this thesis, show that the studied fly ash<sup>1</sup> starts to form melt phases above 1273 K. After sufficient time, at temperatures above 1473 K, this leads to a homogeneous melt phase, which forms a glass upon fast cooling. It has also been shown that the strongly altering fly ash compositions cause varying glass compositions. As seen in the second chapter, the melts from fly ash are highly corrosive and also contain heavy metals and salts, that evaporate easily from the melt. During slow cooling, the obtained glass is sensible to crystallize, because of the relatively high calcium oxide concentrations ( $\text{CaO} > 25 \text{ wt.}\%$ ). Crystallization behavior depends, among other things, on the glass composition and the rate of cooling [1]. This high CaO content can thus result in high liquidus temperatures with, e.g., devitrite or wollastonite as possible crystalline species appearing below the liquidus temperature.

---

<sup>1</sup>The fly ash discussed in this chapter and elsewhere in this thesis is fly ash from municipal solid waste incineration facilities exclusively.

Most glass properties change with the glass composition (e.g., density, viscosity, etc.). So do the thermodynamic properties, e.g., enthalpy, entropy or heat capacity, thermodynamic potentials or the liquidus temperature. The chemical activities of the different species in a glass melt are indispensable for quantitative treatment of a glass melt and its environment (reactivity, vapor pressures, etc.). The corrosion of refractory materials by a glass melt or the evaporation of volatile species from the glass melt are important phenomena in industrial glass melting processes [2–5]. The liquidus temperature is important for the temperature range for shaping or forming of glass into a final product. In the foam glass formation process, crystallization should be avoided.

To produce an insulating foam glass from the vitrified fly ash melts, the melt must very often be adopted to have the adequate properties for foam glass production. Afterwards, for the designing of the foam glass itself, the foam must have sufficient mechanical strength and optimal insulating properties. Therefore, the glass must be homogeneous and free of any crystals. Crystals in the glass influence the apparent viscosity of the glass melt and thus the foaming behavior [6]. They also influence the structural integrity of the foam due to differences in thermal expansion between the glass and the crystals. This can result in open or cracked lamellae between adjacent bubbles, which reduces the insulation behavior of the foam and enhances further coalescence of bubbles during foaming [6]. Compositional modifications in the melt phase can change the crystallization tendency of the fly ash melt. Due to the strongly altering composition of fly ash, which is observed in practice, the fly ash melt composition also varies [7,8]. These compositional variations cause fluctuations in glass properties as well as differences in crystallization behavior.

In order to optimize the preparation of glass melts from fly ash, applicable for foam glass production and to respond to the strongly varying composition, a general and fundamental model to predict the chemical activity of the glass melt components is desired. Such a model can also be used to predict for example the liquidus temperature of a multicomponent glass melt. In that case, such a model can be used to optimize the selection of the compositional additions to the fly ash melt in order to prevent or minimize crystallization and to process the fly ash melt into a foamable glass, which is not prone to crystallization.

In this chapter, a thermodynamic model is presented, which estimates chemical activities in multicomponent silicate glass melts as a function of the oxide glass composition and the temperature. The model is based on a fundamental thermodynamic approach and estimates the chemical activities in the glass melt of the oxides and the structural compounds. The structural compounds are stoichiometric crystal phases that exist in the phase diagram and that can be formed/crystallize below the liquidus line (e.g.  $\text{Na}_2\text{O} \cdot \text{SiO}_2$ ).

The chapter is structured as follows: First, a literature overview is given, discussing concepts and models to calculate the chemical activity and liquidus temperatures in multicomponent silicate oxide mixtures. Consecutively, the equations for a new activity model are derived and the model is validated for a few silicate compositions with experimental data presented in literature. The model is applied to a glass with a typical fly ash composition. Finally, the model is used to calculate the parts of the liquidus line of the binary sodium silicate system.

## 3.1 Introduction

The liquidus temperature, of two, three or four component glass systems can be obtained from experimentally determined phase diagrams, which are available for a large number of oxide systems forming silicate glass melts [9, 10]. However, for multicomponent glass melts, the liquidus temperature can not be easily obtained from these phase diagrams and either empirical or sophisticated theoretical models are required to predict the liquidus temperature from a given oxide glass composition.

Several models to calculate the liquidus temperature have been proposed in literature. Backman et al. [11] calculated the liquidus temperature of multicomponent soda-lime-silicate glasses ( $\text{SiO}_2$  concentration between 70 and 77 wt.%) with an empirically derived polynomial model based on the oxide glass composition. The model is linear in terms of participating oxides (in wt.%) and uses different, by regression of experimental results determined, coefficients for the different oxides in the glass. These coefficients, which are based on extensive experimental work, relate glass composition and liquidus temperature. In order to optimize the model, it was extended by Karlsson et al. [12]. The extension incorporates the presence of stoichiometric compounds (e.g.  $\text{SiO}_2 \cdot \text{Na}_2\text{O}$ ,  $\text{SiO}_2 \cdot 2\text{Na}_2\text{O}$ , etc.) in addition to the single oxides (e.g.  $\text{SiO}_2$ ,  $\text{Na}_2\text{O}$ ,  $\text{CaO}$ , etc.). The developed model enables an estimation of the liquidus temperature within the investigated compositional range with a standard deviation of 25 K. To describe the experimentally observed nonlinearity of the liquidus temperature dependency on glass composition and to improve the polynomial models, Dreyfus et al. [13, 14] used a neural network technique to calculate the liquidus temperature from the glass composition. For three and four component oxide systems, their standard prediction error was between 20 and 40 K. For a five component oxide mixture, the calculated standard prediction error was about 18 K.

The disadvantage of both methods, the polynomial and neural network approach, is that they have no fundamental physicochemical basis, compared to a general thermodynamic approach. They rely on empirically found relationships between the glass composition and the liquidus temperature. This limits the prediction capability of these models outside the compositional range of the underlying experiments. The equations to describe the liquidus temperature of the glass systems are fitted to experimental results, which restricts applications outside the range of experimental conditions. Also, adding one or more components needs reconsideration of the system. This implies that all parameters have to be fitted again to the results of a new experiments. The number of required experiments, increases tremendously with the number of components.

A general approach to calculate the liquidus temperature of glasses is given by Buler [15]. He describes a thermodynamic criterion for crystallization from a supercooled liquid. The model is based on the determination of the Gibbs energy decrement as the driving force of crystallization during crystallization from a supercooled melt (glass). However, the calculation of the Gibbs energy decrement depends on the chemical activity of the participating species, which is not always known. Calculations are therefore only possible by assuming activities or activity coefficients, respectively. Buler only applied his approach to binary silicate systems assuming activity coefficients. However, this shows that a gen-

eral basic thermodynamic approach is desired to determine the liquidus temperature of complex glasses. Today, the missing information about the chemical activity data limits the application of Buler's method for, e.g., multicomponent glasses.

A more sophisticated approach to determine thermodynamic properties of non-ideal multicomponent liquid systems, such as glass melts was developed by Pelton and Blander [16,17], resulting in the computer program FactSage [18]. This software package uses the so-called modified quasi-chemical approach to calculate thermodynamic properties, based on semi-empirical equations<sup>2</sup>. The theory of the modified quasi-chemical approach as well as its application to binary and ternary systems is given and demonstrated by Pelton et al. [16]. Because of the semi-empirical nature of the model, it contains fitting parameters, to adapt the model. Very accurate results are obtained for systems, for which the model parameters are fitted to existing phase diagrams. In a recent publication on refractory corrosion [2] the computer program ChemSage [19] was partly used to assess the thermodynamic data of the considered system and to perform the thermochemical calculations [2–5]. Outside the optimized range, these systems are less reliable and also have to be optimized and validated again, for instance when components are added to the system. Backman et al. [11] compared experimental liquidus temperature data for multicomponent glasses with predicted data from thermodynamic calculations using the FactSage 2.0 software package. The investigated glasses have a SiO<sub>2</sub> concentration between 70 and 77 wt.%. The predicted liquidus temperatures were on average 50 K higher than the experimental values, which is a rather large deviation. The maximum deviation from the experimental values was even more than 100 K.

This examination shows the high level complexity of liquidus temperature calculations and predictions for multicomponent silicate oxide glasses. Existing models are either semi-empirical and based on extensive experimental work or theoretical using chemical activity calculations. The chemical activity of a species in a glass melt is usually, not known and difficult to determine experimentally. However, the knowledge of the chemical activity data is the key to thermodynamic calculations. It is of major interest not only for the calculation of the liquidus temperature, but also for the derivation of other thermodynamic properties e.g. thermodynamic potentials, enthalpies of formation, vapor pressures or redox equilibria constants. Therefore a theoretical model, free of adjustable

---

<sup>2</sup>A regular solution model assumes random mixed atoms even though the enthalpy of mixing is not zero. The configurational entropy should vary with temperature, which is better treated with the quasi-chemical model, where a non-random distribution of the atoms is realized. It also incorporates a mass balance. The modified quasi-chemical model as developed by Pelton et al. [16] incorporates modifications to the short range ordering of the underlying quasi-chemical model. If a binary mixture of the two pure liquids A and B is considered, the quasi-chemical theory focusses on the energy change for making some A-B bonds in the mixture at the expense of A-A and B-B bonds,  $A-A + B-B = 2A-B$ . As the energy change described by a particular function becomes zero, then the solution is an ideal mixture. As the energy change becomes negative the formation of A-B pairs is favored. As the energy change becomes positive the formation of A-A and B-B pairs are preferred and the solution shows a tendency to immiscibility. When applied to molten silicates, the bonds are formed between the second nearest neighbor ( $M_i$  and Si pairs). The quasi-chemical theory assumes furthermore that pair bond energies are additive and independent of composition. However, to obtain a good agreement between modeled and experimental phase diagrams and thermodynamic data, a polynomial composition dependency of the parameters in the particular function were introduced [9].

parameters, to estimate the chemical activity of single oxides and structural compounds in multicomponent silicate glass melts is going to be presented.

## 3.2 Chemical activity models for multicomponent oxide glass melts

Approaches to the thermodynamic description of multicomponent oxide glasses and their melts are for instance the so-called compound concept of thermodynamics or the modified associate species approach. The compound concept or modified associate species approach are both based on the same assumptions. The names of the approaches are different, because they were developed independently by different investigators. Both thermodynamic approaches are based on the assumption of structural ordering of a glass melt. Application of the compound concept to oxide glasses, was also independently developed and applied by several investigators [20–26]. The modified associate species approach was probably first presented by Hastie et al. [27, 28]. The theoretical background, the experimental validity of this compound concept, and its application for glasses is described by Conradt [25].

According to the compound concept, a glass melt is described by so-called constitutional components, subdivided into two types: the oxides and the structural compounds. These three terms are going to be explained using the sodium-silicate system as an example. For other multicomponent systems other ternary or higher-order compounds have to be included.

**Oxides:** The oxides are the single oxides  $\text{SiO}_2$  and  $\text{Na}_2\text{O}$ . They represent the compositional boundaries (end-members) of the system.

**Structural compounds:** The structural compounds are those species, for which crystalline phase exist in the phase diagram in equilibrium with a melt. They represent the species that can be formed from the oxides and which can crystallize below the liquidus temperature, thus:  $3\text{Na}_2\text{O} \cdot 8\text{SiO}_2$ ,  $\text{Na}_2\text{O} \cdot 2\text{SiO}_2$ ,  $\text{Na}_2\text{O} \cdot \text{SiO}_2$ ,  $2\text{Na}_2\text{O} \cdot \text{SiO}_2$  and  $3\text{Na}_2\text{O} \cdot 2\text{SiO}_2$ .

**Constitutional components:** The constitutional components constitute (define) the system. They represent all **species** in the system, thus the **oxides** and the **structural compounds**. It should be noted that the constitutional components of a glass melt should not be considered as heterogeneous structural phases (units, crystals) floating in the melt, but as stoichiometric entities in the mixture constituting the silicate melt. These constitutional components generate, e.g., by their standard Gibbs free energy values, the thermochemical data (basis) with which the system can be described.

Generally, when using this concept, the system of constitutional components must meet two conditions:

1. The constitutional components must represent the stoichiometry of the system by positive molar amounts.

2. They must comply to the Gibbs phase rule, so that the molar amounts can be chosen independently, within the constraint of mass conservation.

A strong advantage of this approach is, that even in case of multicomponent systems, the model does not need adjustable or fitting parameters. When the constitutional components (single oxides and structural compounds) are chosen to describe the system (glass), the excess Gibbs energy<sup>3</sup> and the heat of mixing can be expected to be negligibly small because its contribution is small compared to the  $\Delta G$  contribution of the pure substance of the components. This is because the constitutional components have a tendency to coexist and not react among each other [25]. Thermodynamically, this approach assumes, by neglecting the excess Gibbs energy and the heat of mixing, the liquid solution to be an ideal mixture of the constitutional components, because considering an ideal mixture of the constitutional components, by definition, the volume change of mixing and the heat of mixing are zero.

With this approach, a multicomponent glass system is considered as an ideal system constituted of the oxides and the structural compounds. The Gibbs free energy of such an ideal system is thus determined by the Gibbs free energy contribution of the oxides and the structural compounds. The equilibrium composition of the glass/melt is the composition for which the Gibbs free energy is minimal.

The compound concept has several advantages for thermodynamic modeling, e.g., the estimation of chemical activities of the constitutional compounds compared to other models:

- i. The choice of structural compounds inside a system of oxides is strictly limited to their existence in the phase diagrams, but none is allowed to be neglected. In case one compound is neglected, the results of the modeling can be significantly influenced, depending on its  $\Delta G$  function.
- ii. Reliable thermochemical data is usually available for the different oxides and compounds, mostly in the solid state and partly in the liquid state.
- iii. The approach is free of adjustable or fitting parameters.

The modified associate species approach, as developed by Hastie et al. [27,28] and recently applied by Besmann et al. [4] and Spear et al. [2,3] for glass and refractory corrosion, also treats a liquid solution as a mixture of solution end-members (oxides) and their components (stoichiometric or structural compounds).

Besmann et al. [4] use fictive structural entities, not existing as condensed phase to optimize the modeled phase equilibria. Additionally, Spear et al. [3] modified thermochemical data in the way that all liquid associate species have formulas that contain two non-oxygen atoms per mole to allow equal weighing of each species with regard to its ideal mixing entropic contribution. An example is that, e.g.,  $\text{Na}_2\text{Al}_2\text{O}_7(l)$  is expressed

---

<sup>3</sup>The excess Gibbs energy describes the deviation of the Gibbs energy from (in this case) the ideal solution behavior:  $G^{excess} = G^{real} - G^{ideal}$



as  $\text{Na}_{2/3}\text{Al}_{2/3}\text{O}_{7/3}(\text{l})$  or  $\text{Na}_2\text{Al}_2\text{O}_7:1/3(\text{l})$ . According to Spear et. al [3], this modification (approach), influencing the ideal mixing energy, is not yet fully understood by the authors. Both modifications (fictive structural entities and the modification to the data) can be understood as a sort of fitting to obtain better results. This approach is therefore different to the compound model, where only structural compounds are used that exist in the phase diagram and that are assumed to show congruent melting<sup>4</sup>. However, congruent melting does not strictly exist considering the compound model or associated species approach, which will be explained in more detail in the next subsection.

### 3.2.1 The compound model approach applied to oxide glasses

A general application of the compound concept to oxide glasses, which have strong non ideal behavior of the single oxides, was developed by Shakhmatkin and co-workers [22–24]. The investigators used this approach to calculate the molar fractions of the structural compounds at a given temperature in silicate glasses<sup>5</sup>. To set up their calculation procedure Shakhmatkin and co-workers use the thermodynamic equilibrium constant  $K$  between the oxides and the different structural compounds. At a given temperature, the  $K$  values are determined from the standard Gibbs free energies of the pure substances (constitutional components in the pure state). According to the concept, they assume ideal solution behavior between the oxides and the structural compounds, thus the chemical activity of a constitutional component equals its molar fraction. For a  $p$ -component system ( $p=2$  for the  $\text{Na}_2\text{O}$ - $\text{SiO}_2$  System), forming  $u$  structural compounds, the oxides not counted, this approach requires to solve:

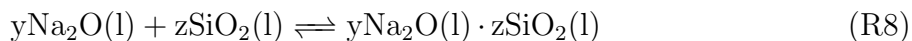
**u** usually nonlinear equations describing the structural component formation equilibria from the oxides (see equation (3.1)).

**p-1** linear equations for the molar fractions of the oxides describing the composition.

**1** linear equation for the overall mass balance.

#### Example:

When applying this procedure to, e.g., the liquid binary  $\text{SiO}_2$  -  $\text{Na}_2\text{O}$  system, an exemplary reaction is:



where  $y$  and  $z$  are integral numbers,  $y$  varies from 1 to 3 and  $z$  is equal to 1, 2 or 8. Using the thermodynamic equilibrium constant  $K$ , we get the equilibrium condition:

$$K_i = \frac{a_{\text{Na}_2\text{O}}^y a_{\text{SiO}_2}^z}{a_{(y\text{Na}_2\text{O} \cdot z\text{SiO}_2)}} \quad (3.1)$$

---

<sup>4</sup>Congruent melting signifies that a binary compound melts at a certain concentration to a liquid of its own composition. Additionally, incongruent melting denotes melting accompanied by decomposition or by reaction with the liquid, so that one solid phase is converted into a liquid, different in composition from the original solid.

<sup>5</sup>Because of the ideal mixture assumption, the molar fractions of the constitutional compounds correspond to their chemical activities.

where  $a_i$  is the activity of the designated species  $i$  in the mixture. The link between the chemical equilibrium reaction and thermodynamics is established with the following relation:

$$K_i = \exp \left[ -\frac{\Delta G_{fi}^0}{RT} \right] \quad (3.2)$$

where  $\Delta G_{fi}^0$  is the standard Gibbs free energy of reaction of species  $i$ ,  $R$  the ideal gas constant and  $T$  the absolute temperature. This approach requires the standard Gibbs free energy change of formation of the given oxides and structural compounds. The  $G_{fi}^0$  values of the constitutional compounds have to be taken from the pure phases in the liquid state. However, Shakhmatkin et al. [23] also use the Gibbs free energy change of formation of the initial oxides in the molten state and the one of the structural compounds in the crystalline state, because thermodynamic data for the liquid state is not always available. This approach ( $G_f^{liquid} = G_f^{solid}$ ) is, by approximation, valid in the vicinity of the melting temperature of the compounds, thus for the majority of silicate glasses in the temperature range between 1173 and 1573 K (900-1300°C). The involved uncertainty is, on the average, close to the uncertainty of the experimental determination of the Gibbs energy of formation [23]. However, in case that the Gibbs free energies of formation from the solid state are used for the calculation of the liquidus temperature, the accuracy of the model will decrease. The chemical activity values calculated with the compound model, developed in this chapter are sensitive to small deviations in  $G_{f,i}^0$  values, which will be shown during the validation of the activity model in subsection 3.2.3. The liquidus temperature is also sensitive to small deviations in chemical activities, which are calculated by the model from the  $\Delta G_{f,i}^0$  values.

Summarizing, using the standard Gibbs free energies of formation of the constitutional components in the liquid state and the mass balance for each element as additional constraints, it is possible to estimate the chemical activity of the different oxides and structural compounds in a mixture (glass or glass melt), which is assumed to be ideal.

Shakhmatkin and co-workers used the compound concept to calculate the liquidus temperature of the binary  $\text{SiO}_2$  -  $\text{Na}_2\text{O}$  system with  $\text{Na}_2\text{O}$  mole fractions between 10 and 40 mol% [26]. The deviation between the calculated liquidus temperature and the literature data lies within 30 K. Their results will be discussed in more detail in section 3.3.1.

The calculation procedure of Shakhmatkin and co-workers has practical limits when expanding to multicomponent systems. The compound  $3\text{Na}_2\text{O} \cdot 8\text{SiO}_2$  for example introduces, already in the binary sodium-silicate system, a nonlinear term of power 8 in the equilibrium equations ( $y=3$  and  $z=8$  in reaction (R8)), which have to be solved. The system of equations becomes more and more complex considering ternary or larger component systems and for some systems a converged numerical solution is difficult or virtually impossible to obtain.

Another application of the compound concept to describe thermodynamic properties of multicomponent glasses or glass melts was developed by Conradt [20,21]. The compound concept was used to calculate the chemical activity of the constitutional components in a glass melt. For the calculation of the activities, the author breaks down the glass melt

composition into the three or four major single oxides constituting at least 85 mol % of the composition. He then determines the exact point of the composition (major oxides) in the phase diagram (ternary or quaternary). The thermodynamic data for the calculation is then chosen from the oxides and the structural compounds surrounding (enclosing) the composition point in the phase diagram (at the edges of the surrounding sub-triangle (ternary) or sub-tetrahedra (quaternary)) in the phase diagrams. Minor components of the glass composition, which were not yet accounted for are added according to a scheme similar to the C.I.P.W. norm<sup>6</sup> calculation from geoscience. The exact procedure of this calculation scheme, also of the implementation of the minor glass components, is given in [21].

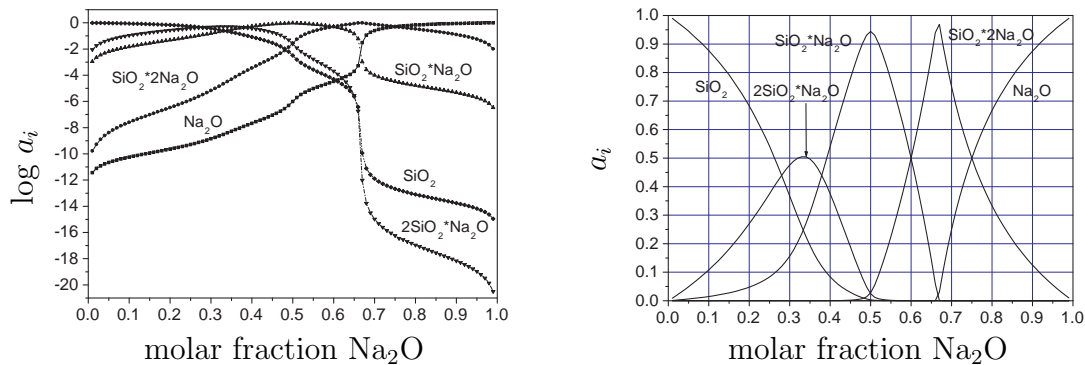
The approach of Conradt requires an expert selection of structural compounds describing the considered system in order to reduce the number of equations to be solved and to avoid too much complexity of the equations. He, as well as Shakhmatkin, uses the Gibbs free energy of formation of the constitutive pure components. However, with this expert selection and thus the reduced number of equations, Conradt is able to calculate the activity also in float glass melts with 9 Oxides, which was not yet shown by Shakhmatkin and co-workers, but which will be shown with the model developed here, but without the expert selection.

Most of the thermodynamic data for the different compounds in oxide glass systems are only available for the crystalline phase. In order to calculate thermodynamic properties for a liquid phase, even below the liquidus temperature or melting temperature of the pure constitutional components, the thermodynamic data of the participating components should also be available for the liquid state. Therefore Conradt uses a so-called vitrification enthalpy and entropy to account for the use of the thermodynamic data from crystalline compounds in a vitrified state. The vitrification enthalpy and entropy of the different compounds is only relevant if the glass temperature is below the liquidus temperature of the constitutional components. Furthermore, the vitrification enthalpy also depends on the cooling rate of each glass, it is not known for many crystalline compounds and is very difficult to determine [25]. The explicit calculation procedure used by Conradt to calculate the activities in multicomponent glass melts is given in [21].

The compound concept, as applied by Shakhmatkin et al., demands for the multicomponent liquid phase, the presence of oxides and structural compounds together as an ideal mixture of the constitutional components<sup>7</sup>. For the Shakhmatkin model, for example, this implies that the mole fractions of the single structural compounds, in the multicomponent mixture, can never be unity, not even at their stoichiometrical composition. This is because all constitutional components are present at all compositions (sometimes at very low concentrations) and the mass balance must be fulfilled ( $\sum x_i = 1$ ). An example, calculated with the model developed in this chapter, is given in figure 3.1. The figure shows the decadic log of the chemical activities, or the molar fractions, respectively, of 5 of the 7

<sup>6</sup>Cross W., Iddings P. J., Pirsson L. V. and Washington H. S.. They were distinguished American petrographers that developed a method of describing rocks from chemical analysis which is called a norm.

<sup>7</sup>Shakhmatkin et al. designate their results to the structure of the melt, calculating  $x_i$ . Because of the ideal mixture assumption,  $a_i = x_i$ , this equals the chemical activity  $a_i$ .



(a) Calculated activities as a function of the sodium molar fraction in a binary sodium-silicate melt. (b) Calculated activities as a function of the sodium molar fraction between 0 and 1 to demonstrate the deviation from unity for e.g., Na<sub>2</sub>O·SiO<sub>2</sub>.

Figure 3.1: Calculated activities data of some constitutional components of the sodium silicate system at the melting temperature of Na<sub>2</sub>O·SiO<sub>2</sub>: 1363K. The structural compounds 3Na<sub>2</sub>O·8SiO<sub>2</sub> and 3Na<sub>2</sub>O·2SiO<sub>2</sub> were omitted for the calculation for reasons of clarity. The reference state for the calculated activities is the pure liquid state.

known constitutional components of the Na<sub>2</sub>O·SiO<sub>2</sub> system at the melting temperature of Na<sub>2</sub>O·SiO<sub>2</sub> (1363 K). The structural compounds 3Na<sub>2</sub>O·8SiO<sub>2</sub> and 3Na<sub>2</sub>O·2SiO<sub>2</sub> were omitted for reasons of clarity. They are however respected during the validation of the model, which is explained later in the text. The calculated activity values of the five components over the complete system range are given in figure 3.1(a). The reference state for the calculated activities is the pure liquid state. It can be seen in figure 3.1(b), that the calculated activities of the structural compounds are never unity, not even the activity of Na<sub>2</sub>O·SiO<sub>2</sub> at its melting temperature. This is because for this example:

$$x(\text{SiO}_2) + x(2\text{SiO}_2 \cdot \text{Na}_2\text{O}) + x(\text{SiO}_2 \cdot \text{Na}_2\text{O}) + x(\text{SiO}_2 \cdot 2\text{Na}_2\text{O}) + x(\text{Na}_2\text{O}) = 1 \quad (3.3)$$

where  $x$  denotes the molar fraction. In other words, if one considers only Na<sub>2</sub>O·SiO<sub>2</sub> as structural compound in the solid state and heats it up to its melting temperature, one expects that the chemical activity of Na<sub>2</sub>O·SiO<sub>2</sub> in the liquid phase at 50 mol% Na<sub>2</sub>O and 50 mol% SiO<sub>2</sub> is unity. However, as demonstrated in figure 3.1, the calculated activity is not unity. This phenomenon has an important consequence on the validity or usability of reported thermodynamic literature data for structural compounds in the liquid state. Literature reference data for the liquid state as given in, e.g., in Barin et al. [29], list thermodynamic data ( $\Delta H$  and  $\Delta S$ ) for the pure species. When the pure solid compound Na<sub>2</sub>O·SiO<sub>2</sub> dissociates at its liquidus temperature, forming itself and all other structural compounds including the two corresponding single oxides in the liquid state, the value of the reported thermodynamic property does not correspond to pure Na<sub>2</sub>O·SiO<sub>2</sub>(l) solely, but a part of it refers to all other components in the melt. This means that the value of the standard Gibbs free energy of one compound in the liquid state will be reduced according to the contributions of all other components in the melt. Thus, as stated earlier,

in the compound model approach, congruent melting can not exist. The use of the solid state pure substance data for the calculations, as proposed by Shakhmatkin et al. [23], can be used in terms of thermodynamic data, because here, the referenced thermodynamic data corresponds solely to the pure solid species, solid solutions excluded and pure immiscibility in the solid state assumed. However, because of the compound approach, using thermodynamic data of the solid state does not resolve the fact that all species exist together.

In our investigations, the reported  $\Delta G_f^0$  values, for the pure liquid state were used when available. In case that the calculation required the  $\Delta G_f^0$  values below the liquidus temperature of a specific constitutional component, the values for the liquid phase were extrapolated to lower temperatures, if available. In case that the values for the liquid state were not available, the one for the solid state were used and the liquid state was estimated using the melting enthalpy  $\Delta H_{mi}$  and the melting entropy  $\Delta S_{mi}$ , which are constant. For congruent melting species  $i$ , the liquid state can thus be estimated from the solid state according to:

$$G_{fi}^l = G_{fi}^s + (\Delta H_{mi} - T\Delta S_{mi}), \quad (3.4)$$

where the index  $l$  and  $s$  denote liquid and solid, respectively.  $\Delta S_{mi}$  is the melting entropy and  $\Delta H_{mi}$  the melting enthalpy of component  $i$  at  $T_{mi}$ . By applying this simplification one assumes thus, that the molar heat capacity of the liquid equals the one of the solid species, which is of course not true, but a reasonable approximation especially around the melting temperature. The error to each constitutional component  $i$  and thus to the complete system, introduced by this assumptions, increases the larger the temperature of the system shifts from the melting temperature of the different species  $i$ . This extrapolation has an additional limitation: the heat of melting as given in standard literature references is also meant for one congruent melting species only, but when a solid species dissociates in all present species, there is not just a heat of melting, but also a heat of dissociation.

The uncertainty of the thermodynamic data derived from literature references and used in the compound model implies deviations of calculated chemical activities and liquidus temperatures from experimental data of these properties. Liquidus temperatures or the calculation of other thermochemical transitions are very sensitive to small deviations of thermodynamic values, e.g., chemical activities and thus small differences can result in significantly deviations in calculated properties. This will also be shown during the validation of some liquidus temperature calculations by the model in section 3.3.1.

Summarizing, the established approach of Shakhmatkin and co-workers may lead to numerical difficulties during the mathematical calculation, when applied to multicomponent systems. In addition to that, the application of reported pure substance data from literature for the liquid state may lead to errors. The approach of Conradt requires an expert selection of the compounds used in addition to the single oxides for the calculation and a vitrification enthalpy and entropy. The approach of Shakhmatkin and co-workers showed good results for binary and ternary solutions, comparing modeled results with experimental data for binary and ternary silicate melts. The solution of the thermodynamic equilibrium equations in the Shakhmatkin approach corresponds to that composition,

where the Gibbs free energy of the system (glass or melt) is minimum. This is a very important, because more robust Gibbs free energy minimization (calculation) routines are available, enabling modeling of complex systems without the need of an expert selection of fitting parameters.

A proven procedure to determine the minimum Gibbs free energy of a multicomponent system of gaseous and condensed phases was developed by Eriksson [30]. This approach iteratively calculates the non-negative set of molar fractions of the system species, which give the lowest possible value of the total Gibbs free energy, satisfying the mass balance as constraints. This procedure was applied in the computer software program SOLGASmix and further developed in ChemSage [19] and FactSage [31]. The commercially available computer program ChemSage [19] was used by Spear et al. [2] and Besmann et al. [4] to compute the Gibbs free energy minimization for their phase equilibria calculations.

The activities in multicomponent glass melts can be calculated by combination of the Shakhmatkin approach and the Eriksson minimization scheme, which is based on a Lagrange minimization procedure. A subjective expert selection of compounds (Conradt method) is not required, nor is the use of fitted parameters, which have to be optimized for each new system, as performed in FactSage [31] necessary. Furthermore, the addition of fictive compounds (Besmann et al. [4]) or modifications to the thermodynamic data [3] can be avoided. It should be noted that fitting parameters either fundamental (non-ideal mixing terms) or fictive may increase the accuracy of the model, because mixing might not be completely ideal. The use of fitting parameters, however, restrict the use of the model inside the fitted composition.

In the next section, the thermodynamic model equations to calculate the chemical activity in a single condensed multicomponent phase, e.g. a glass melt, will be derived. Because of the nature of the model it will be called: "Ideal Mixture Compound Model" or IMCM.

### 3.2.2 Model for chemical activities in oxide glass melts "Ideal Mixture Compound Model" (IMCM)

The compound model to calculate chemical activity values in multicomponent silicate melt systems, developed by Shakhmatkin and co-workers, assumes ideal mixture behavior between the oxides and the defined structural compounds. This means that the activity coefficient  $\gamma$  of the different species  $i$  equals unity. This also implies that liquid phase separation in the liquid phase cannot be determined (calculated), since this would imply non ideal mixing and  $\gamma_i \neq 1$  for some constitutional components. Thus, the activity of species  $i$  (oxide and structural compound) equals the molar fraction of species  $i$  in the multicomponent system. According to Eriksson [30], the equilibrium composition of a system, e.g., a multicomponent glass, can be determined by minimizing the Gibbs free energy of the system. For a condensed single phase system, at uniform temperature  $T$  and

pressure  $P$ , the Gibbs free energy of an ideally mixed system of constitutional components is given by [32]:

$$nG = \sum_{i=1}^p n_i \mu_i \quad \text{with} \quad n = \sum_{i=1}^p n_i \quad (3.5)$$

where  $n$  is the total number of moles of the different species of the single phase system,  $p$  the total number of different species in the single phase,  $n_i$  is the molar amount of species  $i$  in the system, and  $\mu_i$  is the chemical potential of species  $i$ . The chemical potential and the chemical activity  $a$  of species  $i$  are related by:

$$\mu_i = \mu_i^\circ + RT \ln a_i \quad (3.6)$$

with  $\mu_i^\circ$  the chemical potential of species  $i$  at the standard reference state, which is, in this case, defined as the pure liquid phase.

Assuming the glass melt to be an ideal mixture of single oxides and structural compounds, the activity coefficient  $\gamma_i$  equals unity, and

$$x_i \gamma_i = a_i = x_i = \frac{n_i}{n} \quad (3.7)$$

Equation 3.6 for the chemical potential for species  $i$  then becomes:

$$\mu_i = \mu_i^\circ + RT \ln \left( \frac{n_i}{n} \right) \quad (3.8)$$

By minimizing the term  $nG$  in equation (3.5) by changing the molar masses of the different species ( $n_i$  values), the equilibrium concentration of species  $i$  and thus their activity values can be determined. In order to ensure mass conservation during the minimization of  $nG$ , an elemental mass balance is used as constraint for the minimization routine. For the minimization, Lagrange's method of undetermined multipliers was used. A detailed description of the model equations and the minimization scheme is given in the appendix, section 3.7 on page 86. A detailed description of Lagrange method itself, is given by Adams [33].

The activity model, developed in this section, validated for a few cases in the next subsection.

### 3.2.3 Validation of activity model (IMCM) for glass melts

The IMCM, developed in this study, enables an estimation of the equilibrium composition of the constitutional components (oxides and compounds) in multicomponent glass melt phases. According to the ideal mixture assumption of the constitutional components, the molar fraction of the different components correspond to their chemical activities (reference state is the pure liquid).

Further in this chapter, for simplicity, a short notation will be used as acronyms for the different species (oxides and structural compounds) present in the multicomponent glass melts, e.g., S = SiO<sub>2</sub>, A = Al<sub>2</sub>O<sub>3</sub>, C = CaO, M = MgO, NS = Na<sub>2</sub>O · SiO<sub>2</sub>, NS2 = Na<sub>2</sub>O · 2SiO<sub>2</sub>, CNS = CaO · Na<sub>2</sub>O · SiO<sub>2</sub>, etc..

Literature sources providing activity data for different oxides in glasses at different temperature levels are rare. Unfortunately, chemical activity data for structural compounds were not found at all. In this study, the calculated oxide activity values of, e.g.,  $\text{Na}_2\text{O}$ , in a few different glass forming systems, using the IMCM approach, are compared to experimental data derived from literature references. Generally, the reference state for the chemical activity is the activity of the pure oxide or pure structural compound in the liquid state, unless stated otherwise. Therefore, the Gibbs free energy of formation of the pure liquid state was used for the different constitutional components. In case the information for the liquid state ( $\Delta G_{fi}^0(\text{liquid})$ ) was not available it was estimated by adding the congruent melting energy and entropy to the standard Gibbs free energy of the crystalline state according to equation (3.4). This approach assumes that the heat capacity of the solid and liquid state are equal ( $c_P^s = c_P^l$ ), which is of course not the case, but a reasonable approach regarding the lack of more accurate data.

The predicted oxide activities, using the IMC model is compared with modeled and experimental data obtained from literature for the sodium silicate system as an example. According to the binary phase diagram of  $\text{Na}_2\text{O}$  and  $\text{SiO}_2$ , this system consists of the two oxides N and S and the 5 structural compounds: N3S8, N3S2, NS2, NS, N2S [9]. The calculated activities (molar fractions) of the constitutional components, calculated with the IMCM, as a function of the molar fraction  $\text{Na}_2\text{O}$  in the binary system at 1473 K is shown in figure 3.2. The calculations are in fairly good agreement with the modeled values published by Shakhmatkin et al. [23], indicated as dotted lines. The differences between the IMCM of this study and the published results by Shakhmatkin et al. can be explained by differences of the standard Gibbs free energy potentials of the considered reactions ( $\Delta G^0$ ), which were however not published by Shakhmatkin et al.. The standard Gibbs free energy of formation for the compound N3S8 may not be very accurate [26]. Furthermore, examining [9] in more detail, N3S8 does not melt congruently, thus the reported Gibbs free energy of N3S8 is not supposed to be used according to the concept as developed by Shakhmatkin et al.. However, since Shakhmatkin et al. used a value of ( $\Delta G_f^0(\text{N3S8, liquid})$ ) [23] we also used it as constitutional component for reasons of comparison. Deviations in the exact numeric value of ( $\Delta G_f^0(\text{N3S8, liquid})$ ) also have a direct influence on all other concentrations present in the same compositional range (0.1-0.4  $x_{\text{Na}_2\text{O}}$ ), because of the coupling by the mass balance constraint in the calculation. Figure 3.2 shows that the results of the method of minimizing the Gibbs free energy, as presented in this chapter, is comparable to the results of the method presented by Shakhmatkin and co-workers. The effect of differences in the exact value of  $\Delta G_f^0$  on the calculated activity values using the IMCM is shown in figure 3.3. For this calculation the  $\Delta G_f^0$  value of NS was increased by 1% and the activities of all constitutional components were calculated. Figure 3.3 shows, that by increasing  $\Delta G_f^0(\text{NS})$  by 1% the activity of NS increases at  $x_{\text{Na}_2\text{O}} = 0.5$  by 23% and the activity of NS2 decreases at  $x_{\text{Na}_2\text{O}} = 0.33$  by 49%. Neglecting one or more structural compounds would also strongly affect the values of the calculated activity values.

However, the minimization method of the IMCM, that calculates the chemical activities, is easily extendable to multicomponent systems, which is the actual benefit of the mathematical procedure developed in this study.



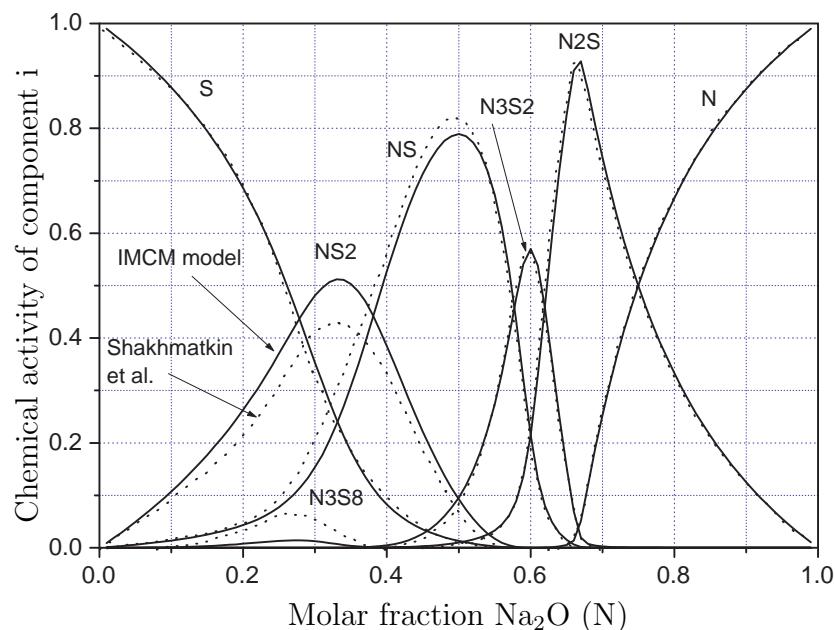


Figure 3.2: Calculated activities of the different constitutional components in the sodium silicate system at 1473K (1200°C). The dotted line represents the calculated values provided by Shakhmatkin and co-workers, presented in [23], the solid line represents the results from the IMC model developed in this study. The constitutional components are denoted in the figure.

The applicability and validity of the developed method for binary and also for multicomponent silicate glass systems is shown by figures 3.4 and 3.5. Figure 3.4 shows the calculated (IMC model) decadic logarithm of the sodium oxide activity in the binary  $\text{SiO}_2$  -  $\text{Na}_2\text{O}$  system between 10 and 70 mol%  $\text{Na}_2\text{O}$  at different temperatures, compared to experimental data published by Allibert et al. [9]. From this figure, it can clearly be seen, that the modeled results are in good agreement, even at different temperature levels, with the experimental data. However, at higher activity levels ( $-\log a = 2 - 3$ ) the deviations between experimental data and the IMC model are somewhat larger. These activities correspond to  $\text{Na}_2\text{O}$  concentrations of 0.6-0.7 mol%  $\text{Na}_2\text{O}$ . This composition range is not very relevant for technical glass melting. In addition to that, when examining the liquidus temperature at  $\text{Na}_2\text{O}$  concentrations of 0.6-0.7 mol%, as also published in [9], the course of the liquidus line is, according to [9], not fully understood.

Figure 3.5 shows that the modeled results for  $a_{\text{Na}_2\text{O}}$  are in fairly good agreement with the experimental data for some ternary and multicomponent silicate systems. The calculated  $\text{Na}_2\text{O}$  activities (IMC model) for the NMS system are constantly higher than the values found by experiments. This deviation may be related to extrapolated  $\Delta G_{fi}^0(\text{liquid})$  values in the model, because not all required thermodynamic data was available in the liquid state and the temperature of 1673 K is relatively high compared to the melting temperatures of several structural compounds in the NMS system. The experimental data

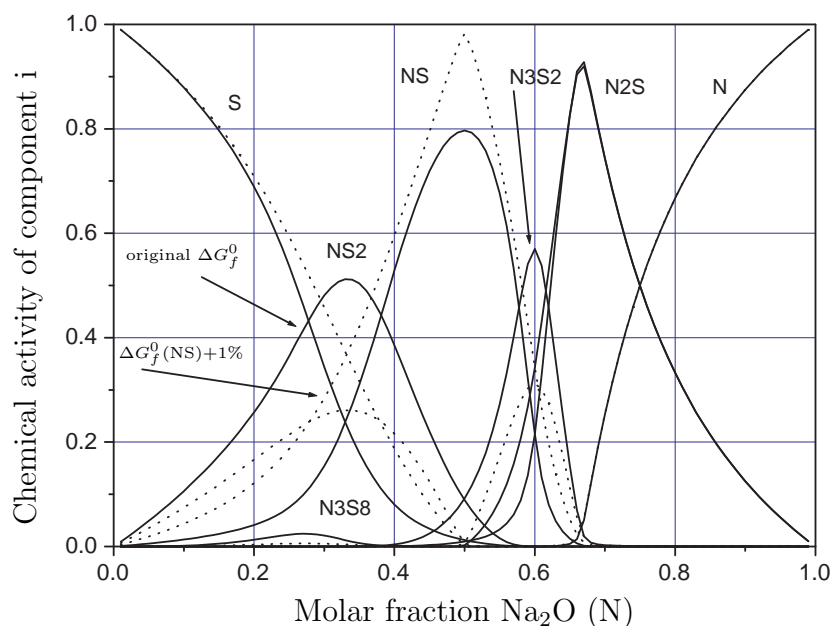


Figure 3.3: Calculated activity data of the different constitutional components of the sodium silicate system at 1473K (1200°C). The solid line represents the calculated activity values from the IMC model. The dotted line represents the calculated activity values for  $\Delta G_f^0(NS)+1\%$ . The constitutional components are denoted in the figure.

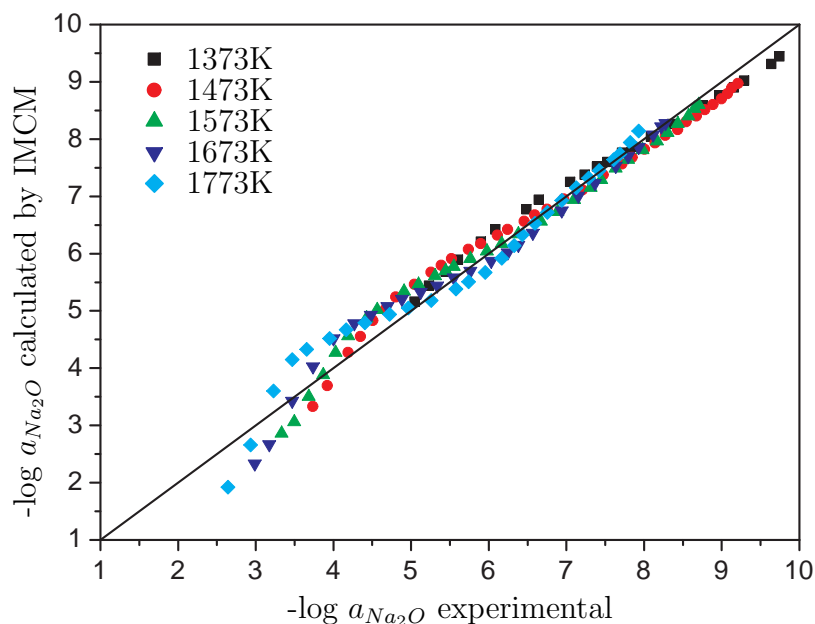


Figure 3.4: Parity plot of the negative decadic logarithm of the Na<sub>2</sub>O activity in the binary system Na<sub>2</sub>O - SiO<sub>2</sub> at different temperatures between 10 and 70 mol% Na<sub>2</sub>O. The calculations were performed with the IMC model, the experimental data has been taken from Allibert et al. [9].

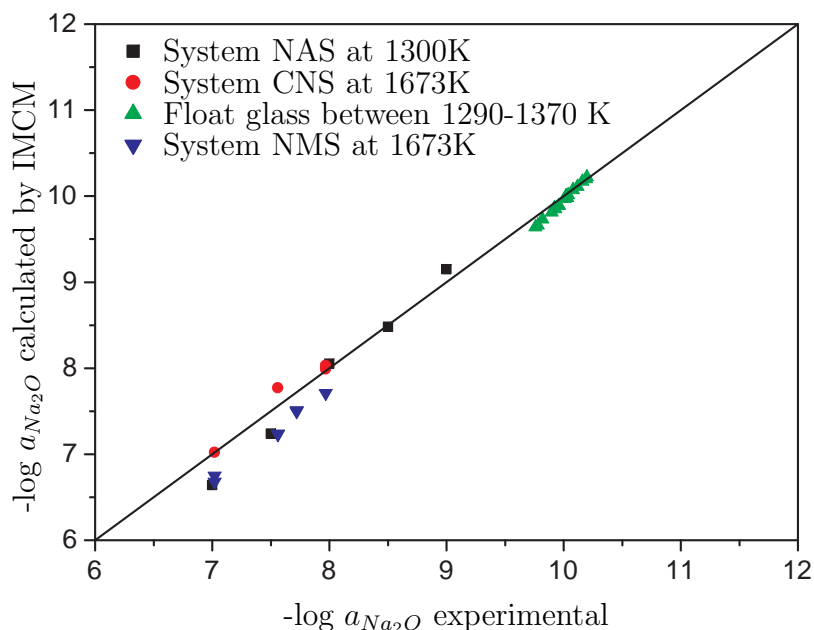


Figure 3.5: Parity plot of the negative decadic logarithm of the  $\text{Na}_2\text{O}$  activity of different glass forming systems at different compositions and temperatures. The calculations were performed with the IMC model, the experimental data has been taken from [9] and [34].

presented in figure 3.5 has been taken from Allibert et al. [9], except the data for float glass, which has been taken from Sardjono [34].

A source of experimentally determined  $\text{Na}_2\text{O}$  activities in float glass between 1280 and 1370 K is the thesis of Sardjono [34]. Float glass is a complex (multicomponent) technical glass, which contains up to 9 to 10 different oxides. This system includes 64 known structural compounds for which thermodynamic data was found and included for the IMCM calculation.

The calculation of chemical activities in glasses with iron oxide introduces another complexity. Iron can be incorporated in glasses as  $\text{FeO}$ ,  $\text{Fe}_2\text{O}_3$  or  $\text{Fe}_3\text{O}_4$  [23, 38, 39]. The concentrations of the different forms of iron oxide also depend on the oxidation state of the glass, thus on the thermodynamic equilibrium between the polyvalent ion (iron) and the dissolved oxygen in the glass. For the calculations with the IMC model, several structural compounds must be found that represent each of the three forms of iron oxide, e.g.,  $2\text{Na}_2\text{O} \cdot \text{Fe}_2\text{O}_3 \cdot \text{SiO}_2$  or  $\text{FeO} \cdot 2\text{SiO}_2$ . A structural compound for  $\text{Fe}_3\text{O}_4$  was not found, which is probably, because  $\text{Fe}_3\text{O}_4$  can be expressed as  $\text{FeO} \cdot \text{Fe}_2\text{O}_3$ . Shakhmatkin et al. [23] used, e.g.,  $2\text{Na}_2\text{O} \cdot \text{Fe}_2\text{O}_3 \cdot \text{SiO}_2$ , for which no Gibbs free energy was published. From equation (3.3) it can be seen that neglecting one or more structural compounds, as discussed earlier in this chapter, can significantly influence the values for the calculated activities by the IMCM. The model calculates the Gibbs free energy minimum of the system by changing the composition of the constitutional components, respecting the

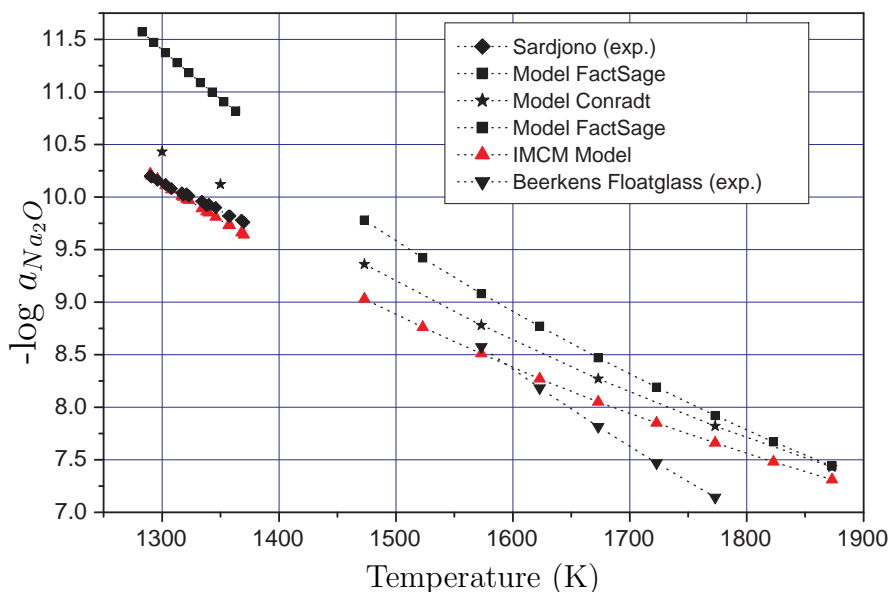


Figure 3.6: Comparison of  $\text{Na}_2\text{O}$  activity data for float glass at different temperatures. Experimental results by Sardjono [34] and Beerkens ( $\text{Na}_2\text{O}$  activity measured by means of a combination of sulfate decomposition measurements and electrochemical analysis) [35]. Modelled results by Conradt [36, 37], FactSage [18] and the IMC model developed in this thesis. Glass composition of glass used by Beerkens in wt.%:  $\text{SiO}_2$ :72.2,  $\text{Na}_2\text{O}$ :13.4,  $\text{CaO}$ :9.5,  $\text{MgO}$ :2.2,  $\text{K}_2\text{O}$ :0.9,  $\text{Al}_2\text{O}_3$ :1.5,  $\text{SO}_3$ :0.2-0.5. For the temperature range 1283-1370 K in wt.%:  $\text{SiO}_2$ :71.65,  $\text{Na}_2\text{O}$ :13.64,  $\text{CaO}$ :9.5,  $\text{MgO}$ :4.01,  $\text{K}_2\text{O}$ :0.173,  $\text{Al}_2\text{O}_3$ :0.571,  $\text{Fe}_2\text{O}_3$ :0.104,  $\text{TiO}_2$ :0.044,  $\text{SO}_3$ :0.22. For the temperature range 1473-1873 K in wt.%:  $\text{SiO}_2$ :72.2,  $\text{Na}_2\text{O}$ :13.66,  $\text{CaO}$ :9.28,  $\text{MgO}$ :1.98,  $\text{K}_2\text{O}$ :0.98,  $\text{Fe}_2\text{O}_3$ :0.0095,  $\text{Al}_2\text{O}_3$ :1.48,  $\text{SO}_3$ :0.49. For the calculation described in this thesis, dissolved  $\text{SO}_3$  in the glass was omitted in the IMC model calculations.

mass balance. In case that only two iron containing species are available, e.g.,  $\text{Fe}_2\text{O}_3$  and  $\text{FeO} \cdot \text{SiO}_2$ , the iron will thus be partitioned among these two components according to their  $\Delta G$  contributions and the mass balance. Neglecting thus one or more structural compounds for, e.g., iron might not influence significantly the activity values for clear float glass compositions, because the iron oxide concentrations are usually very low (0.01 wt.%), but might produce significant deviations in activity values at higher iron concentrations. Applying the model for glasses with an iron oxide concentration of about 3 wt.%, such as vitrified fly ash, can thus significantly influence the calculated activity values.

Sodium oxide activities in float glass are often subject to modeling, because of the importance regarding evaporation and refractory corrosion<sup>8</sup> [2, 5, 40]. Figure 3.6 shows the negative decadic logarithm of the  $\text{Na}_2\text{O}$  activity as a function of temperature for typical soda lime silicate float glasses. The float glass compositions for the lower and higher

<sup>8</sup>Float glass furnaces often have silica crowns, which show corrosion with NaOH in the combustion chamber. The NaOH concentration in the furnace atmosphere depends on the NaOH evaporation from the melt and thus on the  $\text{Na}_2\text{O}$  activity in the glass melt.

*Table 3.1: Main oxides of the vitrified fly ash (glass phase) used in this study. The original composition was normalized to represent 100 wt.%. The original fly ash glass composition is given in table 2.2 on page 38.*

Oxide	Glass phase (wt.%)	Oxide	Glass phase (wt.%)
Na <sub>2</sub> O	1.2	Fe <sub>2</sub> O <sub>3</sub>	3.8
MgO	4.0	K <sub>2</sub> O	0.5
Al <sub>2</sub> O <sub>3</sub>	18.2	TiO <sub>2</sub>	3.4
SiO <sub>2</sub>	35.6	CaO	33.3

temperature regime differ slightly. The figure shows, that the model developed in this thesis is in good agreement with the experimental data from Sardjono [34] (low temperature range). The maximum deviation in activity values ( $a_{\text{Na}_2\text{O}}$ ) between the modeled and experimental values was 24% at 1368 K. The figure also shows that the modeled results follow the temperature dependent results of other published models. The results of Conradt [36] were calculated with his model as explained in the introduction of this chapter. The results obtained using the FactSage software package show large deviations to experimental and moderate deviations, at least for  $T < 1600$  K, to the other modeled results. The deviations of the different models decrease with increasing temperature. Because of the difficulty to measure Na<sub>2</sub>O activities experimentally in a reliable way, it is difficult to determine which model, including the errors in the modeling, gives the most accurate results in this special case. The model developed in this chapter shows fairly good agreement to either experimental and other modeled results (Conradt) for the presented binary and multicomponent systems.

Unfortunately, chemical activity data for single oxides or structural compounds in glasses and their melts equal or similar to vitrified fly ash have not been found in literature. In the following, some exemplary calculations of the activities of the single oxides Na<sub>2</sub>O and CaO and the structural compounds SiO<sub>2</sub> · CaO and CaO · Al<sub>2</sub>O<sub>3</sub> · 2SiO<sub>2</sub> in a glass, melted from fly ash, are going to be presented. The glass composition used for the calculation is given in table 2.2 on page 38, omitting the oxides for which thermodynamic data of the structural compounds was not available. The remaining oxides represent 90 wt.% of the composition of the original glass from fly ash. The remaining masses of the oxides of the original fly ash glass composition were normalized to 100%. The simplified glass composition used for the calculations is given in table 3.1. The calculations with the IMCM will be performed without taking into account iron oxide, because of the lack of thermodynamic data for structural iron oxide compounds. The calculations with the IMC model are going to be compared to results of calculations using the FactSage software package [18], because no other basis for any comparison is available to evaluate the calculated results for this composition. The effect of iron oxide on the activity trends of CaO and Na<sub>2</sub>O is shown by a calculation using the FactSage software package. It should be noted that with FactSage, activities of structural compounds cannot be extracted from the software

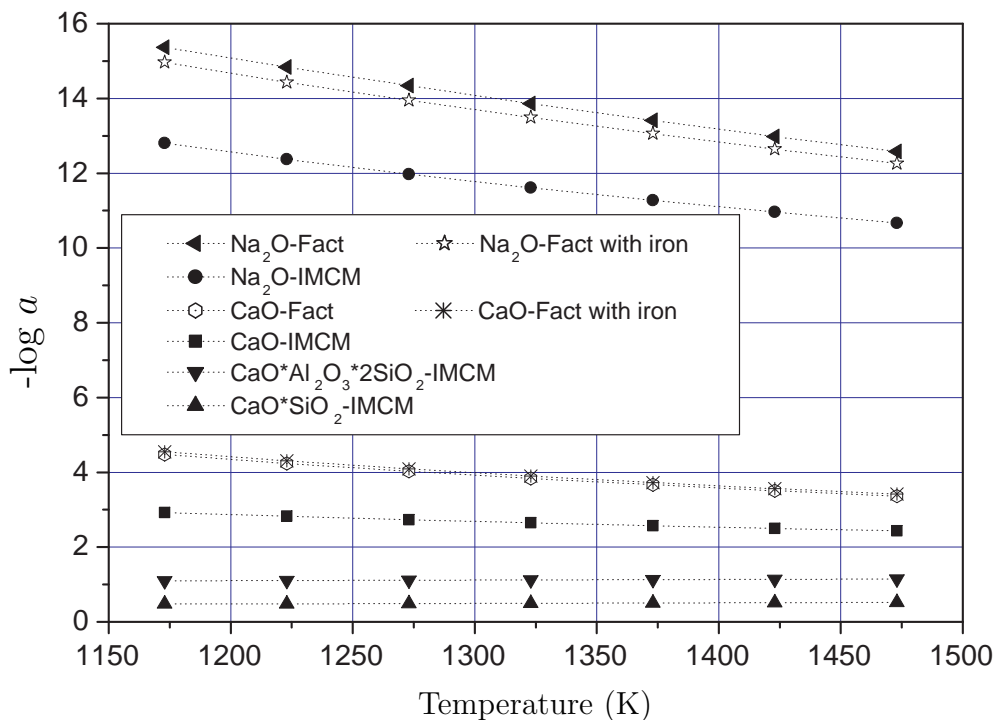


Figure 3.7: Calculated negative decadic logarithm of the chemical activities of  $\text{Na}_2\text{O}$ ,  $\text{CaO}$ ,  $\text{SiO}_2 \cdot \text{CaO}$  and  $\text{CaO} \cdot \text{Al}_2\text{O}_3 \cdot 2\text{SiO}_2$  as a function of temperature calculated with the IMCM. The  $-\log(a)$  values for  $\text{Na}_2\text{O}$  and  $\text{CaO}$  were also calculated with the FactSage software package [18] for the glass with and without iron. The glass composition used for the calculations is given in table 3.1, but  $\text{Fe}_2\text{O}_3$  was omitted for the calculation using the IMCM.

package, when using optimized data sets for glass melts [18]<sup>9</sup>. Figure 3.7 shows the calculated negative decadic logarithm of the chemical activities of  $\text{Na}_2\text{O}$ ,  $\text{CaO}$ ,  $\text{SiO}_2 \cdot \text{CaO}$  and  $\text{CaO} \cdot \text{Al}_2\text{O}_3 \cdot 2\text{SiO}_2$  as a function of temperature for the composition of table 3.1, calculated with the IMCM, excluding iron oxide species. The activities of the single oxides  $\text{Na}_2\text{O}$  and  $\text{CaO}$  were additionally calculated with FactSage for the glass with and without iron oxide, for comparative reasons. Figure 3.7 shows a large deviation between the calculated  $-\log(a)$  values for  $\text{Na}_2\text{O}$  comparing the results of the IMCM and FactSage model. This difference is about three orders of magnitude. The difference of  $a_{\text{Na}_2\text{O}}$  values between the two modeled results for the  $\text{CaO}$  activity value is about two orders of magnitude. Such a large deviation between the two models for the  $\text{Na}_2\text{O}$  activity can also be observed for the calculation of a float glass composition as shown in figure 3.6. The differences can be attributed on the one hand to the different models, e.g., the quasi-chemical approach as applied by Factsage and the ideal mixture approach of the IMCM and thus the way

<sup>9</sup>As mentioned in the introduction to this chapter, the FactSage software is of semi-empirical nature and contains fitting parameters, to adapt the model to e.g. existing phase diagrams and increase its estimation capability. Very accurate results are obtained for systems, for which the model parameters are fitted.

Table 3.2: Glass composition used for exemplary calculation to demonstrate the effect of an increased  $\text{Na}_2\text{O}$  concentration on the  $\text{SiO}_2 \cdot \text{CaO}$  activity.

Oxide	Glass phase (wt.%)	Oxide	Glass phase (wt.%)
$\text{Na}_2\text{O}$	6.5	$\text{K}_2\text{O}$	0.5
$\text{MgO}$	4.2	$\text{TiO}_2$	3.6
$\text{Al}_2\text{O}_3$	19.1	$\text{CaO}$	28.7
$\text{SiO}_2$	37.4		

the thermodynamic data is processed inside the models. The thermodynamic data itself and the choice of components to be taken into account in the models, also influences the chemical activity values. Unfortunately, the choice of species included in the FactSage calculations could not be determined. FactSage calculations of the glass with an iron oxide level of 3.44 wt.% show that the activity of  $\text{Na}_2\text{O}$  is 2.5 times larger than for the glass without iron. An explanation could be as follows using a simple example: Adding, e.g., the oxides  $\text{FeO}$ ,  $\text{Fe}_2\text{O}_3$  and the structural compound  $\text{FeO} \cdot \text{SiO}_2$  into the model for the iron oxide content, the iron will be distributed among these three components (mass balance). However, the structural compound  $\text{FeO} \cdot \text{SiO}_2$  includes  $\text{SiO}_2$ , which is, e.g., not available to form, e.g.,  $\text{Na}_2\text{O} \cdot \text{SiO}_2$ . If less  $\text{Na}_2\text{O} \cdot \text{SiO}_2$  is formed, more  $\text{Na}_2\text{O}$  must be formed to respect the  $\text{Na}_2\text{O}$  mass balance, in case  $\text{Na}_2\text{O}$  is only distributed between  $\text{Na}_2\text{O}$  and  $\text{Na}_2\text{O} \cdot \text{SiO}_2$ . However, because the choice of structural compounds used by FactSage could not be determined, this assumption could not be verified. The  $\text{CaO}$  activity in the iron containing glass, at, e.g., 1173 K, is 15.5% smaller than the one in the glass with no iron oxide (FactSage calculation). The calculated activity values using the IMCM calculated for  $\text{SiO}_2 \cdot \text{CaO}$  and  $\text{CaO} \cdot \text{Al}_2\text{O}_3 \cdot 2\text{SiO}_2$  are very much higher compared to the one for  $\text{Na}_2\text{O}$  (at 1173 K:  $a_{\text{Na}_2\text{O}} = 1.56 \cdot 10^{-13}$ ,  $a_{\text{CS}} = 0.477$  and  $a_{\text{CAS2}} = 0.08$ ). This is because of the high concentrations of  $\text{CaO}$ ,  $\text{SiO}_2$  and  $\text{Al}_2\text{O}_3$  in the glass. This means in terms of crystallization, that  $\text{CaO} \cdot \text{SiO}_2$  would most probable segregate (crystallize) from the melt, because its chemical activity is the closest to the activity of the pure solid phase.

The effect of compositional changes to fly ash glass composition on, e.g., the crystallization tendency can qualitatively be estimated in terms of activity values. As seen in figure 3.7, the chemical activity of the liquid compound  $\text{SiO}_2 \cdot \text{CaO}$  is very high. In case that the activity increases by changing the composition, the crystallization tendency of  $\text{SiO}_2 \cdot \text{CaO}$  also increases and vice versa. For this case an exemplary calculation is shown using the glass composition of table 3.2. Compared to the glass composition of table 3.1 the iron oxide was omitted and 5 wt.% of  $\text{CaO}$  was substituted by  $\text{Na}_2\text{O}$ . Figure 3.8 shows the calculated negative decadic logarithm of the chemical activities of  $\text{Na}_2\text{O}$ ,  $\text{CaO}$ ,  $\text{SiO}_2 \cdot \text{CaO}$  and  $\text{CaO} \cdot \text{Al}_2\text{O}_3 \cdot 2\text{SiO}_2$  as a function of temperature for the compositions of table 3.1 and 3.2, calculated with the IMCM. Figure 3.8 shows, that the activity of  $\text{Na}_2\text{O}$ , at 1173 K, increases two orders of magnitude. At 1173 K, the activity of  $\text{CaO}$  increases, despite the decrease in concentration, by 37% to  $a_{\text{CaO}} = 0.00163$ . The activities of  $\text{SiO}_2 \cdot \text{CaO}$  and  $\text{CaO} \cdot \text{Al}_2\text{O}_3 \cdot 2\text{SiO}_2$  both decrease at 1173 K by 27.3% and 72.7%, re-

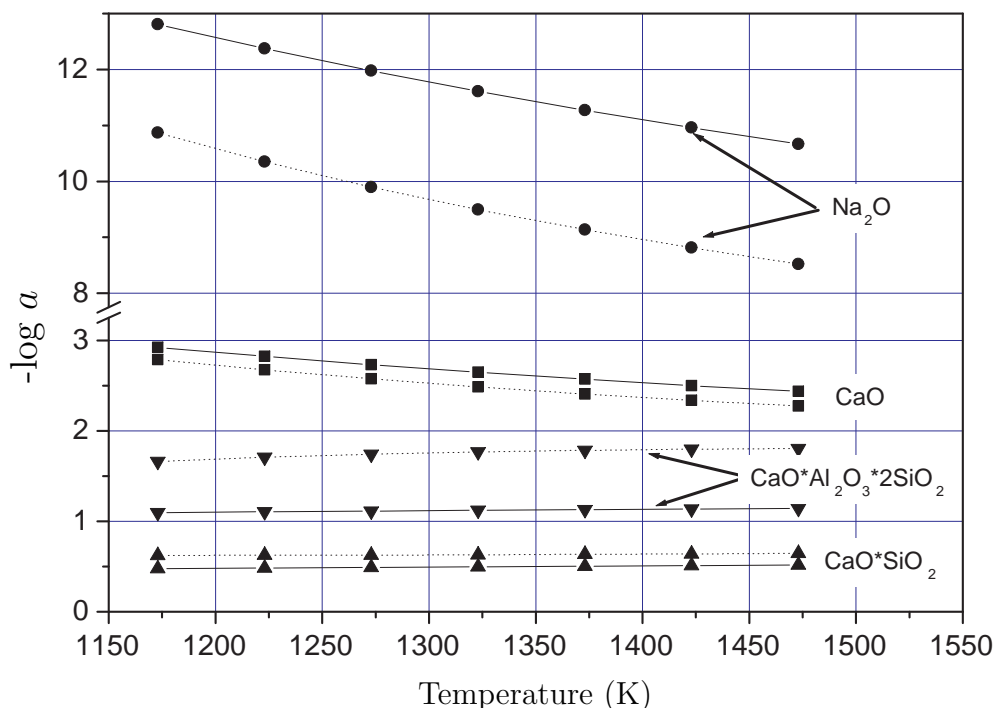


Figure 3.8: Calculated negative decadic logarithm of the chemical activities of  $\text{Na}_2\text{O}$ ,  $\text{CaO}$ ,  $\text{SiO}_2 \cdot \text{CaO}$  and  $\text{CaO} \cdot \text{Al}_2\text{O}_3 \cdot 2\text{SiO}_2$  as a function of temperature calculated with the IMCM. The solid line represents the calculated activity values for the composition of table 3.1, omitting iron oxide. The dotted line represents the calculated activity values for the composition of table 3.2.

spectively. An explanation of the decrease in concentration for the structural compounds could be the association of  $\text{Na}_2\text{O}$  with  $\text{SiO}_2$ . With more  $\text{Na}_2\text{O}$  in the melt, depending on the  $\Delta G_{fi}^0$  values, probably more sodiumsilicates are formed, which reduces the amount of  $\text{SiO}_2$  available to form, e.g.,  $\text{CaO} \cdot \text{SiO}_2$  or  $\text{CaO} \cdot \text{Al}_2\text{O}_3 \cdot 2\text{SiO}_2$ . The decrease in chemical activity of  $\text{SiO}_2 \cdot \text{CaO}$  by substitution of 5 wt% of  $\text{CaO}$  by  $\text{Na}_2\text{O}$  in the glass composition indicates, that its crystallization tendency from the melt can be reduced by adding  $\text{Na}_2\text{O}$  to the glass obtained from fly ash vitrification.

Summarizing, a new and accurate model to calculate the chemical activities of the constitutional components of a multicomponent glass has been derived. It uses only the standard Gibbs free energies of formation of the constitutional pure oxides and pure structural compounds in the considered state (preferably in the pure liquid or vitreous state), which are assumed to be ideally mixed, and the analytical glass composition as input parameters. It is free of any adjustable or fitting parameters and does not need any expert selection of participating compounds. The applicability of the model has one major drawback, namely the availability and precision of the required thermodynamic data of all relevant/required species. The modeled results, such as activity values for  $\text{Na}_2\text{O}$  in a few glass compositions show fairly good agreement with reported experimentally measured values. Because the availability of experimental activity data in multicomponent



glass melts is very limited, the model could not be validated using glass compositions comparable to typical multicomponent vitrified or molten fly ash.

With the aid of a chemical activity model for silicate melts, it is often possible to estimate the liquidus temperature or crystallization tendency of glass melts quantitatively. This will be presented in the next section.

### 3.3 Prediction of liquidus temperatures

The chemical activity model (IMC model) is going to be used to estimate the liquidus temperature of soda lime silicate melts. On the liquidus line or at the liquidus temperature, respectively, a solid and liquid phase are in thermodynamic equilibrium. Assuming ideal solution behavior of the constitutional components in the liquid phase (IMC model) and complete immiscibility for all species  $i$  in the solid state, the following equation for the solid-liquid equilibrium on the liquidus line holds [32]:

$$\begin{aligned} \ln a_i^l = & \frac{\Delta H_i^{sl}}{R T_{mi}} \left( \frac{T_{liq} - T_{mi}}{T_{liq}} \right) \\ & + \frac{\Delta C_{Pi}^{sl}}{R} \left[ \ln \frac{T_{liq}}{T_{mi}} - \left( \frac{T_{liq} - T_{mi}}{T_{liq}} \right) \right] \\ & + \int_{T_{mi}}^{T_{liq}} \frac{1}{R T^2} \int_{T_{mi}}^{T_{liq}} \int_{T_{mi}}^{T_{liq}} \left[ \frac{\partial(C_{Pi}^l - C_{Pi}^s)}{\partial T} \right]_P dT dT dT \end{aligned} \quad (3.9)$$

In this expression,  $a_i^l$  denotes the chemical activity of species  $i$  in the liquid state. The reference state is the activity of pure species  $i$  in the liquid state.  $\Delta H_i^{sl}$  is the enthalpy change of melting (heat of fusion) and  $\Delta C_{Pi}^{sl}$  is the molar heat-capacity change of melting of species  $i$ . Both quantities are evaluated at the melting temperature  $T_{mi}$ . The subscript  $m$  denotes the melting point,  $liq$  refers to the liquidus temperature, respectively.

The third term on the right hand side of equation (3.9) is a second order contribution, which can often be neglected [32]. The molar heat capacity change of melting,  $\Delta C_{Pi}^{sl}$ , can be significant, but is hardly available. When applying the criterion for crystallization of component  $i$  from thermodynamic equilibrium conditions at the liquidus temperature, the molar heat capacity change of melting  $\Delta C_{Pi}^{sl}$  is also often neglected [15, 26]. Hence, in what follows, it is assumed that:

$$\ln a_i^l = \left[ \frac{\Delta H_i^{sl}}{R T_{mi}} \left( \frac{T_{liq} - T_{mi}}{T_{liq}} \right) \right] \quad (3.10)$$

Solving equation (3.10) for  $T_{liq}$ , we have an expression for the liquidus temperature of a specific species  $i$ , ( $T_{liq,i} = T_{liq}$ ). We can finally write:

$$T_{liq,i} = \frac{\Delta H_i^{sl} T_{m,i}}{\Delta H_i^{sl} - R T_{mi} \ln(a_i^l)} \quad (3.11)$$

Two aspects have to be explained in more detail with respect to this method:

1. The activity model results in one activity (with the pure liquid state as reference state) for each species (oxides and structural compounds) at a given glass composition and temperature. This results in one liquidus temperature for each constitutional component. The component with the highest liquidus temperature at a given composition will be the first to crystallize from the melt and will thus determine the so called liquidus temperature of the multicomponent glass.
2. The calculated activity  $a_i^l$  is, at a given glass composition, a function of temperature. The condition for crystallization, as described in equation (3.11), is only valid for  $a_i^l$  at  $T = T_{liq,i}$ . This implies that the liquidus temperature  $T_{liq,i}$  must be determined iteratively. This was be done by the iterative method of false position (regula falsi) [41].

Equation (3.9) and thus equation (3.10) suppose that the activities of the constitutional components in the solid and liquid state on the liquidus line are equal and unity. For  $a_i^l = 1$  equation (3.11) results in  $T_{liq,i} = T_{mi}$ . The usual reference state of chemical activities is that of the most stable state at the considered condition. This means, e.g., the solid state at e.g., 1073 K and the liquid state at, e.g., 1673 K. This is also assumed by equation (3.9) and allows thus to use this condition as criterion to calculate liquidus temperatures. However, this also implies "true" congruent melting, i.e., a species  $i$  exists as pure species in the liquid state at its stoichiometric composition. However, the compound model assumes that in the liquid state all constitutional components are present. One single liquid species does therefore not exist alone. The calculated activity in the liquid state, using the compound approach, has, as reference state, the pure liquid state, which is not unity at the melting temperature of a stoichiometric composition of a structural compound, see figure 3.1. The following two cases for the structural compounds can be distinguished:

$$\begin{aligned} \text{congruent melting} &= \begin{cases} a_i^{ss}, & \text{activity of species } i \text{ in the solid state} \\ & \text{with reference state: pure solid state} \\ a_i^{ll}, & \text{activity of species } i \text{ in the liquid state} \\ & \text{with reference state: pure liquid state} \\ \text{at } T_{m,i}, & a_i^{ss} = a_i^{ll} \end{cases} \\ \text{compound approach} &= \begin{cases} a_i^{ss}, & \text{activity of species } i \text{ in the solid state} \\ & \text{with reference state: pure solid state} \\ a_i^{ll}, & \text{activity of species } i \text{ in the liquid state} \\ & \text{with reference state: pure liquid state} \\ \text{at } T_{m,i}, & a_i^{ss} = 1, a_i^{ll} \neq 1, \text{ thus } a_i^{ss} \neq a_i^{ll} \end{cases} \end{aligned}$$

As a consequence, equation (3.9) and thus equation (3.10) are not supposed to be used as they are, or the chemical activity values, calculated by the IMCM, should not used. The effect of  $a_i^{ss} \neq a_i^{ll}$  at  $T_{mi}$  for the compound model on the calculated liquidus temperatures will be shown in the next section.

Vedishcheva et al.<sup>10</sup> [26] calculated liquidus temperatures in the binary  $\text{SiO}_2$  -  $\text{Na}_2\text{O}$  system with equation (3.11) and compared them with experimental data. They found that the liquidus temperatures calculated using equation (3.11) were approximately 30-50 K lower than the one in the phase diagrams. They attributed this difference to the negligence of the second and third right hand side terms in equation (3.9), thus primarily to the negligence of  $\Delta C_{P,i}^{sl}$ . However, because Vedishcheva et al. use the compound approach for their activity value calculations, they have the same dilemma as described above. The results of their calculations are shown in figure 3.9. The discussion of the results follows in the next section.

Generally there are three main causes for deviations in calculated liquidus temperatures compared to experimentally determined ones:

1. The IMCM (compound) approach, that the activities of the individual constitutional components in the liquid state ( $a_i^l$ ) can never be unity.
2. The estimation of the thermodynamic pure substance data for the liquid state as discussed in section 3.2.1.
3. The negligence of the  $\Delta C_{P,i}^{sl}$  contribution in equation (3.9).

The main reason, why the  $\Delta C_{P,i}^{sl}$  contribution of the second term on the right hand side of equation (3.9) is usually neglected, is that it is difficult to measure and therefore unavailable for most components. Generally,  $\Delta C_{P,i}^{sl}$  does not strongly depend on the glass composition and thus not on the activities. This means that neglecting the  $\Delta C_{P,i}^{sl}$  contribution only influences the temperature level (height) of the calculated liquidus temperatures but not the shape of the curve. The shape of the curve mainly depends on the standard Gibbs free energy values of the different species  $i$ . When estimating the liquidus temperature using equation (3.11), calculated from chemical activity values, the condition that the activities of the constitutional compounds are never unity ( $a_i^l \neq 1$ ), will lead to liquidus temperatures lower than expected. This is related to the different reference states, as discussed above.

A very simple, but effective method to overcome this temperature shift is the introduction of a modification factor, which modifies the activity of species  $i$  in the liquid state ( $a_i^l$ ), to eliminate deviation from unity at the exact composition and melting temperature of the structural compounds, e.g., at the composition 50%  $\text{SiO}_2$  and 50%  $\text{Na}_2\text{O}$  in the binary for the structural compound  $\text{Na}_2\text{O} \cdot \text{SiO}_2$  and at  $T_m(\text{Na}_2\text{O} \cdot \text{SiO}_2)$ . At its melting temperature, the activity of the pure crystalline phase, with reference to the pure solid state, is, by definition, unity. A modification factor  $\gamma_i^*$  for component  $i$  can be calculated based on this information, which remains constant for all other compositions and temperatures.

$$\gamma_i^* = \frac{1}{a_i^l} \bigg|_{\substack{a_i^l = a_{i,st}^l \\ T_i = T_{m,i}}} \quad (3.12)$$

---

<sup>10</sup>Vedishcheva is one of the co-workers of Shakhmatkin and used his model for the liquidus temperature calculations.

where the subscript *st* denotes the stoichiometric composition. This modification factor fixes, during the liquidus temperature calculation, the liquidus temperature of the pure compound *i* at  $T_{mi}$ .

With this modification, equation (3.11) becomes

$$T_{liq,i} = \frac{\Delta H_i^{sl} T_{m,i}}{\Delta H_i^{sl} - RT_{m,i} \ln(a_i^l \gamma_i^*)} \quad (3.13)$$

This modification does not influence the equilibrium composition of the melt at the liquidus temperature  $T_{liq,i}$ , because it is not applied in the IMCM, with which  $a_i^l$  is calculated, but only in equation (3.13). It has thus hardly an influence on the shape of the liquidus line, but only of the height. However, this adaption has one disadvantage. It does not work for the pure oxides. Using the model, as seen in figure 3.2, the calculated activities of the pure oxides (e.g. at the left and right boundary of the phase diagram) are unity, so an adaption of  $a_i^l$  has no effect. This will be shown when discussing the validating the crystallization model in section 3.3.1 on page 76.

From equation (3.13), it can be seen that for a species *i* (oxide and structural compound) in the melt, its pure component melting temperature, its enthalpy of melting, its activity in the considered system and the modification factor  $\gamma_i^*$  must be known to estimate its liquidus temperature. The values for  $T_{m,i}$  and  $\Delta H_i^{sl}$  can be found for most of the compounds in the standard literature references [29, 42]. With the activity  $a_i^l$  calculated by the IMCM, the modification factor  $\gamma_i^*$  can readily be determined.

A calculation scheme has been presented to determine the liquidus temperature from calculated chemical activities in multicomponent glass melts. A modification factor,  $\gamma_i^*$ , has been introduced to correlate the different reference states ( $a_i^{ss} \neq a_i^l$  in the compound model). The validation of the model and the application of the modification factor will be given in the next subsection.

### 3.3.1 Validation of the liquidus temperature calculations

The equation to calculate iteratively the liquidus temperature of multicomponent glasses is given by equation (3.13):

$$T_{liq,i} = \frac{\Delta H_i^{sl} T_{m,i}}{\Delta H_i^{sl} - RT_{m,i} \ln(a_i^l \gamma_i^*)} \quad (3.13)$$

Section 3.2 presented a very general, but straightforward model for the calculation of chemical activities in multicomponent oxide (silicate) glass melts (IMCM). With the activity model and the known melting temperature of the constitutional components, the modification factor  $\gamma_i^*$ , as explained in the previous subsection, can also be calculated. At this stage, all information is available to calculate the liquidus temperature of silicate melts. The results of the comparison between the liquidus temperature calculations and the existing phase diagram [9] will be given in figure 3.9 for the Na<sub>2</sub>O-SiO<sub>2</sub> binary system.

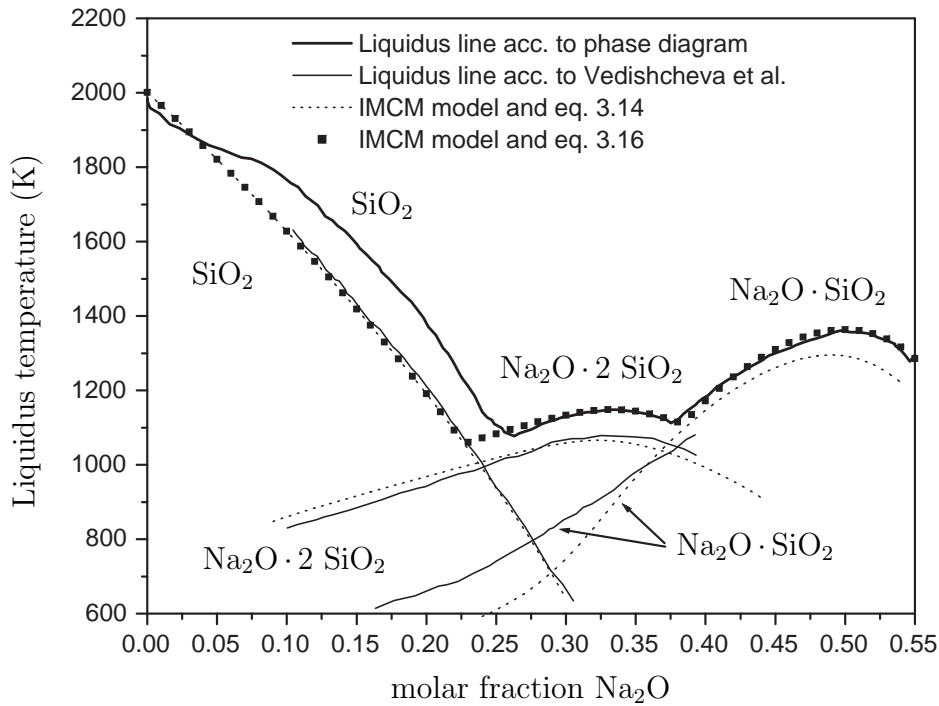


Figure 3.9: Comparison of calculated and experimental liquidus temperatures in the binary  $\text{SiO}_2$  -  $\text{Na}_2\text{O}$  system. The bold straight line represents the liquidus line according to the phase diagram, taken from the slag atlas [9]. The thin line represents the calculated liquidus temperatures according to Vedishcheva et al. [26]. The thin dotted line represents the calculated liquidus temperatures according to equation (3.11) and the IMCM (no adaption). The cubic points represent the liquidus temperature according to equation (3.13) and the IMCM with the adaption ( $\gamma_i^*$ ) as described in section 3.3. For the calculation of the  $\text{SiO}_2$  liquidus line the thermodynamic data of cristobalite has been used.

Figure 3.9 shows a comparison of modeled and experimental liquidus temperature values of the binary sodium-silicate system. The model calculations were performed twofold, with equation (3.11) (without  $\gamma_i^*$ ) and using equation (3.13) (with  $\gamma_i^*$ ) to be able to compare the calculated liquidus temperatures with the data from Vedishcheva et al. [26], who did not do any adaption to the calculate activity values. This means they used equation (3.11) to perform their calculations. The agreement between the IMCM and the results by Vedishcheva et al. are very good. However, both models show significant deviations from the "real" liquidus line. For  $\text{Na}_2\text{O} \cdot \text{SiO}_2$ , Vedishcheva et al. only calculated the liquidus temperature up to a  $\text{Na}_2\text{O}$  molar fraction of 0.4. It can be seen that the curve, calculated with the IMCM, does not follow the modeled curve of Vedishcheva et al. completely, but follows the liquidus line at  $x_{\text{Na}_2\text{O}} > 0.4$  in nearly the same distance as the compound NS2. Unfortunately, Vedishcheva et al. did not report any values for the used standard Gibbs free energy values of the considered compounds nor of any used melting enthalpies, to be able to check or review their results. An important point is that the eutectic composition between NS2 and NS is at the right position compared to the liquidus line from the phase diagram. Figure 3.9 also shows that the introduction of the modification factor  $\gamma_i^*$  gives

very accurate results, except for the single oxide  $\text{SiO}_2$  for  $x_{\text{Na}_2\text{O}} > 0.1$ . This is because for the liquidus temperature calculation of  $\text{SiO}_2$  the standard Gibbs free energy of cristobalite was used. At temperatures between 1743 K and 1143 K and  $0.1 < x_{\text{Na}_2\text{O}} < 0.25$  tridymite will be present [9], with of course different standard Gibbs free energy values. This also shows the sensitivity of the estimated liquidus temperature results on the choice of underlying thermodynamic data. Figure 3.9 shows for the structural compounds, that the shape of the curve remains the same while the temperature shift (height) is modified applying  $\gamma_i^*$ .

For the calculation of the liquidus temperature of multicomponent glasses or even glasses prepared by fly ash vitrification, the program, however, failed to produce plausible liquidus temperatures for the different structural compounds. It has been shown that small differences in  $\Delta G_{fi}^0$  values produce significant deviations in chemical activity values and thus small differences in  $\Delta G_{fi}^0$  values can produce significant deviations in liquidus temperatures applying the developed scheme to multicomponent glass systems. This was also observed by Besmann et al. [4]. The simple modification factor  $\gamma_i^*$ , introduced here, only compensates the height of the liquidus curve and not its shape, which is mainly determined by the  $\Delta G_{fi}^0$  values. Differences in  $\Delta G_{fi}^0$  values influence the course of the liquidus lines and can produce significant deviations in calculated liquidus temperatures compared to experimentally determined liquidus temperatures. In addition to that, the  $\gamma_i^*$  values are calculated from the pure structural compounds at their stoichiometrical composition and melting temperature, most of the time from the binary systems. The application of the  $\gamma_i^*$  values to ternary or multicomponent systems may also produce significant deviations between calculated and experimentally determined liquidus temperatures, because the  $\gamma_i^*$  values may not be constant, which was assumed in the model presented here. Deviations in liquidus temperatures can also be caused by the fact that in multicomponent systems not all structural compounds or their thermodynamic data are known and therefore cannot be incorporated into the model. This results thus in differences in chemical activity. It was observed during the calculations, that neglecting one or more components shows considerable deviations in activity values of the other components and thus in liquidus temperatures.

### 3.4 Concluding remarks

In this chapter, a new calculation model (IMCM) to estimate the chemical activities of constitutional components in multicomponent silicate oxide glass melts has been developed. The model is based on similar assumptions as in the compound concept, developed by Conradt and Shakhmatkin et al. [20–26], but was successfully extended to multicomponent glasses by new calculation algorithms. The model only requires the standard Gibbs free energies of formation of the constitutional single oxides and structural compounds and the analytical glass composition as input parameters. It is free of any adjustable parameters and does not need any expert selection of participating compounds. The Gibbs free energies of the liquid state of the constitutional compounds should be used for glass melts. However, for most of the components the required data is not available. As an approximation, the Gibbs free energies of the crystalline state, to which the change of melting enthalpy and entropy has to be added according to equation (3.4), has been used

for these components. This may lead to only small errors in case that the temperature of the melt is not very different from the melting point of the compound. The advantage, but also drawback of the model is the rigorousness regarding the choice of constitutional compounds. Even for rather simple binary or ternary systems a large number of constitutional components have to be taken into account. Neglecting components may lead to strong deviations of calculated activities of the oxides in the multicomponent system. The modeled chemical activities for  $\text{Na}_2\text{O}$ , even for a float glass melt, for which 64 constitutional compounds had to be used, are in fairly good agreement to the experimental activity data found in the literature. The maximum deviation between the experimentally determined chemical activity of  $\text{Na}_2\text{O}$  in float glass by [34] and the result of the IMCM calculation was 24%. Deviations compared to experimental results and other simulation models were observed. Because activity data of glasses from fly ash melts are not available, the validity of the model for these glass types could not be shown. The incorporation of large iron oxide concentrations in the glass requires that all existing iron oxide containing structural compounds are incorporated into the model. Because of the lack of availability of this data, IMCM calculations for a fly ash glass composition with iron oxide could not be performed. One main limitation, as it is the same for all thermodynamic modeling methods, is the availability of thermodynamic data of all constitutional compounds. As shown during the model validation, small deviations in  $\Delta G_f^0$  result in differences in calculated activities. An increase of 1% in  $\Delta G_f^0$  of  $\text{Na}_2\text{O} \cdot \text{SiO}_2$  showed an increase of  $a_{NS}$  of 23% (at  $x_{\text{Na}_2\text{O}} = 0.5$ ) and a decrease of  $a_{NS2}$  of 49% (at  $x_{\text{Na}_2\text{O}} = 0.33$ ). It is therefore not just important to have appropriate thermodynamic data of the constitutional components, but the data should also be very accurate.

Another even more important issue, when calculating chemical activities but also liquidus temperatures, is the melting enthalpy of the different structural compounds. According to the compound concept, proposed and discussed in this thesis, no constitutional component exists alone, not even at the melting point of a pure structural compound. There are always amounts, even if they are little, of all other constitutional components present (see figure 3.2, section 3.2.3 on page 65). This is the reason, why, even at the stoichiometric composition of one compound, the calculated activity in the melt (relative to the pure liquid compound), at the melting temperature of the compound, will never reach unity values in the model. When using the melting enthalpy of a compound as provided by the literature references, a part of it belongs to other components, because at the moment that a compound melts, other components existing in the system, are probably present (dissociation). This means that in fact, the total melting enthalpy of a specific compound in the liquid state contains melting enthalpy contributions related to all other present components. For the compound approach, this would reduce the reported (literature) melting enthalpies of the pure structural compounds at their stoichiometrical composition and melting temperature.

As an application of this model, parts of the liquidus temperature curve of the binary sodium-silicate system was modeled in good agreement with, in literature reported, phase diagrams using a adaption factor ( $\gamma^*$ ). This adaption was necessary to relate the reference state  $a_i^l$  at the liquidus line to  $a_i^{ss}$ . This factor adjusted the temperature level, but not the shape of the liquidus temperature curve. Calculations of the liquidus temperature of

multicomponent glasses or even glasses with compositions similar to MSW vitrification materials, which were not presented, did not show satisfactory results. It seems that the simple modification of the activity, as presented in section 3.3, which shows good results in the binary  $\text{Na}_2\text{O-SiO}_2$  system is not simply transferable to multicomponent systems. The modification factor, used in the presented approach, can only be calculated from the pure compounds (from binary systems (binary compounds), or ternary systems (ternary compounds)), where the exact melting temperatures of these compounds are known. Liquidus temperature calculations with the model and the modification factor, however not presented in the thesis, have shown, that the application of the determined modification factors to multicomponent glass compositions did not show plausible liquidus temperatures. Small differences in  $\Delta G_{fi}^0$  values influence the activity and also the course of the liquidus lines and can produce significant deviations in calculated liquidus temperatures compared to experimentally determined liquidus temperatures. However, calculations with the IMCM for typical fly ash glass compositions have shown, that the model can qualitatively be used to estimate the influence of compositional changes to the fly ash composition on the crystallization tendency by looking at changes in activity values of the constitutional compounds prone to crystallization.

Despite of the described drawbacks and problems using the IMCM for estimations of liquidus temperatures of multicomponent silicate glasses, it can be applied to assess practical problems in glass melting, e.g., refractory corrosion or the evaporation of certain species from the glass melt. One example is the corrosion of silica refractories in e.g., the crowns of float glass melting furnaces by NaOH. The reactive evaporation of NaOH depends among other things on the chemical activity of  $\text{Na}_2\text{O}$  in the glass melt, which also depends on the concentration of  $\text{Na}_2\text{O}$  at the glass melt interface. Modeling the composition dependent activity in the glass melt, as can be done by the IMC model, can contribute significantly to the modeling and understanding of evaporation of certain species from the glass melt [2, 5, 40].



## 3.5 Nomenclature

$a$	chemical activity	—
$b$	vector with molar amounts (mass balance) acc. to equation 3.14	mole
$g$	element index	—
$h$	relaxation factor acc. to equation (3.36)	—
$j$	element index	—
$i$	species index	—
$k$	total number of different elements in phase	—
$n$	total number of moles in phase	mol
$p$	total amount of different species in phase	—
$u$	number of different structural compounds	—
$x$	molar fraction	—
$y$	stoichiometric variable	—
$z$	stoichiometric variable	—
$\vec{x}$	vector of unknowns acc. to equation (3.33)	—
$\vec{B}$	vector of set of linear equations acc. to equation (3.34)	mole
$C_P$	molar heat capacity	$\text{J} \cdot \text{mol}^{-1} \cdot \text{K}^{-1}$
$G$	molar Gibbs free energy	$\text{J} \cdot \text{mole}^{-1}$
$H$	molar enthalpy	$\text{J} \cdot \text{mole}^{-1}$
$K$	thermodynamic equilibrium constant	—
$L$	Lagrange function acc. to equation (3.16)	—
$P$	pressure	Pa
$Q$	matrix of set of linear equations acc. to equation (3.32)	—
$R$	ideal gas constant	$\text{J} \cdot \text{mol}^{-1} \cdot \text{K}^{-1}$
$S$	molar entropy	$\text{J} \cdot \text{mole}^{-1} \cdot \text{K}^{-1}$
$T$	absolute temperature	K

### SUPERSCRIPTS

$\circ$	standard state (pure liquid or solid at $1.013 \cdot 10^5 \text{Pa}$ (1bar)
$\sim$	estimated
$'$	index for corrected molar masses acc. to equation (3.36)
$f$	formation
$s$	solid
$l$	liquid
$sl$	solid-liquid transition

## SUBSCRIPTS

$c$	crystallization
$f$	formation
$l$	liquid
$i$	compound
$m$	at melting point
$min$	minimal
$s$	solid
$st$	stoichiometric
$P$	at constant pressure
$liq$	at liquidus line (liquidus temperature)
$vit$	vitrification

## GREEK LETTERS

$\alpha$	stoichiometry matrix in mass balance (equation 3.14)	—
$\gamma$	activity coefficient	—
$\gamma^*$	modification factor, see equation 3.12	—
$\lambda$	Lagrangian multiplier	—
$\epsilon$	stop criterion for iteration acc. to equation (3.26)	mol <sup>2</sup>
$\Omega$	correction term acc. to equation (3.35)	—
$\mu$	chemical potential	J · mol <sup>-1</sup>

## NOTES

$\Delta$	Difference	—
----------	------------	---

## 3.6 Bibliography

- [1] H. Scholze. *Glas Natur, Struktur und Eigenschaften*. Springer-Verlag, Berlin Heidelberg New York, 1988.
- [2] K. E. Spear and M. D. Allendorf. Thermodynamic analysis of alumina refractory corrosion by sodium or potassium hydroxide in glass melting furnaces. *J. Electrochem. Soc.*, 149(12):B551–B559, 2002.
- [3] K. E. Spear, T. M. Besmann, and E. C. Beahm. Thermochemical modelling of glass: Application to high-level nuclear waste glass. *Mater. Res. Bull.*, 24(4):37–44, 1999.
- [4] T. M. Besmann and K. E. Spear. Thermochemical modelling of oxide glasses. *J. Am. Ceram. Soc.*, 85(12):2887–2894, 2002.
- [5] M. D. Allendorf and K. E. Spear. Thermodynamic analysis of silica refractory corrosion in glass melting furnaces. *J. Electrochem. Soc.*, 148(2):B59–B67, 2001.
- [6] F. Schill. Über die Kristallisation im Schaumglas. *Silikattechnik*, 15(1):10–13, 1964.
- [7] R. Gutmann. Charakterisierung von verglaster Elektrofilterasche aus Müllverbrennungsanlagen. *Abfallwirtschaftsjournal (Sonderdruck)*, 6:2–11, 1994.
- [8] R. Gutmann and H. Vonmont. Elektrofilterasche aus Müllverbrennungsanlagen - Quantitative Zusammensetzung. *Z. Umweltchem. Ökotox.*, 6(5):257–263, 1994.
- [9] M. Allibert. *Slag Atlas*. Verlag Stahleisen GmbH, Düsseldorf, Germany, second edition, 1995. ISBN 3-514-00457-9.
- [10] E. M. Levin, C. R. Robbins, and H. F. McMurdie. *Phase diagrams for ceramists*. The American Ceramic Society, 1964.
- [11] R. Backman, K. H. Karlsson, M. Cable, and N. P. Pennington. Model for liquidus temperature of multi-component silicate glasses. *Phys. Chem. Glasses*, 38(3):103–109, 1997.
- [12] K. H. Karlsson, R. Backman, M. Cable, J. Peelen, and J. Hermans. Estimation of liquidus temperatures in silicate glasses. *Glastechn. Ber. Glass Sci. Technol.*, 74(7):187–191, 2001.
- [13] C. Dreyfus and G. Dreyfus. The prediction of liquidus temperatures of oxide glasses by non-linear "neutral" regression. *Proc. Int. Congr. Glass, Montpellier, France*, 2002.
- [14] C. Dreyfus and G. Dreyfus. A machine learning approach to the estimation of the liquidus temperature of glass-forming oxide blends. *J. Non Cryst. Sol.*, 318:63–78, 2003.
- [15] P. I. Buler. Thermodynamic criteria of crystallization from supercooled liquid. *Ceram. Intern.*, 16:165–169, 1990.

- [16] A. D. Pelton and M. Blander. Thermodynamic analysis of ordered liquid solutions by a modified quasichemical approach - application to silicate slags. *Metall. Transaction B*, 17B(4):805–815, 1986.
- [17] M. Blander and A. D. Pelton. Thermodynamic analysis of binary-liquid silicates and prediction of ternary solution properties by modified quasi-chemical equations. *Geochim. Cosmochim. Acta*, 51(1):85–95, 1987.
- [18] C. W. Bale, A. D. Pelton, and W. T. Thompson. *FactSage 5.0 User Manual*, 2001. Ecole Polytechnique de Montréal, Royal Military College, Canada.
- [19] GTT Technologies, Herzogenrath, Germany. *ChemSage<sup>TM</sup>*, 1998.
- [20] R. Conradt. A thermodynamic approach to multicomponent oxide glasses. *Glastechn. Ber. Glass Sci. Technol.*, 68 C1:43–50, 1995.
- [21] R. Conradt. A simplified procedure to estimate thermodynamic activities in multicomponent oxide melts. *Molten Salt Forum*, 5-6:155–162, 1998.
- [22] B. A. Shakhmatkin, N. M. Vedishcheva, M. M. Shultz, and A. C. Wright. The thermodynamic properties of oxide glasses and glass-forming liquids and their chemical structure. *J. Non-Cryst. Sol.*, 177:249–256, 1994.
- [23] B. A. Shakhmatkin, N. M. Vedishcheva, and A. C. Wright. Thermodynamic modelling: a reliable instrument for predicting glass properties. *Proc. Int. Congr. Glass, Edinburgh Scotland*, 1:52–60, 2001. Invited papers.
- [24] B. A. Shakhmatkin, N. M. Vedishcheva, and A. C. Wright. Can thermodynamics relate the properties of melts and glasses to their structure? *J. Non-Cryst. Sol.*, 293-295:220–226, 2001.
- [25] R. Conradt. Thermochemistry and structure of oxide glasses. In H. Bach and D. Krause, editors, *Analysis of the composition and structure of glass and glass ceramics*, Schott series on Glass and Glass Ceramics, Science, Technology and Application, chapter 3.6, pages 232–254. Springer Verlag, Berlin, New York, 1999.
- [26] N. M. Vedishcheva, B. A. Shakhmatkin, and A. C. Wright. Thermodynamic modelling of chemical structure: Implications for the crystallization of oxide glasses. *Glastechn. Ber. Glass Sci. Technol.*, 71C:180–185, 1998.
- [27] J. W. Hastie, W. S. Horton, E. R. Plante, and D. W. Bonnell. Thermodynamic models of alkali-metal vapor transport in silicate systems. *High Temp. - High Press.*, 14:669–679, 1982.
- [28] J. W. Hastie and D. W. Bonnell. A predictive phase equilibrium model for multicomponent oxide mixtures: Part II. Oxides of Na-K-Ca-Mg-Al-Si. *High Temp. Sci.*, 19:275–306, 1985.
- [29] I. Barin, F. Sauert, E. Schultze-Rhonhof, and Wang Shu Sheng. *Thermochemical data of pure substances*, volume 1+2. Weinheim, VCH, second edition, 1993.

- 
- [30] G. Eriksson. Thermodynamic studies of high temperature equilibria, III. SOLGAS, a computer program for calculating the composition and heat condition of an equilibrium mixture. *Acta Chemica Scand.*, 25(7):2651–5658, 1971.
- [31] G. Eriksson and K. Hack. ChemSage-A computer program for the calculation of complex chemical equilibria. *Metall. Transaction B*, 21B:1013–1023, 1990.
- [32] J. M. Smith, H. C. Van Ness, and M. M. Abbott. *Introduction to Chemical Engineering Thermodynamics*. Chemical Engineering Series. McGraw-Hill International, fifth edition, 1996.
- [33] R. Adams. *Calculus: a complete course*. Addison-Wesley, 4th edition, 1999.
- [34] P. Sardjono. *Chemisch-thermodynamische Untersuchung über das Verhalten von Natrium während des Floatglasprozesses*. PhD thesis, Aachen University of Technology (RWTH-Aachen), Germany, 1995. In German.
- [35] R. G. C. Beerkens. Sulfate decomposition and sodium oxide activity in soda-lime-silica glass melts. *J. Am. Ceram. Soc.*, 86(11):1893–99, 2003.
- [36] R. Conradt. Soda activity in float glass. Personal communication, 2002.
- [37] R. Conradt. A quantitative approach to the properties of geological and industrial glass forming systems. In Rammlmair et al., editor, *Applied Mineralogy*. Balkena, Rotterdam, 2000.
- [38] C. Rüssel, R. Kohl, and H. A. Schaeffer. Interaction between oxygen activity of  $\text{Fe}_2\text{O}_3$  doped soda-lime-silicate glass melts and physically dissolved oxygen. *Glastechn. Ber. Gass Sci. Technol.*, 61(8):209–213, 1988.
- [39] E. Freude. *Voltammetrische Untersuchungen des Redoxverhaltens polyvalenter Ionen in Glasschmelzen, insbesondere von Technetium*. PhD thesis, Erlangen University, Erlangen, Germany, 1989.
- [40] R. G. C. Beerkens. Modeling the kinetics of volatilization from glass melts. *J. Am. Ceram. Soc.*, 84(9):1952–1960, 2001.
- [41] E. Kreyszig. *Advanced Engineering Mathematics*. John Wiley and Sons, Inc., 8th edition, 1999.
- [42] O. Knacke, O. Kubaschewski, and K. Hesselmann. *Thermochemical properties of inorganic substances*. Springer Verlag, Berlin, 2 edition, 1991.
- [43] W. H. Press, S. A. Teukolsky, W. T. Vetterling, and B. P. Flannery. *Numerical Recipes in C, The Art of scientific computing*. Cambridge University Press, second edition, 1997.

## 3.7 Appendix: Gibbs energy minimization procedure used in IMCM

The thermodynamic model (IMCM), developed in this study, to calculate the chemical activity values of the constitutional components in multicomponent glass melts was presented in subsection 3.2.2 on page 62. To calculate, e.g., the liquidus temperature of multicomponent oxide glass melts, first a model to calculate the chemical activities of the constitutional components of such a system is required. The chemical activity data can then be used in equation (3.11) or (3.13) to determine the liquidus temperature of the considered glass iteratively. In this appendix, the derivation of the chemical activity model is presented. It should be noted that this appendix is supposed to translate a thermodynamic problem into mathematical equations. Mathematical tools, e.g., a Lagrange minimization scheme or a standard value decomposition to solve sets of equations are used. These routines will not be explained in detail, but reference is made to applicable literature references.

### 3.7.1 Governing equations

The activity model calculates the chemical activity of oxides and structural compounds in a multicomponent glass which is assumed to be an ideal solution of the constitutional components. The derivation of the model resulted in equations (3.5) and (3.8), describing the Gibbs free energy of the equilibrium composition of a single phase system:

$$nG = \sum_{i=1}^p n_i \mu_i \quad \text{with} \quad n = \sum_{i=1}^p n_i \quad (3.5)$$

and

$$\mu_i = \mu_i^\circ + RT \ln \left( \frac{n_i}{n} \right) \quad (3.8)$$

By minimizing the term  $nG$  in equation (3.5) by changing the molar masses of the different species ( $n_i$  values), the equilibrium composition and thus the activities of the different species  $i$  can be found.

The minimization of the Gibbs free energy is carried out by an iterative method as developed by Eriksson [30]. During minimization, a non-negative set of mole numbers ( $n_i$ ) of the constitutional entities must be found, which gives the lowest possible value of the total free energy of the system. The conservation of mass for each chemical element acts as constraint for the minimization.

Each species (single oxide and structural compound) exists of different elements (Na, Si, O, etc.), and there are  $k$  different elements in total in the system of concern. The molar quantities of these elements are given by the initial condition and they are independent of the final equilibrium condition (mass balance). This condition is a constraint in the minimization process. The total molar amount  $b_j$  of each element  $j$  is:

$$b_j = \sum_{i=1}^p \alpha_{ji} n_i \quad (3.14)$$

where  $\alpha_{ji}$  is the number of atoms of the  $j$ -th element in a molecule of the  $i$ -th species.  $p$  is the total amount of different species in the phase. An example of equation (3.14) is:

$$\begin{pmatrix} b_{Na} \\ b_{Si} \\ b_O \end{pmatrix} = \begin{pmatrix} 0 & 2 & 2 \\ 1 & 1 & 0 \\ 2 & 3 & 1 \end{pmatrix} \begin{pmatrix} n_{SiO_2} \\ n_{(SiO_2 \cdot Na_2O)} \\ n_{Na_2O} \end{pmatrix} \quad (3.15)$$

### 3.7.2 Minimization routine

Equation (3.5) is minimized by application of Lagrange's method of undetermined multipliers<sup>11</sup>. First, the minimization procedure requires an initial estimation of the number of moles of the different species present in the system ( $n_i$ ). A calculation step results in new values for the number of moles of each species  $i$  in the system, which are then used as new estimates until a convergence criterion is reached.

According to Lagrange's method of undetermined multipliers, the constraint function (mass balance, equation (3.14)) must be incorporated into the so-called cost function (equation (3.5)) and the partial derivatives of the new cost function with respect to  $n_i$  and  $\lambda_j$  must be set to zero [33]. The new cost function  $L$  becomes:

$$L = nG + \sum_{j=1}^k RT\lambda_j \left( b_j - \sum_{i=1}^p \alpha_{ji} n_i \right) \quad (3.16)$$

where the expression  $RT\lambda_j$  is used for convenience as an undetermined multiplier<sup>12</sup> for each element  $j$  instead of the parameter  $\lambda_j$ . The necessary conditions for  $L$  to be minimum and to obey the constraints are:

$$\left( \frac{\partial L}{\partial n_i} \right) = 0 \quad (3.17)$$

$$\left( \frac{\partial L}{\partial \lambda_j} \right) = 0, \quad \text{for } \lambda_j \neq 0 \quad (3.18)$$

Equation (3.17) becomes:

$$\frac{dnG}{dn_i} + \sum_{j=1}^k RT\lambda_j \frac{d}{dn_i} \left( b_j - \sum_{i=1}^p \alpha_{ji} n_i \right) = 0 \quad (3.19)$$

The parameters  $\lambda_j$  and  $n_i$  are the unknowns, which are going to be calculated. The differential Gibbs free energy of the system is:

$$dnG = \sum_{i=1}^p \mu_i dn_i + \sum_{i=1}^p n_i d\mu_i = \sum_{i=1}^p \mu_i dn_i \quad (3.20)$$

---

<sup>11</sup>When extremizing a function subject to certain outside conditions (constraints), it is often difficult to find a close form of the function to be extremized. With Lagrange's method of undetermined multipliers it is not necessary to explicitly solve the conditions. The undetermined multiplier is necessary, because the two gradients, which follow from applying the method, will in general have different magnitudes. For more details see [33]

<sup>12</sup> $\lambda$  is an unknown constant, which does not depend on  $n_i$  and thus  $R$  and  $T$ , being constant for one calculation step, can be put together with  $\lambda$ , which simplifies the equation.

The summation of  $n_i d\mu_i$  is equal to zero at equilibrium, according to Gibbs-Duhem [32]. The combination of equations (3.19) and (3.20) gives the expansion of equation (3.17):

$$\mu_i - \sum_{j=1}^k RT \lambda_j \alpha_{ji} = 0. \quad (3.21)$$

Equation (3.18) becomes:

$$b_j - \sum_{i=1}^p \alpha_{ji} n_i = 0 \quad (3.22)$$

Equation (3.8) is nonlinear in  $n_i$  and  $n$ , which means that equation (3.21) is also nonlinear. This set of nonlinear equations is solved by linearizing equation (3.8) in  $n_i$  and  $n$  around estimated equilibrium values  $\tilde{n}_i$  and  $\tilde{n}$ , respectively, using a Taylor series expansion. Terms involving derivatives of second and higher order are neglected. By this procedure  $n_i$  becomes linearly related to  $\lambda_j$  and the estimated equilibrium composition.

For the Taylor expansion we get:

$$\ln n_i = \ln \tilde{n}_i + \frac{n_i}{\tilde{n}_i} - 1 \quad (3.23)$$

In equation (3.8)  $\ln n$  is expanded analogously to equation (3.23). Equation (3.8) can now be approximated by:

$$\mu_i \approx \mu_i^\circ + RT \ln \left( \frac{\tilde{n}_i}{\tilde{n}} \right) + RT \left( \frac{n_i}{\tilde{n}_i} - \frac{n}{\tilde{n}} \right) = \tilde{\mu}_i + RT \left( \frac{n_i}{\tilde{n}_i} - \frac{n}{\tilde{n}} \right) \quad (3.24)$$

with  $\tilde{\mu}_i$  the estimated chemical potential, calculated with  $\tilde{n}_i$ .

Substitution of equation (3.24) in equation (3.21), gives an expression for the new estimated molar amounts:

$$n_i = \tilde{n}_i \frac{n}{\tilde{n}} - \tilde{n}_i \frac{\tilde{\mu}_i}{RT} + \tilde{n}_i \sum_{j=1}^k \lambda_j \alpha_{ji} \quad (3.25)$$

The calculation scheme is as follows:

1. Determination of starting values:  $\tilde{n}_i$ , e.g.:  $10^{-8}$  for all  $\tilde{n}_i$ .
2. Solving the set of equations (equation (3.22) and linearized equation (3.8), resulting with equation (3.21) in equation (3.25) with the two unknowns  $\lambda_j$  and  $n_i$ ). The solving of the set of equations, which is necessary for each iteration step is going to be explained later in this text (equations (3.27) - (3.34)).

Step 2 results in an equilibrium composition for the approximated Gibbs free energy. However, the linearization will generally not be valid at the new equilibrium composition and a new approximation for the Gibbs free energy has to be made.

3. Using the previously calculated values (step 2) for  $n_i$  as starting value for the next calculation  $n_i \Rightarrow \tilde{n}_i$  and repeating step 2.



By repeating steps two and three (iterations), finally, the minimum Gibbs free energy will be found. During the iterations the value of  $n_i$  converges to  $\tilde{n}_i$ . The iteration process is stopped when the total difference between  $n_i$  and  $\tilde{n}_i$  is smaller than a value  $\epsilon$ , which is the stop criterium:

$$\epsilon = \sum_{i=1}^p (n_i - \tilde{n}_i)^2 \quad (3.26)$$

Calculation step 2, the solving of the linearized set of equations, is going to be explained in more detail in the following:

### Solving the linear set of equations with the unknowns $\lambda_j$ and $n_i$

In order to solve equations (3.21) and (3.22) for  $\lambda_j$  and  $n_i$ , the derived linearizations, equations (3.23) and (3.24) are incorporated into the equations. To solve a set of linear equations, according to:

$$Q \cdot \vec{x} = \vec{B} \quad (3.27)$$

the derived equations are reduced.  $n_i$  in the mass balance (equation (3.14)) is substituted by equation (3.25).

$$b_j = \sum_{g=1}^k \lambda_g \sum_{i=1}^p \alpha_{ji} \tilde{n}_i \alpha_{gi} + \tilde{b}_j \frac{n}{\tilde{n}} - \sum_{i=1}^p \alpha_{ji} \tilde{n}_i \left( \frac{\mu_i^\circ}{RT} + \ln \left( \frac{\tilde{n}_i}{\tilde{n}} \right) \right) \quad (3.28)$$

with:

$$\tilde{b}_j = \sum_{i=1}^p \alpha_{ji} \tilde{n}_i \quad (3.29)$$

and

$$\sum_{i=1}^p \alpha_{ji} \tilde{n}_i \sum_{g=1}^k \lambda_g \alpha_{gi} = \sum_{g=1}^k \lambda_g \sum_{i=1}^p \alpha_{ji} \tilde{n}_i \alpha_{gi} \quad (3.30)$$

The result is one equation for each element with one unknown,  $\frac{n}{\tilde{n}}$ .

An extra equation is generated by substituting  $n_i$  in the mass balance for the melt phase ( $n = \sum_{i=1}^p n_i$ ) by equation (3.25):

$$\sum_{g=1}^k \lambda_g \sum_{i=1}^p \tilde{n}_i \alpha_{gi} = \sum_{g=1}^k \lambda_g \tilde{b}_g = \sum_{i=1}^p \tilde{n}_i \left( \frac{\mu_i^\circ}{RT} + \ln \left( \frac{n_i}{\tilde{n}} \right) \right) \quad (3.31)$$

Equations (3.28) and (3.31) can now be set into the form of equation (3.27), with the symmetrical matrix  $Q$ :

$$Q = \begin{pmatrix} \sum_{i=1}^p \alpha_{1i} \tilde{n}_i \alpha_{1i} & \sum_{i=1}^p \alpha_{1i} \tilde{n}_i \alpha_{2i} & \cdots & \sum_{i=1}^p \alpha_{1i} \tilde{n}_i \alpha_{ki} & \tilde{b}_1 \\ \sum_{i=1}^p \alpha_{2i} \tilde{n}_i \alpha_{1i} & \ddots & & & \tilde{b}_2 \\ \vdots & & & & \vdots \\ \sum_{i=1}^p \alpha_{ki} \tilde{n}_i \alpha_{1i} & & & & \tilde{b}_k \\ \tilde{b}_1 & \tilde{b}_2 & \cdots & \tilde{b}_k & 0 \end{pmatrix} \quad (3.32)$$

The vector  $\vec{x}$  incorporates the unknown variables,

$$\vec{x} = \begin{pmatrix} \lambda_1 \\ \lambda_2 \\ \vdots \\ \lambda_k \\ \frac{n}{\tilde{n}} \end{pmatrix} \quad (3.33)$$

The vector  $\vec{B}$  incorporates the thermodynamic data of the constitutional components,

$$\vec{B} = \begin{pmatrix} b_1 + \sum_{i=1}^p \alpha_{1i} \tilde{n}_i \left( \frac{\mu_i^\circ}{RT} + \ln \left( \frac{\tilde{n}_i}{\tilde{n}} \right) \right) \\ \vdots \\ b_k + \sum_{i=1}^p \alpha_{ki} \tilde{n}_i \left( \frac{\mu_i^\circ}{RT} + \ln \left( \frac{\tilde{n}_i}{\tilde{n}} \right) \right) \\ \sum_{i=1}^p \tilde{n}_i \left( \frac{\mu_i^\circ}{RT} + \ln \left( \frac{\tilde{n}_i}{\tilde{n}} \right) \right) \end{pmatrix} \quad (3.34)$$

From the matrix equation (3.27), vector  $\vec{x}$  can be calculated (which is necessary for each iteration step). The molar fractions of one or more components can tend to zero [30], which can induce singularities during the solving of the set of linear equations<sup>13</sup>. In order to avoid that the solving procedure fails because of possible singularities, the technique of singular value decomposition [43], or SVD, was applied to solve the matrix equation. Using the values in vector  $\vec{x}$  and equation (3.25), the new molar masses  $n_i$  can be calculated from the previously estimated  $\tilde{n}_i$  values. These new  $n_i$  values can become negative, which is physically not realistic. In this case, Eriksson [30] proposes, that all molar masses should be corrected according to equation (3.36) to have new positive molar masses as estimates for the next calculation step. In case of negative  $n_i$  values, according to [30], the difference between initial all positive  $\tilde{n}_i$  and the calculated  $n_i$  values are reduced to obtain positive values for all mole numbers. Therefore  $\Omega_i$  values are calculated according to:

$$\Omega_i = \begin{cases} \frac{\tilde{n}_i}{\tilde{n}_i - n_i} & , n_i \leq 0 \\ 1 & , n_i > 0 \end{cases} \quad (3.35)$$

and the smallest  $\Omega_i$  value is determined ( $\Omega_{\min} = \min(\Omega_i)$ ). For  $\Omega_{\min} < 1$ , new molar numbers for all  $n_i$  values are calculated according to:

$$n'_i = \tilde{n}_i + h \Omega_{\min}(n_i - \tilde{n}_i) \quad \text{with} \quad 0 < h < 1 \quad (3.36)$$

The value for  $h$  is a relaxation factor, which is usually chosen near unity, e.g., 0.99. The calculated  $n'_i$  values are then used as estimates for the subsequent iteration step ( $n'_i \Rightarrow \tilde{n}_i$ ).

---

<sup>13</sup>In case that sets of linear equations of matrices are either singular or else numerically very close to singular, standard techniques to solve these equations or matrices, e.g., Gauss Elimination or LU Factorization, will fail. However, the technique of singular value decomposition can be used to solve such equations. The technique is explained in detail in [43].

## Chapter 4

# Gas forming reactions during heating of mixtures of powdered glass and foaming agent

---

<b>4.1</b>	<b>Introduction . . . . .</b>	<b>93</b>
<b>4.2</b>	<b>Gas forming reactions during foaming . . . . .</b>	<b>99</b>
<b>4.3</b>	<b>Foaming gas identification: experiments, results and discussion . . . . .</b>	<b>101</b>
<b>4.4</b>	<b>Concluding remarks . . . . .</b>	<b>112</b>
<b>4.5</b>	<b>Bibliography . . . . .</b>	<b>114</b>
<b>4.6</b>	<b>Appendix . . . . .</b>	<b>116</b>

---

The production of foam glass from waste glasses is a promising technique to reuse waste glasses or silicate residues. Foam glass was successfully produced from perlite rocks [1,2], from volcanic glassy rocks [3] and waste glasses from cathode ray tubes [4]. Foam material was also produced from crystallized glasses [5]. The foaming of glass powders prepared from vitrified fly ash<sup>1</sup> is also a promising technology for an added value re-use of the fly ash. The distinct and strongly changing composition of fly ash and thus of silicate melts from fly ash, however, makes its reuse difficult. Glass to be used as raw material for conventional foam glass production requires distinct and constant physicochemical properties (viscosity, surface tension, oxidation state etc.). To use glasses with different compositions for foam glass production, a more detailed analysis of the foaming process (type of gases evolved, onset temperature of gas evolution) is required to define process conditions for optimal foam glass production. A more detailed analysis of foam gas evolution during heating of glass powders and powdered reduced forming agents is presented in this chapter.

One of the most effective foam glass production processes, in terms of insulation capability and application as a construction material, is the so-called powder process [6].

---

<sup>1</sup>Fly ash discussed in this chapter and elsewhere in this thesis designates typical fly ash from MSW incineration facilities.

The powder process comprises the mixing of a glass powder with small quantities of a powdered foaming agent and a subsequent heat treatment, consisting of a sinter stage and a foaming stage. The sinter stage takes place at temperatures below the softening point of the glass, to sinter the glass particles forming closed bubbles. For a soda-lime silicate glass, the foaming stage is generally between 1023 and 1373 K to obtain foam gas formation and bubble expansion (growth). The identification of the gas forming reactions and the temperature range at which these reactions occur, related to the glass composition, is essential to understand, control and optimize the production process of foam glass. The foaming process can be subdivided into two main processes. The first process is the production of the foaming gas in the already sintered powder mixture mass by chemical reaction of the glass with a foaming agent, which is the driving force for bubble growth (foaming). The second process is the physical growth of the bubbles due to a pressure increase in the closed pores of the mixture of glass and foaming agent, because of temperature increase and gas release by chemical gas producing reactions.

As mentioned in the first chapter of this thesis, so far, not much information is available in the literature about the type of gas forming reactions during foaming of the powder mixture and their dependencies on, e.g., the concentration of polyvalent ions or the oxidation state of the glass. To study and control bubble growth during foaming of the powder mixture and to optimize adjustments to the glass composition and process parameters (e.g., heating rate and initial bubble size), a fundamental simulation model for modeling bubble growth in foam glass is required. The development of such a model is described in chapter 5. The model calculates the transient bubble growth as function of physicochemical glass properties (composition, gas release potential (oxidation state), glass viscosity, surface tension) and process parameters (initial bubble sizes, heating rate). However, the types of gas forming reactions, which drive bubble growth, and their dependencies on, e.g., the oxidation state, must be identified first as basis for the theoretical model. This identification is discussed in this chapter.

The gas forming reactions between a heated, oxidized molten and iron containing glass (generally used for industrial foam glass production), mixed with a reduced foaming agent (active carbon) are studied using model glasses. The intention of this chapter is not to show the foaming gas evolution of vitrified fly ash itself, but to identify the main foaming gases released and chemical reactions leading to the foaming gas. This is necessary to obtain the necessary chemical information for the modeling of the foaming process in the next chapter.

This chapter is structured as follows: after the introduction, possible chemical gas forming reactions, which are primarily responsible for the foaming process and their onset temperatures, are experimentally identified using a set of model glasses. Especially chemically dissolved oxygen, bonded to polyvalent ions in the glass, is a source of gaseous species required for foam gas reactions and thus foam gas production. Thirdly, the influence of the oxidation state of the glass on the gas forming reactions is studied using iron as example and commonly used polyvalent ion in the glass. Iron is present in fly ash melts up to 3 wt.% and thermodynamic values of reaction enthalpies ( $\Delta H$ ) and entropies ( $\Delta S$ ) for the iron oxide redox reactions in the glass are either available from literature sources

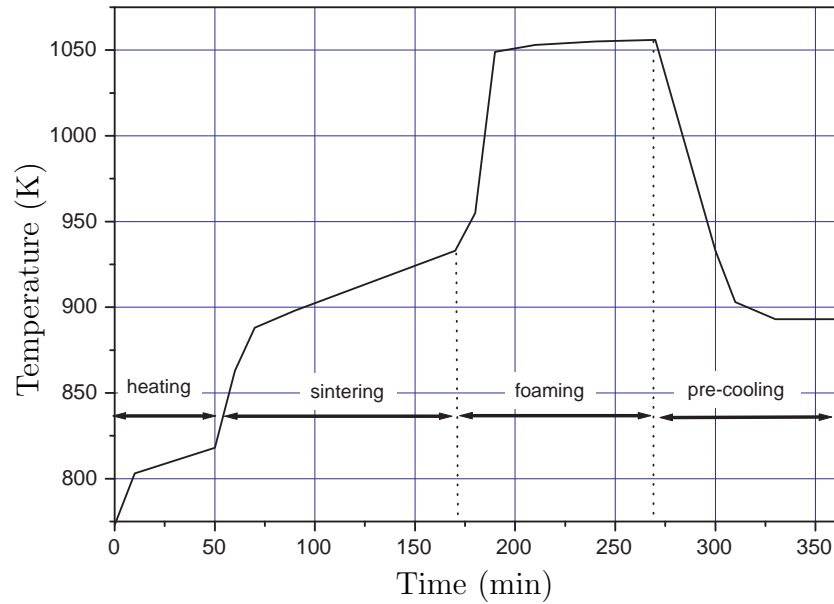


Figure 4.1: Example of the temperature course and foaming stages during the glass foaming process, derived from Schulz [10]. The temperature curve is only used exemplary, because it depends strongly on the properties of the glass and the foaming agent.

or can be determined experimentally [7–9]. In addition to that, the influence of the glass particle sizes on the foaming gas evolution are also studied experimentally. Finally, all experimental results are discussed and main conclusions, related to the chemical foaming gas reactions to be described, are derived.

## 4.1 Introduction

To produce foam glass according to the 'powder process', a mixture of powdered glass and foaming agent has to be heated to temperatures above the softening point of the glass (temperature at which the glass viscosity  $\eta > 10^{6.6} \text{ Pa} \cdot \text{s}$ ). During heating, the voids between the glass particles sinter together, forming small closed bubbles. The bubbles will grow if the gas pressure inside the bubble increases due to temperature increase or chemical gas forming reactions and when this pressure exceeds the pressure value applied by external forces on the bubble (surface tension). The gas evolution from the chemical reaction of the glass with the foaming agent (volume and temperature at which the gas evolution takes place) leads to the pressure increase inside the bubble. This pressure increase is the driving force of the foaming process (bubble growth). The gas release depends on the kind of foaming agent and the type of glass to be foamed. The different steps to transform a powder mix into a foam glass are: heating, sintering, foaming and pre-cooling. The different temperature ranges to foam a soda-lime silicate glass are schematically shown in figure 4.1, which is derived from Schulz [10], and will be discussed in the following.

During the first step, the heating step, the mixture of glass and foaming agent is dried. Heating can be fast until the start of the sinter period. It should be noted that, in case of carbon as foaming agent, the atmosphere in which the foaming takes place should be reduced in oxygen content. Otherwise the carbon will react with the oxygen from the atmosphere, reducing the amount of foaming agent still available for foaming after the voids are closed.

During the sintering stage, the applied heating curve is more gradual to allow the glass particles to first sinter together enclosing the carbon particles homogeneously. A typical volume reduction of approximately 44% occurs due to the sintering. In order to allow homogeneous bubble formation, the applied heating rate is limited, ensuring a uniform temperature and homogeneous glass viscosity throughout the sintered mass and thus uniform foaming gas evolution. The gas forming reactions already start at the sinter temperature, producing the foaming gas. However, foaming of the glass can only start when the glass grains have sintered together and closed bubbles are formed, otherwise foaming gas can easily escape from the powder mixture through the open pores. After this sintering process, the temperature should be increased somewhat faster to allow the gas forming reactions to proceed more rapidly and to obtain the appropriate lower glass viscosity enabling foaming. The required time at  $T_{max}$ , which is the maximum temperature of the foaming stage, depends mainly on the glass viscosity. In order to keep (freeze) the foamed structure after foam formation is finished, the glass is cooled rapidly (pre-cooling period).

In case that the bubbles grow too much, the thickness of the glass lamellae between the bubble gets thinner, and the lamellas can break. Local breakage of the lamellae causes local coalescence. This causes inhomogeneous bubbles sizes and influences the insulation properties of the foam glass. After the pre-cooling period the glass has to be annealed to room temperature to relax the induced thermal stresses in the glass. Mechanical stress inside the foam glass can lead to destruction of the lamellae between the bubbles, which decreases the heat insulation behavior and the mechanical strength of the final foam glass product.

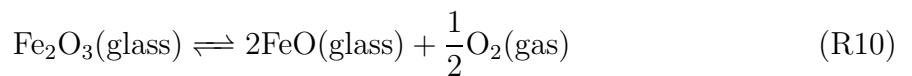
The 'pre-cooling' of the foam body from the foaming temperature to the annealing point ( $\log(\eta/(\text{Pa} \cdot \text{s})) = 12,4$ ) is supposed to "freeze" the foam body to be ready to handle (transfer) it to the next stage (extracting the foam body from the mould and inserting it into the annealinglehr (Pittsburgh Corning process) [11]). Thermal tension introduced by, e.g., cooling, relaxes at the annealing point in approximately 15 minutes. This is why the cooling can be relatively fast from the foaming temperature to the annealing point. The cooling of the foam body from the annealing point to the strain point ( $\log(\eta/(\text{Pa} \cdot \text{s})) = 13,5$ ) must be very low ( $0,2\text{--}0,8 \text{ K} \cdot \text{min}^{-1}$ ), depending on the thickness of the foam body [12,13] to avoid conservation of tensions in the glass. Tension relaxes at the strain point after 15 hours, which means they may remain inside the glass, because cooling rates are usually much faster. For temperatures lower than the strain point cooling rates of  $1\text{--}2 \text{ K} \cdot \text{min}^{-1}$  can be applied to cool the glass down to room temperature without having temporal tension in the glass lamellae between the bubbles during cooling.

The expansion of the bubbles, enclosed in the glass, depends on three main factors: first, the gas evolution inside the bubble due to gas forming reactions at the glass-bubble interface, secondly on the glass viscosity and thirdly on mass transport (diffusion) of dissolved gases from the glass towards the glass-bubble interface. These dissolved gases are the physically and chemically dissolved gases in the glass, e.g., oxygen. The amount of, e.g. oxygen, dissolved in the glass is affected by its oxidation state and the presence of polyvalent ions in the glass. The glass viscosity itself is mainly temperature dependent when the glass composition remains constant. At constant glass composition, the growth of the bubbles (foaming) depends thus mainly on the temperature and the release of dissolved gases from the melt producing a foaming gas by chemical reaction with the (reduced) foaming agent at the glass-bubble interface.

For the previously described foaming process (powder process), two different foaming agents can be used. An neutral foaming agent (e.g.  $\text{CaCO}_3$ ), which produces the foaming gas ( $\text{CO}_2$ ) by thermal decomposition, or a reduced foaming agent (e.g. carbon, silicon carbide or soot), which produces the foaming gas by chemical reaction. For instance using carbon (C) as foaming agent, CO and  $\text{CO}_2$  can be formed, extracting the oxygen from the glass. Generally, the choice of foaming agent influences the foaming process, e.g., temperature of foaming or volume of released gas. Reaction products, e.g., CaO from the  $\text{CaCO}_3$  decomposition, which remain in the bubble, can influence the glass properties such as the glass viscosity or the crystallization behavior. Therefore, to avoid such an effect, reduced foaming agents, which become completely gaseous after the oxidation reaction, may be preferred. Another advantage of, e.g., carbon is that, at an excess of carbon compared to available oxygen, at temperatures above 950 K, CO will mainly be formed according to the Boudouard reaction (R9). This doubles the molar amount of gaseous species compared to  $\text{CO}_2$  as foaming gas, for the same amount of oxygen which is, e.g., produced by  $\text{CaCO}_3$  thermal decomposition.



In case of carbon as foaming agent, oxygen is needed for the foaming gas reactions. The required oxygen in a foam sample can be supplied by two different sources. One is the oxygen physically<sup>2</sup> and chemically dissolved in the glass and the other one is the atmosphere in which the sample is foamed. In oxidized glass melts, containing polyvalent ions, the physical solubility of oxygen is relatively low compared to the chemical solubility [14]. A very large amount of oxygen can be dissolved chemically in the glass for instance by the presence of  $\text{Fe}_2\text{O}_3$ . An example is given by reaction (R10), where oxygen is released from the glass by shifting the equilibrium from the oxidized to the reduced side by adding a reducing agent or increasing the temperature.



Schulz [10] refers to sulfur trioxide ( $\text{SO}_3$ ) or sulphate in the glass as main oxygen donor when using a reduced foaming agent. Sulfur is available at a relatively large concentration

---

<sup>2</sup>the  $\text{O}_2$  dissolved in the holes of the glass network

Table 4.1: Possible reaction products of the reaction  $\text{SO}_4^{2-}(\text{glass}) + \text{C} + \text{H}_2\text{O}(\text{glass})$  depending on the type of reaction and the degree of reduction.

$\text{SO}_4^{2-}(\text{glass}) + \text{C}(\text{s}) + \text{H}_2\text{O}(\text{glass}) \rightleftharpoons$	
Glass	Gas phase products
$\text{Na}_2\text{O}$	$\text{CO}$
$\text{SO}_4^{2-}$	$\text{CO}_2$
$\text{S}^{2-}$	$\text{SO}_2$
	$\text{H}_2\text{S}$
	$\text{H}_2\text{O}$
	$\text{H}_2$

level in oxidized glasses as  $\text{SO}_4^{2-}$ . The concentration of  $\text{SO}_4^{2-}$  in the glass is also influenced by the oxidation state (redox state) of the glass [15] and its maximum solubility in soda-lime silicate glass melts is limited to approximately 0.9 wt.% [14]. At higher concentration levels, sulphate salts segregate from the glass melt [16, 17]. Demidovich [18] showed that  $\text{SO}_4^{2-}$  and dissolved  $\text{H}_2\text{O}$  have a strong influence on the foaming of glass. He presented multiple possible reaction equations of  $\text{SO}_4^{2-}$  and  $\text{H}_2\text{O}$  in the glass at the presence of a reducing agent (either C or already CO). Table 4.1 gives a brief overview of possible reaction products of  $\text{SO}_4^{2-}$  and  $\text{H}_2\text{O}$  and carbon. Unfortunately, the effect of iron in this context was not discussed.

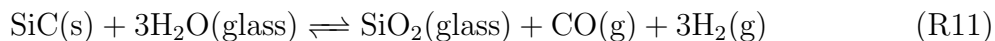
Glasses, melted from fly ash under oxidizing conditions contain up to 3 wt.%  $\text{Fe}_2\text{O}_3$ . However, quantitative data on the effect of  $\text{Fe}_2\text{O}_3$  and its concentration on the foaming gas reactions in foam glass has not been found in literature. This is probably, because in most technical glasses, the iron content is relatively low (0.001 - 0.11 wt.% for, e.g., clear float glass). The glass used for industrially produced foam glass (Pittsburgh Corning) contains about 3 wt.%  $\text{Fe}_2\text{O}_3$ .

Köse [13] used silicon carbide (SiC) powder as reduced foaming agent to foam a soda-lime-silicate glass containing 0.5 wt.%  $\text{Fe}_2\text{O}_3$  and 0.8 wt.%  $\text{H}_2\text{O}$ . The concentration of 0.8 wt.%  $\text{H}_2\text{O}$ , as stated in the thesis, seems very high. Köse also states that he uses waste glass from glass recycling, which is mostly container glass (bottles and jars). However, glasses from which bottles and jars are produced usually do not contain these  $\text{H}_2\text{O}$  concentration levels (maximum 0.03-0.05 wt.% [19]), so it is assumed that this is an error.

For the formation of the foaming gas, Köse assumed that the reaction of the SiC with the sulfates (no concentration in the glass given), the alkali oxides and the water in the glass caused the release of foaming gases. Unfortunately, gas forming reactions by iron oxides in the glass were not discussed. In his thesis it is also stated that carbon monoxide is the major foaming gas. The concentration of CO in the bubbles of the foam was determined to be between 77 and 83 vol.%, after foaming in an air atmosphere and between 96 and 99 vol.% in an argon atmosphere. The samples foamed in an air atmosphere contained in addition to the CO, 8 to 18 vol.%  $\text{N}_2$  and 4 to 9 vol.%  $\text{H}_2$ . No  $\text{CO}_2$  was found and no  $\text{H}_2\text{O}$  was reported. The concentration of  $\text{N}_2$  decreased and the concentration of  $\text{H}_2$  increased



with increasing temperature (1213 - 1253 K) and increasing SiC content (1 and 2 wt.%). A possible reaction for the formation of H<sub>2</sub> was proposed by:



However, no condensed water in the pores was reported and the H<sub>2</sub> concentration is relatively low, compared to the one of CO. This also supports the assumption that the value of 0.8 wt.% H<sub>2</sub>O is probably not correct.

Silicon carbide as foaming agent requires approximately 100 to 200 K higher foaming temperatures, compared to graphite or carbon, because of the lower reactivity of SiC with oxygen, compared to the reaction using carbon at the same temperature. Another disadvantage using SiC is the local formation of SiO<sub>2</sub> by oxidation of the SiC. This may cause a local increase of the glass viscosity at the bubble glass interface and may inhibit thereby the bubble growth.

The differences of 16 vol.% in CO concentration in the foam comparing the two investigated foaming atmospheres (air and argon), found experimentally by Köse [13], is relatively small, even for the small samples (cylinder of 10 mm diameter and 20 mm height). This underlines that the required oxygen for the production of the foaming gas, using a reduced foaming agent, originates predominantly from the glass. It shows that the influence of the atmosphere composition on the gas composition inside the foam bubbles is rather small. This is especially the case for thick sample sizes. Industrially produced foam glasses using carbon or soot as foaming agent are produced continuously in tunnel furnaces with understoichiometric gas firing (Pittsburgh Corning process) [11]. Early carbon oxidation, before the glass has reached its sintering temperature, is thereby prevented.

Concluding, a reduced foaming agent that is converted into gaseous species after oxidation, without leaving much unreacted traces (e.g. CaO from CaCO<sub>3</sub> decomposition), is preferable for the foam glass production. The chemically dissolved oxygen in the glass appears predominantly responsible for the oxidation of the foaming agent and formation of the foaming gas. The influence of the atmosphere on the foaming gas release (foaming gas composition) seems to be rather small. To avoid pre-oxidation of the reduced foaming agent, an atmosphere which is either reduced or free of oxygen (Ar, He etc.) should be considered. Polyvalent ions (sulphate of iron oxide) in the glass, dissolving oxygen chemically appear to influence the foam gas release during the foaming process. The total amount of gas formation during foaming, in this case, can probably be controlled by controlling the oxidation state of the glass.

In addition to the glass viscosity, the following factors mainly influence the foaming behavior, i.e. the temperature of the foaming process and the quantity of the foaming gas, determining the foam expansion during heating of the glass/carbon powder mixture. Other important parameters are:

**SO<sub>4</sub><sup>2-</sup> concentration in glass:** SO<sub>4</sub><sup>2-</sup> in the glass influences its oxidation state and thus its gas release potential. This aspect will not be discussed in this chapter. The interaction between iron and sulfate in silicate glasses is very complex. Therefore

only one sort of polyvalent ion in the glass was chosen, iron oxide. In order to describe the interactions between polyvalent ions and oxygen in the glass with respect to foaming quantitatively, reliable thermodynamic and mass transport data (diffusion) is needed, which is not always available, i.e. diffusion coefficients for  $\text{SO}_4^{2-}$  or  $\text{Na}_2\text{SO}_4$ , respectively or information of other sulphur species in the glass. A more detailed discussion of this aspect will be given in chapter 5.

**$\text{Fe}_2\text{O}_3$  concentration in glass:** The content of iron oxide and the oxidation state of the glass influence its gas release potential.  $\text{Fe}_2\text{O}_3$  or  $\text{FeO}$  can be dissolved in silicate glasses in large quantities (up to 11 wt.% (basaltic glasses)) [14] and this is a major source for chemically dissolved oxygen, which can react with the reduced foaming agent. The influence of iron oxide in glasses with different oxidation states on the gas release, reacting with carbon, will be studied in more detail in the following sections.

**$\text{H}_2\text{O}$  concentration in glass:**  $\text{H}_2\text{O}$  in the glass can react with a reduced foaming agent, forming  $\text{H}_2$  and  $\text{CO}$  or  $\text{CO}_2$ . Given the  $\text{H}_2\text{O}$  concentrations in glass ( $<0.1$  wt.%), the contribution of water to the foaming gas compared to the contribution due to reduction of ferric iron is assumed to be rather small. The effect of water in the glass on foaming is not treated in this chapter.

**Oxidation state:** At a given concentration of a type of polyvalent species in the glass, the oxidation state of the glass in general determines, among other things, the concentrations of chemically and physically dissolved oxygen in the glass [14] and thus the amount of oxygen available to react with the reduced foaming agent. The effect of the oxidation state on the foam gas evolution is experimentally studied in this chapter.

**Foaming agent:** The type of foaming agent, e.g., reduced or oxidized, determines, whether the gas formation is by dissociation ( $\text{CaCO}_3$ ) or by chemical reaction (carbon or  $\text{SiC}$ ). It also determines the temperature at which the foaming process mainly takes place.

**Heating rate:** The heating rate has a distinct influence on the initial bubble formation (sintering) and on the subsequent bubble growth. This was observed during the validation experiments for the bubble model, which is presented in chapter 5.

**Particle size:** The particle size of the glass powder influences the initial bubble size. Smaller glass particles will lead to smaller voids between the particles before the sintering process starts. Smaller initial bubbles after sintering results in more bubbles per unit volume. Smaller glass particle sizes give thinner initial lamellae between the bubbles and thus shorter diffusion distances. This will be discussed in more detail in chapter 5. Finer particle sizes of the foaming agent will lead to a more homogeneous distribution of bubbles throughout the mixture and a larger surface to mass ratio. Since the oxidation of, e.g., carbon particles, is a surface reaction of the carbon particle surface (initially), more foaming gas can initially be produced.

**Foaming temperature:** The temperature at which foaming starts, depends strongly on the glass viscosity ( $\eta > 10^{6.6}$  Pa · s as sort of lower limit) and on the type of foaming agent related to its reactivity towards available oxygen originating from the glass.

**Furnace atmosphere:** The furnace atmosphere can have an influence on the consumption of, e.g., a reduced foaming agent. At the sintering temperature the voids in the powder mixture are not yet closed and, e.g., carbon can react with available oxygen in the furnace atmosphere. This reduces the residual amount of carbon available for foaming reactions after the voids are closed, forming the initial bubbles.

The goal of this chapter is to generate experimental information about the main prevalent gas forming reactions in an iron oxide containing glass-foaming agent mixture to be able to model the transient bubble growth in foam glass, which is presented in chapter 5. First, the gases released during the reaction of a silicate glass powder containing solely iron oxide as polyvalent ion with carbon as foaming agent are identified. Secondly, the influence of the oxidation state and the effect of glass particle size on the foaming gas release rate are experimentally studied.

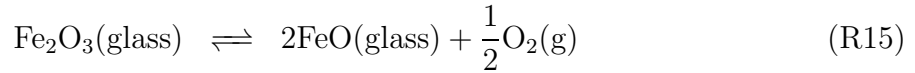
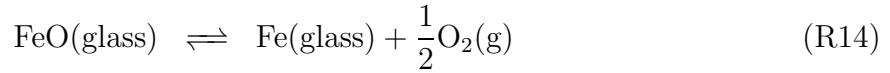
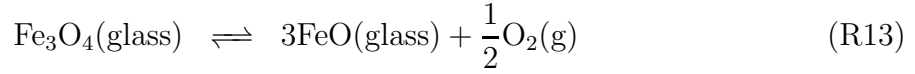
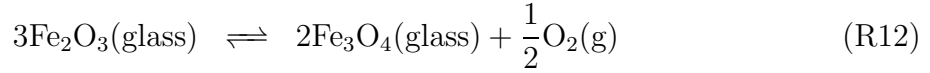
The next section discusses some chemical reactions responsible for foam gas formation in a glass powder containing solely iron as polyvalent ion and carbon as foaming agent.

## 4.2 Gas forming reactions during foaming

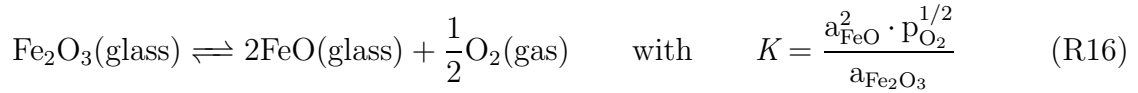
The reactions leading to foam gas production are rather complex and still not completely identified and described in literature. Thermodynamic relations of, e.g., the Gibbs standard free energy of reaction ( $\Delta G^r$ ), are often used to identify, describe and compare the most probable gas forming reactions during foam glass production [13, 18]. As shown in section 2.3 on page 39, this type of consideration requires that each species is in its standard state as a pure substance or that the chemical activities of each reacting species are known. All found literature references [13, 18] used pure substance thermodynamics to describe possible gas forming reactions. Applying pure substance thermodynamics, the chemical activity is assumed to be unity ( $a_i=1$ ). Unfortunately, the chemical activity of, e.g.,  $\text{Fe}_2\text{O}_3$ , dissolved in a soda-lime-silicate glass, is much lower than unity, which makes pure species thermodynamics inappropriate to assess the most probable and main gas foaming reactions between a glass and a reduced forming agent, when the activity values are not known.

In this chapter only soda-lime-silicate glasses with iron ( $\text{Fe}^0$ ,  $\text{Fe}^{2+}$ ,  $\text{Fe}^{3+}$ ) as polyvalent ion are studied. Iron oxide ( $\text{Fe}_2\text{O}_3$  or  $\text{FeO}$ ) can be incorporated in silicate glasses up to 10-11 wt.% (basaltic glasses). Iron in pure solid Fe-O phases can be present as  $\text{Fe}_3\text{O}_4$ ,

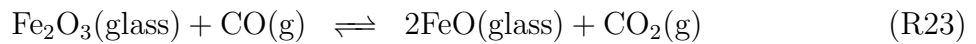
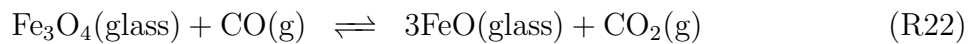
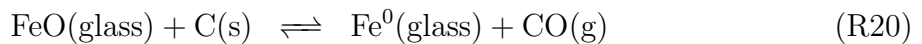
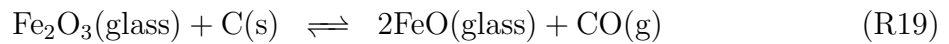
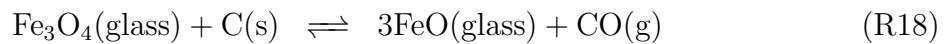
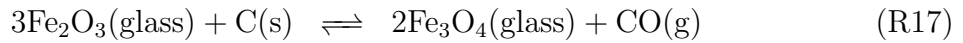
$\text{Fe}_2\text{O}_3$ ,  $\text{FeO}$  and  $\text{Fe}$ . The following possible reactions may take place in the glass [9]:



Reaction (R15) is described by a combination of reaction (R12) and (R13). The distribution of iron ions in soda lime silicate glass between the different states depends on the oxidation state and the related reduction-oxidation equilibrium (also called redox equilibrium), which depends on the glass composition and the melting conditions (e.g. temperature and exchange with oxygen from the atmosphere). The iron oxide equilibrium in an oxidized molten soda-lime-silicate glass at higher temperatures is usually described according to [9]:



where  $K$  is the thermodynamic equilibrium constant,  $a$  the chemical activity and  $p_{\text{O}_2}$  the partial oxygen pressure in the glass in equilibrium with dissolved oxygen in the melt. Rüssel et al. [20] and Freude [21] carried out voltammetric studies on TV-screen glass at temperatures less than 1323 K with an  $\text{Fe}_2\text{O}_3$  content larger than 0.4 wt.%. According to their findings, the reduction of iron oxide in these glasses occurs in two steps. The first reduction step is according to reaction (R12) and the second according to reaction (R13). This shows that there is a possibility that at lower glass temperatures and larger iron concentrations, iron can be incorporated in silicate glasses as  $\text{Fe}_3\text{O}_4$ . The following reactions of the different states of iron oxide in the glass with solid carbon or gaseous CO at the glass/carbon interface are possible:



Own experiments have shown, that the concentration of physically dissolved oxygen in a strongly oxidized molten glass with 3 wt.%  $\text{Fe}_3\text{O}_4$  at 873 K is about 8-10 orders of magnitude smaller than the concentration of ferric iron. Reactions of physically dissolved oxygen in the glass with carbon or CO can therefore be neglected because its contribution to the foaming gas formation is very low, compared to the one of e.g.,  $\text{Fe}_2\text{O}_3$ . This aspect

will be discussed in more detail in section 5.2.6 on page 133. Reactions (R17) to (R20) show that, using carbon, in general four different gas forming reactions can be expected in a glass powder with only iron as polyvalent ion. This leaves reactions (R17) - (R19) and reactions (R21) - (R23) to be considered for the formation of the foaming gas. It should be noted that reactions (R21) - (R23) do not result in an extra gas formation, but change the composition of the gas phase inside the bubble. However, the produced  $\text{CO}_2$  can be reduced to CO according to the Boudouard equilibrium<sup>3</sup> (reaction (R9)), presupposing an excess of carbon.

As shown above,  $\text{Fe}_2\text{O}_3$  in oxidized soda-lime-silicate glasses can in general, develop four different oxidation states, three of them are relevant for foaming. Experiments were designed to study the type and quantity of foaming gases evolving from iron containing glass - carbon reactions and the dependency of gas evolution on the oxidation state of the glass. The experiments are presented in the next section.

## 4.3 Foaming gas identification: experiments, results and discussion

As discussed in the introduction to this chapter, there is hardly any information on the effect of iron oxide and the oxidation state of a glass on foaming gas reactions and gas release during foam glass production (e.g. onset temperature of foaming and type of gaseous species inside the bubble). This section shows an experimental method providing the onset temperature of foaming gas production, the identification of the gaseous gas species and the dependency of the foaming gas evolution as a function of the oxidation state of the glass.

This section is divided into three parts, each part showing the experimental techniques and discussing the results. The first part concerns the qualitative identification of the foaming gases and the onset temperatures of gas formation. The second part shows the quantitative determination of the foaming gas and a proposal of the possible mechanism of the reaction of carbon with iron-oxides in glass. The third part shows the influence of the oxidation state and the glass particle size on the foaming gas evolution.

### 4.3.1 Foaming gas identification experiments

#### Experimental set-up

A schematic overview of the experimental setup with a horizontal tube furnace is given in figure 4.2. The model glasses for these foaming experiments were melted from dry reagent grade chemicals. The compositions of the two different glasses, verified by X-ray fluorescence analysis (XRF), are given in table 4.2. 100 g of raw material batch were mixed and charged into platinum crucibles (95% Pt, 5% Au). After melting for 30 minutes at 1723 K in a Nabertherm HT 16/17 muffle furnace, the glasses were quenched,

---

<sup>3</sup>A more detailed view on the Boudouard equilibrium as a function of temperature is given in Chapter 5, figure 5.7 on page 140.

*Table 4.2: Studied model glass compositions for the foaming gas identification measurements. The glass composition was verified by X-ray fluorescence analysis (XRF).*

Glass/ Oxide	SiO <sub>2</sub> (wt.%)	CaO (wt.%)	Na <sub>2</sub> O (wt.%)	Al <sub>2</sub> O <sub>3</sub> (wt.%)	Fe <sub>2</sub> O <sub>3</sub> (wt.%)	SO <sub>3</sub> (wt.%)
FG 1	68.69	15.46	10.41	5.41	0.01	0
FG 2	68.25	14.21	9.78	4.92	2.83	0

broken to small pieces and remelted in a second step at 1723 K for another 3 hours to improve the glass homogeneity. Afterwards, the glasses were quenched, milled to powder ( $32 < x < 63 \mu\text{m}$ ) and a mixture of 95 wt.% glass and 5 wt.% active carbon ( $d_{50} < 30 \mu\text{m}$ ), the foaming agent, was prepared. Thin layers of the glass/carbon powder mixture were placed on ceramic boats. The intention of the experiments was to avoid foaming of the glass melt (capturing of the gases), but to allow the gases created at the glass/carbon interface to leave the mixture to be analyzed rather than being enclosed. The intention of this chapter is to identify the gas species responsible for foaming (foaming gas) and the chemical reactions, rather than conducting experiments to generate glass foam. Foaming experiments have been conducted to validate the foam bubble growth model, which is going to be developed and discussed in chapter 5. Approximately 1 gram of the mixture was transferred into a mullite boat which was then inserted into a mullite tube. This tube was then flushed with helium gas at  $1.5 \text{ l} \cdot \text{min}^{-1}$ , controlled by a mass flow controller, and heated up to 1473 K with a heating rate of  $40 \text{ K} \cdot \text{min}^{-1}$ . For the qualitative determination of the gaseous species in the continuously evolving gases during the experiment, a Balzers Thermostar type GSD 300 T2 mass spectrometer was used.

## Results

Only the heights of the peaks at 28 and 44 AMU did increase during the heating process. The results of the experiments are shown in figure 4.3. As observed in the figure, the intensity at 28 AMU at the starting temperature is not zero. This value is caused by nitrogen gas, which was still in the system and has nearly the same molecular mass as CO. The used mass spectrometer was not able to separate the signals from CO and N<sub>2</sub>. The normalized AMU 28/4 signal was constant at the beginning of the experiment. The intensities at 14 AMU (N) and 32 AMU (O<sub>2</sub>), did not change during the experiment, so that the intensity increase at 28 AMU were related to an increase in CO concentration and not by N<sub>2</sub> or air leakage.

**Glass without polyvalent ions (FG1):** Glass FG1, without any polyvalent ions, started to react with the carbon at approximately 1360 K, producing carbon monoxide. This CO evolution is probably due to the reaction of the carbon with the oxygen from the glass network at high temperatures exceeding 1400 K.

**Fe<sub>2</sub>O<sub>3</sub> dissolved in the glass (FG2):** The addition of polyvalent ions to the glass composition has a strong impact on the formation of the foaming gas CO. The addition of iron shifts the onset temperature of the gas forming reactions to approximately 900 K.

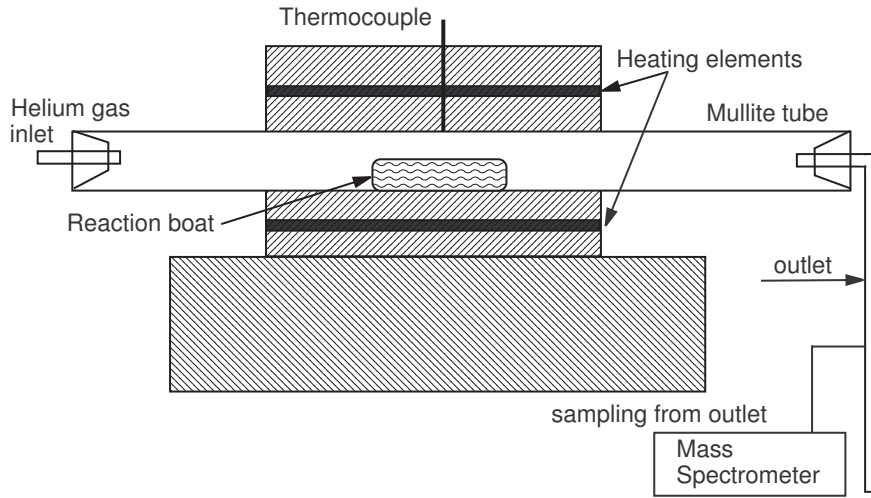


Figure 4.2: Experimental setup for foaming gas identification

Two peaks are detected consecutively with the first maximum at approximately 1200 K and the second one between 1400 and 1470 K.

The formation of  $\text{CO}_2$ , indicated by a small peak, starts at approximately 1060 K. It starts at the same temperature as the CO formation and has its maximum value at 1150 K, decreasing to a lower level than before the raise of 1060 K. The  $\text{CO}_2$  curve does not show the same steady increase as observed for the CO curves between 900 and 1150 K. This would however be expected in case that the reaction of  $\text{Fe}_2\text{O}_3$  and carbon would produce  $\text{CO}_2$  rather than CO at lower temperatures. At an excess of carbon, which was present at all times during the experiment, and an oxygen free atmosphere, the formation of  $\text{CO}_2$  is hardly expected. The results of the foaming gas composition of Köse [13] as presented in the introduction, neither show  $\text{CO}_2$ , not even in the cooled foam samples.

Quantitative analysis of the CO evolution is necessary to determine the exact behavior of iron oxide in the glass in contact with carbon. The quantitative measurement of the CO release will be discussed in the next subsection.

### 4.3.2 Quantitative determination of foaming gas evolution

Quantitative analysis of the evolving gases is carried out under the same conditions as described in the previous subsection. Only CO as a foaming gas species shows considerable evolution and the CO volume will be measured quantitatively for the 2 different glasses (FG1 and FG2). For the analysis of the CO concentration in the He carrier gas flow, exiting the tube, a Siemens Ultramat 22P online sensor (IR absorption, selective for CO) was used, which was calibrated prior to the experiment using certified analyzed gas mixtures. The measured carbon monoxide concentration in the He carrier gas leaving the tube furnace as function of temperature for the glass FG2 is given in figure 4.4 for a new set of experiments. The curve was subtracted by the gas evolution curve of the glass FG1

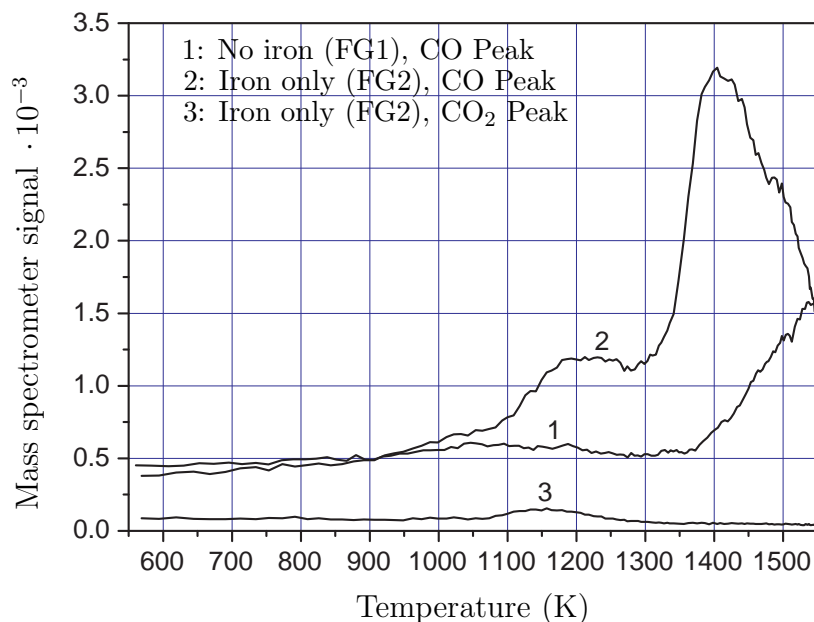


Figure 4.3: CO and CO<sub>2</sub> mass spectrometer peak intensities of the two different glasses (composition in table 4.2) as a function of temperature.

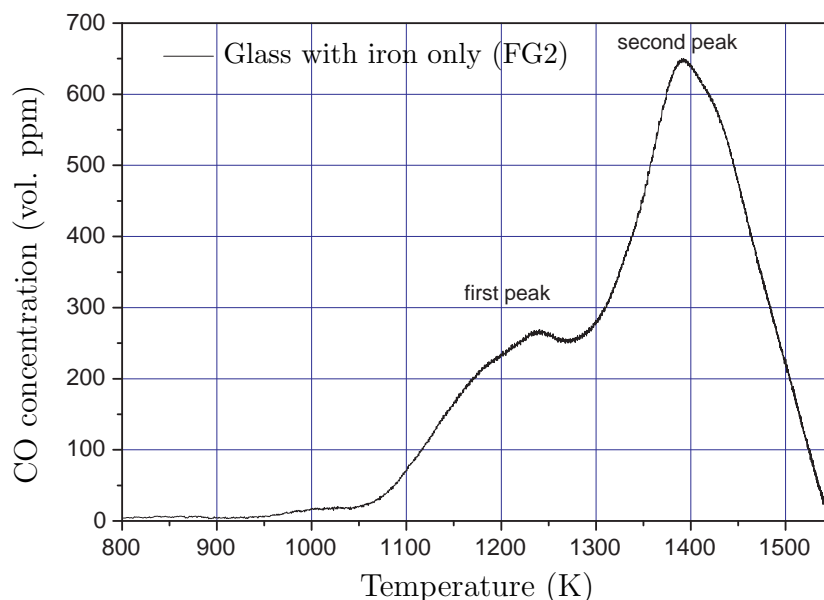


Figure 4.4: CO evolution in the helium carrier gas as a function of temperature of glass FG2. The temperature dependent CO evolution curve of glass FG1 is subtracted from the CO curve of glass FG2 to display the CO evolution solely caused by the presence of iron oxide in the glass.



(no polyvalent ions), to eliminate the production of CO, which results from the reaction of the carbon with the glass network. The onset temperatures of the gas forming reactions are the same as were observed during the qualitative measurements, but because of the subtraction of the baseline of glass FG1, the location of the peaks shifted slightly to higher temperatures. However, comparison of figures 4.3 and 4.4 show the good reproducibility of the different experiments.

The quantitative experiments were performed using the same glasses as for the gas species identification, but different experimental procedures were conducted. Unfortunately, the oxidation state of the glass FG2 was not characterized prior to the experiment, so that a quantitative discussion of the results is not possible here. The total iron concentration was determined expresses as  $\text{Fe}_2\text{O}_3$  (see table 4.2), but not the  $\text{Fe}^{2+}$  and  $\text{Fe}^{3+}$  concentrations. However, these experiments showed the reproducibility of the experiments. It turned out that this experimental setup was not sufficiently reliable to be used to further investigate the influence of the oxidation state on foaming gas evolution, because the heating rate and temperature control was not sufficiently accurate. Therefor another experimental setup was chosen for further experiments, which is described in the next subsection.

### 4.3.3 Influence of oxidation state and glass particle size on foam gas evolution

To investigate the influence of the oxidation state of the glass on the foaming gas evolution, three different glasses based on the composition of the glass with only iron as polyvalent ion (glass FG2), but different oxidation states were molten. Approximately 700 g of each type of glass were prepared by melting in a silica crucible using mixed dry reagent grade chemicals. The partial oxygen pressure in equilibrium with dissolved oxygen in the melt (to characterize the oxidation state of the glass) was measured after melting of the glass. The use of electrochemical sensors to determine the partial oxygen equilibrium pressure in glass melts is a standard technique (Thonthat et al. [22], Beerkens et al. [23]), which is commercially available (RAPIDOX®). The glass melt was kept at 1473 K for about 12 hours for good homogenization prior to further heating. The partial oxygen pressure in the glass melt was determined during cooling of the stirred melt between 1623 and 1473 K as function of temperature. The base oxide composition of the glasses is similar, however, by adding different amounts of active carbon to the raw material batch, different oxidation states in the three glass melts were obtained. The results of the measured partial oxygen equilibrium pressures as function of temperature for the different glass melts are given in the appendix, in figure 4.9 on page 116. In order to determine the exact amount of iron in the glass, the obtained glasses were chemically analyzed by XRF spectroscopy. The results are given in table 4.3.

The oxidation state of the glasses, which can also be characterized by the concentration of chemically dissolved oxygen in the glass, is often expressed by the  $\text{Fe}^{2+}/\text{Fe}^{3+}$  molar ratio or the  $\text{Fe}^{2+}/\text{Fe}_{\text{tot}}$  ratio, respectively. The concentration of chemically dissolved oxygen in the glass denotes the oxygen bound to the highest valency of the polyvalent ion (here  $\text{Fe}_2\text{O}_3$ ) which can be released during reduction of the polyvalent ion to a lower valency state (here FeO). Here we use the  $\text{Fe}^{2+}/\text{Fe}^{3+}$  ratio [14]. The concentration of  $\text{Fe}^{2+}$  can

*Table 4.3: Studied model glasses for redox dependency of foam gas production. Compositions, verified by X-ray fluorescence analysis (XRF). The concentration of  $Fe^{2+}$  was determined from the transmission spectra as described in the text.*

Glass / Oxide	SiO <sub>2</sub> wt.%	CaO wt.%	Na <sub>2</sub> O wt.%	Al <sub>2</sub> O <sub>3</sub> wt.%	Fe <sub>2</sub> O <sub>3</sub> total wt.%	Fe <sup>2+</sup> (wt.% Fe <sub>2</sub> O <sub>3</sub> )
FG 2, no C	67.43	14.79	9.79	5.01	2.95	0.25
FG 2, 0.2 wt.% C	67.26	14.77	10.02	4.96	2.94	0.35
FG 2, 0.5 wt.% C	67.19	14.88	9.93	5	2.97	1.28

be measured by spectrophotometric measurement of the light absorption at a wavelength of 1050 nm on a polished thin slice of glass. Using the extinction coefficient given by Bamford [24], for a soda-lime-silica glass similar to the composition as given in table 4.3, the  $Fe^{2+}$  concentration can be calculated according to:

$$c_{Fe^{2+}} = \frac{E_{1050}}{d \epsilon_{Fe^{2+}}} \quad \text{with} \quad E_{1050} = -\log \tau_{1050} \quad (4.1)$$

where  $c_{Fe^{2+}}$  is the concentration of  $Fe^{2+}$  (expressed in wt.%  $Fe_2O_3$ ),  $E_{1050}$  is the measured extinction at a wavelength of 1050 nm,  $\tau_{1050}$  is the internal transmission at 1050 nm,  $d$  is the sample thickness in cm and  $\epsilon_{Fe^{2+}}$  is the linear extinction coefficient of the  $Fe^{2+}$  absorption band at 1050 nm according to Bamford ( $9.1 \text{ (wt.\% } Fe_2O_3)^{-1} \text{ cm}^{-1}$ ).  $\tau_{1050} = T^*/0.92$ , where  $T^*$  is the measured transmission (incident light perpendicular to glass surface) of the sample including transmission losses at the two polished surfaces (2 times 4%). The measured values for the  $Fe^{2+}$  concentration expressed in wt.%  $Fe_2O_3$  are given in table 4.3.

After the melting and cooling, the glasses were milled to powder and sieved in four different size classes ( $x$ =diameter) ( $<32\mu\text{m}$ ,  $32 < x < 63\mu\text{m}$ ,  $63 < x < 125\mu\text{m}$  and  $125 < x < 250\mu\text{m}$ ). Subsequently, the glass powder was mixed with 5 wt.% active carbon ( $d_{50} < 30\mu\text{m}$ ). Approximately 1 gram of the mixture was transferred into a mullite reaction boat and inserted into a quartz tube, which then was flushed with helium gas. For all experiments, a helium carrier gas flow of  $1.5 \text{ Nl} \cdot \text{min}^{-1}$  was used, which was controlled by a mass flow controller. For these experiments, a different setup compared to figure 4.2 was chosen. The new setup, which is schematically shown in figure 4.5, has two advantages compared to the one used before. The use of a quartz glass tube provided better heat transfer from the furnace to the sample and also the furnace temperature could be controlled in a more accurate way. The second advantage was that the sample could directly be inserted into a preheated furnace, to study the first CO peak, observed in, e.g., in figure 4.4, as a function of the glass oxidation state in more detail.

In the following subsection, the influence of glass oxidation state, and the glass particle size on the foaming gas evolution will be discussed<sup>4</sup>.

---

<sup>4</sup>The peaks of the curves of the second set of experiments are lower than the peaks in the first set (see figure 4.4). This is because the heating rate used for the first set was much higher.

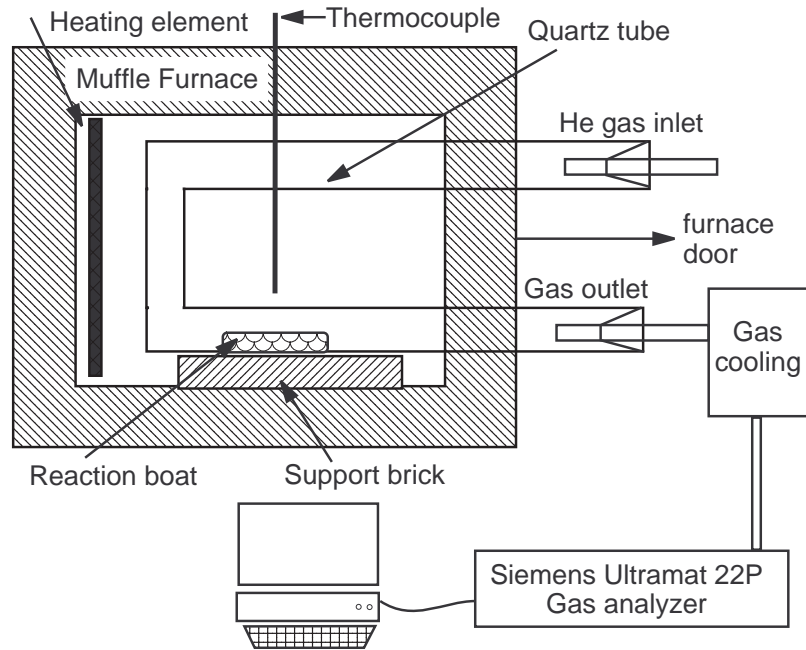
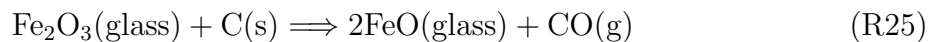


Figure 4.5: Experimental setup for experiments determining the influence of the glass oxidation state, particle size and heating rate on gas production from powdered glass and carbon mixtures.

### Influence of the oxidation state of the glass on foaming gas production

As previously discussed in the introduction, the oxidation state of the glass seems to influence the amount of foaming gas produced during heating of the powdered glass/carbon mixture. The effect of glass oxidation state on the foaming gas evolution was studied by measuring the CO concentration in the He carrier gas as function of temperature for the three glasses with different initial oxidation states. The applied heating rate was  $10 \text{ K} \cdot \text{min}^{-1}$  and the glass particle size was  $32 < d < 63 \mu\text{m}$ . The results are given in figure 4.6. Figure 4.6 shows that the height of the first peak, between 1080 and 1260 K, becomes smaller with decreasing  $\text{Fe}_2\text{O}_3$  ( $\text{Fe}^{3+}$ ) concentration in the glass. It can also be observed, that the second peak is not affected by the oxidation state of the glass. This shows, that this peak is not related to the initial  $\text{Fe}^{3+}$  concentration in the glasses. Assuming that the following irreversible reaction:



takes place, the conversion of ferric to ferrous iron can be determined by calculation of the molar amounts of CO produced, calculated from the flow rate and the surfaces under the first peaks of figure 4.6. The surface under the first peak was determined by integrating the curve as a function of time from the start of the experiment ( $t=0$ ) until the minimum between the two peaks. The surface under the complete curve was determined from  $t=0$  until the last value. Standard deconvolution of the peaks did not give a good approximation of the experimental curves and was therefore not carried out. Because the molar ratio between  $\text{Fe}_2\text{O}_3$  and CO according to reaction (R25) is 1:1, the conversion  $\Upsilon$

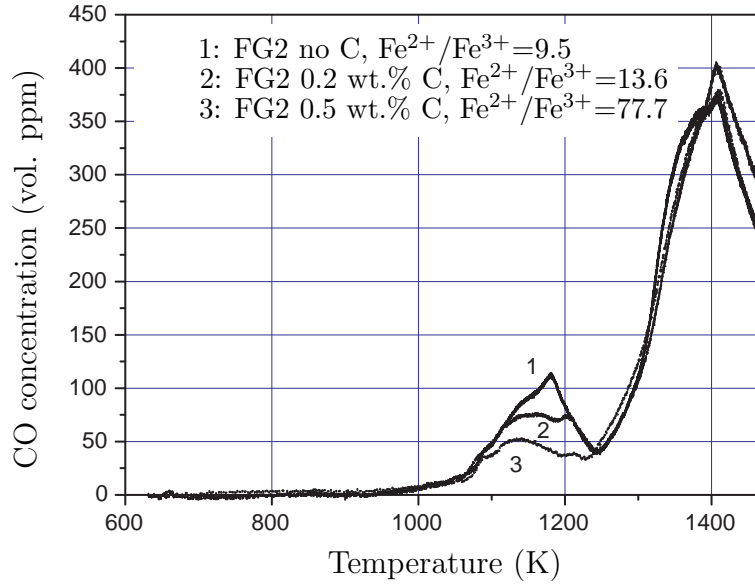
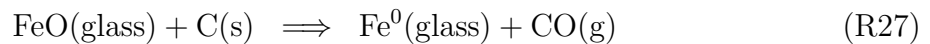
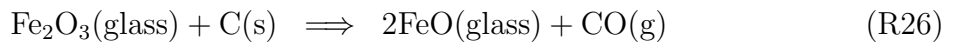


Figure 4.6: CO concentration in the exiting He-carrier gas as a function of temperature for three glasses with differences in initial oxidation state. Heating rate:  $10 \text{ K} \cdot \text{min}^{-1}$ , glass particle size class:  $32 < d < 63 \mu\text{m}$  ( $d$ =diameter).

was calculated by dividing the molar amount of CO under the peaks by the initial molar amount of  $\text{Fe}_2\text{O}_3$  in the glass.

$$\Upsilon_1 = \frac{n_{\text{CO}}(\text{first peak})}{n_{\text{Fe}_2\text{O}_3}(\text{initially in glass})} \quad [\%] \quad (4.2)$$

The conversion was calculated to be 55% on an average basis for this particle size and heating rate. The exact values for the three glasses are given in table 4.4. At higher temperatures and under the highly reducing conditions, it can be possible that the present ferrous iron ( $\text{Fe}^{2+}$ ) can be reduced to pure metallic iron ( $\text{Fe}^0$ ). The second peak of the curves in figure 4.6 does not depend on the oxidation state of the glass and the differences in peak height and surfaces seem to be not significant. Assuming, that the ferric iron in the glass is reduced completely to the ferrous state according to reaction (R26) and that subsequently the ferrous iron is reduced to pure metallic iron according to reaction (R27),



a second conversion factor is defined as:

$$\Upsilon_2 = \frac{n_{\text{CO}}(\text{both peaks})}{(3n_{\text{Fe}_2\text{O}_3} + n_{\text{FeO}})(\text{initially in glass})} \quad [\%] \quad (4.3)$$

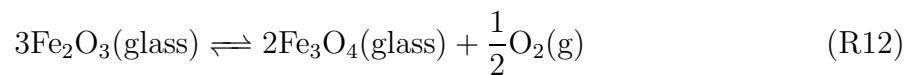
The overall conversion factor ( $\Upsilon_2$ ), based on reactions (R26) and (R27) is, on an average basis, 94.8 %. The exact values are given in table 4.4.

Table 4.4: Redox state of the three used glasses expressed as ratio of the concentrations ( $\text{mol} \cdot \text{m}^{-3}$ ) of  $\text{Fe}^{2+}$  and  $\text{Fe}^{3+}$  and two conversion factors as defined in the text by equations 4.2 and 4.3.

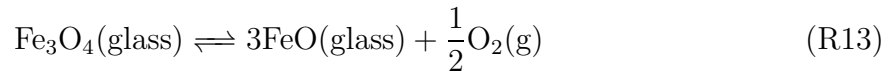
Glass	Redox (molar) [ $\text{Fe}^{2+}$ ]/[ $\text{Fe}^{3+}$ ] (%)	Conversion factor $\Upsilon_1$ acc. to (4.2) (%)	Conversion factor $\Upsilon_2$ acc. to (4.3) (%)
FG 2, no C	9.3	57.6	91.0
FG 2, 0.2 wt.% C	13.6	52.9	95.1
FG 2, 0.5 wt.% C	77.7	55.6	98.3

Because the CO concentration, measured from the glass without polyvalent ions (FG1), was subtracted from the measured curves of the samples presented in figure 4.6, it is assumed that the extra released CO, from the reaction with the carbon, comes exclusively from the reaction of the different forms of iron oxide ( $\text{Fe}_2\text{O}_3$  and  $\text{FeO}$ ) in the glass. From the overall mass balance, expressed by  $\Upsilon_2$ , it is assumed that during heating to temperatures up to 1450 K, the present iron oxide in the glass is probably completely reduced to its metal state according to reactions (R26) and (R27).

The relevant temperature regime for foaming in industrial processes is between 850 and 1200 K. This is where the first peak is found. This first peak of the different curves in figure 4.6, however, shows, that only 55 % of the available  $\text{Fe}_2\text{O}_3$  has reacted with the carbon to  $\text{FeO}$  and  $\text{CO}$ , assuming that reaction (R25) takes place exclusively. However, as mentioned in section 4.2 on page 99, the reduction of ferric iron in the glass can occur in two steps, depending on the oxidation state in the glass. These two steps are represented by reactions (R12):



and reaction and (R13):



In case that only reaction (R12) takes place exclusively, the conversion of  $\text{Fe}_2\text{O}_3$  with carbon to  $\text{CO}$  and  $\text{Fe}_3\text{O}_4$  would give a factor of 1/3, thus less than 55 %. Reactions (R12) and (R13) depend on the oxidation state of the glass. The reaction of oxygen from the glass with the carbon occurs at the glass/carbon interface. In this type of experiments, the reactions at the glass/carbon interface are irreversible, because the carbon monoxide is transported away with the carrier gas. Because of the depletion of oxygen in the glass at the interface, the oxidation state inside the particles, in the glass, can change, thus also the valency state of iron present in the glass from the interface to the interior can change<sup>5</sup>. Depending on the local oxidation state in the glass, the equilibrium reactions (R12) or (R13) or a combination of both, can take place. It can be seen from figure 4.6, that the

<sup>5</sup>This complex circumstance is explained in more detail in chapter 5, section 5.2.6 on page 133

curve of the first peak does not go back to  $y = 0$  before developing the second peak. This indicates, that there are overlapping reactions producing these curves. Time delays of the reactions can be caused by the relatively slow diffusion process in the glass. The oxidation states of the glass determine which equilibrium reaction in the glass will take place predominantly. Starting from an oxidized glass and considering only temperatures lower than 1323 K, the reduction of  $\text{Fe}_2\text{O}_3$  to  $\text{FeO}$  in the glass can go via the formation of  $\text{Fe}_3\text{O}_4$  (see reactions (R12) or (R13)) [20] [21]. Equilibrium thermochemistry of the ferric/ferrous iron equilibrium (R14) in glass melts is very well studied at higher temperatures [8, 9, 25, 26], and specific, concentration dependent experimentally determined values for  $\Delta H$  and  $\Delta S$  are determined<sup>6</sup>. However, for the formation of  $\text{Fe}_3\text{O}_4$  in soda-lime-silicate glass melts no adequate thermochemical information is available. Therefore, the oxidation state and temperature dependent foaming gas emission cannot exactly be quantified.

To study the first peak in more detail and to establish a relation between the available amount of oxygen for the foaming gas production and the oxidation state in the glass, the experiments were conducted at a constant temperature of 1173 K with the same glass compositions. The temperature of 1173 K was chosen, because at this temperature the first peak, as shown in figure 4.6, shows a maximum. This temperature also corresponds to foaming temperatures of industrial foaming processes. A fourth glass was molten in the same way as the others, with an addition of 0.25 wt.% carbon to the raw material batch to obtain an additional glass for the isothermal experiments. The powder mixture was inserted into the tube at ambient temperature and flushed with the carrier gas for five minutes prior to the insertion of the tube into the preheated furnace at 1173 K. The total molar amount of CO evolved during the isothermal experiments was then measured. After the preparation of the glass melts, the partial oxygen pressures of the different melts are determined during cooling between 1623 and 1473 K, as described earlier in this section. The results of the experiments are given in the appendix in figure 4.9 on page 116. To relate the molar amount of CO to the oxidation state of the glass at 1173 K, the linear fit of the measured partial oxidation states, expressed as  $\log(p_{\text{O}_2}/\text{bar})$  as a function of temperature were extrapolated to 1173 K. To determine the molar amount of released CO during the isothermal experiment, the surface under the curve of the glass FG1 (without polyvalent ions) was subtracted from all other surfaces of the glasses with different oxidation states. The experimental results of the CO concentration measurements as function of time are given in the appendix in figure 4.11 on page 117.

Figure 4.7 shows the experimentally determined molar amount of released CO during the isothermal experiment as a function of the decadic logarithm of the partial oxygen pressure in the glass at 1173 K. This relation shows that redox reactions of glass components affect the foaming gas evolution in the temperature range suitable for foaming. It also shows that measuring the partial oxygen pressure during the melting of the glass allows an estimation of the foaming capability of a glass at constant iron concentration.

It has thus been shown that the oxidation state of the glass influences the evolution

---

<sup>6</sup>A more detailed discussion of the determination of thermodynamic values from soda-lime-silica glasses is given in chapter 5, section 5.2.6 on page 133

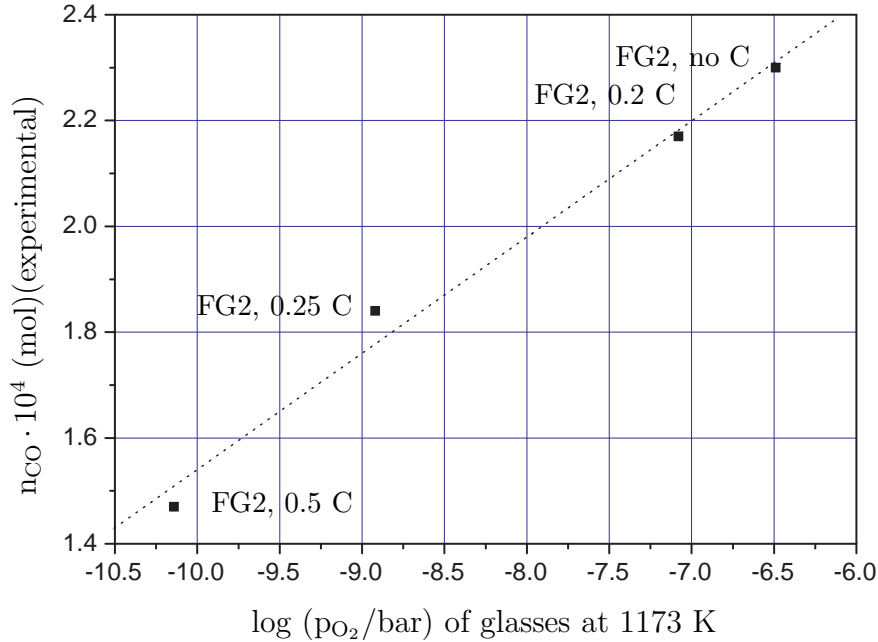


Figure 4.7: Experimentally measured molar amount of released CO (corrected surfaces under the curves of figure 4.11) under isothermal conditions at 1173 K for a period of 37 minutes as a function of the extrapolated decadic logarithm of the partial oxygen equilibrium pressure of the different used glasses,  $p_{O_2}$  at  $T = 1173$  K. For the measured partial pressures, see figure 4.9 in the appendix on page 116. The dotted line represents a linear fit of the data points.

of the foaming gas in a predictable way. Another important process step is the mass transport of the polyvalent ions and/or the oxygen through the glass melt. In case that the rate of CO formation is governed by a diffusion process (diffusion of oxygen or polyvalent ions in the glass), the formation rate of the foaming gas should be influenced by the glass particle size. The effect of the glass particle size on the CO release is discussed in the next subsection.

### Effect of the glass particle size on the foaming gas release

To study the effect of the glass particle size on the foaming gas release, the four different prepared particle size classes of the most oxidized glass (FG2 no C) were mixed with the carbon powder as described before and the release of CO as function of temperature was measured at a heating rate of  $10 \text{ K} \cdot \text{minute}^{-1}$ . The results of the experiments are given in figure 4.8. It can be seen, that the particle size has a large influence on the foam gas production. A very strong difference can be seen between the size range of  $32 < d < 63$  and  $63 < d < 125 \mu\text{m}$ . At smaller particle sizes, the specific surface areas are larger and more glass carbon contacts exist and diffusion distances are relatively short. The measured CO concentration in the He-carrier gas of the largest particle size range of  $125 < d < 250$ , shows nearly one single slope. The chemically dissolved oxygen or the polyvalent ions in the glass, respectively, must diffuse from the inside of the glass particle to the outside, where

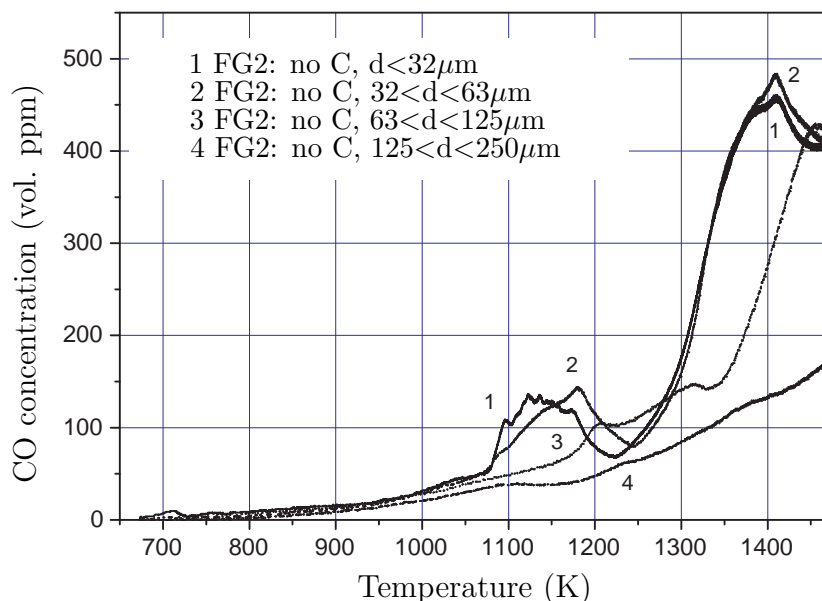


Figure 4.8: CO concentration in He-carrier gas of the most oxidized glass (FG2) as a function of temperature for 4 different glass particle sizes. The heating rate for the experiments:  $10 \text{ K} \cdot \text{minute}^{-1}$ .

they can react with the carbon. The diffusion distances from the inside of the particles to the interfaces are much larger, for larger particles. Larger particles (classes:  $63 < d < 125$  and  $125 < d < 250$ ) also seem to shift the gas formation to higher temperatures.

## 4.4 Concluding remarks

The objective of this part of the study was to identify the foaming gas species in a mixture of a powdered oxidized soda-lime-silicate glass containing iron as polyvalent ion and powdered carbon as reduced forming agent. Furthermore, it was intended to identify the chemical gas forming reactions and their dependency on the oxidation state of the glass. Carbon monoxide has been identified as main foaming gas. It has furthermore been shown that the formation of the foaming gas depends strongly on the presence of polyvalent ions and their valency states, thus on the oxidation state of the glass. The reduction of ferric iron to the ferrous state CO forming oxygen and subsequent reaction with the carbon to CO can be attributed to the primary chemical reaction responsible for the foaming gas evolution in the relevant temperature range for foam glass production (1050-1250 K). However, a possible formation of, e.g.,  $\text{Fe}_3\text{O}_4$  as an intermediate compound could neither be affirmed nor excluded. At temperatures above 1250 K, the reactions are even more complex including the reduction of ferrous iron to the metallic state and probably reactions of carbon with the glass network. This has been shown by the CO evolution of the glass FG1 without polyvalent ions. It has furthermore been observed that the rate of foaming gas reactions seems to depend on mass transport processes in the glass. An almost linear relationship between the foaming gas emissions and the decadic logarithm of the partial equilibrium oxygen pressure of the glass at 1173 K was found for a glass



with only iron oxide. An oxidation state analysis of the glass melt allows an estimation of the foaming capability already during the glass melting process.

The results from this chapter can be used for the modeling of bubble growth, which will be presented in the next chapter. The important results from this chapter are:

- CO is the only gas species formed at the glass/carbon interface. Reaction (R26) should be integrated in the modeling describing foam gas evolution and consequently bubble growth during the foaming process. Inside a closed bubble with carbon, an equilibrium between C, CO and CO<sub>2</sub> can be established, because the foaming gas (closed foam) is not transported away as in the experiments discussed in this chapter. Thus the Boudouard equilibrium will be respected during the modeling in chapter 5.
- The oxidation state of the glass influences the foaming gas evolution during foaming,
- The particle size influences foaming gas evolution. Diffusion in the glass is probably gas formation rate determining.

From the results of this chapter, a probable mechanism of foaming gas formation and bubble growth can be derived. The glass for foam glass production should have a high concentration of polyvalent ions, e.g., iron oxide. Furthermore, these polyvalent ions should be at a high oxidation state level, thus the iron oxide should preferably be in form of Fe<sub>2</sub>O<sub>3</sub>, rather than in the form of FeO. At the glass bubble interface, the Fe<sub>2</sub>O<sub>3</sub> is reduced by the carbon to CO and FeO, according to reaction (R25). As a consequence, the interface becomes depleted of Fe<sub>2</sub>O<sub>3</sub>: Fe<sub>2</sub>O<sub>3</sub> diffuses from the bulk of the glass towards the interface, where it reacts either with solid carbon or now present CO (from the first reactions), forming CO or CO<sub>2</sub> (reaction (R23)), respectively. The formed CO<sub>2</sub> can be reduced to CO (T < 1200 K) by the Boudouard equilibrium according to (R9). The produced FeO remains in the glass and diffuses from higher to lower concentrations towards the bulk. The production of CO inside the closed bubble leads to a pressure increase. At a sufficient low viscosity of the glass, the bubble can grow. This leads to larger bubbles and thinner lamellae between the bubbles.

A soda-lime-silicate glass with only iron as polyvalent ion was used to study the foaming gas evolution. Compositions of glasses prepared from vitrified fly ash are different, however their compositions must be adopted closely to the one used here to produce a high quality foam glass, e.g., Pittsburgh Corning foam glass, see table 1.3 in the introduction on page 19. Glasses from fly ash can also contain other polyvalent ions like sulphur or chromium species in the glass, which influence the oxidation state of the glass or the chemically dissolved oxygen content and thus effect the foam gas evolution.

## 4.5 Bibliography

- [1] E. R. Saakyan, M. G. Badalyan, and A. S. Danielyan. Granulated foamed glasses from perlite rocks. *Glass and Ceramics (English translation of Steklo i Keramika)*, 41(3-4):102–103, 1984.
- [2] K. Zähringer. *Etude thermohydraulique du phénomène d’expansion de la perlite. Application à un four industriel*. PhD thesis, Ecole Centrale Paris, Paris, France, 1998. Thesis in French.
- [3] E. R. Saakyan. Multifunctional foam glasses from volcanic glassy rocks. *Glass and Ceramics (English translation of Steklo i Keramika)*, 48(1-2):3–5, 1991.
- [4] E. Bernardo, G. Scarinci, and S. Hreglich. Foam glass as a way of recycling glasses from cathode ray tubes. *Glastechn. Ber. Glass Sci. Technol.*, 78(1):7–11, 2005.
- [5] N. I. Min’ko, Y. L. Belousov, K. M. Ermolenko, and V. A. Firsov. Foam materials based on crystallized glasses. *Glass and Ceramics (English translation of Steklo i Keramika)*, 43(9-10):445–447, 1986.
- [6] M. Hübscher. Schaumglas, Teil I: Eigenschaften und Anwendung. *Silikattechnik*, 5(6):243–247, 1954.
- [7] H. Müller-Simon. Electron exchange reactions between polyvalent elements in soda-lime-silica and sodium borate glasses. *Glastechn. Ber. Glass Sci. Technol.*, 69(12):387–395, 1996.
- [8] H. Müller-Simon. On the interaction between oxygen, iron and sulfur in industrial glass melts. *Glastechn. Ber. Glass Sci. Technol.*, 67(11):297–303, 1994.
- [9] A. Wondergem-de Best. *Redox behavior and fining of molten glass*. PhD thesis, Eindhoven University of Technology, Eindhoven, The Netherlands, 1994.
- [10] E. O. Schulz. Schaumglas, Teil II: Zur Verfahrenstechnik bei der Herstellung von Schaumglas. *Silikattechnik*, 5(8):343–346, 1954.
- [11] Dr. Hans Strauven, Pittsburgh Corning Europe N.V. Industrial foaming process of Foamglas®. Personal communication, 2001.
- [12] B. K. Demidovich, V. L. Piletskii, N.P. Sadchenko, E. P. Melnik, M. Y. Firer, and S. S. Akulich. A new production line for the manufacture of high quality foam glass. *Glass and Ceramics (English translation of Steklo i Keramika)*, 29(10):651–654, 1972.
- [13] S. Köse. *Untersuchungen zur Blähdynamik des Schaumglases*. PhD thesis, Eidgenössische Technische Hochschule (ETH) Zürich, Switzerland, 1981.
- [14] H. Scholze. *Glas Natur, Struktur und Eigenschaften*. Springer-Verlag, Berlin Heidelberg New York, 1988.
- [15] R. G. C. Beerkens. Sulfate decomposition and sodium oxide activity in soda-lime-silica glass melts. *J. Am. Ceram. Soc.*, 86(11):1893–99, 2003.

- 
- [16] E. Kordes. Theoretische Berechnung der Gleichgewichte zwischen geschmolzenen Na-Ca-Silikaten und der Sulfatgalle bei 1200°C. *Zeitschrift anorg. allg. Chem.*, 266:105–117, 1951.
- [17] E. Kordes, B. Zöfelt, and H. Pröger. Die Mischungslücke im flüssigen Zustand zwischen Na-Ca-Silikaten und Na<sub>2</sub>SO<sub>4</sub>. *Zeitschrift anorg. allg. Chem.*, 264:255–271, 1951.
- [18] B. K. Demidovich. *Foam Glass*. Nauki i Teknika, Minsk, 1975. In Russian.
- [19] R. G. C. Beerkens. Oxygen-fired glass furnaces: expectations and experiments in the glass industry in the last 15 years. In *Proc. XX A.T.I.V. Conference, Technology and Techniques for Glass Manufacturers*, pages 132–141, September 2005. Parma (Italy).
- [20] C. Rüssel, R. Kohl, and H. A. Schaeffer. Interaction between oxygen activity of Fe<sub>2</sub>O<sub>3</sub> doped soda-lime-silicate glass melts and physically dissolved oxygen. *Glastechn. Ber. Glass Sci. Technol.*, 61(8):209–213, 1988.
- [21] E. Freude. *Voltammetrische Untersuchungen des Redoxverhaltens polyvalenter Ionen in Glasschmelzen, insbesondere von Technetium*. PhD thesis, Erlangen University, Erlangen, Germany, 1989.
- [22] T. Thonthat and G. Odon. Redox des calcins de recyclage. *Verre*, 3(5), 1997.
- [23] R. G. C. Beerkens, A. Faber, J. Plessers, and T. Thontat. Methods for the characterization of redox state of cullet and batches in glass manufacturing. *Glass International*, pages 371–375, 1997.
- [24] C. R. Bamford. *Colour generation and control in glass*. Elsevier Scientific Publishing Company, Amsterdam, New York, 1977.
- [25] H. Müller-Simon. Temperature dependence of amber color generation in soda-lime-silica glass. *Glastechn. Ber. Glass Sci. Technol.*, 73(1):28–30, 2000.
- [26] R. Pyare and P. Nath. Kinetics and thermodynamics of ferrous-ferric equilibrium in sodium aluminoborate glasses. *J. Non. Cryst. Sol.*, 69:59–67, 1984.

## 4.6 Appendix

### 4.6.1 The partial oxygen pressure in the glass

This subsection describes the experimental determination of the partial oxygen pressure in the glass melts used in subsection 4.3.3 on page 105. The partial oxygen pressure in equilibrium with chemically dissolved  $O_2$  in the melts of the four glasses was measured during cooling of the melts as described in subsection 4.3.3. The result of this measurement is given in figure 4.9 as  $\log(pO_2/\text{bar})$  as a function of temperature.

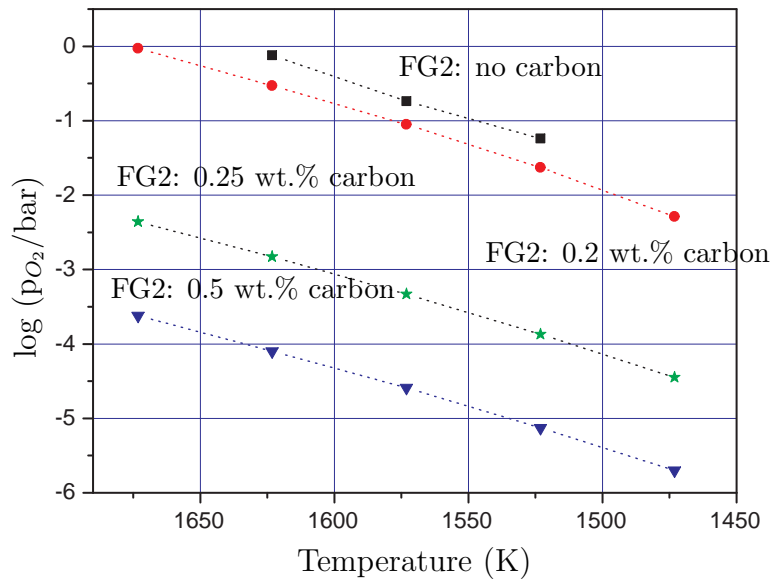


Figure 4.9: Measured partial oxygen equilibrium pressure as function of temperature of model glass melt FG2. The expressions next to the lines indicate the amount of carbon added to the raw material batch to obtain different oxidation states in the glass. The glass composition is given in table 4.3 on page 106.

### 4.6.2 Experimental results of CO release at T=1173 K

In figure 4.10, the experimental results of the measured CO evolution for the glass without iron oxide (FG1) for four different particle size classes is given. This result was used to subtract the CO evolution from the base glass (FG1) in contact with the carbon from the curves obtained from the glasses with iron as polyvalent ion. The initial increase in concentrations can be attributed to the heating of the sample, because it was inserted into the preheated furnace. In contrast to the glass with iron oxide, the evolution of CO does not depend on the particle size.

Figure 4.11 shows the CO Emission as a function of time at  $T = 1173$  K for the four glasses with iron (FG2) and the reference glass without any polyvalent components (FG1). The curve of FG1 was extrapolated to 37 minutes for the surface integration.

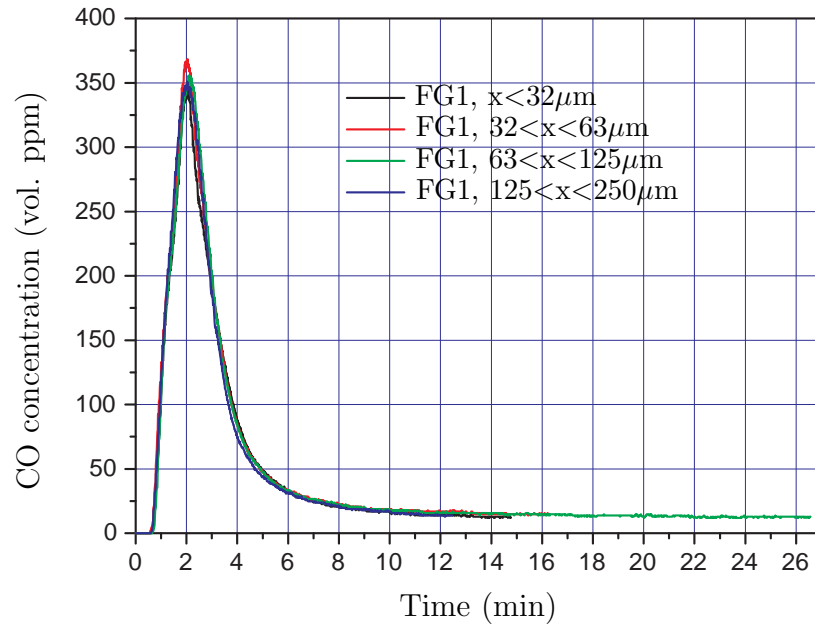


Figure 4.10: CO Emission as a function of time of the glass without any redox influencing components (FG1) for different particle sizes at  $T = 1173 \text{ K}$ .

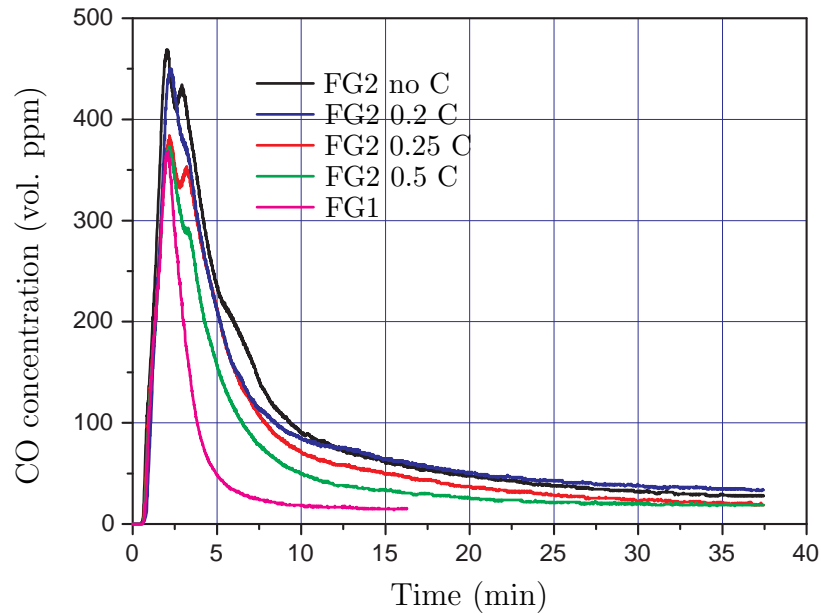


Figure 4.11: CO Emission as a function of time at  $T = 1173 \text{ K}$  for the four glasses with iron (FG2) and the reference glass without polyvalent ions. The curve of FG1 was extrapolated to 37 minutes for surface area integration. The labels behind the FG2 in the graph denote the amount of carbon in wt.% added to the batch to produce differences in the glass oxidation state.



# Chapter 5

## Physicochemical model for bubble growth in foam glass

---

5.1	Introduction . . . . .	120
5.2	Governing equations for bubble growth model . . . . .	126
5.3	Numerical solution of the model equations . . . . .	143
5.4	Experimental validation of the simulation model for foam glass . . . . .	148
5.5	Process Parameter study . . . . .	166
5.6	Model calculations, results and discussion . . . . .	169
5.7	Concluding remarks . . . . .	176
5.8	Nomenclature . . . . .	178
5.9	Bibliography . . . . .	181
5.10	Appendix . . . . .	186

---

In the previous chapter, some parameters influencing the bubble growth and gas evolution during foaming of a glass-carbon mixture were described. It has been shown, that, in addition to physical conditions (e.g., temperature or particle size), also chemical properties of the glass, e.g., the partial oxygen equilibrium pressure (oxidation state), and the polyvalent ion concentrations, have an important impact on gas evolution inside the bubbles, which controls bubble growth. To study the effect of various physicochemical properties, e.g., glass viscosity, surface tension or glass melt composition and also the effect of process parameters, e.g., initial bubble size or heating rate on the bubble growth in foam glass, a validated, preferably a general applicable first principles model is required. In this chapter, a first principle model is described to estimate the transient (time dependent) bubble growth in foam glass as a function of physical, chemical and process parameters. The model provides a tool to optimize the foaming process for foam glass production. The model's estimation capability and accuracy is tested and discussed against results of controlled laboratory foaming experiments.

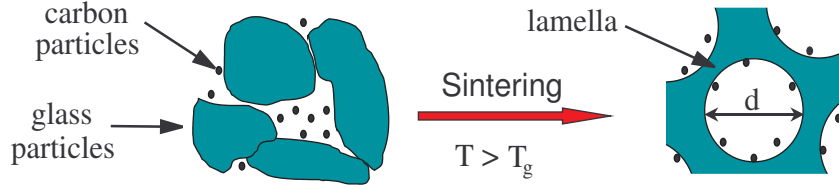


Figure 5.1: Schematic representation of initial bubble formation during sintering of a glass/carbon powder mixture for foam glass production.  $T_g$  denotes the glass transition temperature.

In the first section, the introduction, the physics and transfer processes involved in foaming process are described and a literature overview of bubble growth models in viscous liquids is given. Next, the assumptions of the model, developed in this chapter, are presented and discussed, followed by the derivation of the governing mathematical equations for the description of bubble growth in a mixture of powdered glass and reduced foaming agent. The mathematical approach used to solve these equations plus boundary conditions is presented, which is followed by the validation of the model with results of controlled laboratory foaming experiments. The model will then be used in a parameter study, to calculate the effect of some relevant process parameters on bubble growth.

## 5.1 Introduction

Bubble growth in foam glass, as well as some parameters and chemical reactions influencing the foam gas forming process were very briefly described in section 4.1 on page 93. In the following, the foaming process is described for a heated mixture of glass powder with carbon as reducing foaming agent, to develop a mathematical model for the transient description of bubble growth in the foaming glass.

To produce foam glass according to the 'powder process', a mixture of powdered glass and a foaming agent (in this case carbon) has to be heated to temperatures above the softening point of the glass (viscosity of  $10^{6.6}$  Pa·s). During heating, the glass particles sinter together enclosing the voids, in which the carbon particles are captured. Thus, a large number of initial small bubbles is formed. To obtain a low density foam with a large gas volume fraction, these initial bubbles have to grow and the glass mass with the enclosed bubbles has to expand. This also results in thinner glass lamellae between the bubbles. The sintering and initial formation of the bubbles is schematically shown in figure 5.1. The foaming potential of an oxidized molten glass strongly depends on its gas releasing capability, i.e., the amount and rate of gas volume produced by chemical reaction of the chemically and physically dissolved oxygen with the carbon as foaming agent. The bubbles can grow if the gas pressure inside the bubble increases and exceeds the pressure applied or acting by external 'forces' on the bubble (e.g. surface tension). The growth rate of the bubbles is affected by the glass viscosity which acts as a resistance against



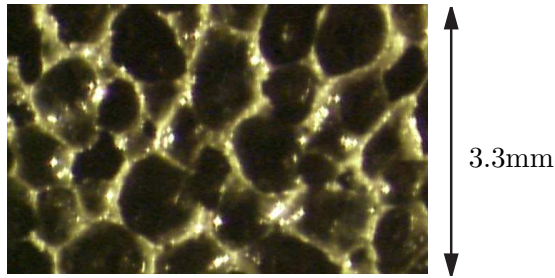


Figure 5.2: Cellular foam structure in industrial foam glass after foaming.

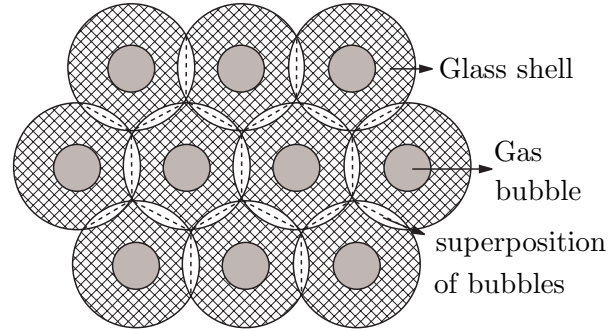


Figure 5.3: Cellular model of outlined spherical bubbles with a shell of constant volume and slight superposition of the spherical cells. Dotted lines represent symmetry lines.

deformation. The foaming gas evolution, leading to the pressure and volume increase inside the bubble is the driving force for the bubble growth. This gas release depends on the mass transport of chemically and physically dissolved oxygen from the bulk of the glass around the bubble to the bubble surface to react with the carbon, forming CO or CO<sub>2</sub> gas. Mass transport processes in glass melts can be described by diffusion processes [1,2]. The influence of the concentration of polyvalent ions and the oxidation state of the glass, i.e., the partial oxygen equilibrium pressure, on the gas releasing potential of the glass and thus the bubble growth was shown and discussed in the previous chapter. Most developed models, describing bubble growth or shrinkage in a glass melt, consider one spherical bubble in an infinite glass melt<sup>1</sup>. In order to model bubble growth in foam glass, that approach, however, cannot be used. Köse [3] showed, that the approach of an infinite melt around the bubble can only be used to describe the early stages of the bubble growth in foam glass, thus just after the glass particles have sintered together, forming very small initial bubbles (radius  $\sim 10\mu\text{m}$ ). He also showed that this approach becomes increasingly incorrect as the bubbles grow. This is caused by the cellular structure of the foam glass at the later stages of the foaming process. A typical cellular structure is given in figure 5.2, which shows the final cellular structure of an industrially produced foam glass. Clearly, it can be seen that the assumption of infinite glass volume surrounding the bubble is incorrect for the later or final stage of the foaming process. The cellular packed structure also shows, that each bubble is surrounded by a finite volume of glass. Furthermore, the bubbles in the foam are rather polygonal than spherical. This deviation from sphericity drastically increases the difficulty of mathematical modeling. However, assuming outlined spherical cells with slight, volumetrically equal overlap (superposition) at the boundaries, as schematically shown for a 2D-projection in figure 5.3, Princen [4] has proven that by assuming spheres instead of polygons, an error of less than 5% is introduced. This relation was established by comparing cellular models of packing

<sup>1</sup>A literature overview of models developed to describe bubble growth of shrinkage in fluids and glasses is going to be described later in this introduction.

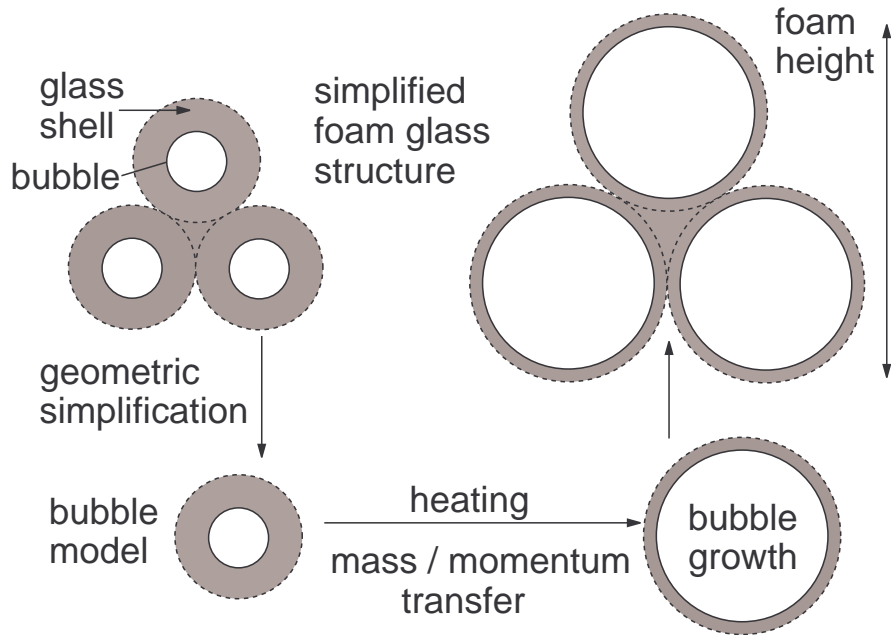


Figure 5.4: Schematic representation of foam model

with systems of closely spaced bubbles. The dotted lines in figure 5.3 represent symmetry boundaries outlining a unit cell, thus by describing one unit cell, all cells can be described.

Assuming for the model, that the initial amount of bubbles will not change, thus no coalescence, the relative volume expansion for one unit cell (gas bubble plus glass mass around one bubble), multiplied with the initial amount of bubbles results in the final foam volume.

Foaming gas can be lost at the outer foam boundary to the atmosphere in which the glass is foamed by collapse of bubbles. Because of the high foam volume to outside top surface ratio in practice, this effect is neglected here. It might however be significant in small scale laboratory foaming experiments. Loss of dissolved gases in the glass towards the outer interface or reaction of these gases with the atmosphere is also neglected. Excluding the loss of foaming gas or oxygen at the outer boundary of the real foam glass, oxygen, physically and chemically dissolved, can completely react to CO or  $\text{CO}_2$ <sup>2</sup>, presupposing sufficient carbon in the mixture. If all released gas is enclosed inside the foam body, the maximum gas volume, which can be formed, can therefore be calculated. With known maximum foaming gas volume and the glass volume, the final foam volume can also be calculated. This however, requires, that the glass volume must remain constant, thus the loss of oxygen from the glass has no influence on the glass volume. Coalescence of bubbles during foaming reduces the total amount of bubbles and may change the kinetics of foaming gas formation, but has no effect on the maximum possible foaming gas volume.

<sup>2</sup>This is in contrast to the previous chapter, where the  $\text{CO}_2$  formation was excluded. Here, inside the bubble, a quasi closed system is formed from which the gas cannot leave. Therefore the thermodynamic equilibrium between CO and  $\text{CO}_2$  should be respected.

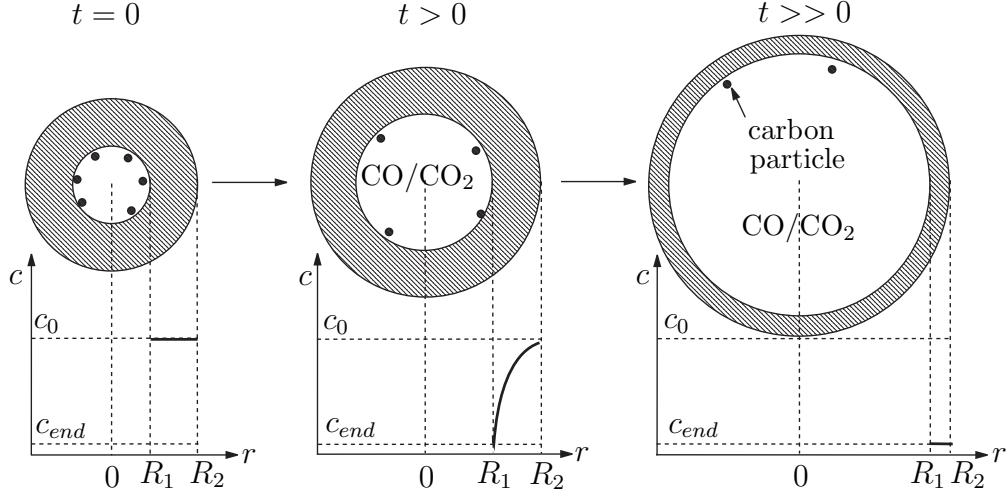


Figure 5.5: Schematics of bubble growth and concentration profiles in the glass shell ( $c$ =concentration,  $R_1$ =inner radius,  $R_2$ =outer radius and  $t$ =time,  $R_1(t)$  and  $R_2(t)$ ).

For the foam model being developed in this study, the approach of Arefmanesh and Advani [5] is followed. One spherical bubble with an initial radius surrounded by a finite volume of glass melt surrounding the bubble is considered. This structural approximation is a considerable simplification. It reduces a three dimensional problem to a single dimensional problem in spherical coordinates.

The schematics of the structural simplification to reduce the model for a foam bubble to one isolated bubble with a shell and the translation to foam height after the expansion of the individual bubbles is given in figure 5.4. An important aspect for the modeling of the bubble growth process is the influence of the expanding bubble, surrounded by the glass melt, on the concentration profiles of the diffusing species (polyvalent ions) in the glass shell. Considering a spherical bubble surrounded by a shell of glass, the shell thickness decreases during the expansion of the bubble, because constant glass volume is assumed. This effect is schematically shown in figure 5.5. The shrinkage of the glass shell causes the concentration profiles to be compressed, which increases the slope of the profiles and thus the molar fluxes of the diffusing components.

The shrinkage or growth of an isolated spherical gas bubble surrounded by an infinite fluid, in which diffusion takes place, has been subject to extended research for a long time. Approximate analytical solutions for bubble growth or shrinkage have been derived by many authors. Epstein and Plesset [6] derived a model including the effect of surface tension but ignoring the effect of the stretching of the fluid shell, thus the convection transport in the diffusion equation was neglected (quasi-stationary model). Concentration profiles have been calculated to determine the concentration gradients and mass flux at the fixed gas/melt boundary and the mass flux of gases released from the melt. The gas fluxes are used to determine the boundary motion or change in bubble size. The approach

as applied by Epstein and Plesset will result in growth rates significantly different from practical situations. The moving fluid sphere (stretched glass shell), which surrounds the expanding gas bubble, leads to a compression of the concentration profile of the dissolved and diffusing species in the glass. This consequently increases the concentration gradient and thus increases the molar flux of the gaseous species from the fluid into the bubble.

Readey and Cooper [7] derived a set of differential equations for bubble dissolution, bubble growth or spherical grain dissolution in infinite fluids, which accounts for the moving fluid sphere. They neglected, however, the time derivative in the diffusion equation<sup>3</sup> to calculate the mass transport from the glass into the bubble and replaced it by an approximate solution. That this simplification can cause considerable deviations in bubble expansion or shrinkage was shown by Cable and Evans [8] and Duda and Vrentas [9], who also solved the equations by Readey and Cooper numerically. Approximate analytical solutions for the change in bubble radius with time were also presented by Subramanian and Chi [10] and Weinberg et al. [11] and were compared to the numerical finite difference solution. Weinberg et al. found large differences in the effect of surface tension on the bubble growth comparing the approximate solutions and the finite difference solution. The effect of surface tension was then investigated in detail by Weinberg [12]. He concluded, that in case of a growing bubble, the surface tension forces tend to retard the growth rate. The effect of viscosity, surface tension, convection and inertia on the growth of a bubble in an infinite liquid were also numerically studied by Szekely et al. [13]. They found that the effect of surface tension on bubble growth is minor, except at the initial stages of growth. The viscosity however, plays a significant role.

Summarizing, for particular cases, approximate solutions to describe the growth of a bubble in an infinite medium are in good agreement to the finite difference solution, which is considered to be closest to the exact solution. However, in foam glass for example, the starting conditions for foaming are small bubbles at low temperature, thus high glass viscosity. This means that the effect of both parameters, surface tension and viscosity on bubble growth should be incorporated into the model, which is going to be developed in this chapter. The accurate incorporation of the effect of the moving fluid sphere (shell) as well as surface tension and viscosity effects into the model requires a numerical solution of the equations for bubble growth, including the description of mass transport in the glass to be able to find and calculate an accurate solution.

Gas bubbles dissolve faster in glass melts by the presence of fining agents dissolved in the melt [14–17]. This is due to physically dissolved gases, released by decomposition reactions in the melt and diffusion of these gases from the melt to the bubble surfaces. The models developed for bubble dissolution and growth in fluids, as described above, were often used to describe the elimination of gas bubbles in glass melts. The calculated results are based on approximate analytical and numerical solutions, incorporating one or more diffusing gases and sometimes a chemical reaction at the glass-bubble interface, but most of the time not with incorporation of redox reactions in the melt [11, 18–23]. Subramanian and Chi [10] also discussed the effect of chemical reactions on bubble dissolution

---

<sup>3</sup>The diffusion equation is given by equation (5.21) on page 131 including the conditions for its validity and applicability.

in more detail. However, only a first order irreversible reaction was considered. Other solutions for the influence of chemical reactions on concentration profiles of dissolved gases in glass melts surrounding a bubble are also given by Weinberg and Subramanian [24]. In an earlier study, Soung and Sears [25] discussed the effect of the chemical reaction order on bubble growth. They solved their equations numerically. The derived models can be applied for most irreversible chemical reacting systems, however, an extension is needed in case of chemical equilibrium reactions, such as most redox reactions in glass behave.

Beerkens et al. [1, 17] were first to present the effect of redox reactions on concentration profiles of dissolved fining gases and polyvalent ions in glass melts and thus on bubble growth at temperatures above 1673 K. They assumed that only oxygen is the diffusing species. In these papers, an effective diffusion coefficient for oxygen was derived, based on the assumption of local thermodynamic equilibrium of polyvalent ions and dissolved oxygen at all positions in a molten glass melt. Based on this approach, Yoshikawa et al. [26, 27] developed a model for transient bubble growth in glass melts. The diffusion equation for spherical coordinates including convective transport (moving fluid sphere) was solved numerically by Yoshikawa et al.. A simple mass balance equation to calculate the change in bubble radius was used. The effect of surface tension and glass melt viscosity on the bubble growth rate was omitted. This is reasonable for low viscous glass melts at high temperatures and relatively large bubbles. At higher viscosity levels, the bubble growth will be retarded, because a higher pressure is needed to 'move' and stretch the viscous glass. Especially the effect of viscosity is important when considering bubble growth in foam glass, because at foaming temperatures between 925 and 1225 K, the glass viscosity is very high, compared to glasses at 1673 K. This will be explained in more detail later in this chapter. Both authors (Beerkens et al. and Yoshikawa et al.) consider an infinite glass melt volume and polyvalent species in the glass melt. In their approach, the concentration of the physically dissolved oxygen in the glass solely depends on the ratio of the oxidized and reduced form of the polyvalent ion in the glass. They also assume that the oxidized and reduced metal ion remains locally immobile, i.e., they do not diffuse, but only change in valency. The oxygen and other dissolved gases diffuse in the melt.

Glasses, used for foam glass production, contain multiple polyvalent ions, e.g., iron and sulfate. Therefore, the approaches by Beerkens and Yoshikawa cannot directly be used for the system here due to the mutual interaction of the different redox equilibria. As already stated before, with only one sort of polyvalent ion present in the glass, the local concentration of the physically dissolved oxygen in the glass solely depends on the local ratio of the oxidized and reduced form of this polyvalent ion species in the glass, at local equilibrium conditions. With two sorts of polyvalent ions in the glass, e.g., iron and manganese, the concentration of the physically dissolved oxygen determines the ratios of the oxidized and reduced forms of both polyvalent species. With two or more sorts of polyvalent ions in the glass (iron and sulphur), a simple description of the so-called effective diffusion coefficient for oxygen, based on the reaction equilibria, is not possible. All polyvalent species and oxygen interact according to local redox reaction equilibria and may diffuse simultaneously through the glass. This means, that diffusion equations including terms for production or consumption by chemical equilibrium reactions must be solved for each component, i.e. polyvalent ions and physically dissolved oxygen.

The model, described in this chapter, numerically calculates the bubble growth in foam glass using a finite difference scheme. The model includes diffusion in the glass melt layer, bubble growth kinetics limited by the glass viscosity and surface tension effects, as well as the described effect of the moving (stretching) glass shell on bubble growth. The model takes into account the mobility of multiple polyvalent ions and oxygen in the glass and assumes permanent local thermodynamic equilibrium between the oxidized and reduced form of the mobile polyvalent ions and locally dissolved gases. These diffusion processes will govern the bubble growth during foam glass production, because it influences the flux of reactant, providing the oxygen, at the glass/bubble interface.

So far, all necessary information has been discussed to be able to translate a complex foam structure into a simpler bubble model to be able to derive mathematical equations. The governing equations for the above discussed model will be presented in the next section.

## 5.2 Governing equations for bubble growth model

In this section, the governing equations describing the mass transfer processes of dissolved species in a glass melt surrounding a bubble and the equations for the bubble growth are derived. First, the major model assumptions are stated and defended. In order to derive an expression for the bubble growth rate, the equations of continuity and motion are used. This results in the appropriate equation to describe the transient bubble growth. The diffusion equation is used to describe the mass transport inside the glass towards the bubble, including the effect of the stretching of the glass shell, which compresses the concentration profiles. The thermodynamic equilibrium between the polyvalent ions in the glass is accounted for by a source term in the diffusion equations. The ideal gas law is applied to determine the pressure in the bubble, combined with the assumption of thermodynamic equilibrium between C, CO and CO<sub>2</sub> in the bubble (Boudouard equilibrium with the activity of C being unity ( $a_C = 1$ ), presupposing an excess of carbon inside the bubble at all times.

The mathematical formulation of the model consists of one partial differential equation for each diffusing species (polyvalent ions and physically dissolved oxygen) with appropriate initial and boundary conditions plus three ordinary differential equations: The first one describes the molar oxygen flux from the chemically and physically dissolved oxygen arriving at the glass-bubble interface. The second one describes the bubble growth and the third one the heating rate. A schematically representation of the system to be modeled is given in figure 5.5.

### 5.2.1 Model assumptions

The model equations are set up for spherical coordinates with the origin of the coordinate system at the bubble center. The main assumptions for the mathematical model are:

- i. The glass melt around the bubble is incompressible and the glass mass density is constant in time ( $\frac{\partial \rho}{\partial t} = 0$  and  $\nabla \rho = 0$ ).
- ii. The glass behaves as a Newtonian fluid, i.e., the viscosity depends, by this definition, only on temperature, the pressure, and also the chemical composition of the fluid, but not on the displacement rate [28].
- iii. The bubble is perfectly spherical, which means that all expressions for the directions perpendicular to the radial one are eliminated ( $v_\theta = v_\phi = 0$  and  $\frac{\partial}{\partial \theta} = \frac{\partial}{\partial \phi} = 0$ ).
- iv. There is no coalescence of bubbles. Only one bubble with its spherical glass shell is considered.
- v. The outside interface of the glass shell (at  $r = R_2$ ) is impermeable for gaseous species. This follows from the symmetry assumption, that the outer boundary of the shell is the interface between two bubbles of the same size, including their shell ( $\frac{\partial c}{\partial r}|_{r=R_2} = 0$ ).
- vi. For the calculation of the pressure and the gas volume inside the bubble, only C, CO and CO<sub>2</sub> are present and their concentrations or partial pressures, respectively, obey thermodynamic equilibrium. A permanent excess of carbon is assumed, thus  $a_C = 1$
- vii. Gravity is neglected.
- viii. Diffusion of foaming gases (CO and CO<sub>2</sub>) into the glass is neglected due to their low total solubility (CO<sub>2</sub> solubility:  $7.92 \cdot 10^{-5} \text{ mol} \cdot \text{m}^{-3} \cdot \text{Pa}^{-1}$  at 1173 K, [29]), compared to the chemical solubility of O<sub>2</sub>, which is  $10^3 - 10^5$  times higher.

Most models discussed earlier in this chapter consider isothermal cases. Foam glass is produced during heating of, e.g., a glass - carbon powder mixture up to a certain temperature range, at which the main foaming takes place. This makes it necessary to consider it being a non isothermal system. However to simplify the calculation, the temperature is assumed to be constant for each small time step, i.e., there is no temperature gradient in the bubble/glass-shell domain. The temperature course is derived from the heating rate of the furnace in which the powder mix is foamed. Important material properties, e.g., viscosity, surface tension, reaction equilibrium constants and diffusion coefficients are considered to be temperature dependent in the model. The diffusion coefficients are assumed to be independent of the concentrations of polyvalent ions in the glass shell and independent of space.

### 5.2.2 Equation of continuity

The equation of continuity for a fluid is, according to Bird et al. [30]:

$$\frac{\partial \rho}{\partial t} = -(\nabla \cdot \rho \mathbf{v}) \quad (5.1)$$

where  $\rho$  is the fluid density,  $t$  the time and  $\mathbf{v}$  the mass average velocity vector. For an incompressible fluid (assumption i), we obtain as condition:

$$(\nabla \cdot \mathbf{v}) = 0 \quad (5.2)$$

Spherical symmetry (assumption iii) eliminates expressions for the directions  $\phi$  and  $\theta$ . With constant glass mass density (assumption i) we obtain for the continuity equation for the glass phase:

$$(\nabla \cdot \mathbf{v}) = \frac{1}{r^2} \frac{\partial}{\partial r}(r^2 v_r) = 0 \quad (5.3)$$

where  $r$  is the radial coordinate in spherical coordinates and  $v_r$  the mass average velocity of the fluid in the  $r$ -direction. Integration of equation (5.3) between the two boundaries  $R_1$  and  $R_2$ , where  $R_1$  is the inner radius of the bubble and  $R_2$  the outer radius, results in:

$$r^2 v_r = \text{constant} = R_1^2 v_{R_1} \quad \Leftrightarrow \quad v_r = \frac{R_1^2}{r^2} v_{R_1} \quad (5.4)$$

with  $v_{R_1}$  being the growth rate of the bubble radius  $R_1$ ,  $v_{R_1} = \frac{dR_1}{dt}$ .

### 5.2.3 Momentum equation

Fluid incompressibility (assumption i), perfectly spherical bubble shape (assumption iii), symmetry and negligence of gravity (assumption vii) results in the following form for the momentum equation according to Bird et al. [30]:

$$\rho \left[ \frac{\partial v_r}{\partial t} + v_r \frac{\partial v_r}{\partial r} \right] = -\frac{\partial p}{\partial r} - \frac{1}{r^2} \frac{\partial}{\partial r}(r^2 \tau_{rr}) + \frac{\tau_{\theta\theta} + \tau_{\phi\phi}}{r} \quad (5.5)$$

with  $\tau_{rr}$  being the radial component of the stress tensor in  $r$ -direction.  $\tau_{\theta\theta}$  and  $\tau_{\phi\phi}$  are, analogously, the stress tensor components in the indicated directions  $\theta$  and  $\phi$ . Assuming a Newtonian fluid (assumption ii),  $\tau_{rr}$  is derived by, see Bird et al. [30]:

$$\tau_{rr} = -\mu \left[ 2 \frac{\partial v_r}{\partial r} \right] + \left( \frac{2}{3} \mu - \kappa \right) (\nabla \cdot \mathbf{v}) \quad (5.6)$$

where  $\mu$  is the dynamic viscosity of the liquid and  $\kappa$  the dilatational viscosity<sup>4</sup> [30]. With the conditions of equation (5.2), we get:

$$\tau_{rr} = -2\mu \frac{\partial v_r}{\partial r} \quad (5.7)$$

Analogously, the equations for  $\tau_{\theta\theta}$  and  $\tau_{\phi\phi}$  become:

$$\tau_{\theta\theta} = -\mu \left[ 2 \left( \frac{1}{r} \frac{\partial v_\theta}{\partial \theta} + \frac{v_r}{r} \right) \right] + \left( \frac{2}{3} \mu - \kappa \right) (\nabla \cdot \mathbf{v}) = -2\mu \frac{v_r}{r} \quad (5.8)$$

$$\tau_{\phi\phi} = -\mu \left[ 2 \left( \frac{1}{r \sin \theta} \frac{\partial v_\phi}{\partial \phi} + \frac{v_r + v_\theta \cot \theta}{r} \right) \right] + \left( \frac{2}{3} \mu - \kappa \right) (\nabla \cdot \mathbf{v}) = -2\mu \frac{v_r}{r} \quad (5.9)$$

---

<sup>4</sup>The dilatational or bulk viscosity is introduced by [30] to derive Newton's law of viscosity. If the fluid is a gas it is often assumed that it acts as a monoatomic gas for which  $\kappa$  is identical to zero. For fluids it is often assumed that they are incompressible, for which  $(\nabla \cdot \mathbf{v} = 0)$  and the term containing  $\kappa$  is discarded anyway [30], which is the case here.



The momentum equation then becomes:

$$\rho \left[ \frac{\partial v_r}{\partial t} + v_r \frac{\partial v_r}{\partial r} \right] = -\frac{\partial p}{\partial r} - \frac{1}{r^2} \frac{\partial}{\partial r} \left( -2\mu \frac{\partial v_r}{\partial r} \cdot r^2 \right) - 4\mu \frac{v_r}{r^2} \quad (5.10)$$

The temperature range of foaming is between 873 and 1173 K and the corresponding dynamic viscosity  $\mu$  of the soda-lime-silicate glass lies between  $10^{10}$  and  $10^4$  Pa·s, estimated by the so-called Vogel-Fulcher-Tamman (VFT) equation [28]. The parameters of the VFT equation (giving viscosity as a function of temperature) are determined by Lakatos et al. [31], see subsection 5.10.3 on page 189. The duration of the foaming process is between 0.5 and 1 hour and the bubble radius changes 3 orders of magnitude from typically  $10^{-5}$  to  $10^{-2}$  m [3]. The Reynolds number:  $Re = \frac{\rho v_R 2R}{\mu}$  is smaller than  $10^{-9}$  inside the whole foaming regime. In other words: for highly viscous fluid (glasses) the two terms of the left hand side of equation (5.10) can be neglected, because  $v_r$  is very small and changes very slowly. Therefore the inertia term  $v_r \frac{\partial v_r}{\partial r}$  and the instationary term  $\frac{\partial v_r}{\partial t}$  can be neglected. This simplifies equation (5.10) to:

$$-\frac{\partial p}{\partial r} - \frac{1}{r^2} \frac{\partial}{\partial r} \left( -2\mu \frac{\partial v_r}{\partial r} \cdot r^2 \right) - 4\mu \frac{v_r}{r^2} = 0 \quad (5.11)$$

The integration of equation (5.11), combined with equation (5.4), between  $r = R_1$  and  $r = R_2$ , the two borders of the glass shell, is given in the appendix, in subsection 5.10.1 on page 186 and results in:

$$p_l(R_1) - p_l(R_2) = 0 \quad (5.12)$$

where  $p_l(R_1)$  is the pressure of the liquid at the inner radius  $r = R_1$  and  $p_l(R_2)$  the pressure of the liquid at the outer radius  $r = R_2$ . It should be noted that  $R_1$  and  $R_2$  are functions of time ( $R_1(t)$  and  $R_2(t)$ ). For simplicity we write the influence of the surface tension at  $r = R_1$  on the bubble growth, a force balance at the two boundaries of the shell is derived.

#### 5.2.4 Force balance at bubble shell

To determine the different pressures acting in the glass phase at  $r = R_1$  and  $r = R_2$ , as well as the effect of the surface tension at  $r = R_1$  on the bubble growth, a force balance is derived. With no external forces present on the liquid, the force balance can be derived according to figure 5.6. As mentioned (assumption v), the interface at  $r = R_2$  is not a real interface, but the border to the glass shell of the neighboring bubble. Because one bubble with its shell is considered, the reference pressure is the pressure applied on the whole system (bubble+glass shell). Because of the symmetry consideration of the bubble structure in the considered model foam, the pressure ( $p_{ref}$ ) acting on the glass shell at  $r = R_2$  (the reference pressure for the bubble growth) is the ambient gas pressure during the real foaming process. For the force balance we obtain:

at  $r = R_1$ :

$$p_b + \tau_{rr,g}(R_1) = p_l(R_1) + \tau_{rr,l}(R_1) + \frac{2\sigma}{R_1} \quad (5.13)$$

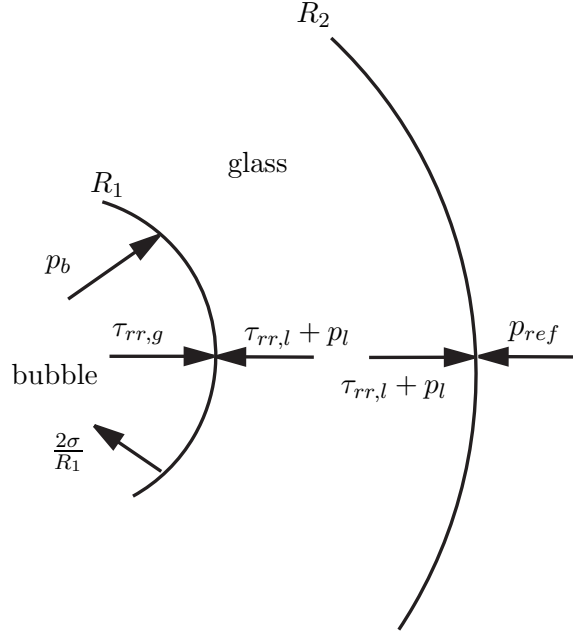


Figure 5.6: Force balance over bubble shell, arrows indicate direction of force.

at  $r = R_2$ :

$$p_{ref} = p_l(R_2) + \tau_{rr,l}(R_2) \quad (5.14)$$

where  $p_b$  is the pressure of the gas in the bubble,  $p_{ref}$  the reference pressure, and  $\sigma$  is the temperature dependent surface tension. The term  $\frac{2\sigma}{R}$  represents the tension acting perpendicular to the liquid surface on the liquid due to surface tension. The radial stress of the gas phase viscosity  $\tau_{rr,g}$ , is very small compared to  $\tau_{rr,l}$ , the one of the liquid and can therefore be neglected [32].  $\tau_{rr,l}$  is given by equation (5.6). Combining equations (5.7) and (5.4), we obtain for the Newtonian fluid (assumption ii) at the inner radius ( $R_1$ ) and the outer radius ( $R_2$ ):

$$\tau_{rr,l}(R_1) = \frac{4\mu}{R_1} \frac{dR_1}{dt} \quad \text{and} \quad \tau_{rr,l}(R_2) = \frac{4\mu}{R_2} \frac{dR_2}{dt} \quad (5.15)$$

From the force balance and equation (5.12) we obtain:

$$p_b - p_{ref} - \frac{2\sigma}{R_1} - 4\mu \left( \frac{dR_1}{dt} \frac{1}{R_1} - \frac{dR_2}{dt} \frac{1}{R_2} \right) = 0 \quad (5.16)$$

Because the total volume of the glass in the shell ( $V_l$ ) is constant (assumption i),  $R_1$  and  $R_2$  are related through:

$$V_l = \frac{4}{3}\pi(R_2^3 - R_1^3) = \text{constant} \quad (5.17)$$

Thus:

$$R_2 = \left[ \frac{V_l}{\frac{4}{3}\pi} + R_1^3 \right]^{\frac{1}{3}} \quad (5.18)$$

To be able to derive a formula for the change of the radius  $R_1$ , it is necessary to calculate the change of  $R_2$  in terms of the  $R_1$ .

$$\frac{dR_2}{dt} = \frac{dR_2}{dR_1} \frac{dR_1}{dt} = \frac{R_1^2}{\left(\frac{3V_l}{4\pi} + R_1^3\right)^{\frac{2}{3}}} \frac{dR_1}{dt} \quad (5.19)$$

Combining equations (5.16), (5.18) and (5.19), the equation for the bubble growth is obtained:

$$\frac{dR_1}{dt} = \frac{\frac{3V_l}{4\pi} + R_1^3}{4\mu \frac{3V_l}{4\pi}} (\Delta p R_1 - 2\sigma) \quad \text{with} \quad \Delta p = p_b - p_{ref} \quad (5.20)$$

Equation (5.20) shows, that the pressure in the bubble ( $p_b$ ) must be  $2\sigma$  larger than the reference pressure ( $p_{ref}$ ) to stretch the fluid (glass) around the bubble against the surface tension. The viscosity retards the expansion velocity. The pressure increase inside the bubble depends on the mass transport of the polyvalent ions in the glass to the bubble-glass interface and the resulting chemical gas forming reactions at the glass-bubble interface. The mass transport equations inside the glass melt are described in the next subsection.

### 5.2.5 Mass transport in the glass melt shell

The diffusion equation, plus a source term to describe species formation or reaction caused by chemical equilibrium reactions is used to calculate the mass transport of a species in the glass shell. Diffusion in the melt and convection of the melt (stretching of glass shell) is taken into account. The inter-diffusion coefficient  $D_i$  of species  $i$  in the glass depends on temperature. Furthermore it is assumed that  $D_i$  is independent of the spatial variable and the local concentrations of the different species in the glass. The general equation for the concentration profile in a liquid with diffusion and chemical reaction can be written according to Bird et al. [30].

$$\frac{\partial c_i}{\partial t} + (\mathbf{v} \cdot \nabla c_i) = (D_i \nabla^2 c_i) + \Psi_i \quad (5.21)$$

where  $c_i$  is the local concentration of species  $i$ .  $D_i$  is the inter-diffusion coefficient for species  $i$ .  $\Psi_i$  is a production term describing the generation of component  $i$  per unit volume by chemical reactions in the glass. These reactions are reduction-oxidation (redox) reactions consuming or producing oxygen and involve polyvalent ions with different valencies. The index  $i$  denotes different species. The diffusion equation for spherical coordinates in radial direction (assumption iii) can then be written as:

$$\frac{\partial c_i}{\partial t} + v_r \frac{\partial c_i}{\partial r} = D_i \left[ \frac{1}{r^2} \frac{\partial}{\partial r} \left( r^2 \frac{\partial c_i}{\partial r} \right) \right] + \Psi_i \quad (5.22)$$

The combination of equation (5.4) and (5.22) results in equation (5.23):

$$\frac{\partial c_i}{\partial t} = \frac{D_i}{r^2} \frac{\partial}{\partial r} \left[ r^2 \frac{\partial c_i}{\partial r} \right] - \frac{R_1^2}{r^2} \frac{dR}{dt} \frac{\partial c_i}{\partial r} + \Psi_i \quad (5.23)$$

A more specific description of the source term  $\Psi_i$ , describing the production or consumption of species  $i$  to maintain chemical equilibrium between the polyvalent species and the dissolved gases in the diffusion domain, will be given in subsection 5.2.6 on page 133.

### Initial and boundary conditions

At  $t = 0$ , the start of the modeled foaming process, the bubble is at its initial size,  $R_1(0)$  and  $R_2(0)$ , and does not grow. All polyvalent ions are at their initial concentrations and in thermodynamic equilibrium. For the initial conditions, we obtain:

#### Initial conditions ( $t = 0$ )

$$r = r; \quad c_i = c_{i,0} \quad (5.24)$$

$$r = R_1; \quad r = R_{1,0} \quad (5.25)$$

$$r = R_1; \quad \frac{dR_1}{dt} = 0 \quad (5.26)$$

$$r = R_2; \quad r = R_{2,0} \quad (5.27)$$

$$r = r; \quad \Psi_i = 0 \quad (5.28)$$

### Boundary conditions

A sudden change in concentration of species  $i$  at the inner side of the glass shell ( $r = R_1$ ), as foaming starts in the model, is the result of a fast chemical reaction inside the bubble, which will be discussed in subsection 5.2.7 on page 139. The flux of gas forming species (species in the glass that react at the inner surface to release  $O_2$  gas from the melt) from the glass melt towards the gas bubble is described by a mass transfer relation. The outer radius of the shell ( $r = R_2$ ) is the border to the shell of the neighboring bubble. No mass is exchanged with the surrounding shells. For the boundary conditions, we get:

$$r = R_1; \quad t > 0; \quad D_i \frac{\partial c_i}{\partial r} = \chi_i c_{i,ox} \quad (5.29)$$

$$r = R_2; \quad t > 0; \quad \frac{\partial c_i}{\partial r} = 0 \quad (5.30)$$

where  $\chi_i$  is the mass transfer coefficient for oxygen from species  $i$  from the glass surface to the gas phase in the bubble<sup>5</sup>. The index *ox* denotes species that deliver oxygen, thus the oxidized form of the polyvalent ion and physically dissolved oxygen. In the model,  $\chi_i$  was set to be very high to describe that all oxygen at the glass bubble interface is instantaneously consumed.

---

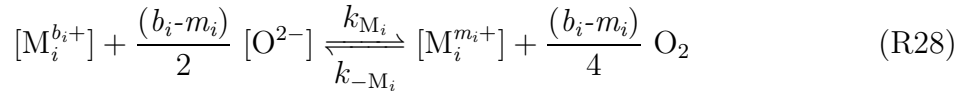
<sup>5</sup>Oxygen is also chemically dissolved in the glass in form of, e.g.,  $Fe_2O_3$  and this oxygen reacts at the interface with C or CO producing FeO and CO or  $CO_2$ , respectively. The mass transfer coefficient  $\chi_i$  also describes the mass transfer of the oxygen from, e.g.,  $Fe_2O_3$  into the bubble.

### 5.2.6 Thermodynamic equilibrium in the glass

In case of the presence of polyvalent ions in a glass melt, the thermodynamic equilibrium between the different oxidation states of the polyvalent ions and physically dissolved oxygen influences the diffusion process of the polyvalent species in their prevalent oxidation state [1]. The source term  $\Psi_i$  in equation (5.23) represents the molar rate of production of species  $i$  (at its oxidation state) per unit volume caused by reactions of these polyvalent ions in the glass melt or oxygen to maintain thermodynamic equilibrium during concentration and temperature changes. The interaction of the thermodynamic equilibrium of the redox couples (redox reactions of polyvalent species, e.g.  $\text{Fe}^{2+}/\text{Fe}^{3+}$ ,  $\text{S}^{6+}/\text{S}^{4+}/\text{S}^0/\text{S}^{2-}$ ) and the diffusion process can be explained as follows:

Starting from thermodynamic equilibrium conditions in the glass melt, the diffusion process, due to a change in concentration of the different polyvalent species disturbs locally the thermodynamic equilibrium. Fast chemical redox reactions of the polyvalent ions will then re-establish the equilibrium. This implies mutual interaction of all present redox couples and physically dissolved oxygen in the glass melt. One criterion for the approach of thermodynamic equilibrium in the glass melt is that the velocity of re-establishment (reaction kinetics) is much faster than the diffusion process. Rüssel [33] stated that chemical relaxation in a soda-lime-silicate glass doped with iron is about 1 s at 823 K and gets faster with increasing temperature. Thus the establishment of chemical reaction equilibria is assumed to be faster than the diffusion and bubble growth process. It is important to note that in case of thermodynamic equilibrium, a temporary distortion of the thermodynamic equilibrium can only be compensated by the chemical reaction of the polyvalent ions and oxygen until the new equilibrium state is reached. The mutual interaction of all polyvalent ions and oxygen in the glass at each position must be considered when modeling the influence of redox state and the presence of polyvalent ions in the glass on bubble growth.

Starting from a general ionic reaction equation, which can be used to describe the reactions of the different redox couples plus oxygen, e.g.,  $\text{As}_2\text{O}_5/\text{As}_2\text{O}_3$ ,  $\text{Sb}_2\text{O}_5/\text{Sb}_2\text{O}_3$ ,  $\text{Ce}_2\text{O}_3/\text{CeO}_2$ ,  $\text{Fe}_2\text{O}_3/\text{FeO}$ ,  $\text{Mn}_2\text{O}_3/\text{MnO}$ , the general notation is [34]:



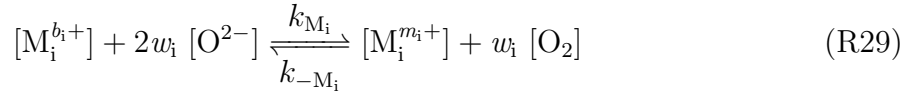
where  $[\text{M}_i^{b_i+}]$  denotes the concentration of the oxidized species of the polyvalent ion in the melt and  $[\text{M}_i^{m_i+}]$  the concentration of the reduced one ( $b_i > m_i$ ).  $k_{M_i}$  and  $k_{-M_i}$  denote the reaction rate constants. In case of only one type of polyvalent ion in the glass, the reduction of one mole  $[\text{M}_i^{b_i+}]$  results in the production of  $\frac{(b_i - m_i)}{4}$  mole  $\text{O}_2$ .

The oxygen ion activity or free oxygen ion concentration is often called the measure for the basicity of the glass. In silicate melts, the basicity is not only determined by redox reactions, but also by structural aspects [35] and by the presence of alkaline and alkaline earth ions [36]. The  $[\text{O}^{2-}]$  concentration in the glass is very large compared to the changes caused by redox reactions. Thus  $(a_{\text{O}_2-})$ , the chemical activity of  $\text{O}^{2-}$ , can be assumed to be constant for certain glass types and temperatures, as it is done here.

Applying Henry's Law:

$$[O_2] = L_{O_2} p_{O_2} \quad (5.31)$$

where the solubility of molecular oxygen  $L_{O_2}$  refers to physically dissolved oxygen and  $p_{O_2}$  being the partial pressure of dissolved oxygen with which the glass melt is in equilibrium, reaction (R28) can be written as:



with:

$$w_i = \frac{(b_i - m_i)}{4} \quad \text{and} \quad b_i > m_i \quad (5.32)$$

Reaction equilibrium (R29) can now be expressed in terms of activities as:

$$K' = K a_{O^{2-}}^{2w_i} = \frac{a_{M_i^{m_i+}}}{a_{M_i^{b_i+}}} p_{O_2}^{w_i} \quad (5.33)$$

where  $K$  is the thermodynamic equilibrium constant and  $K'$  a modified equilibrium constant proportional to  $K$ .  $p_{O_2}$  is the oxygen vapor pressure in equilibrium with physically dissolved oxygen in the melt assuming ideal gas. The concentration of physically dissolved oxygen, at isothermal conditions, expressed as the partial oxygen equilibrium pressure, solely depends on the ratio of the oxidized and reduced form of a polyvalent ion and vice versa (see equation (5.33)). This approach was used by Beerkens et al. [1] to calculate the penetration depth of oxygen into the glass melt during a change of temperature or atmosphere in a glass furnace. The concentrations of the polyvalent ions were only affected by the thermodynamic equilibrium, i.e., adapting to changes in local partial oxygen pressure. The polyvalent ions were considered to be locally immobile. They were considered to change the valency, but the total concentration of polyvalent ions was assumed to be locally constant.

In order to use the thermodynamic equilibrium constant  $K$  in terms of concentration instead of activities, it is defined:

$$K^* = K' \frac{\gamma_{M_i^{b_i+}}}{\gamma_{M_i^{m_i+}}} = \frac{[M_i^{m_i+}]}{[M_i^{b_i+}]} p_{O_2}^{w_i} \quad (5.34)$$

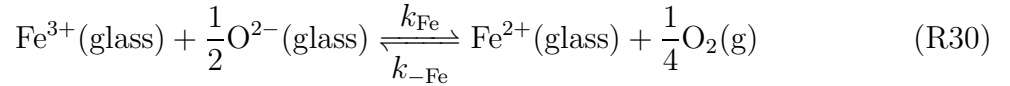
where  $\gamma$  denotes the activity coefficient and  $[M_i^{m_i+}]$  the concentration of  $M_i^{m_i+}$  in  $\text{mol} \cdot \text{m}^{-3}$ . Assuming ideal gas behavior, constant  $O^{2-}$  activity and constant activity coefficients  $\gamma_i$ , equation (5.34) can be used to experimentally determine  $K^*$ . The deviation or experimental determination of  $K^*$  will be discussed later in this chapter.

In case of foam glass to be produced from an iron oxide containing glass, it is assumed that, in addition to the physically dissolved oxygen, ferric iron ( $\text{Fe}^{3+}$ ), as carrier of the chemical dissolved oxygen diffuses in the glass and is reduced to the ferrous state ( $\text{Fe}^{2+}$ ) at the glass bubble interface. The concentration of physically dissolved oxygen in a strongly oxidized molten glass with 3 wt.% iron oxide at 873 K is about 8-10 orders of magnitude

smaller than the concentration of ferric iron. Due to the low concentration of physically dissolved oxygen compared to the concentration of ferric iron, a bubble would hardly grow, if only oxygen would react with the carbon at the glass-bubble interface and no  $\text{Fe}^{3+}$  would diffuse to the glass - bubble interface. This will be explained in more detail later in this chapter. The transport of physically dissolved oxygen in the glass is very low and can be neglected for the formation of the foaming gas. It is however necessary to determine the local, physically dissolved, oxygen concentration, because the physically oxygen concentration determines the concentration ratios of the different valency states of the different redox couples in the glass. The iron ions ( $\text{Fe}^{2+}$  and  $\text{Fe}^{3+}$ ) are mobile with individual inter-diffusion coefficients. The case described by Beerkens et al. [1] shows that the high concentration of iron has a very strong effect on the concentration profiles of physically dissolved oxygen. Due to the low equilibrium concentration of the physically dissolved oxygen, the physically dissolved oxygen flux from the glass towards the bubble interface, remains low. The oxygen is mainly delivered to the bubble by reduction of  $\text{Fe}^{3+}$  at the glass - bubble interface.

In the presence of multiple polyvalent species in the glass melt, the concentrations of the reduced and oxidized forms of the different polyvalent ions are determined by the partial oxygen pressure in the glass and the total concentration of the polyvalent species. All concentrations of the oxidized and reduced forms of each of the polyvalent ions plus physically dissolved oxygen and their interaction to maintain local chemical equilibrium during the diffusion process or temperature changes must be modeled.

For instance, the  $\text{Fe}^{2+}/\text{Fe}^{3+}$  equilibrium can be written according to :



The relation between the molar reaction rate (denoted as  $Q$ ) of the oxidized and reduced form of one polyvalent species  $i$  for reaction (R29) and the physically dissolved oxygen, can be written exemplary for the  $\text{Fe}^{2+}/\text{Fe}^{3+}$  equilibrium:

$$Q_{(\text{R30})} = Q^{\text{Fe}^{2+}} = -Q^{\text{Fe}^{3+}} = 4Q^{\text{O}_2} \quad (5.35)$$

More specific, the molar reaction rate of reaction (R30) in this case is:

$$-Q^{\text{Fe}^{3+}} = Q_{(\text{R30})} = k_{\text{Fe}} [\text{Fe}^{3+}] [\text{O}^{2-}]^{1/2} - k_{-\text{Fe}} [\text{Fe}^{2+}] p_{\text{O}_2}^{1/4} \quad (5.36)$$

where  $k_{-\text{Fe}}$  and  $k_{\text{Fe}}$  are the reverse and forward reaction rate constants for this specific reaction. The physical solubility of oxygen in soda lime silicate melts, assuming the validity of Henry's law, between 1473 and 1773 K was estimated by Beerkens [17] to be:

$$L_{\text{O}_2} = 13.7 \cdot 10^5 \exp(-6633/T) \left[ \frac{\text{mol}}{\text{m}^3 \text{ Pa}} \right], \quad \text{T(K)} \quad (5.37)$$

Based on concentrations, and because for this case:

$$k_{-\text{Fe}} = k'_{\text{Fe}}/K''_{\text{Fe}}, \quad \text{with} \quad k'_{\text{Fe}} = k_{\text{Fe}} \cdot [\text{O}^{2-}]^{1/2} \quad (5.38)$$

reaction (5.36) can be written as:

$$-Q_{(R30)} = k'_{\text{Fe}} \left[ \frac{[\text{Fe}^{2+}]}{K''_{\text{Fe}}} \left( \frac{[\text{O}_2]}{L_{\text{O}_2}} \right)^{1/4} - [\text{Fe}^{3+}] \right] \quad (5.39)$$

$K''_{\text{Fe}}$  denotes the equilibrium constant based on concentration. Equations (5.35) and (5.39) represent the set of equations to describe the molar rates of production or consumption of  $\text{Fe}^{2+}$ ,  $\text{Fe}^{3+}$  and  $\text{O}_2$  to maintain equilibrium.

The presence of multiple polyvalent ions in a glass requires a more detailed view on the mutual interaction of the different polyvalent ions and the physically dissolved oxygen. This will be presented in the next part of this subsection demonstrating the interaction of iron and sulphur, the most common present redox couples in technical glasses and in foam glasses.

In a soda lime silicate glass, containing iron and sulphur as polyvalent species, the presence of, e.g., sulphur species influences the concentration of physically dissolved oxygen and thus the ferrous/ferric iron ratio and vice versa. Sulphur shows two relevant redox equilibria in glass melts [37]. One is the transition from  $\text{S}^{6+}$  to  $\text{S}^{4+}$  and the other one is the transition from  $\text{S}^{4+}$  to  $\text{S}^{2-}$ . The transition from  $\text{S}^{4+}$  to  $\text{S}^0$  is not discussed in this context [37]. Beerkens [38] report, that  $\text{S}^0$  or  $\text{S}_2$  gas may be formed in soda-lime-silica glasses, doped with fining agents at very low oxidation states ( $p_{\text{O}_2} < 10^{-9}$  bar at 1673 K), but the sulphur gas will probably dissolve only physically at very low solubility levels. The solubility, estimated on the molecular size of  $\text{S}_2$  is reported to be below  $0.02 \text{ mol} \cdot \text{m}^{-3} \cdot \text{bar}^{-1}$  [38]. The low solubility would thus lead to  $\text{S}_2$  gas formation, which was not observed during the experiments in the previous chapter. The transition from  $\text{S}^{4+}$  to  $\text{S}^0$  is therefore not considered in our consideration. For oxidized or mildly reduced glasses, the redox transition from  $\text{S}^{6+}$  to  $\text{S}^{4+}$  must be considered as for stronger reduced glasses, the transition from  $\text{S}^{4+}$  to  $\text{S}^{2-}$  becomes important [37, 39].

The Gibbs free energy of a chemical reaction ( $\Delta G^r$ ) and the thermodynamic equilibrium constant  $K$  are defined as [40]:

$$\Delta G^r \equiv \sum_i \nu_i G_i^r = -R_g T \ln K^r = -RT \ln \left( \prod_i (a_i)^{\nu_i} \right) \quad (5.40)$$

where  $\nu_i$  denotes the stoichiometric number of moles of species  $i$  in the reaction equation,  $R_g$  is the ideal gas constant,  $T$  the absolute temperature,  $K$  the chemical equilibrium constant of the considered reaction and  $a_i$  the activity of species  $i$ . The chemical activity of a species  $i$  is defined as:

$$a_i = \gamma_i x_i \quad (5.41)$$

where  $\gamma_i$  denotes the activity coefficient and  $x_i$  the mole fraction of species  $i$ .  $\Delta G^r$  is the difference of the Gibbs free energies of the products and reactants weighed by their stoichiometric coefficients.  $\Delta G^r$  is constant if the temperature and pressure of the system is constant and equal for all species.  $\Delta G^r$  can be expressed as:

$$\Delta G_i^r = \Delta H_i^r - T \Delta S_i^r \quad (5.42)$$



Table 5.1: Experimentally determined reaction enthalpies  $\Delta H^{*r}$  and reaction entropies  $\Delta S^{*r}$  of the  $\text{Fe}^{2+}/\text{Fe}^{3+}$ , the  $\text{S}^{6+}/\text{S}^{4+}$  and the  $\text{S}^{4+}/\text{S}^{2-}$  equilibrium in soda lime silica glasses used for container or float glass production according to [37]. The reference state is 1 bar pressure.

Redox couple	$\Delta H^{*r}$	$\Delta S^{*r}$	Reaction
	$\text{kJ mol}^{-1}$	$\text{J mol}^{-1}\text{K}^{-1}$	
$\text{Fe}^{3+}/\text{Fe}^{2+}$	103	47	$\text{Fe}^{3+} \rightleftharpoons \text{Fe}^{2+} + \frac{1}{4} \text{O}_2$
$\text{S}^{6+}/\text{S}^{4+}$	250	130	$\text{S}^{6+} \rightleftharpoons \text{S}^{4+} + \frac{1}{2} \text{O}_2$
$\text{S}^{4+}/\text{S}^{2-}$	540	120	$\text{S}^{4+} \rightleftharpoons \text{S}^{2-} + \frac{3}{2} \text{O}_2$

where  $\Delta H_i^r$  is the reaction enthalpy change and  $\Delta S_i^r$  the reaction entropy change. Assuming that the activity coefficients  $\gamma_i$  of reaction (5.41) are unity or constant,  $K$  can be written in terms of concentration ( $K^*$ ). This was shown by equation (5.34) on page 134. Taking the ferrous/ferric iron redox couple as an example, and measuring the partial oxygen equilibrium pressure in the hot glass melt and the concentrations of the ferrous and ferric iron afterwards in the cooled glass, experimental enthalpy and entropy values ( $\Delta H^{*r}$  and  $\Delta S^{*r}$ ) are to be determined, which are only valid for this type of glass. By this method it is furthermore assumed that there is no redox reaction during cooling and one polyvalent species in the glass. For a soda lime silicate glass with iron as polyvalent ions,  $K^*$  can be calculated according to

$$-R_g T \ln K_{Fe}^* = \Delta H_{Fe}^{*r} - T \Delta S_{Fe}^{*r} \quad (5.43)$$

where  $\Delta H_{Fe}^{*r}$  and  $\Delta S_{Fe}^{*r}$  can be determined experimentally. The procedure is explained in more detail in the appendix, section 5.10.5 on page 197.

Values for the specific reaction enthalpies and entropies of the two different sulphur reactions and for iron in soda-lime-silicate glasses, used for container or float glass production, were experimentally determined by Müller-Simon [37] and are presented in table 5.1. It must be mentioned, that the thermodynamic values  $\Delta H_i^{*r}$  and  $\Delta S_i^{*r}$  and thus the equilibrium constant  $K^{*r}$ , strongly depend on the glass composition and on the concentration of polyvalent ions in the glass melt, because they are based on concentrations instead of chemical activities.

The values given in table 5.1 are for typical commercial soda-lime-silicate glass compositions. The glasses considered for foam glass production have much higher concentrations of polyvalent ions than usual soda-lime-silicate glasses. The concentration of iron oxide expressed as  $\text{Fe}_2\text{O}_3$  is about 3 wt.% and the concentration of sulfate is about 0.5 wt.%. This implies that a certain error is made when using data of other glass compositions, than usual soda-lime-silica glasses. For the validation of the model in this study, two soda-lime-silicate glasses with iron oxide added as polyvalent ion in larger concentrations, were prepared. The values of  $\Delta H^{*r}$  and  $\Delta S^{*r}$  of the iron redox couple were experimentally determined and used for the model validation. The procedure of the experimental determination of  $\Delta H^{*r}$  and  $\Delta S^{*r}$  is explained in section 5.10.5 on page 197.

The strength of the model is the calculation of mutual interaction of multiple polyvalent ions and physically dissolved oxygen. However, for example calculations with the foam bubble model, the thermodynamic values  $\Delta H_i^{*r}$  and  $\Delta S_i^{*r}$  for the sulfate redox couples of table 5.1 are going to be used.

To calculate the local concentrations of the different forms (oxidized and reduced) of the polyvalent ions in the glass, the local partial oxygen pressure in the glass melt or the physically dissolved oxygen concentration, respectively, must be known, plus the thermodynamic values  $\Delta H_i^{*r}$  and  $\Delta S_i^{*r}$  for the considered redox reaction and the total local concentration of each of the polyvalent species. To calculate the equilibrium concentrations of the polyvalent ions in the glass, which are used as initial concentrations (initial conditions) in the model, before mass transfer starts, the total concentrations<sup>6</sup> ( $\text{mol} \cdot \text{m}^{-3}$ ) for iron ( $[Fe_{tot}]$ ) and sulfur ( $[S_{tot}]$ ) in this example are:

$$[Fe_{tot}] = [Fe^{3+}] + [Fe^{2+}] \quad \text{and} \quad [S_{tot}] = [S^{6+}] + [S^{4+}] + [S^{2-}] \quad (5.44)$$

The concentration of physically dissolved oxygen can be calculated from the measured partial oxygen pressure and relation (5.31). The initial concentrations of the different valency states of the polyvalent ions, if  $S^0$  is not taken into account, can be calculated according to:

$$[Fe^{3+}] = \frac{[Fe_{tot}]}{\frac{K_{Fe^{3+}/Fe^{2+}}^* L_{O_2}^{1/4}}{[O_2]^{1/4}} + 1} \quad (5.45)$$

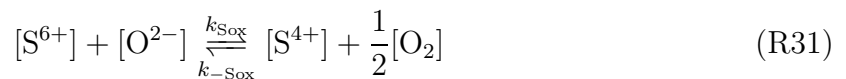
$$[S^{4+}] = \frac{[S_{tot}]}{\frac{K_{S^{4+}/S^{2-}}}^{''} \frac{L_{O_2}^{3/2}}{[O_2]^{3/2}} + \frac{[O_2]^{1/2}}{K_{S^{6+}/S^{4+}}^* L_{O_2}^{1/2}} + 1} \quad (5.46)$$

$$[S^{6+}] = [S^{4+}] \frac{[O_2]^{1/2}}{K_{S^{6+}/S^{4+}}^* L_{O_2}^{1/2}} \quad (5.47)$$

where all three equations are coupled by the concentration of physically dissolved oxygen ( $[O_2]$ ).

In the first part of this subsection, the equations for calculating thermodynamic equilibria compositions in glasses have been shown. The second part showed a practical example (Fe/S containing glass) for better understanding of the redox reactions of multiple polyvalent ions in glasses.

Analogously to equation (5.39), the molar reaction rate for reaction:



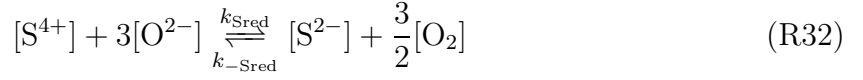
is

$$-Q_{(R31)} = k_{S_{ox}} \left[ \frac{[S^{4+}]}{K_{S^{6+}/S^{4+}}} \cdot \left( \frac{[O_2]}{L_{O_2}} \right)^{1/2} - [S^{6+}] \right] \quad (5.48)$$

---

<sup>6</sup>The total concentrations ( $\text{mol} \cdot \text{m}^{-3}$ ) of the polyvalent ions were determined using a sample at room temperature. The volume increases due to thermal expansion during temperature increase (application of values at 1023 K) has not been corrected.

For reaction:



the molar reaction rate is:

$$-Q_{(R32)} = k_{Sred} \left[ \frac{[S^{2-}]}{K''_{S^{4+}/S^{2-}}} \cdot \left( \frac{[O_2]}{L_{O_2}} \right)^{3/2} - [S^{4+}] \right] \quad (5.49)$$

It should be noted that the molar reaction rates  $Q_i$  are only valid for the specific reaction for which they are set-up. The reaction rate constants  $k_i$  are very high to maintain equilibrium. All reactions are coupled by  $[O_2]$  and in addition to that,  $[S^{4+}]$  can be formed by reduction of  $[S^{6+}]$  according to reaction (R31) or by oxidation of  $[S^{2-}]$  according to reaction (R32). The production terms  $\Psi$ , belonging to the mass transfer equation (5.23), for the 6 diffusing species in this example are:

$$\begin{aligned} \Psi_{Fe^{3+}} &= -Q_{(R30)} \\ \Psi_{Fe^{2+}} &= Q_{(R30)} \\ \Psi_{O_2} &= \frac{1}{4}Q_{(R30)} + \frac{1}{2}Q_{(R31)} + \frac{3}{2}Q_{(R32)} \\ \Psi_{S^{6+}} &= -Q_{(R31)} \\ \Psi_{S^{4+}} &= Q_{(R31)} - Q_{(R32)} \\ \Psi_{S^{2-}} &= Q_{(R32)} \end{aligned} \quad (5.50)$$

The equations for the bubble growth, the equation for the mass transport of species in the glass and the condition of local thermodynamic redox equilibrium have been described so far. In order to model the bubble growth rate, the changing gas content and the pressure increase inside the bubble must be calculated. This depends on the chemical reactions inside the bubble and the mass transport of chemically and physically dissolved oxygen from the glass to the glass-bubble interface. The equations are derived in the next subsection.

### 5.2.7 Chemical reaction in the gas phase and mass conservation at glass-bubble interface

The bubble contains carbon particles, which are assumed to permanently cover parts of each bubble surface (excess of carbon). The carbon particles inside the bubble can react at the glass-bubble interface with the oxidized species of the polyvalent ions and the physically dissolved oxygen. One possible reaction of carbon with oxygen producing CO and  $CO_2$  is:



Assuming thermodynamic equilibrium in the gas phase, the partial pressure of the different gaseous species according to reaction (R33) inside the bubble can be calculated from Gibbs free energy data of pure substances, assuming ideal gas behavior and a carbon activity of unity [41] and no other gases in the bubble. The distribution of the three different gaseous species as a function of temperature according to reaction (R33) inside

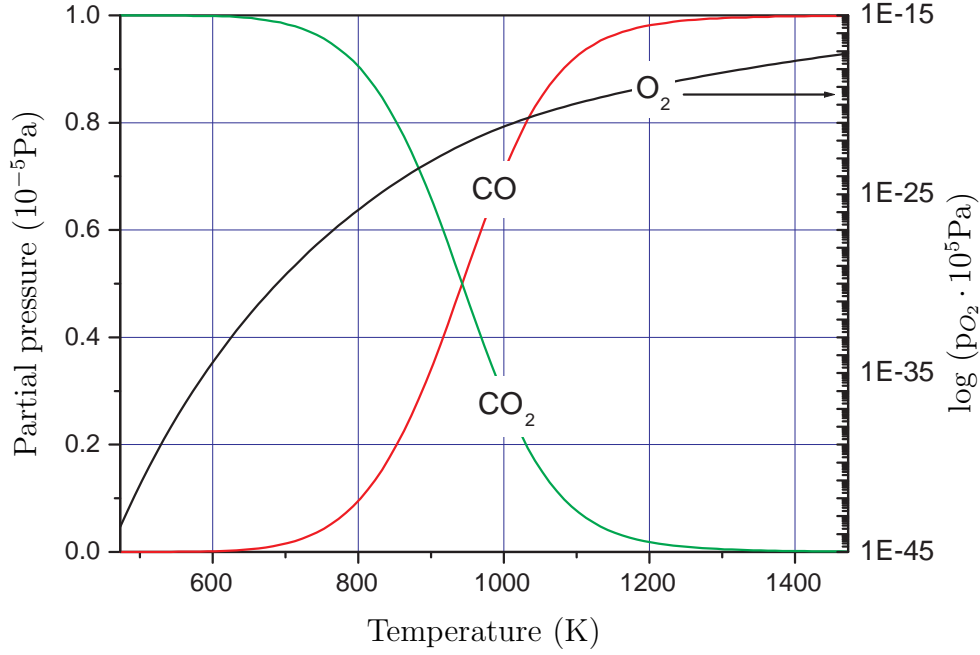
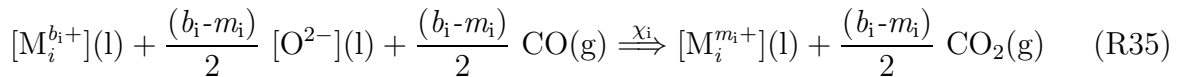


Figure 5.7: Equilibrium partial pressures of CO, CO<sub>2</sub> and O<sub>2</sub> according to reaction (R33) as a function of temperature at 10<sup>5</sup> Pa total pressure and  $a_C = 1$ , determined with the FactSage 5.1 Software package to calculate chemical equilibrium compositions [42].

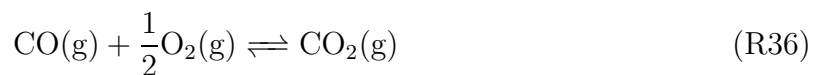
the bubble at 10<sup>5</sup> Pa total pressure and unity carbon activity is exemplary shown in figure 5.7. It can be observed from this figure that the concentration of oxygen in the bubble is very small compared to the concentrations of CO and CO<sub>2</sub> and that the equilibrium partial pressure of CO is larger than  $0.5 \cdot 10^5$  Pa above 943 K. Because the contact surface between the carbon particles and the glass is small, it is probable that also the carbon monoxide reduces the oxidized form of the polyvalent ion and also reacts with the physically dissolved oxygen at the glass-bubble interface. Neglecting the partial oxygen pressure inside the bubble, all of the oxygen forms either CO or CO<sub>2</sub> (an excess of carbon is assumed). The equilibrium reaction between the solid carbon particles and the gaseous species in the bubble can be described by the Boudouard reaction:



The concentration of physically dissolved oxygen in the glass is very low and its contribution to the formation of CO and CO<sub>2</sub> is thus also very low. The chemically oxygen in form of the oxydized form of the polyvalent ion reacts at the interface with C or CO to CO or CO<sub>2</sub>, respectively. The reaction of the oxydized form of a polyvalent ion at the interface with CO can generally be written as:



The reaction for the physically dissolved oxygen becomes:



It is assumed that oxygen is the only species, which is exchanged between the glass melt and the gas phase in the bubble. This oxygen is available at the interface in the form of the oxidized form of the polyvalent species  $i$  and in the form of the physically dissolved oxygen. Oxygen mass conservation at the interface leads to the following equation for the molar transfer rate ( $O_2$ ) from the physically dissolved oxygen and the oxidized form of the polyvalent ion in the glass at the surface:

$$\frac{\partial n_{O_2}}{\partial t} = 4\pi R_1^2 \sum_i D_{ox,i} w_{i,ox} \frac{\partial c_{ox,i}}{\partial r} \bigg|_{r=R_1} \quad (5.51)$$

where the index  $ox$  denotes the oxidized form of the polyvalent species ( $i$ ) and physically dissolved oxygen. The reduced form of the polyvalent ion, e.g., FeO in an iron oxide containing glass, diffuses back into the glass.  $D_{ox,i}$  is the inter-diffusion coefficient of the oxidized form of the polyvalent species  $i$ .

### 5.2.8 Pressure inside bubble

The foaming gas inside the bubble is generated by the oxidation of C into CO and CO<sub>2</sub>, respectively. An increase in oxygen release from the glass into the bubble increases the moles of gaseous species in the bubble and thus the pressure, in case of constant bubble radius. Assuming that all oxygen from the glass becomes, at an excess of carbon, either CO or CO<sub>2</sub>, the Boudouard equilibrium as given in reaction (R34), can be used to calculate the partial pressure of CO and CO<sub>2</sub> and thus the total pressure in the bubble (at constant radius). The total pressure inside the bubble (isothermal situation) is:

$$p_{b,tot} = (n_{CO_2} + n_{CO} + n_{b,0}) \frac{V_b}{R_g T} \quad (5.52)$$

where  $n_{b,0}$  is the initial amount of gaseous species at  $t = 0$  (without CO and CO<sub>2</sub>) with no bubble growth and  $V_b$  the bubble volume.  $n_{b,0}$  can be calculated from equation (5.54):

$$n_{b,0} = \frac{p_{b,0} \frac{4}{3} \pi R_{1,0}^3}{R_g T_0} \quad (5.53)$$

$p_{b,0}$  (isothermal case) is calculated from equation (5.16), with the derivatives of the radius with respect to time equal to zero:

$$p_{b,0} = p_{ref} + \left( \frac{2\sigma}{R_1} \right) \bigg|_{t=0} \quad (5.54)$$

where  $p_{ref}$  is the reference pressure at  $R_2$ , the outer boundary of the glass shell. Assuming thermodynamic equilibrium in the gas phase at all times, we can write for the equilibrium constant of reaction (R34):

$$K_{p,b}(T) = \frac{a_{CO}^2}{a_{CO_2} a_C} \quad (5.55)$$

For ideal gases,  $a_i$  is defined as  $a_i = p_i/p^o$ . Applying the ideal gas law and  $a_c = 1$ , we obtain for  $p^o = 10^5$  Pa:

$$K_{p,b} p^o = K'_{p,b} = \frac{n_{CO}^2}{n_{CO_2}} \frac{R_g T}{V_b} \quad (5.56)$$

The equilibrium constant  $K_{p,b}$  can be calculated from thermodynamic data of pure substances, given in Barin et al. [43], using the standard Gibbs energy change of reaction (R34) at the desired temperature according to:

$$K_{p,b} = \exp \left[ \frac{-\Delta G^{r0}}{R_g T} \right] \quad \text{with} \quad \Delta G^{r0} = \sum_i \nu_i G_i^0 \quad (5.57)$$

where  $\Delta G^{r0}$  is the standard Gibbs energy change of the reaction,  $\nu_i$  is the stoichiometric number and  $G_i^0$  the standard-state Gibbs energy of species  $i$  at given temperature and  $p^o = 10^5$  Pa pressure. Since we assume that the oxygen partial pressure inside the bubble is zero, all oxygen will form either CO or CO<sub>2</sub>. The oxygen molar balance (distribution) between CO and CO<sub>2</sub> inside the bubble is:

$$n'_{O_2} = n_{CO_2} + \frac{1}{2} n_{CO} \quad (5.58)$$

where  $n'_{O_2}$  denotes the moles of oxygen (O<sub>2</sub>) distributed among CO and CO<sub>2</sub>. The combination of equations (5.56) and (5.58) results in a quadratic equation:

$$n_{CO}^2 + \frac{K'_{p,b} V_b}{2 R_g T} n_{CO} - \frac{K'_{p,b} V_b}{R_g T} n'_{O_2} = 0 \quad (5.59)$$

which gives the following solution for the amount of moles CO ( $n_{CO}$ ) in the bubble as function of  $n'_{O_2}$ :

$$n_{CO} = -\frac{K'_{p,b} V_b}{4 R_g T} + \sqrt{\left( \frac{K'_{p,b} V_b}{4 R_g T} \right)^2 + \frac{K'_{p,b} V_b}{R_g T} n'_{O_2}} \quad (5.60)$$

The amount of CO<sub>2</sub> ( $n_{CO_2}$ ) can be calculated from equation (5.58). The change of  $n'_{O_2}$  is determined by equation (5.51). The pressure inside the bubble can then be calculated at every time step according to:

$$p_{b,tot} = (n_{CO} + n_{CO_2} + n_{b,0}) \frac{R_g T}{\frac{4}{3} \pi R_1^3} \quad (5.61)$$

with  $R_1$  the radius of the bubble at every time step calculated with equation (5.20).

### 5.2.9 Heating rate

In the calculation process, the temperature in the system is considered to be uniform through the sample at each time step. It is assumed that there is no temperature gradient in the diffusion domain (glass shell) and the bubble. The temperature-time dependency is described by an applied linear heating rate function. Introducing the heating rate  $h$  (K/s) until the final foaming temperature is reached, we can write:

$$T = \begin{cases} T_0 + ht & , t < t_{foam} \\ T_{foam} & , t \geq t_{foam} \end{cases} \quad (5.62)$$

where  $T_0$  is the initial temperature at which the calculation procedure starts and  $t_{foam}$  the time, when the final foaming temperature is reached.

So far, the physicochemical model equations, which describe the foaming process have been derived. The implementation of the derived equations into a computer simulation model is described in the next section.

## 5.3 Numerical solution of the model equations

The description of transport of physically dissolved oxygen and polyvalent ions in the glass by diffusion, combined with local thermodynamic equilibrium of the redox reactions and the moving fluid sphere, cannot be solved analytically. Even the simplified geometry of a spherical bubble introduces significant complexity in the diffusion equation. Therefore, a numerical method is used to solve the model equations. This section describes the numerical solution method for the set of all previously derived model equations and given boundary conditions.

Using the constant volume assumption of the glass shell, it is possible to simplify the mass transfer equation for each mobile species  $i$  (equation (5.23)). As already discussed, the growing bubble compresses the diffusion domain ( $R_2 - R_1$ ), which becomes thinner after each calculation step. This implies, that with the origin of the coordinate system at the center of the bubble, the location of the radii  $R_1$  and  $R_2$  changes during the calculation. This means for the calculation, that the domain in which the calculations are performed has to be re-meshed after each time step, which is mathematically very difficult. Applying a Lagrangian coordinate transformation, which is commonly used in aerodynamic problems [44], it is possible to transform the description of the moving system relative to a fixed axis system into an axis system moving with the glass shell. This significantly simplifies the numerical calculation. It eliminates the convection term of the diffusion equation<sup>7</sup>. To do this, the space and time variables  $r$  and  $t$  must be transformed into the new fixed coordinate system with a new spacial variable function  $\xi(r, t)$  and a new time variable  $\Theta$ , respectively. The general scheme of the coordinate transformation was taken from Anderson [44] and is given in the appendix in subsection 5.10.2 on page 187.

Furthermore, dimensionless groups are defined to simplify the equations for mass transport in the glass shell, the bubble growth, the mass balance at the glass-bubble interface and the heating rate. This is followed by the formulation of the final transformed model equations. For the numerically solving of the set of model equations, the computer program *Matlab*® was used, which provides a routine to solve partial differential equations. Because of the complexity of the model equations and the generality of the provided code, modifications to the code were necessary. The modifications to the code in order to obtain stable numerical solutions are given in the appendix in section 5.10.4 on page 195. Finally, the modified numerical routine was checked with a simple reduced case, for which a simple analytical solution exists. In this simple case, convection, thermodynamic redox equilibria and bubble growth were not considered. The numerically calculated concentration profiles are compared with the analytical solution.

The derivation and sources of the physical property data, e.g., the viscosity, the surface tension and the diffusion coefficients is not given in this section, but in the appendix to this chapter in subsection 5.10.3 on page 188. The governing model equations are as follows:

---

<sup>7</sup>second term of the right side of equation 5.23 on page 131

– the equation for the bubble growth:

$$\frac{dR_1}{dt} = \frac{\frac{3V_l}{4\pi} + R_1^3}{4\mu \frac{3V_l}{4\pi}} (\Delta p R_1 - 2\sigma) \quad \text{with} \quad \Delta p = p_b - p_{ref} \quad (5.20)$$

– the diffusion equation for the mass transport of species  $i$  in the glass:

$$\frac{\partial c_i}{\partial t} = \frac{D_i}{r^2} \frac{\partial}{\partial r} \left[ r^2 \frac{\partial c_i}{\partial r} \right] - \frac{R_1^2}{r^2} \frac{dR}{dt} \frac{\partial c_i}{\partial r} + \Psi_i \quad (5.23)$$

– the equation for the total oxygen mass transfer at the glass-bubble interface:

$$\frac{\partial n_{O_2}}{\partial t} = 4\pi R_1^2 \sum_i D_{ox,i} w_{i,ox} \frac{\partial c_{ox,i}}{\partial r} \bigg|_{r=R_1} \quad (5.51)$$

– the equation for the heating rate:

$$T = \begin{cases} T_0 + ht & , t < t_{foam} \\ T_{foam} & , t \geq t_{foam} \end{cases} \quad (5.62)$$

The following subsections will show the non-dimensionalization and the transformation of the equations in order to derive computable sets of equations for mass transport in the diffusion domain (glass melt) and for the bubble growth.

### 5.3.1 Spatial variable in diffusion domain

The radii  $R_1$  and  $R_2$  are time dependent radii ( $R_1(t)$ ,  $R_2(t)$ ). For simplicity we write  $R_1$  and  $R_2$ . Based on our assumption of spherical symmetry of the bubble and the domain in which we want to solve the equations, we can make use of a Lagrangian coordinate transformation. Including the non dimensionalization, based on the constant the shell volume [5],  $\xi$  is defined according to :

$$\xi = \frac{r^3 - R_1^3}{(R_2^3 - R_1^3)}, \quad R_1 \leq r \leq R_2 \quad (5.63)$$

The volume of the glass shell is:

$$V_l = \frac{4}{3}\pi(R_2^3 - R_1^3) = \text{constant} \quad (5.64)$$

we further define:

$$\beta = (R_2^3 - R_1^3) = \text{constant} \quad (5.65)$$

### 5.3.2 Dimensionless groups

The introduction of dimensionless variables simplifies the formulation of the model equations. It must be noted that the diffusion coefficient, the surface tension and the viscosity are temperature and thus time dependent material properties. In order to use them in



dimensionless groups, they are generally written in a form with a temperature dependent factor, such as:

$$Z(T) = Z_0 \cdot \epsilon(T^*) \quad (5.66)$$

where  $Z_0$  is the property value at  $t = 0$  and  $\epsilon(T^*)$  depends on the dimensionless temperature. The specific functions  $\epsilon(T^*)$  are derived in the appendix in subsection 5.10.3 on page 188. Dimensionless groups are introduced for time, temperature, viscosity, surface tension and molar flux:

#### – Time

For the dimensionless time parameter, we use the inter-diffusion coefficient of  $\text{Fe}^{3+}$  respectively at  $t = 0$  as reference, denoted with the subscript *ref* ( $D_{\text{Fe}^{3+},0} = D_{\text{ref}}$ ) to define the dimensionless time  $\Theta$ . For the dimensionless time, we write:

$$\Theta = \frac{D_{\text{ref}} \cdot t}{\beta^{\frac{2}{3}}} \quad (5.67)$$

#### – Temperature

The dimensionless temperature is defined as:

$$T^* = \frac{ht + T_0}{T_0} \quad (5.68)$$

with  $T_0$  the temperature at  $t = 0$ .

#### – Bubble radius

Using the constant volume parameter  $\beta$ , as defined in equation (5.65), we define the dimensionless bubble radius  $\zeta$  as follows:

$$\zeta = \frac{R_1}{\beta^{\frac{1}{3}}} \quad (5.69)$$

#### – Viscosity and surface tension

The following two dimensionless numbers in which the glass viscosity and the glass surface tension included, are defined as follows:

The term  $\Delta p$  is a pressure difference between the pressure in the bubble and the reference pressure (see equation (5.20)). We define:

$$\eta = \frac{\Delta p \beta^{\frac{2}{3}}}{\mu_0 D_{\text{ref}}} \quad (5.70)$$

where  $\mu_0$  is the glass viscosity at  $t = 0$ . Furthermore, we define

$$\phi = \frac{\sigma_0 \beta^{\frac{1}{3}}}{\mu_0 D_{\text{ref}}} \quad (5.71)$$

where  $\sigma_0$  is the surface tension of the glass at  $t = 0$ .

### – Molar flux

The amount of extra moles (production of gas molecules) in the bubble relative to the amount of moles oxygen (chemical and physical) dissolved in the glass shell at  $t = 0$ , gives the following dimensionless expression:

$$n^* = \frac{n - n_0}{\frac{4}{3}\pi\beta c_{tot}} \quad (5.72)$$

with:

$$c_{tot} = \sum_i w_{i,ox} c_{i,ox} \Big|_{t=0} \quad (5.73)$$

and  $n_0$  the amount of moles of gas molecules in the bubble at  $t = 0$ . The index  $ox$  denotes the moles of chemically dissolved oxygen (available from the oxidized form of the polyvalent species  $i$ ) plus physically dissolved oxygen (see equation (5.51)).

## 5.3.3 Formulation of transformed equations

### – Equation for bubble growth

The parameter  $\beta$  as defined in equation (5.65) is proportional to the volume of the glass and is used together with equation (5.69) for the non-dimensionalization of the equation for the bubble growth. In dimensionless form we get for equation (5.20):

$$\frac{d\zeta}{d\Theta} = \frac{(1 + \zeta^3)}{4z(T^*)} (\eta\zeta - 2\phi f(T^*)) \quad (5.74)$$

with  $z(T^*)$  and  $f(T^*)$  the temperature dependency of the viscosity and the surface tension, respectively, as derived in subsection 5.10.3.

### – Diffusion equation

Combined with equation (5.74), the diffusion equation<sup>8</sup> (5.23) becomes:

$$\frac{\partial c_i}{\partial \Theta} = \frac{9}{z(T^*)^{d_i}} \frac{D_i}{D_{ref}} \frac{\partial}{\partial \xi} \left[ \left( \xi + \zeta^3 \right)^{\frac{4}{3}} \frac{\partial c_i}{\partial \xi} \right] + \Psi_i \frac{\beta^{\frac{2}{3}}}{D_{ref}} \quad (5.75)$$

with  $z(T^*)^{d_i}$  the temperature dependency of the diffusion coefficients and  $\Psi_i$  given by equation (5.50). For the derivation of  $z(T^*)^{d_i}$  reference is made to the appendix, section 5.10.3 on page 191.

### – Mass balance for oxygen at glass-bubble interface

$$\frac{\partial n^*}{\partial \Theta} = \frac{9\zeta^4}{c_{tot} D_{ref}} \sum_i w_{i,ox} D_{i,ox} z(T^*)^{-d_{i,ox}} \frac{\partial c_{i,ox}}{\partial \xi} \Big|_{\xi=0} \quad (5.76)$$

---

<sup>8</sup>The mathematical procedure (differentiation rules), which has been used to transform the coordinate system and to derive the transformed equations is given in the appendix, subsection 5.10.2 on page 187.

– Equation for heating rate

$$\frac{\partial T^*}{\partial \Theta} = \frac{h\beta^{\frac{2}{3}}}{T_0 D_{ref}} \quad (5.77)$$

In order to check the correct programming of the equations and the modifications to the *Matlab*<sup>®</sup> solving scheme<sup>9</sup>, especially the ones to the discretization scheme, a simple analytical solution was derived, which is compared to the result of the developed model. This comparison is shown and discussed in the next subsection.

### 5.3.4 Analytical solution

Approximate solutions for the bubble growth under certain conditions are published by several authors [6, 7]. However, the shrinking of the glass shell thickness, non-isothermal diffusion and the influence of redox reactions on the diffusion profiles cannot be accurately calculated with an analytical solution, but needs numerical solving techniques. This was described in the previous subsection. However, the correctness and accuracy of the numerical solution (discretization) and the modifications to the code can be partially checked with an analytical solution, when simplifying equation (5.75) to a special reduced case.

Considering an isothermal case and neglecting the influence of terms taking thermodynamic equilibrium into account, and also neglecting the bubble growth or shrinking of the glass shell respectively, the model equation

$$\frac{\partial c_i}{\partial t} = \frac{D_i}{r^2} \frac{\partial}{\partial r} \left[ r^2 \frac{\partial c_i}{\partial r} \right] - \frac{R_1^2}{r^2} \frac{dR}{dt} \frac{\partial c_i}{\partial r} + \Psi_i \quad (5.23)$$

reduces to a simple diffusion equation in spherical coordinates, by neglecting the last two terms on the right side of equation (5.23). Assuming further a large bubble radius (1 m) and a thin shell thickness (10  $\mu$ m), the glass shell in the numerical model equation for the concentration profile approaches the shape of a plane sheet, for which a simple analytical solution is available. The diffusion equation for slab coordinates and for a single diffusing species only, for which an analytical solution exists is:

$$\frac{\partial c}{\partial t} = D \frac{\partial^2 c}{\partial x^2} \quad (5.78)$$

with the following initial and boundary conditions:

$$c = c_0, \quad \text{at} \quad t = 0 \quad (5.79)$$

$$\frac{\partial c}{\partial x} = 0, \quad \text{at} \quad x = 1 \quad (5.80)$$

$$c = 0, \quad \text{at} \quad x = 0 \quad (5.81)$$

---

<sup>9</sup>The numerical implementation of the transformed equations into the computer program *Matlab*<sup>®</sup> to solve the set of equations is described in more detail in the appendix, section 5.10.4 on page 195.

It should be noted, that the analytical solution at the left boundary ( $x = 0$ ) requires a concentration of the diffusing species of 0 at  $t > 0$ . This is realized in the numerical code by choosing a very large mass transfer coefficient (seen equation (5.29)) for the oxygen from the glass towards the bubble, so that  $c_i(x = 0) = 0$  for ( $t > 0$ ), leading to a very steep concentration profile in the glass.

A simple analytical solution for this equation is given by Smith et al. [45]. They give an analytical solution for heat transfer which can be readily transformed because of the analogy to this mass transfer process. For short diffusion times, where the Fourier number  $Fo = Dt/x^2$  is much smaller than 0.1, the penetration theory can be applied. According to the analytical solution, the concentration for short times can be calculated with:

$$\frac{c}{c_0} = \operatorname{erf}\left(\frac{x}{2\sqrt{Dt}}\right) \quad (5.82)$$

where erf is the error function. For longer times (Fourier number  $\gg 0.1$ ) another solution is obtained.

$$\frac{c}{c_0} = \exp\left(-\frac{\pi^2 Dt}{4d^2}\right) \cos\left(\frac{\pi x}{2d}\right) \quad (5.83)$$

where  $d$  is the thickness of the glass shell and  $x$  the spatial grid.

The result of the comparison of the analytical solution using equations (5.82) and (5.83) and the numerical solution using the dimensionless equation for one diffusing species only ( $\text{Fe}_2\text{O}_3$ ) is given in figure (5.8). The comparison shows, that the concentration profile, calculated with the numerical model is in very good agreement with the analytical solution.

The comparison of the numerical and analytical solution of the presented reduced case showed, that the model gives accurate results for the calculation of the concentration profiles for this reduced example case. However, to show the usefulness of the numerical model to predict the bubble growth for the complex condition of a foaming mixture of powdered glass and foaming agent, the model must be verified experimentally. The experimental validation of the numerical model is shown and discussed in the next section.

## 5.4 Experimental validation of the simulation model for foam glass

The applicability and reliability or validity range of the simulation model to predict bubble growth in foam glass, is investigated experimentally. This section presents first, experimental techniques to determine the required input parameters for the simulation model and then results of foaming experiments and finally the comparison of the experimental and simulation results. The first subsection presents both, the experimental and theoretical approach, to determine the input parameters for the model. The second subsection describes the experimental setup for the foaming experiments and the data analysis techniques to extract quantitative values for the bubble expansion rate from experimental

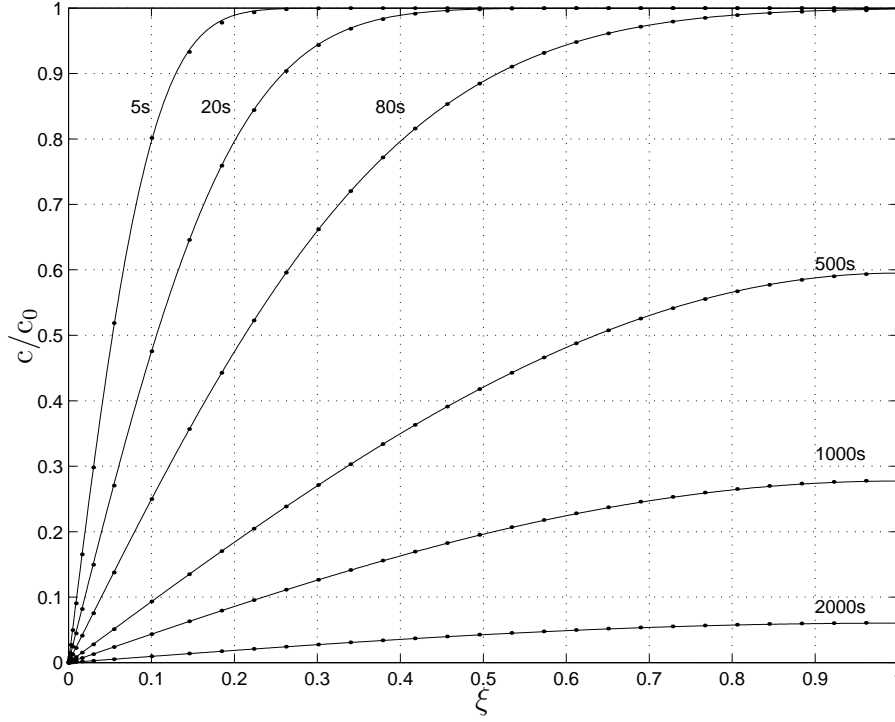


Figure 5.8: Concentration profiles for  $\text{Fe}_2\text{O}_3$  ( $c_{\text{Fe}_2\text{O}_3}/c_{\text{Fe}_2\text{O}_3}^0$ ), comparison of analytical and numerical solutions at different times. — = analytical solution, • = numerical solution.

data. In the last subsection, the experimental and modeled results are compared and discussed.

#### 5.4.1 Determination of model input parameters

The model input parameters, which are required for performing the model simulation of bubble growth in a foaming glass melt are:

- The physicochemical glass properties, e.g. glass viscosity, surface tension and density to be calculated from the glass composition (see section 5.10.3 on page 188).
- The initial concentration of the diffusing species in the glass ( $\text{Fe}_2\text{O}_3$ ,  $\text{FeO}$  and  $\text{O}_2$ ).
- Values for the reaction enthalpy and -entropy for the redox reactions of the polyvalent ions in the glass.
- The initial average bubble size in the just sintered carbon-glass powder.
- The initial thickness of the foam glass shell.
- The initial amount of foam bubbles per unit foam volume ( $N_V$ ).
- The imposed heating rate of the experiment.

Table 5.2: Glass composition of the two glasses used for the foaming experiments. The composition was measured by X-ray fluorescence analysis (XRF).

Glass	SiO <sub>2</sub> (wt.%)	CaO (wt.%)	Na <sub>2</sub> O (wt.%)	Al <sub>2</sub> O <sub>3</sub> (wt.%)	MgO (wt.%)	Fe <sub>2</sub> O <sub>3</sub> <sup>(a)</sup> (wt.%)
Foam, no C	69.48	5.5	13.26	5.68	3.06	2.99
Foam, 0.2 wt.% C	69.08	5.73	13.25	5.73	3.0	3.18

<sup>(a)</sup> Total iron concentration expressed as wt.% Fe<sub>2</sub>O<sub>3</sub>

The inter-diffusion coefficients of the polyvalent ion in the glass were taken from literature references, as described in the appendix, section 5.10.3. For the experiments on glass foaming (model validation), two different glasses with the same bulk composition, with only iron as polyvalent ion, but a difference in oxidation state were molten from reagent grade chemicals. This means that only the diffusion of iron as polyvalent ion was considered. The reaction at the glass-bubble interface is:



In the bubble (with carbon particles), the concentrations of CO and CO<sub>2</sub> will change according to the Boudouard reaction as shown in reaction (R34) assuming  $a_c = 1$  at all times. It is furthermore assumed, that the reaction reaches instantaneous equilibrium, meaning that there is no mass transfer or reaction kinetic limitation neither at the interface nor inside the bubble. This results in a purely glass phase diffusion rate limited process.

In order to determine the above mentioned glass properties (composition, concentration of diffusing species and thermodynamic properties), several measurements have been performed, which are presented in the following.

### Glass preparation and analysis

For the preparation of the glasses, used for the foaming experiments, 600 g of glass batch were molten for each type of glass in a silica crucible. The difference of the oxidation state of the glass was achieved by adding 0.2 wt.% of active carbon to the second glass batch. The partial oxygen pressure was measured during cooling of the prepared melt between 1623 and 1373 K using an electrochemical sensor (RAPIDOX®). For the applicability, measurement technique and the interpretation of the sensor signal to characterize the oxidation state of the melt, reference is made to [46, 47]. The results of the measured oxygen activities or partial oxygen pressures in the melt are given in figure 5.32 in the appendix on page 197. After melting of the glass, it was annealed and samples were prepared for chemical (X-ray fluorescence (XRF)) and IR-spectrophotometric analysis. From the composition of the oxides in the glass it is possible to estimate the glass properties required for the model study, e.g., glass viscosity, surface tension and density. The results of the chemical analysis are given in table 5.2. The concentration of iron oxide in the Fe<sup>2+</sup> state was determined by IR-spectrophotometric measurement of the transmission spectrum as described in chapter 4, section 4.3.3 on page 105. The measured transmission

Table 5.3: Ferrous and ferric iron concentration of the glasses used for the foaming experiments and the values of the enthalpy and entropy differences,  $\Delta H^{*r}$  and  $\Delta S^{*r}$  for reaction (R30). The ferrous iron concentration was determined by IR-spectrophotometry as described in chapter 4, section 4.3.3 on page 105.

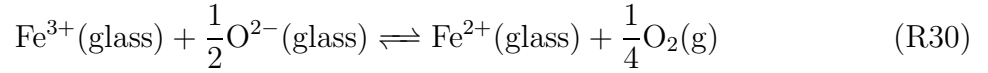
Glass	Fe <sup>3+</sup> (a) (wt.%)	Fe <sup>2+</sup> (b) (wt.%)	$\Delta H^{*r}$ (kJ · mol <sup>-1</sup> )	$\Delta S^{*r}$ (J · mol <sup>-1</sup> · K <sup>-1</sup> )
Foam, no C	2.73	0.26	138.9	63.8
Foam, 0.2 wt.% C	2.15	1.03		

(a) wt.% of total Fe<sub>2</sub>O<sub>3</sub> in the Fe<sup>3+</sup> form

(b) wt.% of total Fe<sub>2</sub>O<sub>3</sub> in the Fe<sup>2+</sup> form

as a function of the wavelength of the two glasses is given in figure 5.33 on page 198 of the appendix. With the known concentration of Fe<sup>2+</sup>, the concentration of Fe<sup>3+</sup> can be calculated according to equation (5.44).

With the known partial oxygen pressure in the glass and the concentration of the ferrous and ferric iron (assuming no redox reactions during cooling), the thermodynamic values for  $\Delta H^{*r}$  and  $\Delta S^{*r}$  for reaction



with

$$K^* = K' \frac{\gamma_{M_i^{m_i+}}}{\gamma_{M_i^{b_i+}}} = \frac{[M_i^{m_i+}]}{[M_i^{b_i+}]} p_{\text{O}_2}^{w_i} \quad (5.34)$$

can be calculated according to equation (5.124), by plotting  $\frac{1}{4} \ln p_{\text{O}_2} + \ln \frac{[\text{Fe}^{2+}]}{[\text{Fe}^{3+}]}$  against  $\frac{1}{T}$  and deriving the values of the slope and the intercept of the linear regression fit.

$$\frac{1}{4} \ln p_{\text{O}_2} + \ln \frac{[\text{Fe}^{2+}]}{[\text{Fe}^{3+}]} = \frac{-\Delta H^*}{R_g} \frac{1}{T} + \frac{\Delta S^*}{R_g} \quad (5.124)$$

The derivation of equation (5.124) and the conditions under which equation (5.124) can be used are given in the appendix in section 5.10.5 on page 197. The measured concentration of the ferric and ferrous iron and the determined values for  $\Delta H^{*r}$  and  $\Delta S^{*r}$  are given in table 5.3. It should be noted that the values for  $\Delta H^{*r}$  and  $\Delta S^{*r}$  are based on the measured concentrations of the polyvalent ions in the glass and not on their chemical activity as strictly demanded by thermodynamics. This restricts its use to this glass composition only.

Finally, after the different measurements, the glass from the melting experiment was milled to a powder with a grain size smaller than 63  $\mu\text{m}$  and mixed with 2 wt.% active carbon ( $d_{50} < 30 \mu\text{m}$ ) as foaming agent. This powder mix is the starting material for the foaming experiments. The sample preparation and the input data determination from the experiments is explained in the next subsection.

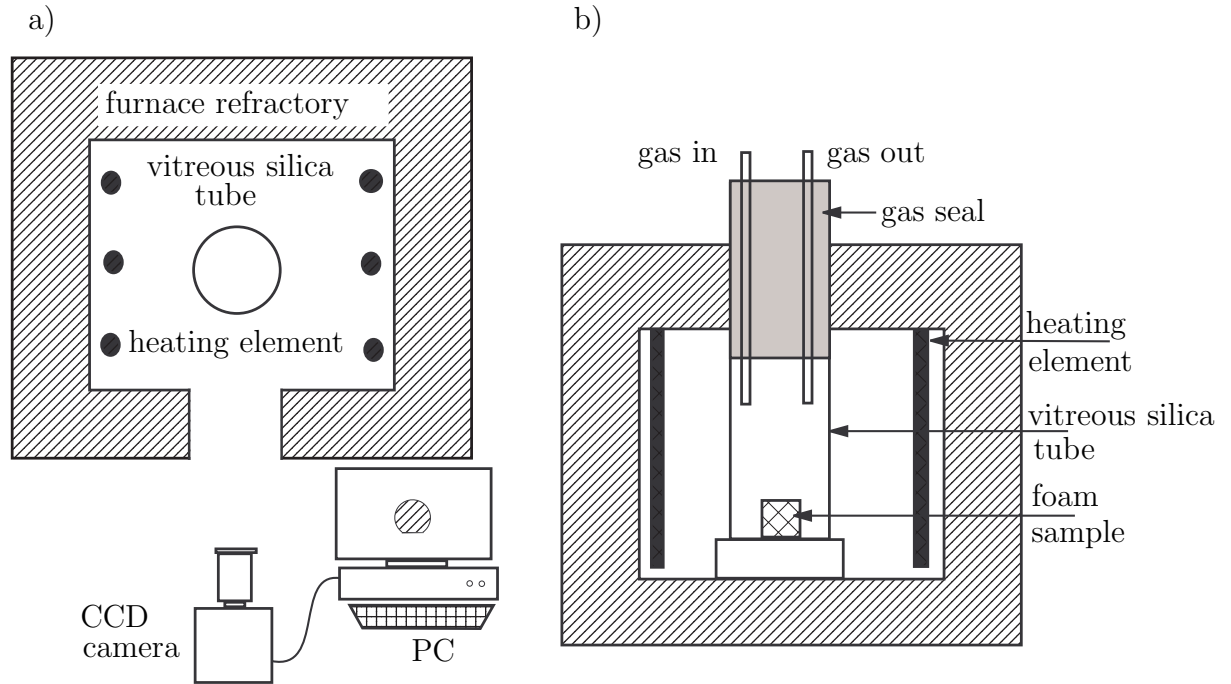


Figure 5.9: Schematics of setup for foaming experiments. a: top view and b: front view.

### Foaming experiments and input data determination

The foaming experiments have two objectives. The first one is the determination of some of the model input parameters, namely the initial amount of bubbles per unit Volume ( $N_V$ ), the initial average bubble size, or initial average bubble radius and the initial average thickness of the glass shell per bubble. The second objective is the validation of the model calculations as discussed in sections 5.2 and 5.3. The type of experiments for both objectives are the same, but the experiments to determine the input parameters were stopped after the sintering of the sample. At this stage, the glass particles have sintered together forming small gaseous inclusions, the starting point for the modeling. It should be noted that the modeling of either the sintering of the glass grains or of the initial bubble formation is outside the scope of this study.

The preparation of the samples was the same for both types of experimental objectives. Samples of 5 g of the glass-carbon powder mixture were pressed with a force of 30 kN to small cylinders with a diameter of 20 mm and a height of 10 mm. The samples were dried for 12 hours at 403 K and then inserted into a vertical vitreous silica tube, which was covered by an air tight lid with two tubes and flushed with a flow of 1.5 Nl/min nitrogen gas ( $N_2$ ) to avoid oxidation of the carbon by the atmosphere. A schematic view of the experimental setup is given in figure 5.9. From ambient temperature, the samples were heated to 923 K with a heating rate of  $10 \text{ K} \cdot \text{min}^{-1}$ . To determine the initial conditions, the samples were kept at 923 K for 30 minutes. Then the furnace was switched off and the samples were cooled down inside the tube. In order to determine the input parameters for



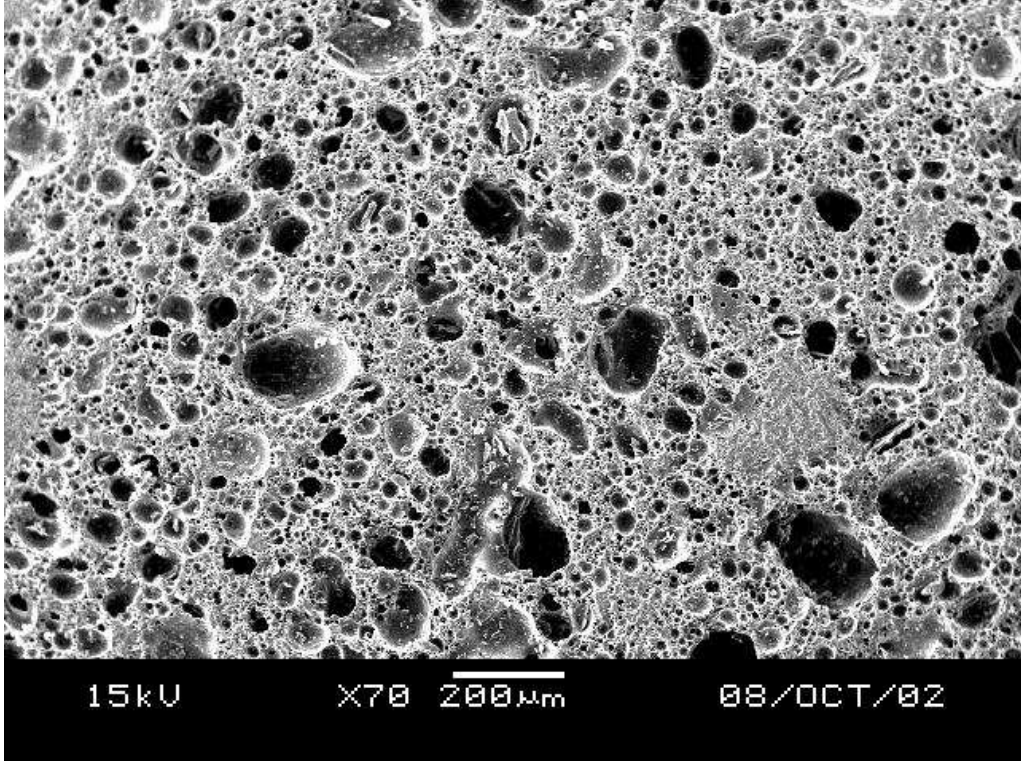


Figure 5.10: Picture of a glass and carbon powder sample after sintering and prior to the foaming process. The picture was taken with a Jeol JSM-5600 electron microscope.

the model from these experiments, the samples were cut and cross sections of the sintered samples were digitally pictured with a Jeol JSM-5600 electron microscope. A picture of such a cross section is shown in figure 5.10.

Different techniques are available to determine the number of bubbles per unit volume,  $N_V$ , from 2-dimensional sample cross section pictures [48]. These techniques are based, e.g., on measuring the diameter or the area of the cutted spheres or the measurement of the penetration lengths of areas by straight lines (for non spherical shapes). The Schwartz-Saltykov method [49] is a very good method to determine the number of bubbles from 2-dimensional pictures. The method is based on the measurement of the diameters of cutted spheres (bubbles) in 2-dimensional pictures. As seen in figure 5.10, the bubbles are rather polyhedral than spherical. For polyhedral bubbles, Schwartz-Saltykov propose  $N_V$  to be calculated according to:

$$N_V = 0.744 \frac{N_A^2}{N_L} \quad (5.84)$$

where  $N_L$  is the average number of bubbles per unit length and  $N_A$  the number of bubbles per unit area. These two parameters were determined by digital picture analysis, which is explained in the appendix in section 5.10.6 on page 200. Next to the value for the number of bubbles per unit volume, the initial bubble radius must be known as input parameter for the bubble model. Generally, for the used model, the following equations

Table 5.4: Results of bubble dimensions analysis in the samples before foaming starts.  $N$  denotes the total amount of bubbles in the sample.

Glass	$N_L$ (mm <sup>-1</sup> )	$N_A$ (mm <sup>-2</sup> )	$N_V$ (mm <sup>-3</sup> )	$N$ (-)	$R_1$ (mm)	$R_2$ (mm)
Foam, no C <sup>(a)</sup>	12.62	154.9	1496	$4.13 \cdot 10^6$	$3.55 \cdot 10^{-2}$	$5.42 \cdot 10^{-2}$
Foam, 0.2 wt.% C	6.975	48.63	252.3	$1.07 \cdot 10^6$	$7.96 \cdot 10^{-2}$	$9.82 \cdot 10^{-2}$

<sup>(a)</sup> The picture of this sample is given in figure 5.11(a)

must hold [3]:

$$\left( \frac{V_{\text{gas}}}{V_{\text{glass}}} \right)^{\text{model}} = \left( \frac{V_{\text{gas}}}{V_{\text{glass}}} \right)^{\text{foam}} \quad (5.85)$$

and

$$V_{\text{gas}}^{\text{model}} = \frac{V_{\text{gas}}^{\text{foam}}}{N} \quad \text{with} \quad N = N_V V^{\text{foam}} \quad (5.86)$$

where  $N$  is the total amount of bubbles and  $V^{\text{foam}}$  the total volume of the experimental foam sample. The index "foam" denotes the real foam glass sample and the index "model" the unit cell of the model, thus the bubble with its glass shell.  $V_{\text{gas}}$  denotes the gas volume enclosed in the sample, thus the volume of vacancies between the glass grains and not the physically or chemically dissolved gas in the glass ( $V_{\text{tot}} = V_{\text{gas}} + V_{\text{glass}}$ ). The average bubble radius  $R_1$  and the shell thickness ( $R_2 - R_1$ ) can be calculated from equations (5.85) and (5.86) with known  $(V_{\text{gas}}/V_{\text{glass}})^{\text{foam}}$  and  $N_V$ . The results of these calculations are given in table 5.4.

## 5.4.2 Foaming experiments

Heating experiments with two different heating rates ( $2 \text{ K} \cdot \text{min}^{-1}$  and  $5 \text{ K} \cdot \text{min}^{-1}$ ) for each powder mixture of the two glass types were performed to validate the foam model. The heating period started at 923 K after the sintering period and ended at 1023 K where the samples were kept for one hour. The volume expansion was derived from digital pictures taken from the foam sample using a Philips LDH 0703130 CCD video camera, which was positioned at the front of the furnace. The schematic representation of the experimental setup is given in figure 5.9. Because the volume change of the sample during the sintering period is low, pictures were taken with a frequency of one picture per minute. During the heating period and the residence time at the maximum foaming temperature, a frequency of one picture per five seconds was chosen.

Four representative pictures, representing the different stages of the foaming, are given in figure 5.11. Figure 5.11(a) shows the initial pressed cylinder at ambient temperature. Prior to the experiment, the dimensions of the pressed cylinder (diameter and height) were measured to be able to translate pixel dimensions to metric units. Figure 5.11(b) shows the foam body after the sintering stage at 923 K for 30 minutes. As expected, the sample has contracted/densified [50]. Figure 5.11(c) shows the foam body after the

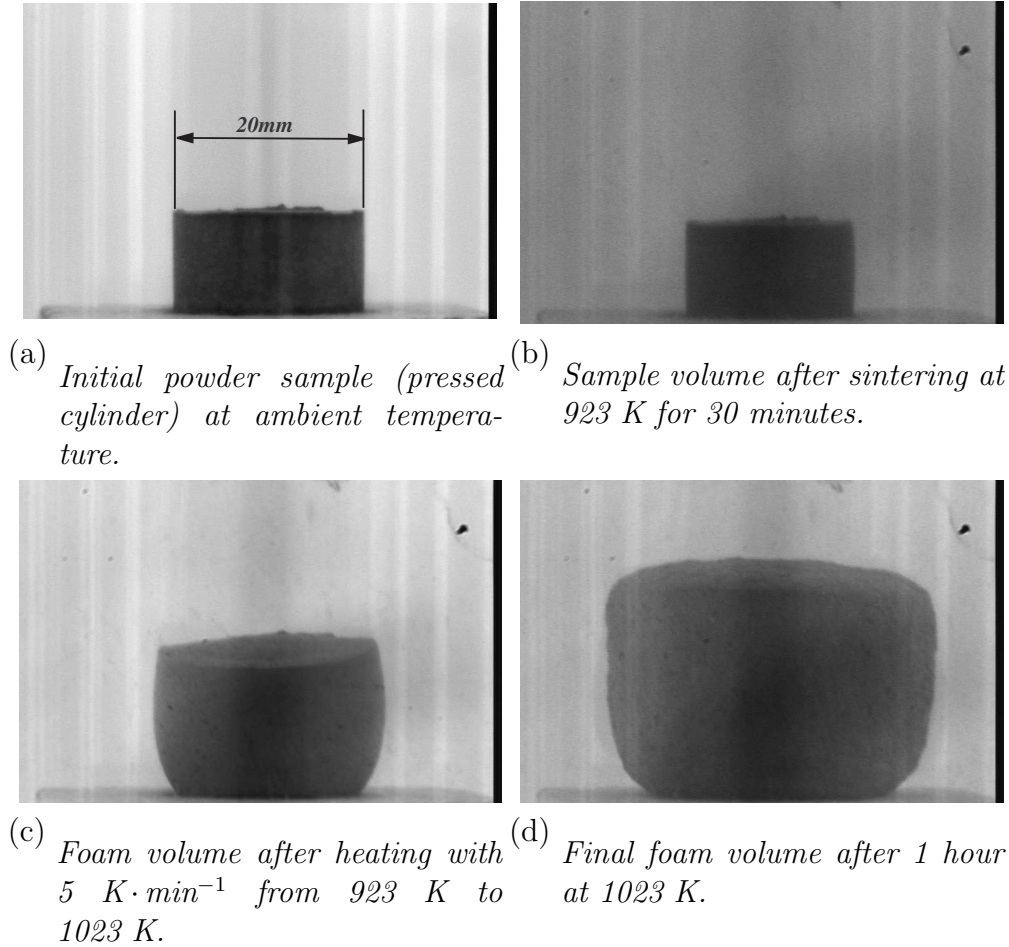


Figure 5.11: Different stages of foam expansion of the most oxidized glass mixed with 2 wt.% carbon powder. The scale as indicated in picture 5.11(a), is the same for all pictures.

heating period from 923 K with a rate of  $5 \text{ K} \cdot \text{min}^{-1}$  to the actual foaming temperature of 1023 K. The foam body has already gained volume compared to the initial volume. The final volume of the sample is reached during the residence time at the maximum temperature. The final foam body from which a picture was taken is shown in figure 5.11(d).

To determine the volume expansion from the different pictures, the pictures were digitally analyzed. The picture analysis method to extract the volume expansion data from the pictures is given in the appendix in section 5.10.6 on page 200. The results of the volume expansion experiments as a function of time are given in figures 5.12 and 5.13. Both figures show the absolute foam volume as a function of time and temperature. Figure 5.12 shows the results for two heating rates, using the most oxidized glass (no carbon added to the glass forming raw material batch) and figure 5.13 the results for the more reduced glass. The volumes of the foam samples of the four glasses do not change in the first 45 minutes heating ( $10 \text{ K} \cdot \text{min}^{-1}$ ), which is from room temperature to  $\pm 833 \text{ K}$ . One exception is the reduced glass with the lower heating rate after sintering, where the volume contraction starts 3 minutes earlier than for the other experiments. After this

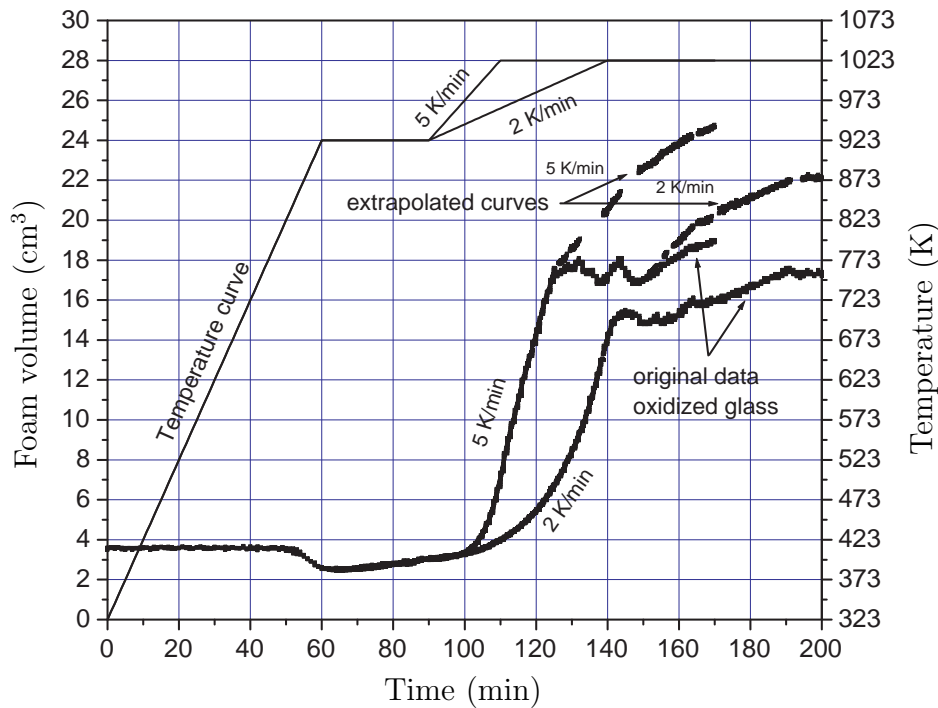


Figure 5.12: Foam expansion of original and extrapolated curves of the oxidized glass with two different heating rates as a function of the time.

time, the volume contraction or sintering starts and reaches a minimum volume at 923 K, the beginning of the isothermal sinter period of 30 minutes. It can be seen that the volume contraction during sintering is about 28 vol.% of the initial volume. During the isothermal sinter period at 923 K, the volume increases steadily, but with different slopes depending on the type of glass. The more reduced glass shows a steeper expansion during the sintering period, than the oxidized glass. After sintering, the volume of the foam body of the reduced glasses is about 30 vol.% larger and for the oxidized glasses 15 vol.% lower, compared to the initial volume of the sample. After the sintering period, the glasses were heated with two different heating rates ( $2 \text{ K} \cdot \text{min}^{-1}$  and  $5 \text{ K} \cdot \text{min}^{-1}$ ). The graphs show abrupt changes in foam volume during the final growth stages. The glasses heated with  $5 \text{ K} \cdot \text{min}^{-1}$ , show this abrupt change after 124 minutes of the experimental duration, or 14 minutes after the maximum foaming temperature is reached. The glasses heated with  $2 \text{ K} \cdot \text{min}^{-1}$ , show this abrupt change in volume after 138 minutes of the experimental duration for the reduced glass and 141 minutes for the oxidized glass. This is approximately the time at which the lower heating rate ends (after 140 minutes). After the glasses show this abrupt change in volume, the foam volume shows fluctuations during the residence time at 1023 K until the experiment was stopped.

Comparison of the two glass types shows differences in volume expansion during the sintering period. This could be attributed to two effects. One is the difference in viscosity of the two glasses. As seen in figure 5.29 on page 190, the measured viscosity of the reduced glass is slightly lower as the one of the oxidized glass. This implies that the

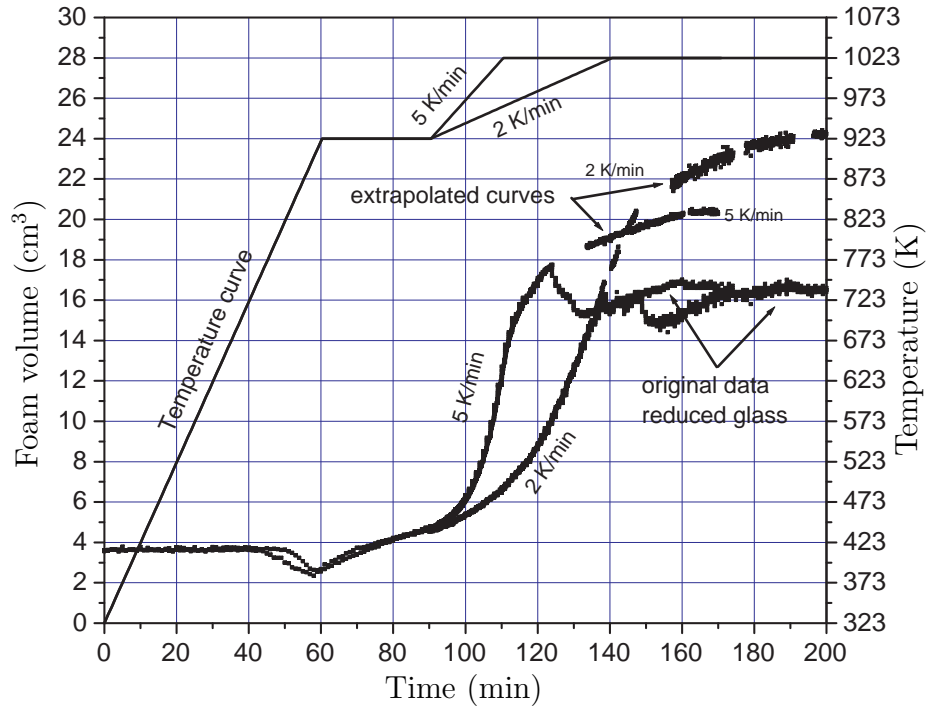


Figure 5.13: Foam expansion of original and extrapolated curves of the reduced glass (1 wt.% of carbon added to the glass batch) with two different heating rates as a function of the time.

glass grains of the reduced glass sinter together more easily and forming the closed bubble system earlier. At lower viscosities, the diffusion coefficient is higher, which also increases the bubble growth. The second effect can be the smaller bubbles. As seen in table 5.4, the reduced glass has more and smaller bubbles, which also increases the growth of the bubbles, because smaller bubbles grow faster than larger bubbles, which will be discussed later in this chapter.

The abrupt change of the volume expansion observed for all four experiments after reaching the final foaming temperature, can be explained by foaming gas loss at the outer boundary of the foam body. In addition to that, it was also observed during the maximum foaming temperature, that the samples have a relatively rough surface. This is probably caused by bubbles which have broken open at the outer surface of the foam body. By this, the foam body lost foaming gas. This behavior is not included in the model. Furthermore, observations during the experiment after reaching the maximum foaming temperature showed deformation of the foam sample, different from the foam expansion observed during heating. The foaming gas loss has a significant influence on the maximum foam height. This implies that the final volume of the foam body will not be reached compared to the modeled one, because in the model it was assumed that no gas is lost at the boundaries and all gas is used for bubble expansion. Because of the abrupt change in foam volume due to gas loss and consequently change in bubble growth rate, a comparison of the experiments with modeled results appears to be hardly

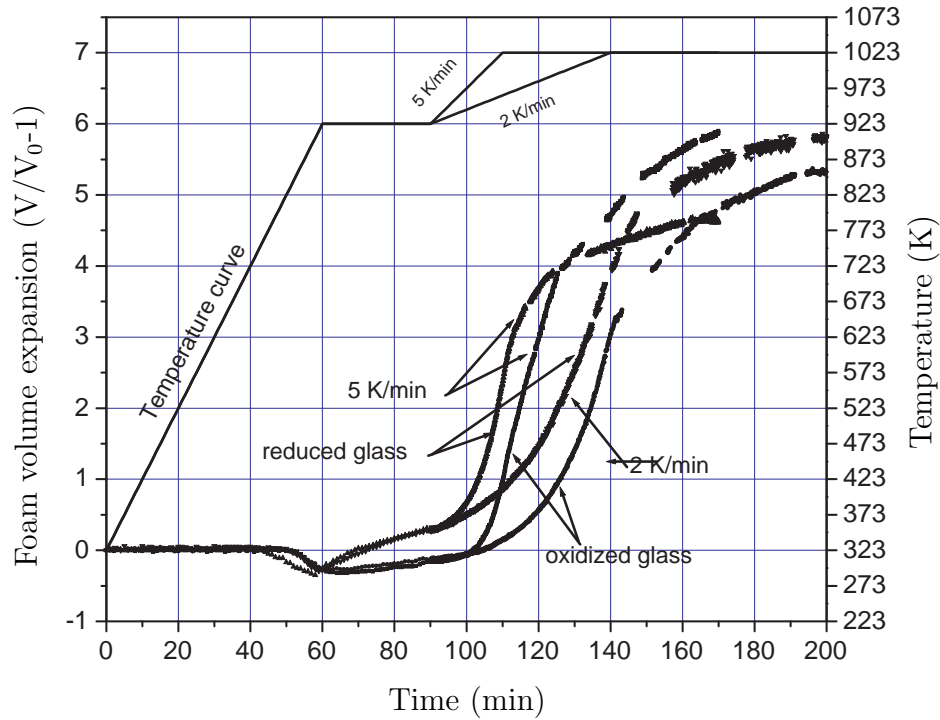


Figure 5.14: Relative foam expansion of the extrapolated curves as a function of time ( $V_0 = V(t=0)$ ).

possible. Comparing experimental and modeled results of the effect of oxidation state and heating rate on foam evolution is therefore difficult. An adaption to the experimental graphs, as given in figures 5.12 and 5.13, has been performed. This adaption tries to describe a probable volume expansion in the case that the abrupt changes did not occur. To extrapolate the volume expansion for the time that the foam volume did not expand, the original experimental curve was linearly extrapolated. The slope of the extrapolated curve was calculated to be the average between the slope before and after the volume loss. This was done for every time that the volume expansion stopped and the volume decreased. The result of the adaption and the comparison of the four different experiments is given in figure 5.14. The figure shows the relative foam expansion  $((V \cdot V_0^{-1}) - 1)$ , with  $V_0 = V(t_{\text{calc}} = 0)$  as a function of time. Comparing the curves of the two heating rates of one type of glass, it is expected, that the final foam volume that will be achieved is equal for both heating rates, because the same amount of foaming gas is available. Figure 5.14 shows, that this is clearly not the case, which means, that the loss of foaming gas during the experiment is probably more significant, than expected.

The comparison of the experimentally determined and calculated foam expansion during heating of the foam sample, after sintering, is presented in the next subsection.

### 5.4.3 Comparison of experimental and modeled glass foam volume expansion

Figures 5.15 and 5.16 show both results of the experimental (including correction for gas loss) and modeled volume expansion during heating of the pressed cylinder of the glass-carbon mixture after sintering. The graphs show the relative foam expansion as a function of time for both heating rates for the reduced molten glass (figure 5.15) and the oxidized molten glass (figure 5.16). It can be seen from the two figures, that there is a strong disagreement between the experimental and modeled results, with respect to the foam volume. As observed from the figures, in the beginning of the foaming process (0-10 minutes), the simulation slightly underestimates the real volume expansion whereas later, during the isothermal foaming, the volume expansion is strongly overestimated by the model. The different possible causes, that could explain the disagreement between the experimental and calculated foam expansion rates are discussed in the following.

Foaming gas loss through open pores during sintering is one possible cause for gas loss during the experiments. In the model it is assumed, that physically ( $O_2$ ) and chemically dissolved ( $Fe_2O_3$ ) in the glass finally react completely with the carbon to either CO or  $CO_2$ . One cause of possible foaming gas loss is the gas forming reactions before and during the sinter period. There, the glass already reacts with the carbon, but not all pores are yet transformed to closed bubbles. Foaming gas can thus leave the sample through the open pores and is not available for the expansion of the bubbles. Another indication of foaming gas loss, as seen in figures 5.12 and 5.13 and described in the previous section, is the abrupt volume decrease during foaming. This starts after the heating period has ended. This is after 20 minutes for the glasses with 5 K/min heating rate and 50 minutes for the glasses with 2 K/min. From then on, the deviations between the experimental and the modeled bubble growth rates increase. The amount of foaming gas loss before and during the sinter period and during the described abrupt volume changes was not determined, therefore a reliable quantitative estimation of gas loss that did not lead to foam expansion could not be performed. Of course, collapse of bubbles at the surface of the foam during the foaming process leads to gas loss from the glass mass. This gas loss also contributes to the mismatch between modeled (not taking gas loss into account) and foam volumes observed during the experiment.

In the initial stages of foaming, the modeled volume expansion slightly underestimates the experimental foam expansion and afterwards it overestimates the observed foam volume. As can be observed in figure 5.14, the volume of the samples slightly increases during the sinter period. The considered cell (bubble plus its shell) is already in motion and expanding when the sinter period ends and the temperature starts to increase. At this time, the model starts without any motion and ambient pressure inside the bubble to start the expansion in the model must first be built up. This might be an explanation of the retarded expansion of the modeled bubble expansion compared to the one observed from the experiment. The initial foaming regime is plotted separately in figures 5.17 and 5.18.

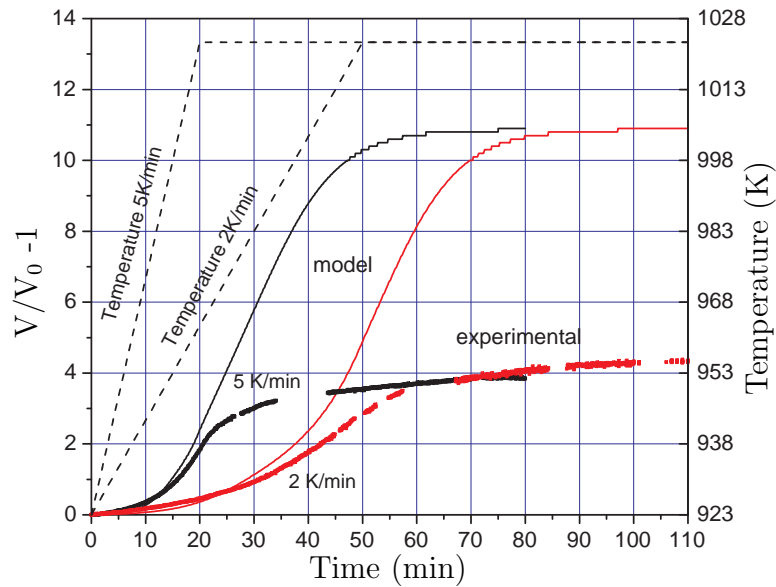


Figure 5.15: Relative foam volume expansion of the glass-carbon powder mixture as a function of time observed from the experiments (corrected for gas loss) and from model calculations for the reduced molten glass after sintering.  $V_0 = V(t_{calc} = 0)$ .

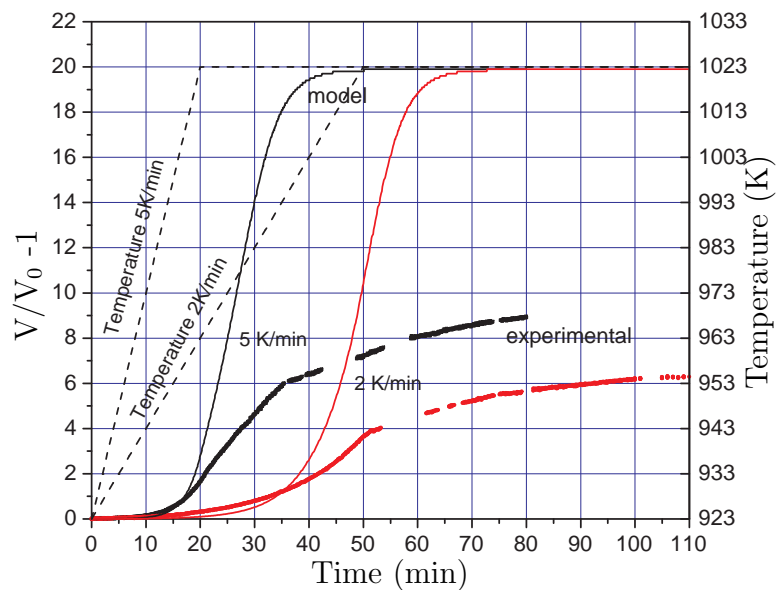


Figure 5.16: Relative foam volume expansion of the glass-carbon powder mixture as a function of time observed from the experiments (corrected for gas loss) and from model calculations for the oxidized molten glass after sintering.  $V_0 = V(t_{calc} = 0)$ .



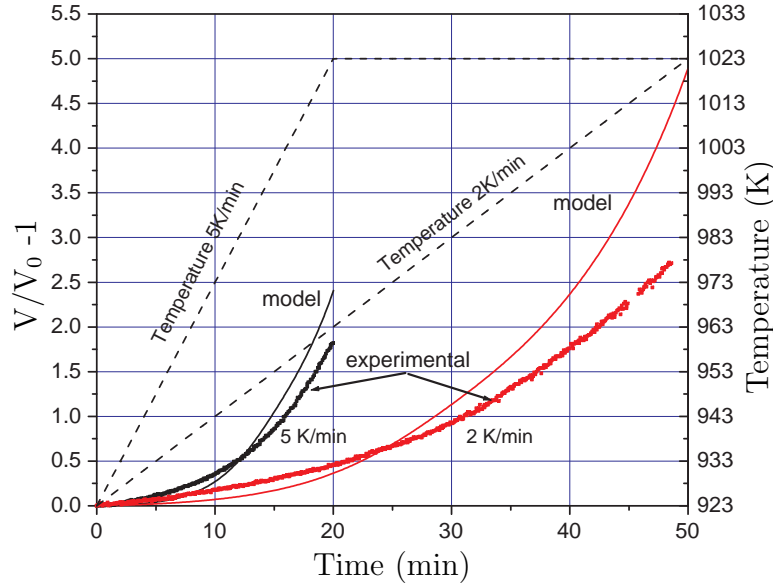


Figure 5.17: Initial stages of relative foam volume expansion of the glass-carbon powder mixture as a function of time observed from the experiments (corrected for gas loss) and from model calculations for the reduced molten glass after sintering.  $V_0 = V(t_{calc} = 0)$ .

The different parameters influencing the volume expansion, the glass composition, the oxidation state and the glass viscosity, have been determined relatively accurate. However, there are two other parameters, that will have a strong influence on the foam expansion rate. These are:

- the diffusion coefficients of  $\text{Fe}_2\text{O}_3$  and  $\text{FeO}$  (this will not influence the final foam height);
- the initial bubble radius and the initial shell thickness.

The inter-diffusion coefficient for  $\text{Fe}^{3+}$  or  $\text{Fe}_2\text{O}_3$  has been estimated from a Stokes plot, as given in section 5.10.3 to be:

$$\log D_{\text{Fe}^{3+}}(T) = (-0.71 \pm 0.04) \log \mu(T) - (9.3 \pm 0.2) \quad (5.116)$$

The error range of  $\pm 0.04$  on the slope and  $\pm 0.2$  on the intercept, on a logarithmic scale shows, that this inaccuracy will have an influence on the modeled expansion rate of the foam. Furthermore, referring to figure 5.10, the initial bubbles have large differences in size. The initial bubble size and the thickness of the shell around the bubble influence the volume expansion rate of the bubble. The influence of initial bubble size and shell thickness on bubble growth rate is complex and will be discussed in more detail in the parameter study, section 5.5 on page 166. The influence of the diffusion coefficient on the volume expansion is demonstrated in figure 5.19. Figure 5.19 shows that using a smaller diffusion coefficient (case 2 versus case 1), the modeled volume expansion approaches the experimental curve after  $\pm 12$  minutes. As can be seen from the figure, the very initial growth rate (0-10 minutes) is hardly influenced by variations in diffusion coefficient. It

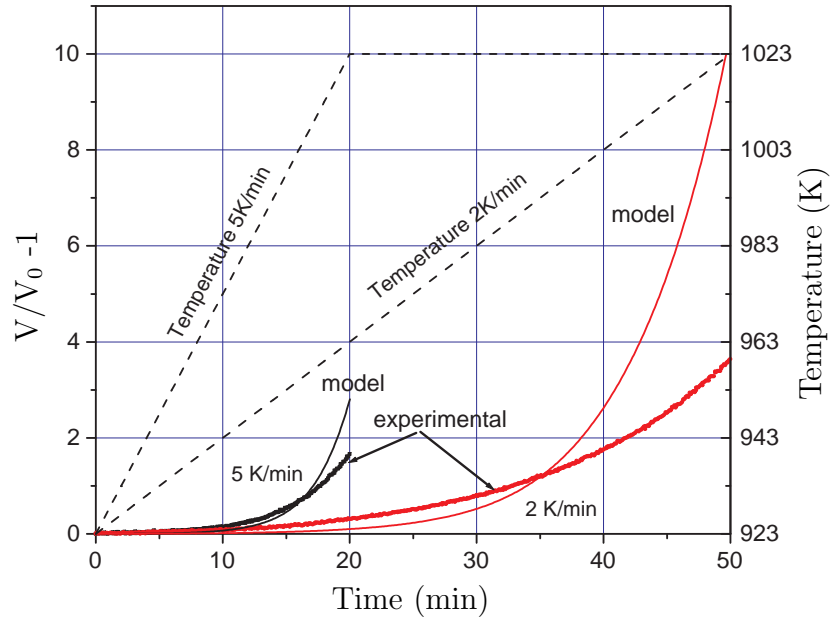


Figure 5.18: Initial stages of relative foam volume expansion of the glass-carbon powder mixture as a function of time observed from the experiments (corrected for gas loss) and from model calculations for the oxidized molten glass after sintering.  $V_0 = V(t_{calc} = 0)$ .

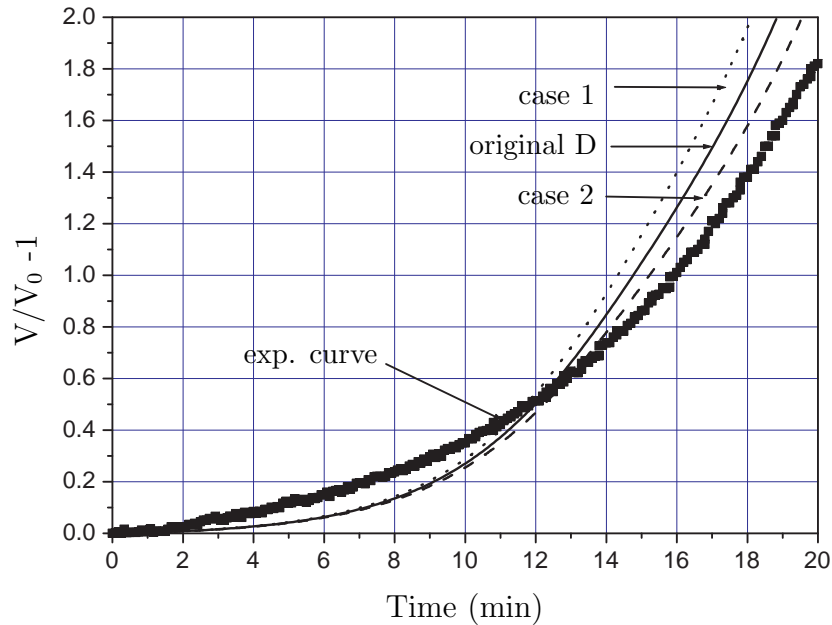
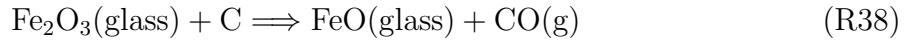


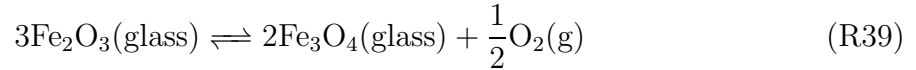
Figure 5.19: Relative volume expansion as a function of time for different inter-diffusion coefficients compared to experimental foam volume expansion. The temperature dependent inter-diffusion coefficient inside its error range as given by equation (5.116) Case 1:  $\log D = -0.67 \log \mu - 9.5$ , case 2:  $\log D = -0.75 \log \mu - 9.1$ ,  $\mu$  in  $\text{Pa} \cdot \text{s}$ .

should be noted that under the assumptions of this model, a constant volume of glass around the bubble finally delivers a constant amount of oxygen for the foaming gas production. In addition to that, the value of the inter-diffusion coefficient does not affect the final produced foam gas volume.

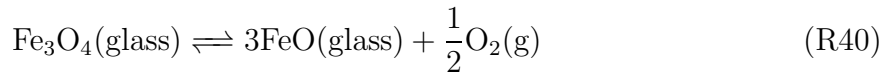
The results from chapter 4 have shown, that around 1000-1100 K the volume of released CO detected by quantitative gas analysis is only 55% of the CO expected from the conversion of  $\text{Fe}_2\text{O}_3$  to FeO according to:



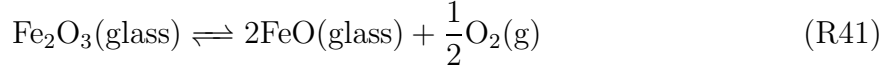
As discussed in chapter 4, Rüssel [51] and Freude [52] carried out voltammetric studies on soda lime silicate glasses at temperatures less than 1323 K with an  $\text{Fe}_2\text{O}_3$  content larger than 0.4 wt.%. According to their findings, the reduction of iron oxide in these glasses probably occurs in two steps. The first reduction step is according to reaction



and the second reduction step is according to:



The combination of both reactions is:



Reaction equilibrium (R41) is usually used to describe the iron redox equilibrium at higher glass melt temperatures. There is a possibility that at lower glass temperatures and larger iron concentrations, iron can be incorporated in silicate glasses as  $\text{Fe}_3\text{O}_4$ . According to Rüssel [51], there is a reasonably fair agreement between the measured reaction potentials and the theoretical potentials for the pure solid Fe-O System<sup>10</sup>. With the relation

$$E^0(T) = -\frac{\Delta G^0(T)}{n'' \cdot F} \quad (5.87)$$

where  $E^0(T)$  is the temperature dependent standard reaction potential,  $n''$  the number of electrons transferred (here 2),  $F$  the Faraday constant ( $96485.34 \text{ C} \cdot \text{mol}^{-1}$ ), the standard pure phase Gibbs free energy of the species  $\text{Fe}_3\text{O}_4$ ,  $\text{Fe}_2\text{O}_3$ , FeO and  $\text{O}_2$  can be used as a first estimate for the description of reaction equilibrium (R39) in the glass, assuming the same activity coefficients for all the involved ion species. Figure 5.20 shows the standard potentials for the three iron oxide reactions (R39), (R40) and (R41), which were calculated with the  $G^0(T)$  values from the pure solid phases. It can be seen that the reduction

<sup>10</sup>Molten glass is, like an aqueous solution an electrolyte. With three electrodes dipped into a glass melt, a working, counter and reference electrode, and applying a potential between the working and the reference electrode, redox reaction equilibria between electro active species (polyvalent ions) can be forced in one direction. In a so called voltammogram, the measured current between the counter and the working electrode is plotted as function of the potential applied between the working and the reference electrode. This potential is the so called reaction potential. The standard potential can be derived from standard pure species Gibbs free energy changes of chemical reactions (see equation (5.87)). Experimentally, the formal potential  $E^{0'}(T)$  can be determined from the voltage at the position of the peak in the voltammogram, see [53].

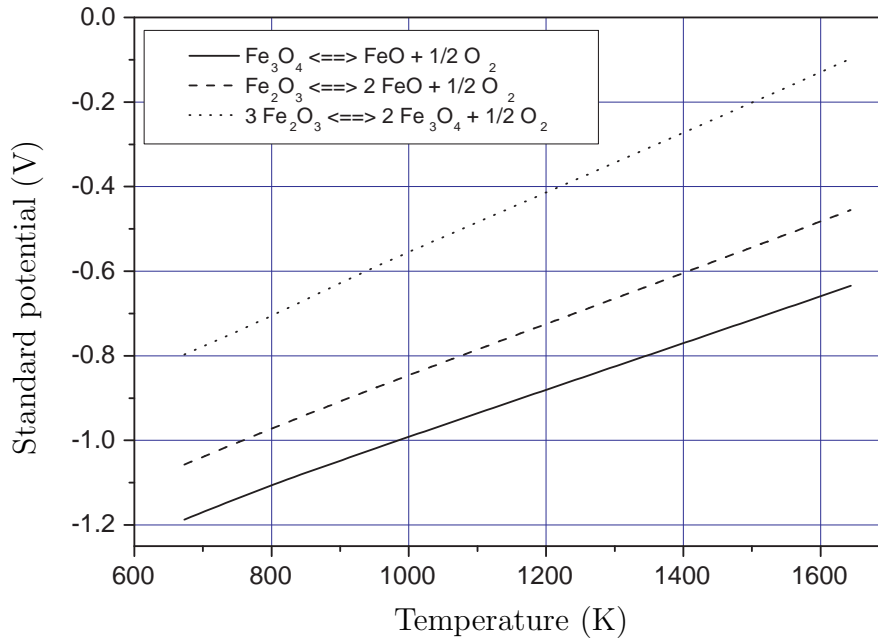


Figure 5.20: Standard potentials for three iron oxide reactions. The standard potentials ( $E^0$  values) are calculated using equation (5.87) applying the  $G^0(T)$  values from the pure solid phases.

step from  $\text{Fe}_2\text{O}_3$  to  $\text{Fe}_3\text{O}_4$  (R39) takes place at potentials higher than for reaction (R41). The reduction step from  $\text{Fe}_3\text{O}_4$  to  $\text{FeO}$  takes place at much lower potentials and was not observed by [53], but found by [51] and [52]. A lower  $E^0(T)$  value means that more reducing power is needed to reduce the iron oxide. In addition to that, the carbon in the glass carbon powder mixture applies a certain reduction on, e.g.,  $\text{Fe}_2\text{O}_3$ . In case this reduction capacity is not strong enough to reduce the ferrous iron to the ferric state, part of the  $\text{Fe}_2\text{O}_3$  will be present in the form of  $\text{Fe}_3\text{O}_4$ . At higher temperatures and higher  $E^0(T)$  value, a lower reduction is required to reduce the iron oxide and then, the reduction of, e.g.,  $\text{FeO}$  to metallic iron as proposed in chapter 4 to explain the second peak observed in figure 4.6 on page 108 might even be probable.

Unfortunately, no experimentally determined thermodynamic values ( $\Delta H^{*r}$  or  $\Delta S^{*r}$ ) were found for reactions (R39) or (R40) of iron oxide dissolved in the glass melt at concentration levels used in this investigation. As can be seen from the stoichiometry of reactions (R39), (R40) and (R41), the production of 1 mole CO from 1 mole of iron oxide ( $\text{Fe}_2\text{O}_3$ ) changes significantly depending on the predominant reduction step. The predominant reduction step may depend on temperature and oxidation state of the glass. Thus it seems, that more than one reduction step causes the formation of the foaming gas and that not only  $\text{Fe}_2\text{O}_3$  is present in the glass, but also  $\text{Fe}_3\text{O}_4$  may exist. However, the effect of  $\text{Fe}_3\text{O}_4$  in the glass on the foaming gas formation and its interaction with  $\text{Fe}_2\text{O}_3$  could not be quantified. Under certain assumptions, however, the concentration of possible  $\text{Fe}_3\text{O}_4$ ,  $\text{Fe}_2\text{O}_3$  and  $\text{FeO}$  in the glass can be estimated. According to Rüssel [51], there is a reasonably fair agreement between the measured reaction potentials in glass melts and

Table 5.5: Estimated values for the equilibrium composition between  $\text{Fe}_3\text{O}_4$ ,  $\text{Fe}_2\text{O}_3$  and  $\text{FeO}$  in an iron oxide containing glass with (2.99 wt.% of  $\text{Fe}_2\text{O}_3 \Rightarrow 936.13 \text{ mol} \cdot \text{m}^{-3}$ ), at  $T = 923 \text{ K}$  and  $T = 1173 \text{ K}$ .

Parameter	Value at 923 K	Value at 1173 K	Unit
$K_I^*$	$2.1388 \cdot 10^{-7}$	$1.9035 \cdot 10^{-4}$	-
$K_{II}^*$	$4.9663 \cdot 10^{-12}$	$2.0169 \cdot 10^{-8}$	-
$p_{\text{O}_2}$	$1.15 \cdot 10^{-17}$	$6.23 \cdot 10^{-11}$	bar
$[\text{Fe}_3\text{O}_4]$	304	301.6	$\text{mol} \cdot \text{m}^{-3}$
$[\text{Fe}_2\text{O}_3]$	11.4	15.6	$\text{mol} \cdot \text{m}^{-3}$
$[\text{FeO}]$	0.13	0.3	$\text{mol} \cdot \text{m}^{-3}$

the theoretical potentials for the pure solid Fe-O compounds. Applying equation (5.87), the equilibrium constant  $K$  can be calculated according to equation (5.40). The equilibrium constant  $K$  for species in solution is defined for activities of the reacting species and not directly for concentrations. Applying the same assumptions, which lead to equation (5.34) and assuming here that  $K = K^*$ ,  $K^*$  can be calculated from standard Gibbs free energy ( $G^0$ ) values. For reaction (R39) it is assumed here, that:

$$K_I^* \approx \frac{[\text{Fe}_3\text{O}_4]^2}{[\text{Fe}_2\text{O}_3]^3} p_{\text{O}_2}^{1/2} \approx \exp \left( -\frac{\Delta G^0(\text{R39})}{R_g T} \right) \quad (5.88)$$

and for reaction (R40) it is assumed here that:

$$K_{II}^* \approx \frac{[\text{FeO}]^3}{[\text{Fe}_3\text{O}_4]} p_{\text{O}_2}^{1/2} \approx \exp \left( -\frac{\Delta G^0(\text{R40})}{R_g T} \right) \quad (5.89)$$

The total concentration of Fe ( $\text{mol} \cdot \text{m}^{-3}$ ) in the glass, distributed among  $\text{Fe}_3\text{O}_4$ ,  $\text{Fe}_2\text{O}_3$  and  $\text{FeO}$  can be calculated according to:

$$c_{\text{Fe}} = 3[\text{Fe}_3\text{O}_4] + 2[\text{Fe}_2\text{O}_3] + [\text{FeO}] \quad (5.90)$$

With the known partial oxygen pressure of  $p_{\text{O}_2} = 1.15 \cdot 10^{-17}(\text{bar})$  at 923 K, experimentally obtained from the oxidized molten glass (2.99 wt.% of  $\text{Fe}_2\text{O}_3$ ) at higher temperatures and extrapolated to 923 K, it is possible to estimate the equilibrium concentrations of the three iron oxide species at 923 K in the glass without reduction by carbon. The calculated equilibrium constants  $K^*$  were calculated using the FactSage software package [42] at 923 K and at 1173 K for comparative reasons. The results of the calculations are given in table 5.5. In consideration of the mentioned assumptions and conditions, the estimated equilibrium composition indicates, that  $\text{Fe}_3\text{O}_4$  instead of  $\text{Fe}_2\text{O}_3$  is predominantly present in the glass at both temperature levels. The calculation does not take the presence of carbon into account and only considers the equilibrium condition of the glass prior to foaming. The distribution between  $\text{Fe}_3\text{O}_4$ ,  $\text{Fe}_2\text{O}_3$  and  $\text{FeO}$  also depends on the local partial  $\text{O}_2$  pressure, which is, during foaming, also influenced by the present carbon. It is thus not yet clear, which chemical gas forming reactions are predominantly responsible for the gas forming and thus responsible for the final foam height. More research is required to obtain more quantitative information on the equilibrium distribution between

$\text{Fe}_3\text{O}_4$ ,  $\text{Fe}_2\text{O}_3$  and  $\text{FeO}$  in an iron containing soda-lime-silicate glass at high iron oxide concentrations and lower temperatures in order to estimate the amount of oxygen that can be supplied by the glass for foam gas formation. In addition to that, the influence of the foaming gas reactions on the distribution of the three oxides inside the glass during the foaming process should be analyzed.

It has been shown, that the model cannot directly be used to predict the maximum foam height, but it can be used to estimate the expansion behavior of bubbles in various sintered glass powder mixtures and under various process conditions such as initial bubble size, shell thickness or heating rate. This will be presented in the next section.

## 5.5 Process Parameter study

As discussed earlier, information of various glass properties and process parameters is required to perform the necessary simulations with the foam model. The foaming process of the sintered glass powder is usually a downstream process, after the glass has been melted, cooled, grinded and mixed with a powdered foaming agent. The process parameters, which influence foaming of the obtained glass powder, mixed with the foaming agent, and control the foam quality are, as discussed earlier, the following two parameters.

1. The initial bubble size;
2. The heating rate.

Foam glass is mainly used for heat and sound insulation applications. The size of the bubbles and the pressure inside the bubbles in the cold final foam product influences its insulation behavior. The initial size of the bubbles and thus the glass shell thickness is influenced by the particle size of the glass powder. The temperature influences the glass melt properties, e.g., glass viscosity, surface tension and diffusion coefficients, and thereby the mass transport inside the glass and thus the production rate of foaming gas. The maximum foam expansion depends on the concentration of the chemically dissolved oxygen in the glass, because this determines the available oxygen for the  $\text{CO}/\text{CO}_2$  formation gas reactions. Glass viscosity, diffusion coefficients of polyvalent species, surface tension etc., are strongly related to the glass composition and can be influenced by changes to the glass composition during melting.

The next subsection presents results of a parameter study using the developed bubble model, showing the effect of the initial bubble size and the heating rate on the modeled bubble expansion. For this study the glass composition of the reduced glass (Foam, 0.2C) is used. Its composition is given in table 5.2 on page 150. The following two subsections describe the effect of the two different parameters on the bubble growth.

### 5.5.1 Influence of initial bubble size on bubble growth

The experimentally determined average initial bubble radius in the sintered powder of the reduced glass is given in table 5.4 on page 154. The initial radii of the cell (bubble plus glass) were  $R_1=79.6 \mu\text{m}$  and  $R_2=98.2 \mu\text{m}$ . For this type of study, the initial bubble radius

Table 5.6: Initial dimensions for five different cases to study the influence of the initial bubble size on the bubble growth rate. The volume of the glass shell was kept constant at  $1.85 \cdot 10^6 \mu\text{m}^3$  per bubble. The initial shell thickness  $d_0$  was calculated from the volume of glass around the bubble and  $R_1$ . The cell volume denotes the sum of the bubble and glass volume.

Initial conditions:	A	B	C	E	F
$R_1 (\mu\text{m})$	32	56	80	104	128
$R_2 (\mu\text{m})$	78.05	85.19	98.46	116.16	136.44
Shell thickness $d (\mu\text{m})$	46.05	29.19	18.46	12.16	8.44
Initial cell volume $V_0 (\mu\text{m}^3)$	$1.99 \cdot 10^6$	$2.59 \cdot 10^6$	$4.00 \cdot 10^6$	$6.75 \cdot 10^6$	$1.06 \cdot 10^7$

is going to be changed by keeping the glass volume per cell constant at  $1.85 \cdot 10^6 \mu\text{m}^3$ . This also enables the study of the effect of different shell thicknesses on the bubble growth. The studied radii are given in table 5.6. The calculations start at 923 K and a heating rate of 5 K/min to 1023 K, where the temperature will be kept constant. This heating rate was also applied for the model validation experiments.

Figure 5.21 shows the calculated relative volume expansion of the bubble with the surrounding glass shell and also the relative pressure inside the bubble as function of time. It can be seen, that for smaller initial bubble sizes, bubble growth starts somewhat later. This is because the glass volume was kept constant and thus a smaller bubble is surrounded by a thicker glass shell and a larger force (a higher gas pressure inside the bubble) is required to initiate the volume expansion. It can also be seen, that the slope of the volume increase is larger for smaller bubbles, than for larger bubbles. For thicker glass shells, resistance against stretching of the shell due to the glass viscosity is stronger. This is expressed equation (5.20) on page 131. It should be noted that the differences in final relative foam volume (second right ordinate in figure 5.21) is caused by the differences in initial bubble size. At constant glass shell volume, a smaller bubble requires a larger relative pressure to let the bubble grow. It should be noted that with a heating rate of 5 K/min, the maximum foaming temperature of 1023 K is reached after 20 minutes. Because the ordinate in figure 5.21 shows the relative pressure increase, negative relative pressures are possible, because the initial pressure is the ambient pressure plus the surface tension contribution ( $\frac{2\sigma}{R_1}$ ), which becomes smaller during bubble growth.

Figure 5.22 shows the relative change of the glass shell thickness as function of time for the five cases. It can be seen, that smaller initial bubbles and thicker initial glass shells lead to a retarded bubble expansion. But the relative thinning of the glass shell increases for smaller bubbles. The model only describes one cell, but in real foam glass many bubbles expand simultaneously, influencing each other. In case that the critical thicknesses of the glass lamellae between the bubbles are reached, the lamellae can break causing coalescence and thus causing inhomogeneous bubble size distribution and decreasing gas pressures in the bubble.

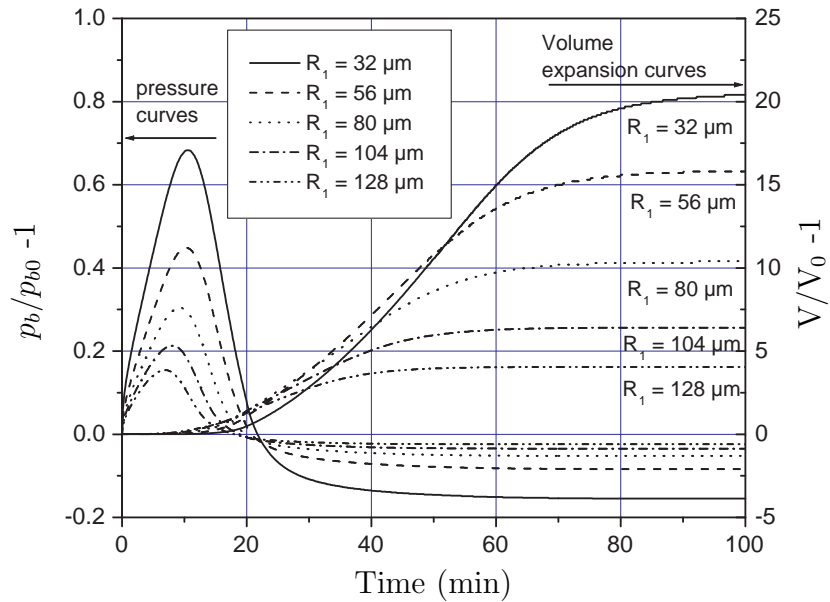


Figure 5.21: Relative cell volume increase  $V/V_0 - 1$  and pressure inside bubble calculated for different initial bubble radii. The glass shell volume per cell has been kept constant for the calculation. The heating rate is 5 K/min.

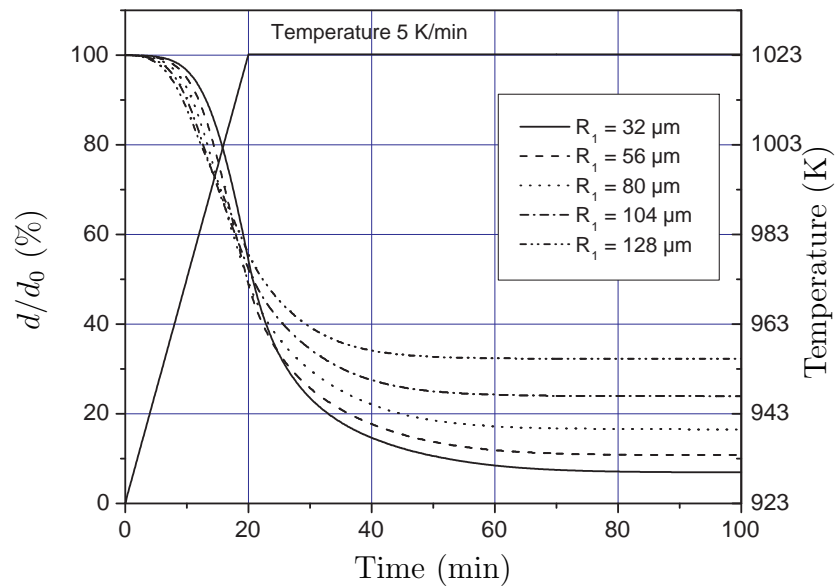


Figure 5.22: Relative change of the glass shell thickness as function of initial bubble radius for the five cases of table 5.6 and applied temperature. The glass shell volume per cell has been kept constant in the calculation. The heating rate is 5 K/min.



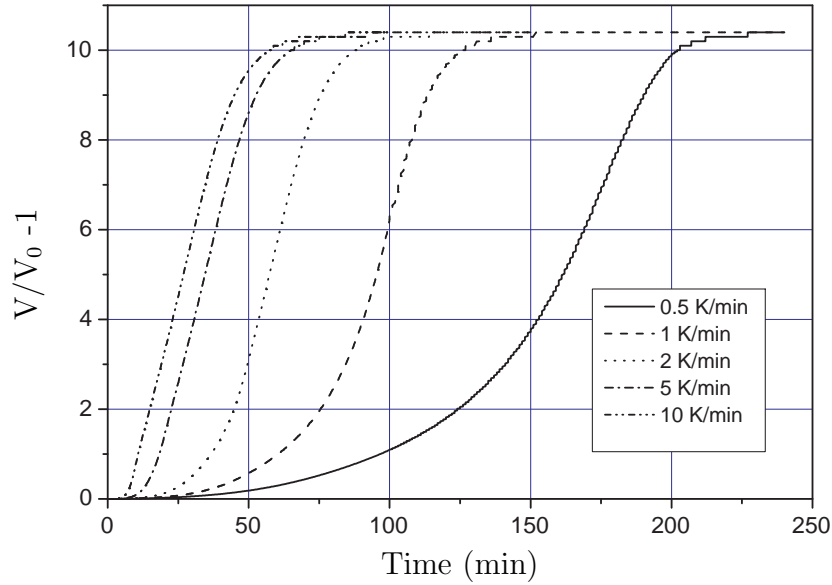


Figure 5.23: Relative cell volume increase for 5 different heating rates of case C of table 5.6 as function of time.

### 5.5.2 Influence of heating rate on bubble growth rate

As observed from experiments and expected during the validation of the model, the heating rate has a distinct influence on the bubble growth rate. The conditions for the bubble size and shell thickness of case C from table 5.6 are used and the heating rates of 0.5, 1, 2, 5 and 10 K/min are applied to investigate the effect of heating rate on foam bubble growth according to the model. The results are given in figure 5.23. The heating rate clearly influences the growth rates of the bubbles. Increasing heating rates enhance chemical gas forming reactions. The pressure increases more rapidly inside the bubble. This can also be observed in figure 5.24. Because of the equal shell thicknesses and glass composition for the calculation, the maximum and minimum pressures reached are equal for all five cases, whereas the pressure relaxation, due to the expansion of the glass shell is slower for lower heating rates.

This section has shown, that the model can be applied to estimate trends in expansion behavior of bubbles in foam glass as function of two main process parameters (initial bubble size and heating rate). However, the model contains also basic physicochemical relations, including the interaction of multiple polyvalent ions in the glass. The effect of oxidation state and redox interaction on the concentration profiles of the diffusing species and bubble growth will be presented and discussed in the next section.

## 5.6 Model calculations, results and discussion

The previous section showed a parameter study to demonstrate the capability of the model to simulate the effect of two main process parameters on bubble growth in a glass

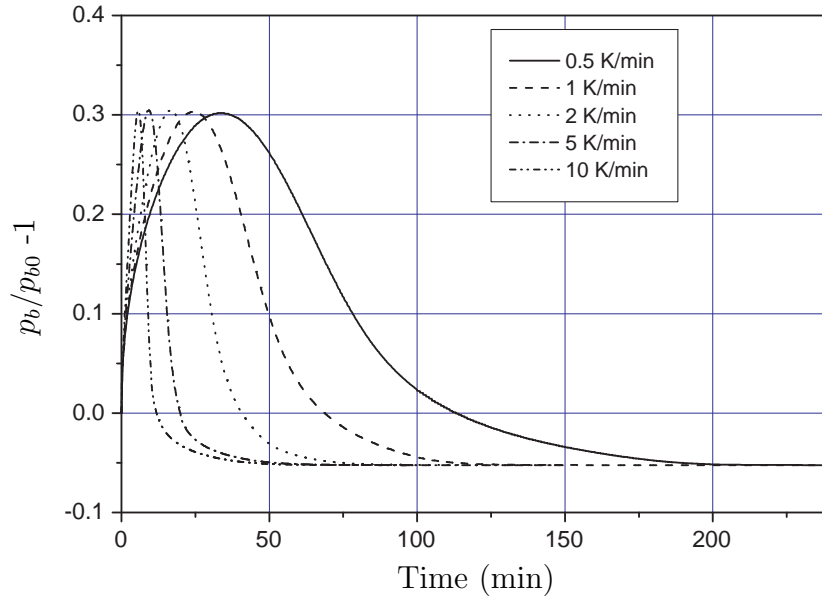


Figure 5.24: Relative bubble pressure evolution for 5 different heating rates of case C of table 5.6 as function of time.

foam. The strength of the model, however, is the inclusion of the effect of thermodynamic equilibrium reactions between physically and chemically dissolved oxygen in the glass shell. For an oxidized molten soda-lime-silicate glass containing iron oxide and sulphate, this is the interaction between  $\text{Fe}^{3+}$ ,  $\text{Fe}^{2+}$ ,  $\text{S}^{6+}$ ,  $\text{S}^{4+}$ ,  $\text{S}^{2-}$  and physically dissolved oxygen ( $\text{O}_2$ ). In this section, this interaction will be discussed in more detail. An exemplary simulation will be showing / discussing the following four topics:

1. The concentration profiles of the five polyvalent ions and physically dissolved oxygen in the glass shell;
2. The effect of differences in inter-diffusion coefficients on the concentration profiles in the glass;
3. The method with which thermodynamic equilibrium was implemented into the model: proof that thermodynamic equilibrium is maintained at all times
4. The effect of local thermodynamic equilibrium conditions between the diffusing species on the growth of a bubble, versus no thermodynamic equilibrium condition in the glass melt.

It should be noted that this is an exemplary calculation, showing the model's capability rather than a quantitative treatment, because the estimated data (diffusion coefficients, thermodynamic data) is not very accurate.

The glass composition for the study is given in table 5.7. The thermochemical values for  $\Delta H^{*r}$  and  $\Delta S^{*r}$ , required for the thermodynamic equilibrium reaction constants in the glass, were taken from table 5.1 on page 137. As discussed in the appendix, section

*Table 5.7: Glass composition (wt.%) used for exemplary model calculations.*

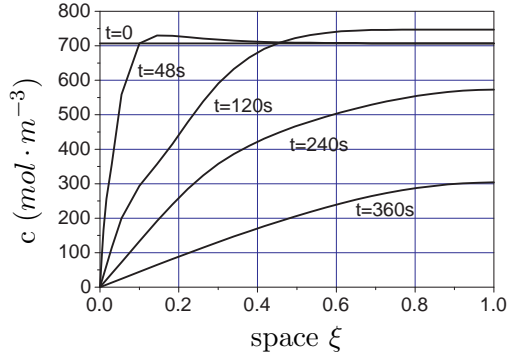
SiO <sub>2</sub> (wt.%)	CaO (wt.%)	Na <sub>2</sub> O (wt.%)	Al <sub>2</sub> O <sub>3</sub> (wt.%)	Fe <sub>2</sub> O <sub>3</sub> (wt.%)	MgO (wt.%)	K <sub>2</sub> O (wt.%)	SO <sub>3</sub> (wt.%)
72	10	11.3	2	3	0.6	0.6	0.5

*Table 5.8: Interdiffusion coefficients and initial concentrations of the six diffusing species at 1023 K, calculated according to the relations derived in section 5.10.3.*

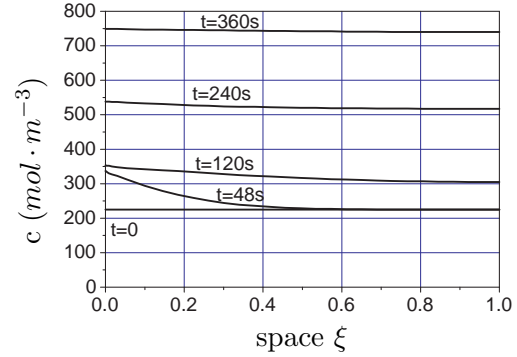
Species	$D_i$ (1023 K) (m <sup>2</sup> · s <sup>-1</sup> )	$c_{i,0}$ (1023 K) (mol · m <sup>-3</sup> )
Fe <sup>3+</sup>	$2.7 \cdot 10^{-14}$	707.1
Fe <sup>2+</sup>	$7.2 \cdot 10^{-13}$	224.6
O <sub>2</sub>	$4.4 \cdot 10^{-14}$	$1.46 \cdot 10^{-11}$
S <sup>6+</sup>	$3.1 \cdot 10^{-15}$	100.4
S <sup>4+</sup>	$3.1 \cdot 10^{-15}$	54.4
S <sup>2-</sup>	$1.0 \cdot 10^{-14}$	0.02

5.10.3 on page 193, inter-diffusion coefficients for the different sulphur species are not available. As proposed, one for SO<sub>3</sub>, as derived by Hermans [54], can be used, as first estimate, for all sulphur species in this model. However, to demonstrate the models capability, the diffusion coefficient for S<sup>2-</sup> was estimated by the one for O<sup>2-</sup>, having the same charge as S<sup>2-</sup>. The estimated diffusion coefficients and the assumed initial concentrations of the six diffusing species are given in table 5.8. The initial bubble radius for this calculation was 32 μm and the shell thickness was taken to be 42.7 μm. The temperature for this simulation is taken at 1023 K and kept constant for the entire calculation. The initial concentrations of the diffusing species were calculated using the thermodynamic equilibrium constants and the relations discussed in section 5.2.6.

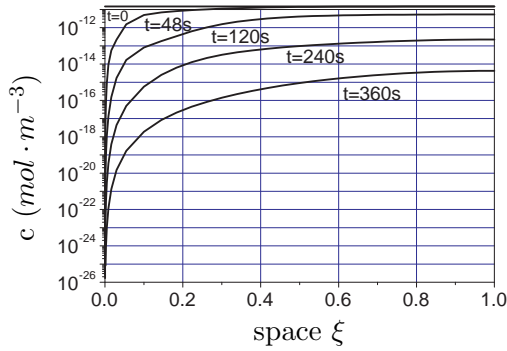
The concentrations as function of the spacial variable  $\xi$  of the six diffusing species at t=0, t=48s, t=120s, t=240s and t=360s, are given in figure 5.25. Figure 5.25(a) shows the concentration profile of Fe<sup>3+</sup>. It can be seen, that the concentration at t=48s and t=120s is locally larger than the initial concentration (t=0). This means that iron oxide in the ferrous state (Fe<sup>2+</sup>) is either locally oxidized to the ferric state (Fe<sup>3+</sup>), or that the local total iron concentration (Fe<sub>tot</sub>) has changed, due to differences in inter-diffusion coefficient between (Fe<sup>3+</sup>) and (Fe<sup>2+</sup>). The latter phenomenon will be discussed later in this section. This is one effect of the presumed thermodynamic equilibrium in the glass and the differences in diffusion coefficients between the diffusing species. The effect of differences in diffusion coefficient on the concentration profiles can also be seen in figure 5.25(b), showing the concentration profile of Fe<sup>2+</sup>. The estimated diffusion coefficient for Fe<sup>2+</sup> is more than one order of magnitude larger than the value for Fe<sup>3+</sup>. Figure 5.25(c) shows the concentration profile of physically dissolved O<sub>2</sub>. The initial concentration of O<sub>2</sub> is already very low at this temperature. As discussed earlier in this chapter, because of its low concentration in the glass at the applied temperature, the contribution of physically



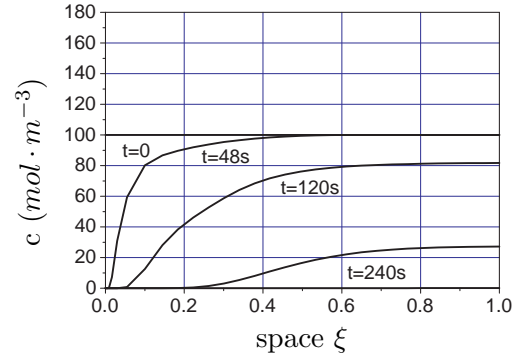
(a)  $Fe^{3+}$  concentration as function of the spatial variable  $\xi$  for 5 different times.



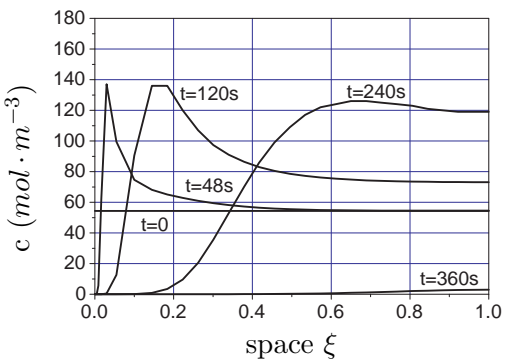
(b)  $Fe^{2+}$  concentration as function of the spatial variable  $\xi$  for 5 different times.



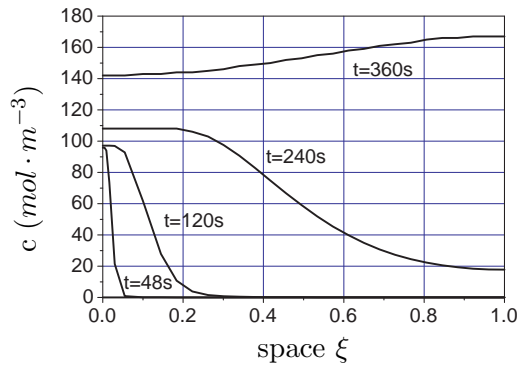
(c)  $O_2$  concentration as function of the spatial variable  $\xi$  for 5 different times.



(d)  $S^{6+}$  concentration as function of the spatial variable  $\xi$  for 5 different times.



(e)  $S^{4+}$  concentration as function of the spatial variable  $\xi$  for 5 different times.

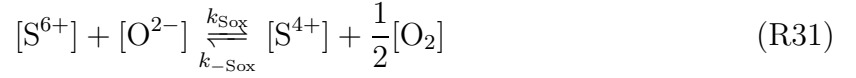


(f)  $S^{2-}$  concentration as function of the spatial variable  $\xi$  for 5 different times.

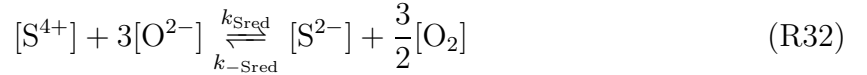
Figure 5.25: Concentration profiles of the polyvalent ions and physically dissolved oxygen inside the diffusion domain as function of the spatial variable  $\xi$  at  $t=0$ ,  $t=48s$ ,  $t=120s$ ,  $t=240s$  and  $t=360s$ . The total time domain: 480s.

dissolved  $O_2$  to the formation of the foaming gas is very low. However,  $[O_2]$  links the concentration of the different valency states of all mutual interacting polyvalent ions with each other and is thus the most important species.

Figures 5.25(d), 5.25(e) and 5.25(f) show the concentration profiles of the three sulphur species in the glass. In oxidized glasses, the  $S^{6+}/S^{4+}$  equilibrium is predominant, whereas the  $S^{4+}/S^{2-}$  equilibrium is predominant in case of a more reduced oxidation state [55]. It should be noted that in this model the formation of any sulfur containing foaming gases is not considered. Foaming gas analysis experiments, as have been described in chapter 4, were conducted with a sulphur and iron containing glass. The results from the mass spectrometer analysis of the evolving gases did not show any sulphur containing gaseous species. Experimentally determined values for  $\Delta H^{*r}$  and  $\Delta S^{*r}$  from [55] were applied in the model. The oxidation state dependent predominance, of the sulfur redox reactions, as described by [55], can be seen in figure 5.25(e): Because of thermodynamic equilibrium at  $t=0$  and the oxygen consuming reaction at the glass-bubble interface, the glass will be depleted of oxygen and the concentration of  $S^{6+}$  continuously decreases to produce oxygen and to maintain the thermodynamic equilibrium. This is shown in figure 5.25(d). This is also why the concentration of  $S^{2-}$  increases continuously. However,  $S^{4+}$  is locally produced by reduction of  $S^{6+}$  according to reaction (R31)



and consumed according to reaction (R32).



The concentration profiles of  $S^{4+}$  in figure 5.25(e) for  $t=48s$ ,  $t=120s$  and  $t=240s$ , show, that because of the strongly reduced condition at the left boundary near the glass-bubble interface ( $0 < \xi < 0.1$ ),  $S^{4+}$  is consumed, i.e. reaction (R32) seems predominant, whereas it is produced according to reaction (R31) deeper inside the glass where the oxidation state is not yet low enough for the  $S^{4+}/S^{2-}$  equilibrium. It should be noted, that the concentration profile of  $S^{4+}$  depends on the concentrations of the iron ions and the physically dissolved  $O_2$ . Since  $SO_2$  evolution from the glass requires  $S^{4+}$  at the surface. At  $\xi = 0$  hardly any  $S^{4+}$  is available to generate  $SO_2$  gas.  $S^{2-}$  is predominantly present at the surface and hardly forms sulphur containing gases. This can be one explanation for the fact that during qualitative experiments as described in chapter 4 (but not published here), no sulphur containing gaseous species were detected with the used mass spectrometer in a glass with iron and sulphur as polyvalent species.

The polyvalent ion species in the glass and  $O_2$  diffuse and mutually interact the glass shell. This and the different diffusion coefficient values also influences the local total element concentrations  $[Fe_{tot}]$  and  $[S_{tot}]$ . Figure 5.26 shows the total element concentration, expressed as sum of the polyvalent ions for four different times ( $t=0$ ,  $t=48s$ ,  $t=120s$ , and  $t=360s$ ) as function of the spatial variable  $\xi$ . Figure 5.26(a) shows the total iron concentration as function of  $\xi$  for four different times. The hump, which is seen, e.g., for  $t=48s$ ,

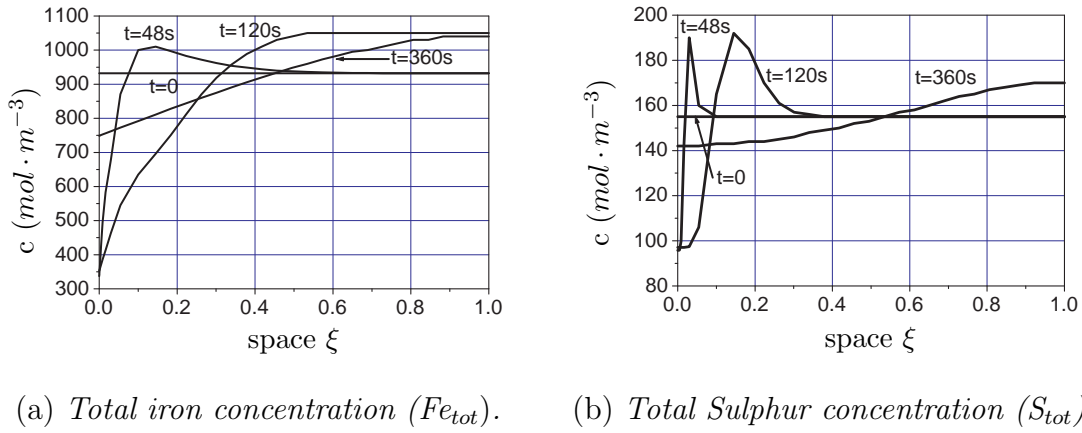


Figure 5.26: Total element concentration,  $Fe_{tot}$  and  $S_{tot}$  for four different times ( $t=0$ ,  $t=48s$ ,  $t=120s$ , and  $t=360s$ ) as function of the dimensionless spatial variable  $\xi$ .

showing that the total iron concentration can locally be different from the initial concentration can be explained by the difference in diffusion coefficients between the ferrous and ferric iron and the condition of the local thermodynamic equilibrium. This 'hump' is also known and experimentally validated for tin diffusion in float glass, where the total tin concentration as function of the penetration depth also shows such a hump [56, 57].

The model takes into account local thermodynamic equilibrium of the polyvalent ions and physically dissolved oxygen in the glass. One exception, as stated during the numerical implementation of the model, is the very first volume of glass between the glass-bubble interface and the first gridpoint for the calculation. Because of numerical instabilities, the production term in equation (5.21) was omitted in the boundary condition. To implement thermodynamic equilibrium into the model a method using very high reaction rate constants as discussed in section 5.2.6 on page 133 was used. Presuming thermodynamic equilibrium, written in a mathematical way, the following reaction (equation) must hold for, e.g., the iron oxide redox couple:

$$\varpi = \frac{[Fe^{2+}]}{[Fe^{3+}]} - \frac{K_{Fe}^* \cdot L_{O_2}^{1/4}}{[O_2]^{1/4}} = 0 \quad (5.91)$$

All concentrations of the diffusing species at each location are calculated during the simulation and the equilibrium constant  $K^*$  and the oxygen solubility  $L_{O_2}$  are also known, so local equilibrium can easily be checked. This is presented in figure 5.27, which shows the difference between the two terms of equation (5.91), thus the calculated  $\varpi$  values, for  $t=360s$  as function of the spatial variable  $\xi$ . The values of  $\varpi$  are between  $10^{-4}$  and  $10^{-8}$ , which is low and sufficient accurate to presume local thermodynamic equilibrium.

The influence of taking into account thermodynamic equilibrium, thus mutual interaction of the diffusing species on the mass transport processes in the glass and on the relative radius change of the bubble as function of time, is given in figure 5.28. The expression "no thermodynamic equilibrium in the glass" in figure 5.28 means mathematically, that the source term  $\Psi$  was omitted for this type of calculation. The equilibrium in the glass

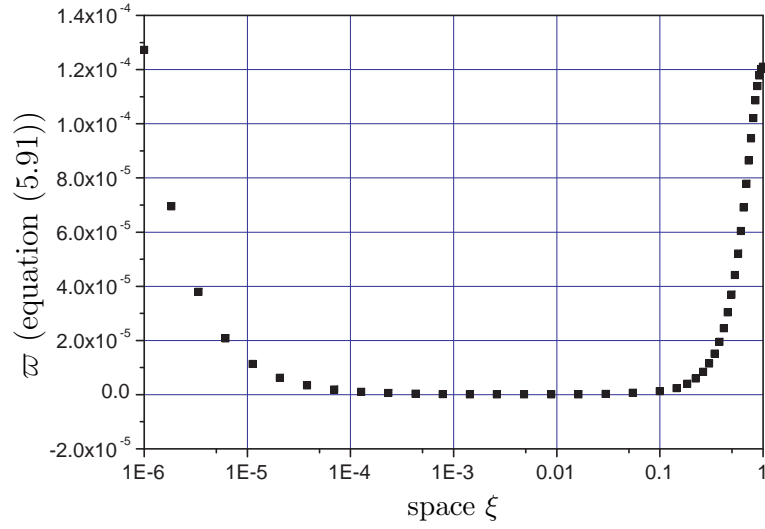


Figure 5.27: Difference between the two terms of equation (5.91) for  $t=360s$  as function of the dimensionless spatial variable  $\xi$ .

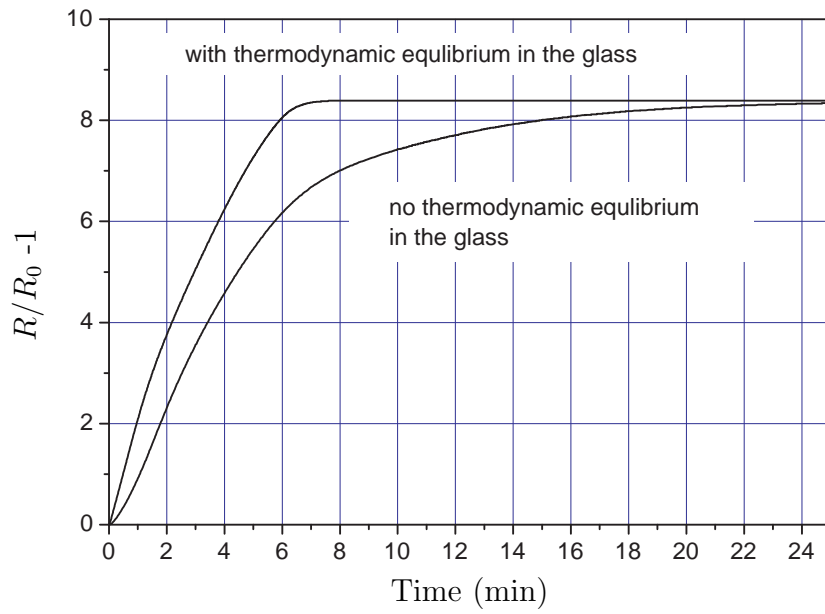


Figure 5.28: Effect of thermodynamic equilibrium in the glass on the relative radius change of the bubble as function of time.

causes a faster growth rate of the bubble and the final volume is reached three times earlier. It increases thus the molar flux of oxygen at the glass-bubble interface.

## 5.7 Concluding remarks

In this chapter, a numerical simulation model to estimate single bubble growth in a foaming mass of sintered glass powder, mixed with a reduced foaming agent, has been developed. The growth of the individual foam bubbles was related to the total foam expansion. The model is based on a first principal approach. It describes mass transfer processes by diffusion and the effect of local redox equilibrium reactions of multiple polyvalent ions and physically dissolved oxygen in the glass on the mass transport in the glass and thus on the concentration profiles of the diffusing species. The model requires, as input parameters, the glass composition including the concentrations of the different polyvalent ions and of physically dissolved oxygen, as well as the initial bubble size and the initial glass shell thickness. The bubble growth rate depends in the following parameters:

- The total concentration of the polyvalent ions in the glass melt;
- The oxidation state of the polyvalent ions in the glass melt;
- The glass melt viscosity;
- The surface tension. This effect is most significant at the initial stages of the bubble growth ( $R_1 \ll 0.1\text{mm}$ ).

The model validation has shown, that the model can be used to estimate the bubble growth of foam glass in the initial stages, but the developed model strongly overestimates the final foam height. There are several possible causes for the overestimation of the foam height at extended foaming time:

**Loss of reaction gases through open pores** before and during sintering. This is because foaming gas reactions partly start before the pores are closed. After the pores have been closed, probably not sufficient active reducing agent is available and oxygen is lost. This effect, however, does not explain the smaller deviations between modeled and experimental volume increase during the initial stages of the foaming process.

**The amount and type of foaming agent** and its distribution in the mixture of glass powder plus foaming agent is also important for the foaming process. Industrially foaming processes use between 0.2 and 0.6 wt.% of foaming agent in the mixture. Probably the particle size and the type of reduced foaming agent and its distribution has a significant influence on the foaming gas production.

**The sintering and applied temperatures** also influence the bubble growth. At low sintering temperatures, the pores will still not be closed when the heating starts. At too high sintering temperatures, the initial bubbles are not formed properly, e.g., inhomogeneous shell thicknesses, before the foaming gas reactions start. This can result in early breakage of the bubbles, especially at the outer surface of the foam



sample. At too high foaming temperatures, the glass viscosity will be too low and the bubbles will grow too fast, which can cause tear or collapse of the bubbles. If this happens at the outer surface of the foam body, large bubbles break open and foaming gas can be lost. This could explain the intense foam volume rate decrease observed during the validation experiments, just after reaching the final foaming temperature.

**The exact oxygen producing reactions** inside the glass, i.e., which iron oxide species ( $\text{Fe}_3\text{O}_4$  or  $\text{Fe}_2\text{O}_3$ ) is predominantly responsible for the supply of oxygen and the stage of iron oxide reduction.

Foaming gas, which suddenly escapes from the experimental foam sample is partially responsible for the strong deviation between experimental and modeled volume expansion at higher temperatures and foaming times. It seems that more accurate foaming experiments have to be performed in future studies to better understand the above mentioned possible factors causing a reduction of entrapped foaming gas volume.

The effect of the heating rate on the transient bubble growth, predicted by the model, is in good agreement with the observed initial real foam expansion rate. The parameter study for the two main process parameters, the initial bubble size (depending on the size of the glass powder particles) and the heating rate has shown, that these parameters significantly influence the bubble growth rate. The choice of initial glass particle size, which directly influences the initial bubble size (and number of bubbles) and shell thickness is thus important for the bubble growth rate.

The model respects mutual interaction and local thermodynamic equilibrium of the diffusing species in the glass shells in the foam glass. There are two main advantages or extensions of the present model compared to other models:

- Compared to the foam glass model of Köse [3], this model has a strict fundamental approach and, e.g., no experimentally foaming gas volume determination is required to calculate the volume expansion of the foam sample. It should be noted that Köse did only model the initial and medium stages of the foam expansion and that his model was not able to determine the final foam volume.
- Present models describe bubble growth during fining of soda-lime silicate melts including thermodynamic equilibrium as presented by Beerkens et al. and Yoshikawa et al. [1, 27]. This model, however takes equilibrium between multiple polyvalent ions (more than 2) at a time into account. This would be considerable modification to the already present models.
- This model calculates diffusion of not only physically dissolved oxygen, but also inter-diffusion of polyvalent ion species in the glass.

Despite the deviations between the modeled and experimental foam expansion rates, this model can provide a tool to optimize process conditions and glass properties for obtaining required glass foams. In addition to that, the model can provide, with some modifications, a considerable improvement to existing bubble models, describing fining in industrial glass melting processes.

## 5.8 Nomenclature

$a$	activity	—
$a'$	experimentally determined constants for viscosity calculation	$\text{Pa} \cdot \text{s}$
$b$	charge of the oxidized polyvalent ion	—
$b'$	experimentally determined constants for viscosity calculation	$\text{Pa} \cdot \text{s} \cdot \text{K}$
$c$	concentration	$\text{mol} \cdot \text{m}^{-3}$
$c'$	experimentally determined constants for viscosity calculation	$\text{K}$
$d$	thickness of glass shell, see equation (5.83)	$\text{m}$
$g$	array dimension	—
$h$	heating rate	$\text{K} \cdot \text{s}^{-1}$
$h_x$	height of one pixel	$\text{mm}$
$h_y$	width of one pixel	$\text{mm}$
$k$	chemical reaction rate	$\text{mol} \cdot \text{m}^{-3} \cdot \text{s}^{-1}$
$k'_{Fe}$	modified chemical reaction rate (see equation 5.38)	$\text{mol}^{3/2} \cdot \text{m}^{-11/2} \cdot \text{s}^{-1}$
$m$	charge of the reduced polyvalent ion	—
$n$	amount of moles	$\text{mol}$
$n^*$	dimensionless number of moles	—
$n'$	moles distributed between CO and CO <sub>2</sub> see equation (5.58)	$\text{mol}$
$n''$	number of electrons transferred in electrochemical reactions	—
$p$	pressure	$\text{Pa}$
$p'$	factor for viscosity calculation (see equation (5.108))	$\text{mol} \cdot (\text{mol SiO}_2)^{-1}$
$\tilde{p}$	partial pressure of diffusing species in bubble	$\text{Pa}$
$q$	array dimension	—
$r$	radial coordinate in spherical coordinates	$\text{m}$
$s$	scaling factor to translate pixel dimensions in metric units	$\text{mm} \cdot \text{pixel}^{-1}$
$t$	time	$\text{s}$
$v$	mass average velocity	$\text{m} \cdot \text{s}^{-1}$
$\mathbf{v}$	mass average velocity vector	$\text{m} \cdot \text{s}^{-1}$
$w$	$(b-m)/4$ , (see equation (5.32))	—
$x$	spatial grid point of analytical solution, see equation (5.83)	$\text{m}$
$A$	constant in VFT equation (5.107)	$\text{Pa} \cdot \text{s}$
$B$	constant in VFT equation (5.107)	$\text{Pa} \cdot \text{s} \cdot \text{K}$
$C$	constant in VFT equation (5.107)	$\text{K}$
$x_i$	molar fraction of species i	—
$D$	diffusion coefficient	$\text{m}^2 \cdot \text{s}^{-1}$
$E^0$	Standard reaction potential	$\text{V}$
$F$	Faraday constant ( $96485.34 \text{ C} \cdot \text{mol}^{-1}$ )	$\text{C} \cdot \text{mol}^{-1}$
$G$	molar Gibbs free energy	$\text{J} \cdot \text{mol}^{-1}$
$H$	molar Enthalpy	$\text{J} \cdot \text{mol}^{-1}$
$\Delta H^{*r}$	experimentally determined, molar reaction enthalpy based on concentration	$\text{J} \cdot \text{mol}^{-1}$
$K$	thermodynamic equilibrium constant	—
$K'$	modified thermodynamic equilibrium constant	—
$K^*$	modified thermodynamic equilibrium constant	$(\text{mol} \cdot \text{m}^{-3})^{(2w_i)}$
$K''_{Fe}$	modified thermodynamic equilibrium constant	$\text{m}^{3/2} \cdot \text{mol}^{-1/2}$

	based on concentration (see equation 5.38)	
$K_p$	equilibrium constant for gaseous reaction in bubble	—
$K'_{p,b}$	modified equilibrium constant based on pressure	Pa
$L$	solubility of gas in liquid	$\text{mol} \cdot \text{m}^{-3} \cdot \text{Pa}^{-1}$
$\vec{L}_x$	vector of length $g$	—
$\vec{L}_y$	vector of length $q$	—
$M^{b+}$	oxidized species of the polyvalent ion	—
$M^{m+}$	reduced species of the polyvalent ion	—
$N$	total number of bubbles in sample	—
$N_A$	number of bubbles per unit area	$\text{mm}^{-2}$
$N_L$	number of bubbles per unit length	$\text{mm}^{-1}$
$N_V$	number of bubbles per unit volume	$\text{mm}^{-3}$
$N_x$	number of bubbles in x-direction of picture	—
$N_y$	number of bubbles in y-direction of picture	—
$Q$	molar rate of production	$\text{mol} \cdot \text{m}^{-3} \cdot \text{s}^{-1}$
$R$	bubble radius	m
$Re$	Reynolds number	—
$R_g$	ideal gas constant	$\text{J} \cdot \text{mol}^{-1} \cdot \text{K}^{-1}$
$S$	molar Entropy	$\text{J} \cdot \text{mol}^{-1} \cdot \text{K}^{-1}$
$\Delta S^{*r}$	experimentally determined, molar reaction entropy based on concentration	$\text{J} \cdot \text{mol}^{-1} \cdot \text{K}^{-1}$
$T$	absolute temperature	K
$T_g$	glass transformation temperature	K
$T^*$	dimensionless temperature	—
$V$	volume	$\text{m}^3$
$W$	weight% contribution of different species in glass	—
$Z$	property function, see equation (5.66)	—

#### SUPERSCRIPITS

0	standard state
$r$	reaction
$d_i$	temperature dependency of inter-diffusion coefficient (equation (5.121))

## SUBSCRIPTS

<i>ref</i>	reference
<i>b</i>	inside bubble
<i>foam</i>	foam
<i>g</i>	gas
<i>i, j</i>	indices
<i>l</i>	liquid
<i>r, <math>\phi, \theta</math></i>	spherical coordinates
<i>ox</i>	oxidized form of polyvalent ion plus phys. dissolved oxygen
<i>R</i>	at radius R
0	initial value (at = 0)
<i>tot</i>	total

## GREEK LETTERS

$\beta$	volume factor, see equation (5.65)	$\text{m}^3$
$\gamma$	activity coefficient	—
$\zeta$	dimensionless bubble radius, see equation (5.69)	—
$\eta$	dimensionless group, see equation (5.70)	—
$\epsilon$	see property function Z (equation (5.66))	—
$\kappa$	dilatational viscosity	$\text{Pa} \cdot \text{s}$
$\mu$	dynamic viscosity	$\text{Pa} \cdot \text{s}$
$\nu$	stoichiometric number	—
$\xi$	dimensionless spatial variable, see equation (5.63)	—
$\rho$	fluid density	$\text{kg m}^{-3}$
$\sigma$	surface tension	$\text{N m}^{-1}$
$\varsigma$	dimensionless spatial variable, see subsection 5.3.4	—
$\tau$	stress tensor	$\text{Pa}$
$\varpi$	difference from thermodynamic equilibrium (equation 5.91)	—
$\varphi$	dimensionless time parameter, see subsection (5.3.4)	—
$\phi$	dimensionless group, see equation (5.71)	—
$\chi$	mass transfer coefficient for oxygen from glass to bubble	$\text{m s}^{-1}$
$\Theta$	Fourier number, see equation (5.67)	—
$\Psi$	source term for molar rate of production	$\text{mol} \cdot \text{m}^{-3} \cdot \text{s}^{-1}$

## NOTES

$\nabla$	Nabla operator
$\Delta$	Difference

## 5.9 Bibliography

- [1] R. G. C. Beerkens and H. de Waal. Mechanism of oxygen diffusion in glass melts containing variable-valence ions. *J. Am. Ceram. Soc.*, 73(7):1857–1861, 1990.
- [2] J. M. Hermans. *Diffusion in Multicomponent Silicate Glass Melts*. PhD thesis, RWTH Aachen, Germany, 2004.
- [3] S. Köse. *Untersuchungen zur Blähdynamik des Schaumglases*. PhD thesis, Eidgenössische Technische Hochschule (ETH) Zürich, Switzerland, 1981.
- [4] H. M. Princen, M. P. Aronson, and J. C. Moser. Highly concentrated emulsions, II. Real systems. The effect of film thickness and contact angle on the volume fraction in creamed emulsions. *J. Colloid. Interface Sci.*, 75(1):246–270, 1980.
- [5] A. Arefmanesh and S. G. Advani. Diffusion induced growth of a gas bubble in a viscoelastic fluid. *Rheol. Acta*, 30:274–283, 1991.
- [6] P. S. Epstein and M. S. Plesset. On the stability of gas bubbles in liquid-gas solutions. *J. Chem. Phys.*, 18(11):1505–1509, 1950.
- [7] D. W. Readey and A. R. Cooper. Molecular diffusion with a moving boundary and spherical symmetry. *Chem. Eng. Sci.*, 21:917–922, 1966.
- [8] M. Cable and D. J. Evans. Spherically symmetrical diffusion-controlled growth or dissolution of a sphere. *J. Appl. Phys.*, 38(7):2899–2906, 1967.
- [9] J. L. Duda and J. S. Vrentas. Mathematical Analysis of bubble dissolution. *AIChE Journal*, 15(3):351–356, 1969.
- [10] R. S. Subramanian and Bo Chi. Bubble dissolution with chemical reaction. *Chem. Eng. Sci.*, 35:2185–2194, 1980.
- [11] M. C. Weinberg, P. I. K. Onorato, and D. R. Uhlmann. Behavior of bubbles in glass melts: I, dissolution of a stationary bubble containing a single gas. *J. Am. Ceram. Soc.*, 63(3-4):175–180, 1980.
- [12] M. C. Weinberg. Surface tension effects in gas bubble dissolution and growth. *Chem. Eng. Sci.*, 36:137–141, 1981.
- [13] J. Szekely, G. P. Martins, and S. D. Fang. Bubble growth by diffusion, the effect of viscosity, inertia and surface tension. *VDI Berichte*, 182:13–22, 1972.
- [14] M. Cable and M. A. Haroon. Action of arsenic as a refining agent. *Glass Technol.*, 11(2):48–53, 1970.
- [15] L. Něméc. Refining of glass melts. *Glass Technol.*, 15(6):153–156, 1974.
- [16] L. Něméc. Refining in the glassmelting process. *J. Am. Ceram. Soc.*, 60(9-10):436–440, 1977.

- [17] R. G. C. Beerkens. Chemical equilibrium reactions as driving force for growth of gas bubbles during refining. *Glastechn. Ber.*, 63K:222–236, 1990. 2. International Conference "Advances in the fusion and processing of glass".
- [18] F. Krämer. Mathematisches Modell der Veränderung von Gasblasen in Glas-schmelzen. *Glastechn. Ber.*, 52(2):43–50, 1979.
- [19] M. C. Weinberg, P. I. K. Onorato, and D. R. Uhlmann. Behavior of bubbles in glass melts: II, dissolution of a stationary bubble containing a diffusing and a nondiffusing gas. *J. Am. Ceram. Soc.*, 63(7-8):435–438, 1980.
- [20] M. Cable and J. R. Frade. Diffusion-controlled growth of multi-component gas bubbles. *J. Mater. Sci.*, 22:919–924, 1987.
- [21] M. Cable and J. R. Frade. Numerical solutions for diffusion-controlled growth of spheres from finite initial size. *J. Mater. Sci.*, 22:149–154, 1987.
- [22] L. Něméc. The behavior of bubbles in glass melts. Part 1. Bubble size controlled by diffusion. *Glass Technol.*, 21(3):134–138, 1980.
- [23] L. Něméc. The behavior of bubbles in glass melts. Part 2. Bubble size controlled by diffusion and chemical reaction. *Glass Technol.*, 21(3):139–144, 1980.
- [24] M. C. Weinberg and R. S. Subramanian. The dissolution of a stationary bubble enhanced by chemical reaction. *Chem. Eng. Sci.*, 36(12):1955–1965, 1981.
- [25] W. Y. Soung and J. T. Sears. Effects of reaction order and convection around gas-bubbles in a gas-liquid reacting system. *Chem. Eng. Sci.*, 30:1353–1356, 1975.
- [26] H. Yoshikawa and Y. Kawase. Significance of redox reactions in glass refining processes. *Glastechn. Ber. Glass Sci. Technol.*, 70(2):31–40, 1997.
- [27] H. Yoshikawa, H. Miura, and Y. Kawase. Dissolution of bubbles in glass melts with equilibrium redox reactions: approximations for a moving bubble boundary. *J. Mat. Sci.*, 33:2701–2707, 1998.
- [28] H. Scholze. *Glas Natur, Struktur und Eigenschaften*. Springer-Verlag, Berlin Heidelberg New York, 1988.
- [29] C. Kröger and N. Goldmann. Kohlendioxydlöslichkeiten in Gläsern. *Glastechn. Ber.*, 35(11):459–466, 1962.
- [30] R. B. Bird, W. E. Stewart, and E. N. Lightfoot. *Transport Phenomena*. John Wiley & Sons, Inc., second edition, 2001.
- [31] T. Lakatos, L.-G. Johansson, and B. Simmingsköld. Viscosity temperature relation in the glass system  $\text{SiO}_2\text{-Al}_2\text{O}_3\text{-Na}_2\text{O-K}_2\text{O-CaO-MgO}$  in the composition range of technical glasses. *Glass Technol.*, 13(3):88–95, 1972.
- [32] Wen-Jei Yang and Hsu-Chieh Yeh. Theoretical study of bubble dynamics in purely viscous fluids. *AIChE Journal*, 12(5):927–931, 1966.

- 
- [33] C. Rüssel. Redox reactions during cooling of glass melts - A theoretical consideration. *Glastechn. Ber. Glass Sci. Technol.*, 62(6):199–203, 1989.
- [34] R. Pyare, S. P. Singh, A. Singh, and P. Nath. The  $\text{As}^{3+}$  -  $\text{As}^{5+}$  equilibrium in borate and silicate glasses. *Phys. Chem. Glasses*, 23(5):158–168, 1982.
- [35] F. G. K. Baucke and J. A. Duffy. The effect of basicity on redox equilibria in molten glasses. *Phys. Chem. Glasses*, 32(5):211–218, 1991.
- [36] H. Müller-Simon. Electron exchange reactions between polyvalent elements in soda-lime-silica and sodium borate glasses. *Glastechn. Ber. Glass Sci. Technol.*, 69(12):387–395, 1996.
- [37] H. Müller-Simon. Temperature dependence of amber color generation in soda-lime-silica glass. *Glastechn. Ber. Glass Sci. Technol.*, 73(1):28–30, 2000.
- [38] R.G.C. Beerkens. Amber chromophore formation in sulphur- and iron-containing soda-lime-silica glasses. *Glastchn. Ber. Glass Sci. Technol.*, 76(4):166–174, 2003.
- [39] H. Müller-Simon. Oxygen balance in sulfur-containing glass melts. *Glastechn. Ber. Glas. Sci. Technol.*, 71(6):157–165, 1998.
- [40] J. M. Smith, H. C. Van Ness, and M. M. Abbott. *Introduction to Chemical Engineering Thermodynamics*. Chemical Engineering Series. McGraw-Hill International, fifth edition, 1996.
- [41] I. Barin, F. Sauert, E. Schultze-Rhonhof, and Wang Shu Sheng. *Thermochemical data of pure substances*, volume 1+2. Weinheim, VCH, second edition, 1993.
- [42] C. W. Bale, A. D. Pelton, and W. T. Thompson. *FactSage 5.0 User Manual*, 2001. Ecole Polytechnique de Montréal, Royal Military College, Canada.
- [43] I. Barin, O. Knacke, and O. Kubaschewski. *Thermochemical properties of inorganic substances*. Springer-Verlag, Düsseldorf, 1977.
- [44] J. D. Anderson Jr. *Computational fluid dynamics, the basics with application*, chapter 5.2, pages 171–175. McGraw-Hill, Inc., 1995.
- [45] J. M. Smith, E. Stammers, and L. P. B. M. Janssen. *Fysische transportverschijnselen*, volume 1. Delftse Uitgevers Maatschappij b.v., 1986. In Dutch, ISBN 90-6562-050-8.
- [46] T. Thonthat and G.Oddon. Redox des calcins de recyclage. *Verre*, 3(5), 1997.
- [47] R. G. C. Beerkens, A. Faber, J. Plessers, and T. Thontat. Methods for the characterization of redox state of cullet and batches in glass manufacturing. *Glass International*, pages 371–375, 1997.
- [48] E. E. Underwood. *Quantitative Stereology*. Addison-Wesley Publ. Company, 1970.
- [49] S. A. Saltykov. *Stereometrische Metallographie*. VEB Deutscher Verlag für Grundstoffindustrie, Leipzig, Germany, 1974. Translated from russian.

- [50] D. W. Richardson. *Modern Ceramic Engineering*. Marcel Dekker, Inc. New York, 2 edition, 1992.
- [51] C. Rüssel, R. Kohl, and H. A. Schaeffer. Interaction between oxygen activity of  $\text{Fe}_2\text{O}_3$  doped soda-lime-silicate glass melts and physically dissolved oxygen. *Glastechn. Ber. Glass Sci. Technol.*, 61(8):209–213, 1988.
- [52] E. Freude. *Voltammetrische Untersuchungen des Redoxverhaltens polyvalenter Ionen in Glasschmelzen, insbesondere von Technetium*. PhD thesis, Erlangen University, Erlangen, Germany, 1989.
- [53] A. Wondergem-de Best. *Redox behavior and fining of molten glass*. PhD thesis, Eindhoven University of Technology, Eindhoven, The Netherlands, 1994.
- [54] J.M. Hermans. Diffusion in soda-lime-silica glass melts. Personal Communication, 2006.
- [55] H. Müller-Simon. On the interaction between oxygen, iron and sulfur in industrial glass melts. *Glastechn. Ber. Glass Sci. Technol.*, 67(11):297–303, 1994.
- [56] D. Moseler, C. Müller-Fildebrandt, G. Heide, G. H. Frischat, W. Meisel, A. Maldener, A. Zouine-Thimm, and F. Rauch. Zinn im Floatglas. AiF Abschlußbericht 11460N, Institut für Nichtmetallische Werkstoffe, Claustal University of Technology, Germany, 2000.
- [57] C. Müller-Fildebrandt. *Wechselwirkung von Zinnschmelze und Floatglas*. PhD thesis, Claustal University of Technology, Germany, 2000.
- [58] A. Dietzel. Praktische Bedeutung und Berechnung der Oberflächenspannung von Gläsern, Glasuren und Emails. *Sprechsaal*, 75(9/10):82–85, 1942.
- [59] M. Kizilyalli, J. Corish, and R. Metselaar. Definitions of terms for diffusion in the solid state, IUPAC recommendations . *Pure Appl. Chem.*, 171(7):1307–1325, 1999.
- [60] J. de Strycker, S. Gerlach, G. von der Gönna, and C. Rüssel. Voltammetric studies of  $\text{Fe}^{2+}/\text{Fe}^{3+}$ -redox equilibria in some  $\text{Na}_2\text{O}$  -  $\text{CaO}$  -  $\text{Al}_2\text{O}_3$  -  $\text{SiO}_2$  liquids. *J. Non-Cryst. Sol.*, 272:131–138, 2000.
- [61] G. von der Gönna and C. Rüssel. Diffusivities of polyvalent elements in a  $15\text{Na}_2\text{O}$  -  $85\text{SiO}_2$  glass melt. *J. Non-Cryst. Sol.*, 272:139–146, 2000.
- [62] A. Wiedenroth and C. Rüssel. Thermodynamics of the equilibrium  $\text{Fe}^{2+}/\text{Fe}^{3+}$  and the diffusivity of iron in  $5\text{Na}_2\text{O}$  -  $15\text{MgO}$  -  $x\text{Al}_2\text{O}_3$  -  $(80 - x)\text{SiO}_2$  ( $x=0-20$ ) melts. *J. Non-Cryst. Sol.*, 297:173–181, 2002.
- [63] *CRC Handbook of Chemistry and Physics*. CRC Press, Inc, Boca Raton, Florida, 64 edition, 1983-1984.
- [64] K. Papadopoulos. The solubility of  $\text{SO}_3$  in soda-lime-silica melts. *Phys. Chem. Glasses*, 14(3):60–65, June 1973.



- 
- [65] M. Szurman, G. Heide, G.H. Frischat, and T. Pfeiffer. Sulfur diffusion in silicate melts. In *Proc. 80. Glastechnische Tagung & 8th International Conference , Advances in the Fusion and Processing of Glass*, 2006. Dresden, Germany.
  - [66] The MathWorks Inc. *Matlab®*, *The Language of Technical Computing*, 1984-2002. [www.mathworks.com](http://www.mathworks.com).
  - [67] W. H. Press, S. A. Teukolsky, W. T. Vetterling, and B. P. Flannery. *Numerical Recipes in C, The Art of scientific computing*. Cambridge University Press, second edition, 1997.
  - [68] A. A. Prousevitch, D. L. Sahagian, and A. T. Anderson. Dynamics of diffusive bubble growth in magmas: isothermal case. *J. Geophys. Res.*, 98(B12):22283–22307, 1993.

## 5.10 Appendix

### 5.10.1 Integration of momentum equation

The integration of equation (5.11), combined with equation (5.4), between the two borders of the glass shell ( $R_1$  and  $R_2$ ) is:

$$\int_{R_1}^{R_2} -\frac{\partial p}{\partial r} dr - \int_{R_1}^{R_2} \frac{1}{r^2} \frac{\partial}{\partial r} \left( -2\mu \frac{\partial v_r}{\partial r} \cdot r^2 \right) dr - \int_{R_1}^{R_2} 4\mu \frac{v_r}{r^2} dr = 0 \quad (5.92)$$

Integration of the first term results in:

$$\int_{R_1}^{R_2} -\frac{\partial p_l}{\partial r} dr = p_l(R_1) - p_l(R_2) \quad (5.93)$$

Integration of the second term, substituting equation (5.4), results in:

$$\begin{aligned} \int_{R_1}^{R_2} -\frac{1}{r^2} \frac{\partial}{\partial r} \left( -2\mu \frac{\partial v_r}{\partial r} \cdot r^2 \right) dr &= \int_{R_1}^{R_2} \frac{1}{r^2} \frac{\partial}{\partial r} \left( \frac{4\mu R_1^2 v_{R_1}}{r} \right) dr \\ &= -4\mu R_1^2 v_{R_1} \int_{R_1}^{R_2} \frac{1}{r^4} dr \\ &= -\frac{4}{3} \mu R_1^2 v_{R_1} \left[ \frac{1}{R_2^3} - \frac{1}{R_1^3} \right] \end{aligned} \quad (5.94)$$

The integration of the third term, substituting equation (5.4), results in:

$$\begin{aligned} \int_{R_1}^{R_2} -4\mu \frac{v_r}{r^2} dr &= 4\mu R_1^2 v_{R_1} \int_{R_1}^{R_2} \frac{1}{r^4} dr \\ &= \frac{4}{3} \mu R_1^2 v_{R_1} \left[ \frac{1}{R_2^3} - \frac{1}{R_1^3} \right] \end{aligned} \quad (5.95)$$

The sum of equations (5.94) and (5.95) is zero. The complete integration of equation (5.11) between  $R_1$  and  $R_2$  becomes:

$$p_l(R_1) - p_l(R_2) = 0 \quad (5.96)$$

### 5.10.2 Lagrangian coordinate transformation

This appendix describes briefly the coordinate system transformation which was applied in section 5.3 on page 143 to simplify the mass transport equation. The thinning of the glass shell during bubble growth in the foaming glass (moving fluid sphere) introduces a convective term in the original differential equation and a moving glass domain. Because the radii  $R_1$  and  $R_2$  change during the bubble growth, the domain in which the mass transfer calculations are performed has to be re-meshed after each time step. By applying a Lagrangian coordinate transformation, which is commonly used for solving aerodynamic problems [44], it is possible to transform the description of the moving system relative to a fixed axis system into an axis system moving with the glass shell. This significantly simplifies the numerical calculations. Applying the transformation, the convection term of the mass transfer equation (5.23) on page 131 is eliminated. As a consequence of the transformation, the space and time variables  $r$  and  $t$  are transformed into the new spacial variable function  $\xi(r, t)$  and a new time variable  $\Theta$ , respectively. The coordinate transformation of the space and time variable was done according to Anderson [44] as follows:

For the first derivative of the space variable we obtain the mathematical expression:

$$\frac{\partial}{\partial r} = \frac{\partial}{\partial \xi} \frac{\partial \xi}{\partial r} \quad (5.97)$$

and for the second derivative of the space variable:

$$\frac{\partial^2}{\partial r^2} = \frac{\partial}{\partial r} \left[ \frac{\partial}{\partial \xi} \frac{\partial \xi}{\partial r} \right] = \frac{\partial}{\partial \xi} \frac{\partial^2 \xi}{\partial r^2} + \frac{\partial \xi}{\partial r} \frac{\partial^2}{\partial r \partial \xi} = \frac{\partial}{\partial \xi} \frac{\partial^2 \xi}{\partial r^2} + \frac{\partial^2}{\partial \xi^2} \left( \frac{\partial \xi}{\partial r} \right)^2 \quad (5.98)$$

with

$$\frac{\partial^2}{\partial r \partial \xi} = \frac{\partial}{\partial r} \frac{\partial}{\partial \xi} = \frac{\partial^2}{\partial \xi^2} \frac{\partial \xi}{\partial r} \quad (5.99)$$

For the time variable  $\Theta$  we get:

$$\frac{\partial}{\partial t} = \frac{\partial}{\partial \xi} \frac{\partial \xi}{\partial t} + \frac{\partial}{\partial \Theta} \frac{\partial \Theta}{\partial t} \quad (5.100)$$

The ordinary differential equation for the bubble growth, for the mass balance at the glass-bubble interface and for the heating rate are valid at the left boundary of the diffusion domain and do not contain spatial variables. Therefore the transformation of the time variable simplifies in these cases to:

$$\frac{\partial}{\partial t} = \frac{\partial}{\partial \Theta} \frac{\partial \Theta}{\partial t} \quad (5.101)$$

Table 5.10: Some  $\sigma_i$  values (N/m/wt.%) determined by Dietzel [58] to estimate the surface tension of a soda lime silicate glass at 1173 K. A compositional validity range is not given.

Oxide	$\sigma_i \cdot 10^3$	Oxide	$\sigma_i \cdot 10^3$
	N/m/wt.%		N/m/wt.%
SiO <sub>2</sub>	3.4	Na <sub>2</sub> O	1.5
Al <sub>2</sub> O <sub>3</sub>	6.2	CaO	4.8
MgO	6.6	Fe <sub>2</sub> O <sub>3</sub>	4.5
MnO	4.5	K <sub>2</sub> O	0.1
PbO	1.2	ZnO	4.7
TiO <sub>2</sub>	3.0	ZrO <sub>2</sub>	4.1

### 5.10.3 Physicochemical glass melt properties

#### Surface tension of the glass

A method to calculate the surface tension of a glass melt, based on the glass composition is given by Dietzel [58]. The model is based on an additive technique of surface tension contributions  $\sigma_i$  per weight% of oxide  $i$  in the glass. The  $\sigma_i$  of some oxides are given in table 5.10. The surface tension at 1173 K can then be calculated according to:

$$\sigma = \sum_i \sigma_i W_i \quad (5.102)$$

In most technical glasses, the surface tension decreases with increasing temperature. According to Scholze [28], this temperature dependence is between  $4$  to  $10 \cdot 10^{-3} \text{ Nm}^{-1}$  per 100 K. Dietzel published a temperature dependency of  $4 \cdot 10^{-3} \text{ Nm}^{-1}$  per 100 K, which is used for the simulation. The temperature dependent surface tension then becomes:

$$\sigma(T) = \sigma(1173K) - 0.004 \frac{T - 1173}{100} \quad (5.103)$$

To use the surface tension in the calculation for the bubble model it must be written as function of the dimensionless temperature. Therefore  $\sigma_0 = \sigma(t = 0)$  is calculated at the starting temperature of the model simulation ( $T_0$ ) using equation (5.103). The surface tension as function of the dimensionless temperature  $T^*$  then becomes:

$$\sigma(T^*) = \sigma_0 - 4 \cdot 10^{-5} T_0 (T^* - 1) \quad (5.104)$$

which can also be written as:

$$\sigma(T^*) = \sigma_0 f(T^*) \quad (5.105)$$

with

$$f(T^*) = \left(1 - 4 \cdot 10^{-5} \frac{T_0}{\sigma_0} (T^* - 1)\right) \quad (5.106)$$

Table 5.11: Some factors as determined by Lakatos et al. [31] to calculate the glass melt viscosity using the Vogel-Fulcher-Tamman equation (equation (5.107)) and the compositional validity range of the model parameters. The factors  $a'_i$ ,  $b'_i$  and  $c'_i$  are based on  $p'_i$  values given as mole(component  $i$ )/mole( $\text{SiO}_2$ ).

Oxide	$a'_i$	$b'_i$ (K)	$c'_i$ (K)	validity range in wt.%
$\text{Na}_2\text{O}$	1.4788	-6039.7	-25.07	10-15
$\text{K}_2\text{O}$	-0.835	-1439.6	-321.0	0-8
$\text{MgO}$	-5.4936	6285.3	-384.0	0-4
$\text{CaO}$	-1.6030	-3919.3	544.3	9-13
$\text{Al}_2\text{O}_3$	1.5183	2253.4	294.4	0-7

### Viscosity of the glass melt

The dynamic viscosity  $\mu$  of a glass melt can be estimated using the Vogel-Fulcher-Tamman (VFT) equation according to [28]:

$$\log(\mu/(\text{Pa} \cdot \text{s})) = A + \frac{B}{T - C} \quad (5.107)$$

where A, B, and C are constants which depend on the glass composition and T is the temperature in K. The constants A, B, and C can be either calculated according to the model developed by Lakatos et al.<sup>11</sup> [31] or determined experimentally. According to the model, for soda lime silicate melts, the compositional validity range is given in table 5.11, the VFT constants can be calculated according to:

$$A = -2.4550 + \sum_i a'_i p'_i \quad (5.108)$$

$$B = 5736.4 + \sum_i b'_i p'_i \quad (5.109)$$

$$C = 471.25 + \sum_i c'_i p'_i \quad (5.110)$$

where  $p'_i$  is the molar fraction of oxide  $i$  per mole  $\text{SiO}_2$  and  $a'_i$ ,  $b'_i$  and  $c'_i$  are the Lakatos constants per oxide. The constants are given in table 5.11, together with the compositional validity range of the model for some exemplary oxides. The validity range with respect to viscosity, according to Lakatos et al. is  $10\text{-}10^{12} \text{ Pa} \cdot \text{s}$ . The composition of the glasses used for the validation of the bubble model lies slightly outside the compositional range of the Lakatos model. Therefore, the viscosity of these two glasses was also determined experimentally by the fiber elongation method in order to validate the usage of the Lakatos model for the model calculations. The result of the experimental viscosity determination is given in table 5.12 and graphically shown in figure 5.29. It can be seen that the Lakatos model reconstructs well the temperature-viscosity relation of the model

<sup>11</sup>It should be noted that the values for A,B and C in the publication by Lakatos are calculated in the unit Poise and not in  $\text{Pa} \cdot \text{s}$  as given here. The constant C, which incorporates the temperature was also transformed to K instead of  $^\circ\text{C}$ .

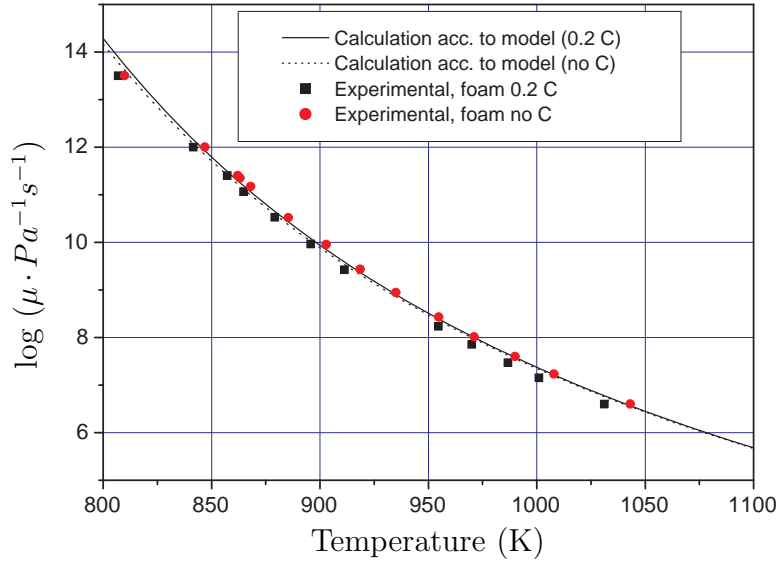


Figure 5.29: Viscosity of glasses used for the foam model validation as a function of temperature. Comparison between the calculated viscosities using the VFT-relation and the Lakatos coefficient [31] and the experimental values, determined by the fiber elongation method.

glasses in this temperature range. For the validation of the numerical model, the experimentally determined viscosity - temperature relations were used.

It should be noted that a foam sample is a mixture of glass and carbon particles. The carbon particles, which have not yet reacted during foaming are present in the viscous glass melt or at its surface as solid suspended particles. This can cause extra friction between the glass and the incorporated particles causing an increase in apparent viscosity. However, Köse [3] has shown that this effect can be neglected for additive concentrations less than 5 vol.%. Therefore, this effect is also neglected in this study.

The viscosity  $\mu$  is a property appearing in the dimensionless numbers given by equations (5.70) and (5.71). However, the viscosity is a temperature dependent property and

Table 5.12: VFT constants  $A, B$  and  $C$  of equation (5.107) for the two glasses used for the model validation. The first two rows represent the model viscosities according to the Lakatos model, the last two rows represent the experimentally determined viscosities according to the fiber elongation method.

Glass	$A$	$B$ (K)	$C$ (K)
Model Foam glass no C (VFT+Lakatos)	-2.5668	4856.1115	509.28
Model Foam glass 0.2wt.% C (VFT+Lakatos)	-2.5632	4843.4023	512.55
Foam glass no C (experimental)	-5.3159	7391.5366	418.63
Foam glass 0.2 wt.% C (experimental)	-5.2412	7089.5044	429.58

therefore it is written in the following form:

$$\mu(T) = \mu_0 10^{g(T)} \quad (5.111)$$

with

$$g(T) = B \frac{T_0 - T}{(T - C)(T_0 - C)} \quad (5.112)$$

where  $\mu_0 = \mu(t = 0)$  and  $T_0 = T(t = 0)$ .  $B$  and  $C$  are according to equation (5.107). Including the dimensionless parameter for the temperature, we get:

$$\mu(T^*) = \mu_0 z(T^*) \quad \text{with} \quad z(T^*) = 10^{g(T^*)} \quad (5.113)$$

and

$$g(T^*) = \frac{B}{T_0} \frac{1 - T^*}{\left(T^* - \frac{C}{T_0}\right) \left(1 - \frac{C}{T_0}\right)} \quad (5.114)$$

### Diffusion coefficients

To calculate the mass transport of physically and chemically dissolved oxygen in the glass melt shell, the diffusion coefficients of the different polyvalent ions and physically dissolved oxygen must be known. Different types of diffusion coefficients exist, depending on the method they were measured. For more detailed reading it is referred to a very profound thesis on diffusion in multicomponent silicate glass melts [2]. A brief definition of diffusion coefficients, taken over from [2], is given as follows:

**The inter-diffusion coefficient** is determined from concentration gradients following Fick's first law, relative to outside references. According to the IUPAC recommendations, the inter-diffusion coefficient is also referred to as "chemical diffusion coefficient" [59].

**The intrinsic-diffusion coefficient** is defined relative to the marker plane, the plane through which no net transfer takes place this plane may not be static relative to outside references.

**The tracer-diffusion coefficient** refers to the diffusion coefficient of labeled atoms in the absence of a gradient in chemical potential. According to the IUPAC recommendations, the tracer-diffusion coefficient is also referred to as "self diffusion coefficient" [59].

The so called inter-diffusion coefficient, is applied in this study. The diffusion coefficients used in this thesis are derived from literature data. It was beyond the scope of this project to experimentally determine the diffusion coefficients in glasses used for foam glass production. Therefore, literature data or calculations based on literature data is used as to find best estimates.

Diffusion coefficients of ions or gases in the glass melt depend on the glass composition. Most measurements of intrinsic diffusion coefficients of polyvalent ion species are carried out for soda-lime glass melts using voltammetric methods with relatively low additions

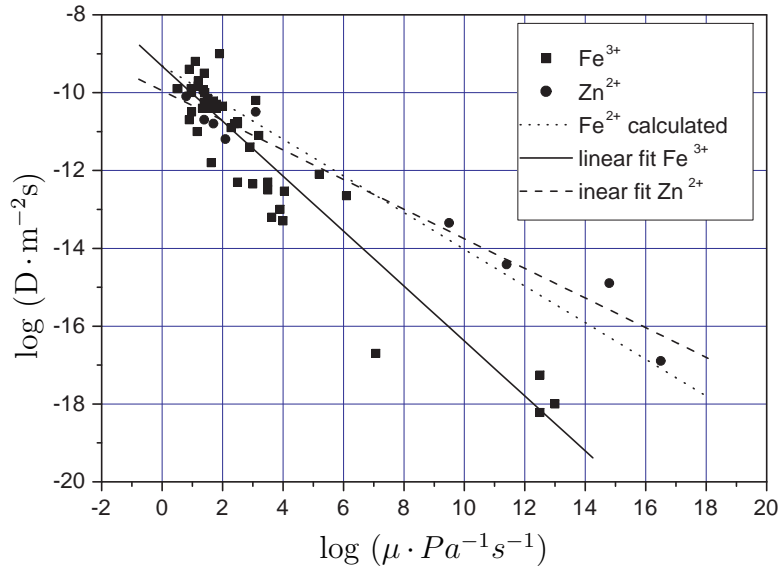


Figure 5.30: Estimated inter-diffusion coefficients of  $\text{Fe}^{3+}$ ,  $\text{Fe}^{2+}$  and  $\text{Zn}^{2+}$  in glass melts versus glass viscosity for different glass compositions according to Hermans [2]. The values for  $\text{Fe}^{2+}$  were calculated as described in the text of this appendix.

of polyvalent species (0.25-0.5 mol% [60–62]), compared to concentrations of polyvalent ions in glasses used for foam glass production. Using voltammetric methods, the intrinsic diffusion coefficient is measured (movement of the ions due to an applied voltage). The glasses used for foam glass production contain up to 3.5 wt.%  $\text{Fe}_2\text{O}_3$ . Regarding the relatively low foaming temperature (873 - 1273 K), also data for inter-diffusion coefficients in highly viscous melts should be considered. Hermans [2] compiled a large data set of inter-diffusion coefficients for different species in different glasses and presented the compilation in so called Stokes plots ( $\log D$  versus  $\log \mu$ ). Thereby, a direct relation between on the one hand the inter-diffusion coefficient and on the other hand the electric charge of the ion and the viscosity of the glass is obtained. With the knowledge of the temperature viscosity relation, e.g., the Lakatos model, a temperature dependent inter-diffusion coefficient can be estimated.

The data as presented by Hermans [2] is plotted in a Stokes plot and fitted by linear regression. The data points together with the regression lines are given in figures 5.30 and 5.31.

### Diffusion coefficient of physically dissolved $\text{O}_2$

Figure 5.31 shows the inter-diffusion coefficient of  $\text{O}_2$  as a function of the glass viscosity as fitted from the data by Hermans [2]. The result of the linear fit is:

$$\log D_{\text{O}_2}(T) = (-0.69 \pm 0.06) \log \mu(T) - (9.2 \pm 0.4) \quad (5.115)$$



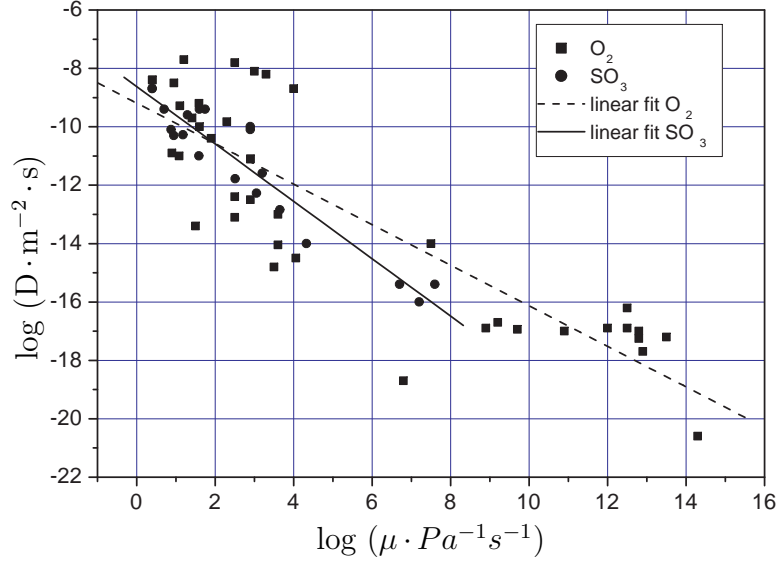


Figure 5.31: Estimated inter-diffusion coefficients of  $O_2$  and  $SO_3$  in glass melts versus glass viscosity for different glass compositions according to Hermans [2]. For the description of the derivation of estimated  $SO_3$  diffusion coefficients see the text.

#### Diffusion coefficient for $Fe^{3+}$ and $Fe^{2+}$

The inter-diffusion coefficient for the two different polyvalent species of iron can be estimated from figure 5.30. The estimated diffusion coefficient of  $Fe^{3+}$  was determined by linear regression:

$$\log D_{Fe^{3+}}(T) = (-0.71 \pm 0.04) \log \mu(T) - (9.3 \pm 0.2) \quad (5.116)$$

The inter-diffusion coefficient for  $Fe^{2+}$  could not be directly extracted from the literature data. A rough estimation can be made by using the equation for  $Fe^{3+}$  and correcting for the charge of the metal ion, which means to multiply the slope of the curve according to the relation found between the apparent inter-diffusion coefficient and the charge of the ion [2], represented by equation (5.116), with  $2/3$ . This results in:

$$\log D_{Fe^{2+}}(T) = (-0.47 \pm 0.03) \log \mu(T) - (9.3 \pm 0.2) \quad (5.117)$$

Another possibility to estimate the inter-diffusion coefficient for  $Fe^{2+}$  is to look at an other metal ion with the same charge and the same ionic radius as  $Fe^{2+}$ . The ionic radius of  $Zn^{2+}$  is  $0.74 \text{ \AA}$ , almost the same as for  $Fe^{2+}$  [63]. The inter-diffusion coefficient of  $Zn^{2+}$ , was also fitted using the data by Hermans and is given in figure 5.30. It is in acceptable agreement compared to the calculated inter-diffusion coefficient of  $Fe^{2+}$ . For the modeling studies, equation (5.117) has been used.

#### Diffusion coefficients for $SO_4^{2-}$ , $SO_3^{2-}$ and $S^{2-}$

Figure 5.31 shows a relation to estimate the inter-diffusion coefficient of sulphur in oxide glasses expressed as the inter-diffusion coefficient of  $SO_3$  [2]. According to Müller-Simon

[37], the relevant sulphur species in soda-lime-silicate glasses are  $\text{SO}_4^{2-}$ ,  $\text{SO}_3^{2-}$  and  $\text{S}^{2-}$  or  $\text{S}^{6+}$ ,  $\text{S}^{4+}$  and  $\text{S}^{2-}$ , respectively. Under oxidizing conditions, sulphur can dissolve in glass as sulphate [64]. Under more reduced conditions sulphur can dissolve in glass, physically as  $\text{SO}_2$  and chemically as sulphite and under more extreme reduced conditions as  $\text{S}^{2-}$ . However, not much information is available about the type of sulphur species diffusing, e.g.,  $\text{SO}_4^{2-}$ ,  $\text{S}^{6+}$  or  $\text{SO}_3$  or about the values of the different diffusion coefficients. Sulphur and iron can practically always be found in glasses prepared from municipal solid waste fly ash. This is the reason for iron oxide and sulphurous species being incorporated into the bubble model. No literature references for diffusion coefficients of these species are available. Therefore one diffusion coefficient for all species can be estimated from the data compiled by Hermans and shown in figure 5.31. The relation between the inter-diffusion coefficient and the viscosity is given by [2]. According to [54, 65], the inter-diffusion coefficient of  $\text{SO}_3$  is:

$$\log D_{\text{SO}_3}(T) = (-0.98 \pm 0.08) \log \mu(T) - (8.6 \pm 0.3) \quad (5.118)$$

However, to demonstrate the model's capability, a different inter-diffusion coefficient for  $\text{S}^{2-}$  was chosen. As a rough estimation for the inter-diffusion coefficient for  $\text{S}^{2-}$ , the tracer-diffusion coefficient for  $\text{O}^{2-}$ , having the same charge as  $\text{S}^{2-}$  was chosen, assuming that both diffusion coefficient as are equal ( $D^{\text{tracer}} = D^{\text{inter}}$ ). The tracer-diffusion coefficient for  $\text{O}^{2-}$  was also derived from data provided by by Hermans to be:

$$\log D_{\text{O}^{2-}}(T) = (-0.54 \pm 0.08) \log \mu(T) - (10.8 \pm 0.5) \quad (5.119)$$

It was beyond the scope of this project to experimentally determine the different diffusion coefficients of the polyvalent ions included in the model. Therefore these estimations from literature references were chosen.

The Fourier number, which is often used to non-dimensionalize the time variable in mass transport equations, cannot be applied in the conventional sense (there  $D$  is assumed to be constant). Here, the inter-diffusion coefficients are temperature dependent. The inter-diffusion coefficients of the different species are assumed to be independent of the spatial position, since the temperature is assumed to be uniform over the diffusion domain and independent on glass composition. It is therefore necessary to transform the equations, describing diffusion, into a constant term and a temperature dependent term, where the constant term is used in the Fourier number to non-dimensionalize the time variable:

$$D_i(T) = D_{i,0} \left( \frac{\mu_{i,0}}{\mu_i(T)} \right)^{d_i} \quad (5.120)$$

where  $D_{i,0}$  and  $\mu_{i,0}$  are the values for the diffusion coefficient and the viscosity at  $t=0$  which means at the beginning of the foaming process. The parameter  $d_i$  describes the different viscosity (temperature) dependencies of the different diffusion coefficients of the species  $i$ . In terms of dimensionless temperature, we obtain:

$$D_i(T^*) = D_{i,0} z(T^*)^{-d_i} \quad (5.121)$$

where  $z(T^*)$  is defined according to equation (5.113).

### 5.10.4 Numerical implementation

The description of diffusion processes of the kind discussed in this chapter cannot be treated analytically and have to be solved using numerical techniques. The computer program *Matlab*<sup>®</sup>, version 6 [66] provides a solver for partial differential equations (*pdepe.m*). This software was used to solve the set of model equations. However, because of the complexity of the model equations and the generality of the provided code and discretization scheme, adaptations to the basic code were necessary. This subsection discusses the modifications and shows that the modified *Matlab*<sup>®</sup> routines can be used to solve these sort of numerical problems. It is not the intention of this subsection to explain numerical solution techniques in detail.

The modifications to the code include at first the implementation of the simultaneous solving of partial and ordinary differential equations. Secondly, modifications in the discretization scheme were required, because of the strong nonlinearity of the source term in the diffusion equation, which induced strong oscillations. Thirdly, an adaption of the spatial grid due to the steep concentration gradients at the glass bubble interface were necessary. The modifications are going to be discussed in more detail in the following.

The model equations consist of multiple partial differential equations (pde's), (one for each diffusing species (equation (5.75)) and three ordinary differential equations (ode's), (bubble growth (equation ((5.74)), molar oxygen flux (equation ((5.76)) and temperature (equation ((5.77))), which have to be computed simultaneously. It was not possible to compute pde's and ode's simultaneously without modifications to the code. The routine *pdepe.m* is actually a routine which defines, e.g., the spatial and time grid. The routine *pdepe.m* then uses another routine (*ode15s.m*) to solve the discretized set of equations. In order to solve the pde's and ode's simultaneously, the ode's were added to the set of discretized pde's and the whole set was sent to the ode solver to be solved.

The second modification to the code was the modification of the discretization scheme. The original code, as provided in the *Matlab*<sup>®</sup> routine *pdepe.m*, uses a central difference scheme. Because of the strong nonlinearity of the source term<sup>12</sup> strong oscillations of the calculated concentration profiles were observed. In order to overcome these numerical instabilities, the discretization scheme was changed to a forward differencing scheme [67].

Another cause of strong oscillations was the source term of the diffusion equation at the position of the left boundary, the bubble-glass interface. From equation (5.50) it can be seen that the molar rate of production of physically dissolved oxygen is negatively correlated with the production rates of the oxidized form of the polyvalent ions. If the concentration of the oxidized form of the polyvalent ion ( $[M_i^{b_i+}]$ ) approaches zero, the numeric value of its production term strongly increases, see for an example with iron oxide

---

<sup>12</sup>The source term describes production or reaction of species to maintain the conditions of thermodynamic equilibrium of the different polyvalent ions in the glass melt. These chemical equilibrium reactions influence the concentration profiles. The derivation of the equations is given in section 5.2.6 on page 133.

equation (5.39).

$$Q_{Fe^{3+}} = -Q_{(R30)} = k'_{Fe} \left[ \frac{[Fe^{2+}]}{K''_{Fe}} \left( \frac{[O_2]}{L_{O_2}} \right)^{1/4} - [Fe^{3+}] \right] \quad (5.39)$$

Because the concentration of the physically dissolved oxygen is about 8 orders of magnitude smaller than the ones of most polyvalent ions (e.g.  $Fe^{3+}$ ), the negative correlation causes numerical instabilities. These instabilities have two reasons. The first one is the large differences in concentration of  $[M_i^{b+}]$  and  $[O_2]$ , and the second one is the boundary condition of the mass transport equation. This boundary conditions of the model describes an irreversible reaction of oxygen from the glass towards the gas bubble. In case that almost all oxygen is consumed at the surface of the bubble, the concentration of  $O_2$  approaches zero introducing the already described numerical instabilities for solving the pde's for the polyvalent ions at  $r = R_1$ . A practical solution to solve this problem is omitting the production term ( $\Psi$ ) in the diffusion equation for all species  $i$  at the left boundary (glass-bubble interface) only. This introduces an error because the production term is a volumetric term and not a surface term, compensating the deviation from thermodynamic equilibrium between the polyvalent ions and physically dissolved oxygen in the very first layer (shell)<sup>13</sup>. In case that the volume of the glass shell between the inner boundary and the first gridpoint of the diffusion domain is small, the error, which is introduced will also be small. This can be achieved by choosing a very short distance between the left boundary and the first gridpoint. The transformed non-dimensional diffusion domain lies between 0 and 1 and a distance of  $10^{-6}$  between the first (the interface) and the second gridpoint was found to be sufficient small to produce numerically stable results. Decreasing this distance even more, did not effect the solution.

Apart from the strong nonlinearity of the source term, the concentration profiles at the inner boundary become very steep due to their compression induced by the expanding bubble [68] and the reduction by carbon. If a spatial mesh is used which is too small, the time steps to be able to solve the equations become very small, sometimes too small for the program to be solved. A too coarse grid at the inner (left) boundary produces very rough concentration profiles, but would be sufficient for the outer (right) boundary. In order to overcome this problem, a logarithmic grid is used, which accumulates more gridpoints near the inner boundary and becomes coarser towards the outer boundary.

With these modifications to the *Matlab*® routines, it is now possible to calculate the bubble growth in foam glass and to study the influence of permanent thermodynamic equilibrium between the polyvalent ions in the glass on their concentration profiles.

---

<sup>13</sup>The griding of the diffusion domain subdivides the glass shell in multiple shells, in which the diffusion equation are computed. Omitting the production term at the left boundary influences the computed result for the first shell and thus the first volume element.

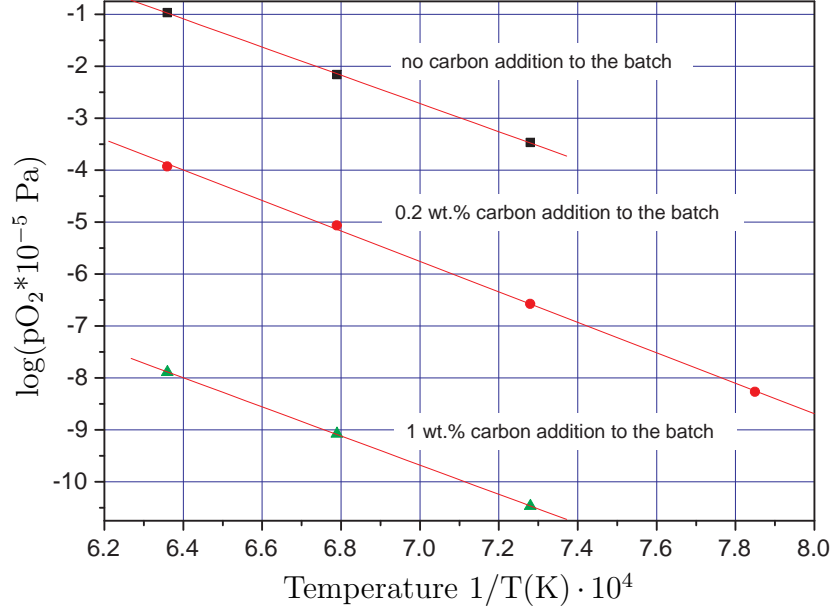
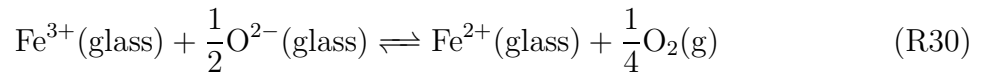


Figure 5.32: Partial oxygen pressure in equilibrium with dissolved oxygen in the glass as a function of the reciprocal temperature of the three different glasses used for the determination of the thermodynamic values  $\Delta H^{*r}$  and  $\Delta S^{*r}$ . The difference between the glasses is the addition of 0.2 wt.% and 1 wt.% of active carbon to the batch.

### 5.10.5 Experimental determination of $\Delta H^{*r}$ and $\Delta S^{*r}$ values of iron oxide redox reactions in the glass melt

This subsection presents the derivation of the equations necessary for the determination of the thermodynamic properties  $\Delta H^{*r}$  and  $\Delta S^{*r}$  of the iron redox equilibrium as expressed in reaction (R30) for the two glasses used for the foaming experiments.



It should be noted that three glasses were prepared and used for the determination of the thermodynamic properties whereas only two glasses were used for the foam model validation.

The values of  $\Delta H^{*r}$  and  $\Delta S^{*r}$ , derived from the equilibrium constant defined on the basis of concentrations rather than activity values, can be calculated, when the partial oxygen pressure in equilibrium with dissolved oxygen in the glass as a function of temperature is known as well as the concentrations of the  $\text{Fe}^{3+}$  and  $\text{Fe}^{2+}$  ions at the same temperature. After the preparation of the glass, the partial oxygen pressure in equilibrium with dissolved oxygen has been measured between 1673 and 1273 K using the method described in [46, 47]. The results are given in figure 5.32. The concentration of the  $\text{Fe}^{2+}$  ions in the glass was measured at room temperature by IR-spectrophotometric transmission measurement as described in chapter 4, section 4.3.3 on page 105. During cooling, the oxidation state of silicate glasses can change. However, as seen in reaction (R30),

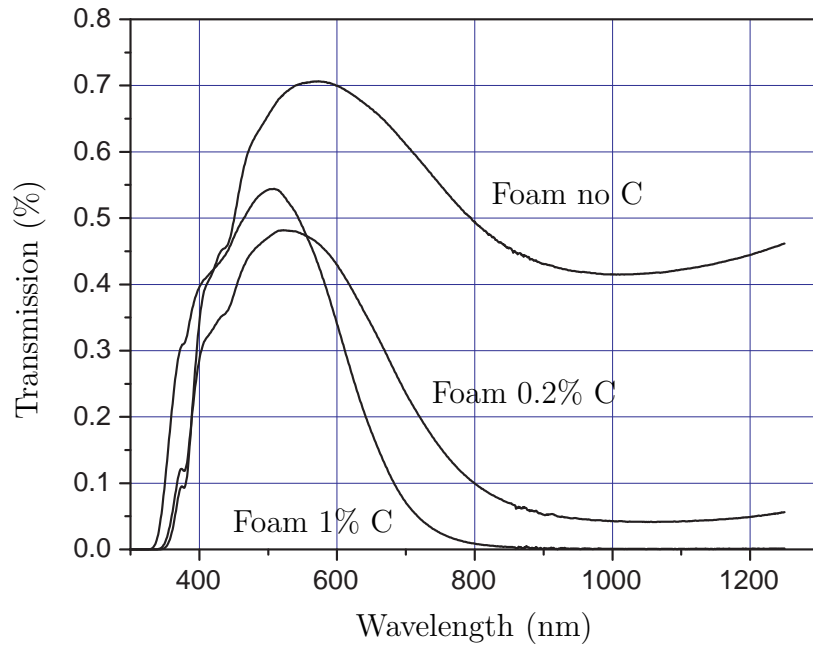


Figure 5.33: Transmission spectra of the three glasses used for the determination of the thermodynamic properties. The method is described in chapter 4, section 4.3.3 on page 105.

the equilibrium reaction shifts to the right side with increasing temperature, producing physically dissolved oxygen, which can leave the glass. During cooling of these glasses containing only iron as polyvalent ion, the concentration of physically dissolved oxygen in the melt, compared to  $[\text{Fe}^{2+}]$ , is negligible and will not lead to significant changes of the  $\text{Fe}^{2+}$  or  $\text{Fe}^{3+}$  concentration. During fast cooling hardly any oxygen from, e.g., the melting atmosphere, can enter the melt. The result of the spectrophotometric measurement of the glasses is shown in figure 5.33. With known  $\text{Fe}^{2+}$  concentration, the concentration of the  $\text{Fe}^{3+}$  can readily be derived from the total iron oxide concentration in the glass. An overview of the measured and calculated concentrations is given in table 5.13 on page 198.

Table 5.13: Measured  $\text{Fe}^{2+}$ , measured total Fe and calculated  $\text{Fe}^{3+}$  concentrations of the different used glasses.  $\tau_{1050}$  denotes the internal transmission value at 1050 nm (%). The composition of the glass is given in table 5.2 on page 150.

Glass	$\tau_{1050}$ (%)	$\text{Fe}_{\text{tot}}$ ( $\text{mol} \cdot \text{m}^{-3}$ )	$\text{Fe}^{2+}$ ( $\text{mol} \cdot \text{m}^{-3}$ )	$\text{Fe}^{3+}$ ( $\text{mol} \cdot \text{m}^{-3}$ )
Foam no C	39.90	918.69	79.57	839.13
Foam 0.2 wt.% C	41.20	983.65	317.75	665.90
Foam 1 wt.% C	0.06	927.97	751.46	176.51

The relation between  $\Delta G^{*r}$  and the equilibrium constant based on concentration  $K^*$ ,

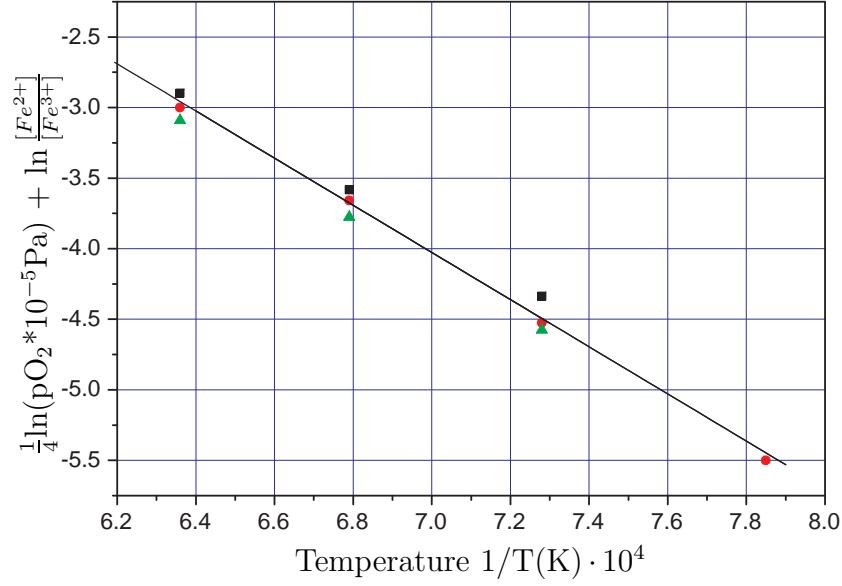


Figure 5.34: Partial oxygen pressure as a function of the reciprocal temperature of the three different glasses. The values for  $\Delta H^{*r}$  and  $\Delta S^{*r}$  were calculated from the slope and the intercept of the regression line as given by equation (5.124)

as was already discussed in section 5.2.6, is:

$$\Delta G^{*r} = \Delta H^{*r} - T \Delta S^{*r} = -R_g T \ln K^* \quad (5.122)$$

where  $\Delta G^{*r}$  is the Gibbs energy change of the reaction,  $\Delta H^{*r}$  the reaction enthalpy and  $\Delta S^{*r}$  the reaction entropy. The reference state is 1 bar pressure for the gaseous species.  $R_g$  denotes the ideal gas constant and  $T$  the absolute temperature.  $K^*$  is the apparent thermodynamic equilibrium constant based on concentration values, which is:

$$K^* = K a_{O_2}^{1/2} \frac{\gamma_{Fe^{2+}}}{\gamma_{Fe^{3+}}} = \frac{[Fe^{2+}] \cdot pO_2^{1/4}}{[Fe^{3+}]} \quad (5.123)$$

where  $a$  denotes the chemical activity and  $\gamma$  the activity coefficients. Combining equations (5.122) and (5.123), we obtain:

$$\frac{1}{4} \ln pO_2 + \ln \frac{[Fe^{2+}]}{[Fe^{3+}]} = \frac{-\Delta H^{*r}}{R_g} \frac{1}{T} + \frac{\Delta S^{*r}}{R_g} \quad (5.124)$$

Equation 5.124 shows that the values of  $\Delta H^{*r}$  and  $\Delta S^{*r}$  can be calculated by plotting  $\frac{1}{4} \ln pO_2 + \ln \frac{[Fe^{2+}]}{[Fe^{3+}]}$  against  $\frac{1}{T}$  and deriving the values of the slope and the intercept of the plotted line. The graphical representation is given in figure 5.34. The determined values are for  $\Delta H^{*r}$ : **138.9 kJ · mol<sup>-1</sup>** and for  $\Delta S^{*r}$ : **63.8 J · mol<sup>-1</sup> · K<sup>-1</sup>**.

### 5.10.6 Image analysis of sintered powder and foam samples and volume expansion determination

This subsection describes two procedures for the determination of the initial model input parameters: the average initial bubble radius and the average thickness of the glass shell around the bubble.

1. The first procedure was applied to determine the number of bubbles per unit volume ( $N_V$ ) of sintered material, just after sintering but before foaming, the initial bubble radius and the initial thickness of the glass shell from cross section pictures of the sintered glass samples as explained in subsection 5.4.1 on page 152.
2. The second procedure uses the same principles as the first method and was used to determine the total volume of the foam body in each picture taken during the foaming experiments as explained in subsection 5.4.2 on page 154.

Both methods use the fact that a digital image consists of pixels, which can be expressed as a 2 or 3 dimensional array, depending whether it is a gray-scale or color image. Such an array represents one dimension for the x direction, one for the y direction and one for the colors. It is thus an (g-by-q-by-3) array in case of a truecolor (RGB) image or an (g-by-q) array in case of a gray image, where g is the number of pixels in x-direction and q the number of pixels in y-direction. A darker object in a gray scale image can be identified because of differences in intensities. With an intensity threshold it is possible to distinguish objects in digital images. The image analysis and the calculations were performed with the use of the computer program *Matlab*®, version 6 [66], which provided a routine to read the digital images and create the accordant arrays.

The next two subsections describe the application of the image analysis methods. The first one describes the extraction of the input data for the model from the images and the second one describes the derivation of the volume expansion from the digital pictures taken during the foaming experiments.

#### Determination of the number of bubbles per unit volume ( $N_V$ )

In order to determine  $N_V$  according to equation (5.84) for polyhedral bubbles [49],

$$N_V = 0.744 \frac{N_A^2}{N_L} \quad (5.84)$$

the average number of bubbles per unit length ( $N_L$ ) and the average number of bubbles per unit area ( $N_A$ ) are needed. An example of a picture from a sample cross section is given in figure 5.10 on page 153. As can be seen from the picture, the bubbles are represented by dark areas and the glass or lamellae by brighter areas, respectively. Thus, the cross sectioned bubbles can be distinguished from the lamellae by a difference in gray-scale intensity. The penetration length, i.e. the number of dark pixels in the bubbles in one direction can be determined for all pixel lines in the x and y direction of the picture. Thus for each pixel line, information on the number of bubbles and for each bubble the number of pixels inside the bubble is obtained. A representative scan of one of the lines is given



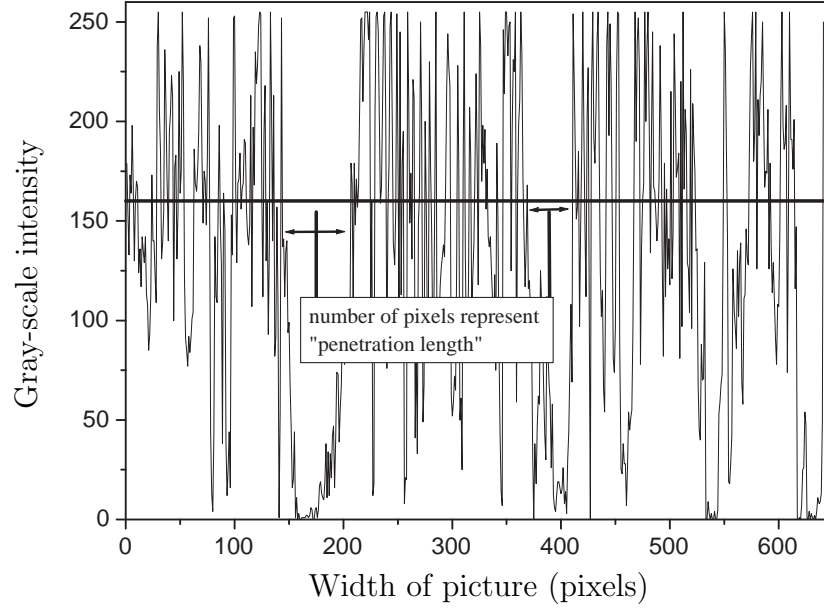


Figure 5.35: Scan in horizontal direction ( $x$ -direction) from  $x = 1$  to  $x = 640$  along pixel-line 230 ( $y = 230$ ) of figure 5.10. The solid horizontal line represents the threshold at 160.

in figure 5.35. The width of the total picture is 640 pixels, as given on the  $x$ -axis of figure 5.35. The horizontal bold line represents the intensity threshold to distinguish between bubble and glass. In this case a threshold of 160 was chosen, which means that intensities lower than 160 are considered to be inside a bubble and counted. Intensities larger than 160 are considered to be glass and were not counted. Prior to the scanning of one image, two vectors  $\vec{L}_x$  and  $\vec{L}_y$  were created with the length of the vector being the amount of pixels in  $x$  and  $y$  direction, respectively, thus  $g$  and  $q$ . The vectors were filled with zeros at all positions as starting values. The scanning of the image in the  $x$  direction started at  $y = 1$  and was performed for  $x = 1$  to  $x = g$  for all  $y$ . Scanning through a bubble, the pixels inside the bubble and below the threshold (penetration length) were counted. For example, when a bubble with ten pixels length was found, the count 1 was added to the 10th position of the vector. The position in the vector designated the number of pixels found in a bubble and the number on a specific position in the vector designated how often a bubble with that number of pixels (length) was found. The scanning in  $y$  direction was performed analogously. From  $\vec{L}_x$  and  $\vec{L}_y$ , the average number of bubbles in the directions  $x$  and  $y$  (pixels) can be calculated with equation (5.125). For the counting of the number of bubbles, only bubbles larger than 5 pixels were counted, to avoid that dark spots in the picture were counted for bubbles.

$$N_x = \frac{\sum_{x=6}^g(\vec{L}_x)}{q} \quad \text{and} \quad N_y = \frac{\sum_{y=6}^q(\vec{L}_y)}{g} \quad (5.125)$$

The average total number of bubbles in the picture can be calculated according to

$$N_{tot} = N_x \cdot N_y \quad (5.126)$$

With a scaling factor  $s$  ( $\text{pixels} \cdot \text{mm}^{-1}$ ) determined from figure 5.10,  $N_L$  and  $N_A$  per unit length can now be calculated with:

$$N_L = \frac{1}{2} \left[ \frac{N_x \cdot s}{g} + \frac{N_y \cdot s}{q} \right] \left( \frac{1}{\text{mm}} \right) \quad \text{and} \quad N_A = \frac{N_{tot} \cdot s^2}{g \cdot q} \left( \frac{1}{\text{mm}^2} \right) \quad (5.127)$$

With  $N_L$  and  $N_A$ ,  $N_V$  can be calculated according to equation (5.84). The initial average bubble radius and initial average shell thickness can be calculated according to equations (5.85) and (5.86) on page 154.

### Determination of the foam volume expansion from the digital images

To determine the volume of the foam sample from a 2 dimensional digital image, it was assumed that the foam sample is a body of rotational symmetry. As seen from figure 5.11 on page 155, the foam body can easily be distinguished by a gray scale threshold. The sum of all pixels in x-directions which are inside the foam body describe the diameter at a certain height and the one in y-direction describe the height. Prior to the experiments, a scaling factor to determine the size of one pixel in x and y direction was determined by taking a picture of the initial cylinder, as represented by figure 5.11(a), from which the exact dimensions were known. A scan through one line of figure 5.11(a) is shown in figure 5.36. It can be seen, that the foam body can clearly be distinguished from the background. The result of the scanning is a vector of the length  $g$  (number of pixels in x-direction) containing the number of pixels inside the foam body, which represents the diameter as also indicated in figure 5.36. The result of this scanning for the four pictures of figure 5.11 is shown in figure 5.37. The figure shows the shrinking of the foam body due to sintering and also the volume expansion.

As seen in figure 5.11, the foam body causes a shadow on the alumina plate on which it was placed inside the furnace. Because of the darkness of the shadow it was also counted during the scanning of the picture and results in a little hump in the image, which is indicated with the circle in figure 5.37. However, the surface covered by this hump was not accounted for during the determination of the volume. For the correction, the course of the curve before the hump was extrapolated linearly to the end of the foam body.

Using the corrected number of pixels in each level as shown for four exemplary samples in figure 5.37, the volume of the foam body  $V_{Foam}$  in one picture can be calculated according to

$$V_{Foam} = \sum_{y=1}^q \pi \frac{(\vec{L}_x \cdot h_x)^2}{4} h_y \quad (5.128)$$

where  $\vec{L}_x$  is the vector of length  $g$ ,  $h_x$  the width of one pixel and  $h_y$  the height of one pixel. The width and height of one pixel, which is necessary to translate number of pixels in the x and y direction to metric units, were determined prior to the experiment by scanning the initial pressed power sample from which the sample diameter and height were measured.

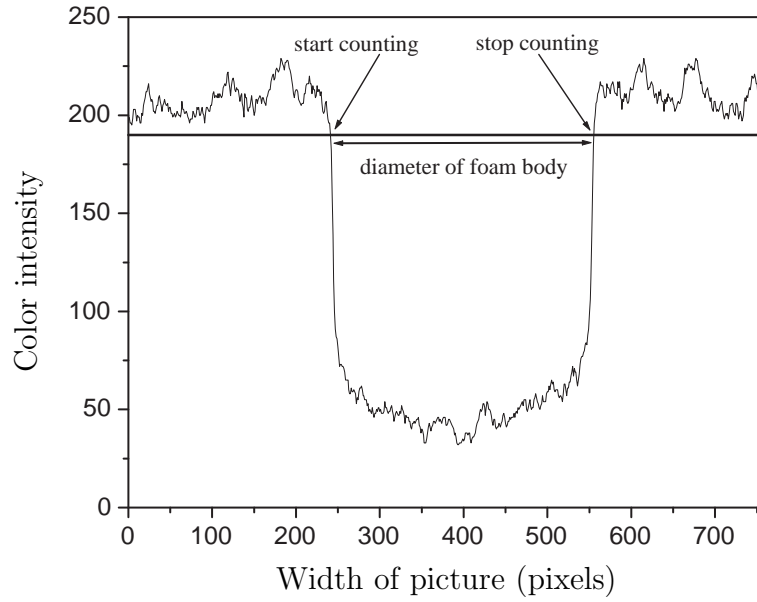


Figure 5.36: Scan in horizontal direction along pixel-line 400 of figure 5.11(a). The solid horizontal line represents the threshold.

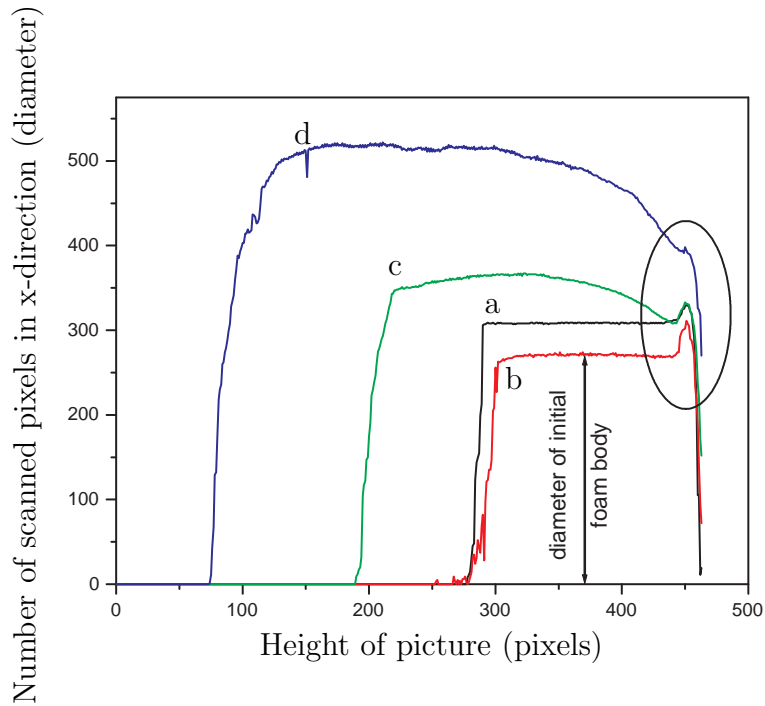


Figure 5.37: Number of pixels in  $x$ -direction for all pixels in  $y$ -direction (height of image) of the four different samples representing the four expansion stages as shown in figure 5.11. a: the initial foam body, b: the foam body after the sintering, c: the foam body after the heating, d: the foam body with its final volume. The circle shows the zone which was corrected for the volume (see text) determination.



# Chapter 6

## Conclusions and outlook

---

<b>6.1</b>	<b>Process steps . . . . .</b>	<b>205</b>
<b>6.2</b>	<b>Optimization tools for fly ash melting and foaming process .</b>	<b>207</b>
<b>6.3</b>	<b>Recommendations for future research . . . . .</b>	<b>211</b>

---

The objective of this study was the establishment of basic understanding (process steps, physics and chemistry involved) and development of technological tools to be able to safely transform fly ash originating from MSW incineration facilities into a high quality foam glass. This chapter describes in the first section the process steps required for the transformation of the fly ash into an environmentally harmless foam glass. The second section describes the developed tools, a thermodynamic model to estimate chemical activities of the constitutional glass components and a physicochemical model to describe the transient bubble growth in foam glass and how they can be applied to optimize the transformation process. The third section gives recommendations for future research.

### 6.1 Process steps

The environmentally harmful components in fly ash (heavy metals, salts and organic toxins) and its strongly altering composition in time make it difficult to use it in the original form, as received from the incineration facility, as raw material for foam glass production. However, its large inorganic fraction allows the production of a glass or glassy phase after being separated from the environmentally harmful parts. The genesis of the fly ash during MSW incineration and factors determining the composition and impurities of the ash have been presented. The main factors are the MSW composition, but also incineration techniques including incineration temperature, combustion gas velocities, flue gas cleaning techniques and cooling rates etc.. Depending on the country, governmental regulations for the storage or reuse of fly ash have to be met. These regulations were the driving force for the development of detoxification techniques in the past. Many detoxification techniques to transform the fly ash into an inert or environmentally harmless fraction have been developed in the past, but not all processes deliver a product which is suitable for glass or foam glass production. In order to produce a homogeneous glass from the fly ash, it must

be heated to temperatures above at least 1473 K. This has been demonstrated by melting experiments with MSW fly ash. These experiments have also shown, that during heating and melting the fly ash above 1473 K, a salt phase floating on top of the glass phase can appear. Depending on the fly ash melting technique or additives applied, glasses with different properties, e.g., oxidation state or chemical composition, can be produced. The oxidation state is an important parameter for foam glass production, because it influences the production of foaming gas in case of the use of a reduced foaming agent (C, SiC, soot etc.). This foaming agent reacts with the glass powder forming large volumes of gaseous species (CO/CO<sub>2</sub>), the gas phase in the foam.

The detoxification of fly ash (removal of heavy metals (Hg, Zn, Cd, Pb etc.)), by use of chlorination agents prior to melting has shown to be very effective for the separation of heavy metals below the melting range of the fly ash. Especially hydrochlorination of the fly ash in packed bed installations is very effective and industrially applicable to obtain a residue, which meets the concentration limits for heavy metals and which is suitable as construction material. It has been shown that, for fly ash, pure substance thermodynamic calculations can be used to compare the reactivity of the different chlorination agents in terms of heavy metal chlorination. The disadvantage of residual chlorine in the fly ash after chlorination, risking its evaporation during melting of fly ash and melting furnace refractory corrosion, can be avoided by precise control of salt layer removal. Salt layer removal by phase segregation upon heating of the detoxified fly ash and scraping it off the melt is a method already applied in practice.

A three step treatment, consisting of first the heavy metal removal by use of chlorination agents, secondly further heating and the subsequent separation of the salt layer after its formation and finally further melting to obtain a homogeneous silicate melt, can lead to a glass product harmless to the environment. This however, includes precise control of the different process steps. First of all, the fly ash should be as homogeneous as possible in terms of composition. Large compositional differences of fly ash (in time and depending on the incineration facility) complicate the control of the detoxification process and increase the variation of the obtained glass composition. Mixing large amounts of fly ash from different incineration facilities results in one large, well mixed fly ash mass with a composition for which the detoxification process can be optimized. The application of, e.g., the CT-Fluapur hydrochlorination process on the site of an incineration facility allows an effective detoxification at relatively low costs, because, e.g., electricity from the power generation of the incineration plant can be used as well as the flue gas cleaning installation, which has not to be installed separately. The CT-Fluapur process is a batch process and glass melting processes are usually continuous processes. This means, that an extra storage (silo) for the detoxified fly ash and a batch preparation installation for the additives must be foreseen. The batch preparation system is necessary to store, weight and mix these additives, which are necessary to obtain a uniform and foamable glass composition after the melting of the fly ash. The additives should be added to the fly ash and mixed prior to the insertion of the mixture into the melting furnace. With a relatively constant fly ash composition, the sort and amount of additives can easily be determined. Melting 1 kg of fly ash in the experiments resulted in 660 g of glass phase with the composition given in table 2.2. To control the glass composition and to obtain a

glass where the main glass oxides are inside the compositional range as given in table 1.3, additions of about 119 g of Soda, 450 g of Sand and about 52 g of Dolomite and 13 g of  $\text{Fe}_2\text{O}_3$  are required and 637 g of glass would be molten from this mixture. The resulting glass composition in wt.% would then be:  $\text{SiO}_2$ : 70.7,  $\text{Na}_2\text{O}$ : 13,  $\text{CaO}$ : 7.7,  $\text{Al}_2\text{O}_3$ : 2.8,  $\text{Fe}_2\text{O}_3$ : 2.6,  $\text{MgO}$ : 2.3. However, the choice and amount of additives must also be optimized in terms of applicability of the additive, e.g.,  $\text{NaCl}$  instead of soda, and of cost. Many glass compositions exist that can result in a high quality foam glass and the one with the best properties at lowest additive prices should be aspired.

After the fly ash has been detoxified and the amount of different additives has been determined, the mixture of fly ash and additives can be prepared and transported into a batch charger, which charges the mixture continuously into the melting furnace. The melting furnace, consisting of different refractory materials, should be divided in two chambers. The first to apply temperatures of about 1473 K to start the phase segregation and to remove the formed salt layer. This section should be heated with electrodes instead of, e.g., natural gas combustion, to avoid, e.g., high combustion gas velocities, which would increase carry-over from the inserted mixture and evaporation of the salt fractions from the melt. A second section is preferred to form a homogeneous melt for which, in general, temperatures above 1673 K are necessary. Glass melting technology, using electrodes or thin glass layers should be applied for the melting. The glass phase is free of the heavy metals and the salt fractions, however, because of the high iron oxide content in the glass, it is very dark and therefore it is difficult to heat it in normal glass melting tanks. To use the obtained glass from the melting procedure for foam glass production, it must be cooled and grinded to a powder. This can be achieved by cooling the glass from the melting tank with cold water, forming brittle glass frits. This introduces large tensions inside the glass, which facilitates subsequent grinding of the glass.

## 6.2 Optimization tools for fly ash melting and foaming process

The glass composition, after detoxification and melting, is of major importance for the production of foam glass. The glass composition determines the glass viscosity, its foaming potential, and its crystallization tendency. These properties are important parameters for foam glass production. During slow cooling, the obtained glass from the fly ash vitrification, after detoxification, salt layer removal and homogenization, without adaption to the composition, is sensible to crystallize, because of the relatively high calcium oxide concentrations ( $\text{CaO} > 25$  wt.%). In addition to that, most glass properties change with the glass composition (e.g., density, viscosity, etc.). The thermodynamic properties, e.g., enthalpy, entropy or heat capacity, the occurrence of redox reactions in the melt and the liquidus temperature also depend on the glass composition. Important aspects of glass melting and foaming therefore depend on these thermodynamic properties of the glass. Vapor pressures and crystallization tendencies, for example, depend on chemical activities of the constitutional components of a glass melt. The redox reactions in the glass providing the oxygen for the foaming process also depend on the thermodynamics of the polyvalent ions in the melt.

An extended calculation model (Ideal Mixture Compound Model, IMCM), describing a glass melt by an ideal mixture of single oxides and structural compounds, has been developed to estimate the chemical activities of the constitutional components in multicomponent silicate glass melts. The model requires the standard Gibbs free energies of formation of the constitutional oxides and structural compounds, the analytical glass composition and the temperature as input parameters. It is free of any adjustable parameters and does not need any expert selection of participating compounds. The advantage, but also drawback of the model, is its rigorousness regarding the choice of constitutional compounds and the underlying thermodynamic data. Neglecting one or more structural compounds (especially compounds present in relatively large concentration levels) can result in strong deviations in calculated activities.

For instance, the modeled chemical activities for  $\text{Na}_2\text{O}$ , in binary, ternary glasses or their melts and even in a float glass melt (for which 64 constitutional compounds had to be used in this model) are in relatively good agreement to the experimental activity data found in the literature. However, also deviations between the experimental results and other simulation models were observed for float glass compositions. Because activity data of glasses from typical fly ash melts are not available, the validity of the model for these glass types could not be shown. The incorporation of large iron oxide concentrations in the glass requires, that all structural iron oxide containing compounds are incorporated into the model. Because of the lack of availability of this data, IMCM calculations for a fly ash glass composition with iron oxide have not been performed.

Because of the strong crystallization tendency of the fly ash melts, the IMC model was developed with the aim to estimate the liquidus temperature of the fly ash melts during the cooling process. The model should be applied to estimate the influence of compositional additions on the liquidus temperature. Parts of the liquidus temperature of the binary sodium-silicate system was modeled with good agreement to the phase diagram, using a constant modification term for each structural compound for the calculated activities by the IMC model. This modification factor adjusted the temperature level, but not the shape of the liquidus temperature curves. However, calculations to determine the liquidus temperature of multicomponent glasses or even glasses with compositions similar to glasses from MSW vitrification, did not show reliable results so far. The modification factor is necessary to account for the fact, that at the melting temperature of a pure structural compound, the activity (reference state the pure liquid) is  $< 1$  due to decomposition of the structural compound (according to the IMCM) during melting. It seems, however, that this kind of modification is not simply transferable to multicomponent glass systems. The modification factor, used in the presented approach, can only be calculated from the pure compounds (from binary systems (binary compounds), or ternary systems (ternary compounds)), where the exact melting temperatures of these compounds are known. Liquidus temperature calculations with the model and the modification factor, however not presented in the thesis, have shown, that the application of the determined modification factors to multicomponent glass compositions did not show plausible liquidus temperatures. The values of the modification factor may not be constant, which was assumed in the model presented here. In addition to that, small differences in  $\Delta G$



values influence the course of the liquidus lines in the model and can produce significant deviations in calculated liquidus temperatures compared to experimentally determined liquidus temperatures.

Another important issue, which is relevant for these types of compound models applied to calculate for instance the liquidus temperature, are the values of, e.g., the melting enthalpies of the different structural compounds. According to the compound concept, proposed and discussed in this thesis, no constitutional compound exists alone, not even at the melting point of a pure structural compound. There are always amounts, even if they are little, of all other system components present. A consequence is therefore, that for compound models, congruent melting does not exist.

The influence of additions to the fly ash melt, for instance to reduce the liquidus temperature, has qualitatively been shown using an exemplary glass composition and comparing calculated activity values for, e.g.,  $\text{CaO} \cdot \text{SiO}_2$  and  $\text{CaO} \cdot \text{Al}_2\text{O}_3 \cdot 2\text{SiO}_2$  before and after an addition of sodium oxide to the glass melt. The substitution of 5 wt.% of CaO by  $\text{Na}_2\text{O}$  showed that the activities of  $\text{SiO}_2 \cdot \text{CaO}$  and  $\text{CaO} \cdot \text{Al}_2\text{O}_3 \cdot 2\text{SiO}_2$  both decreased at 1173 K by 27.3% and 72.7%, respectively. Lower activity values of a specific constitutional compound after a compositional change indicate a lower crystallization tendency.

The compound concept itself is an accepted concept for the description of the chemical activities of the constitutional components in multicomponent glass systems. However, some optimization of thermodynamic data and model assumptions seems necessary to predict glass properties, such as chemical activities and liquidus temperatures, important for industrial glass melting.

Glass to be used as raw material for conventional foam glass production requires distinct and constant physicochemical properties (viscosity, surface tension, oxidation state etc.). To use glasses with varying compositions for foam glass production, a more detailed analysis of the foaming process (type of gases evolved, onset temperature of gas evolution) is required to define process conditions or additives for optimal foam glass production. Bubble growth models for foam glass, based on mass transfer descriptions and taking into account redox reactions in the glass, can support this analysis.

Carbon monoxide has been identified as main foaming gas for a glass with only iron oxide as polyvalent ion. It has furthermore been shown that the formation of the foaming gas depends strongly on the presence of polyvalent ions and their valency states, thus on the oxidation state of the glass. It is assumed that the reduction of ferric iron to the ferrous state releases oxygen from the glass, which can successively react with the carbon, present in the gas inclusions in the sintered powder to CO (1050-1250 K). However, formation of, e.g.,  $\text{Fe}_3\text{O}_4$  as a stable intermediate compound could neither be affirmed nor excluded in this temperature range. No further reduction of  $\text{Fe}_3\text{O}_4$  could limit the  $\text{O}_2$  release. Depending on the oxidation state of the glass, more or less oxygen will be released for foam gas formation. Very little information on the existence of  $\text{Fe}_3\text{O}_4$  in glasses at higher iron oxide concentrations ( $\sim 3$  wt.%) in the glass and relatively low temperatures (1173 K) is available. Qualitative foaming gas identification experiments with glasses containing only

sulfur as well as iron oxide plus sulfur, both did not show other foaming gases than CO. The model calculations with a glass containing iron and sulphur also showed, that  $S^{4+}$  is hardly available at the glass/bubble interface available to generate  $SO_2$  gas. However, the bubbles of industrially produced foam glass, e.g. Pittsburgh Corning foam glass, contain, e.g.,  $H_2S$ . This was not found here, but could be explained by a certain water content in the industrial produced glasses.

Many practical glass foaming procedures are published, most of them as patents, describing practical procedures for foam glass production. Very limited coherent information on the relevant parameters for controlling bubble growth in a sintered powder during foam glass production is available. Especially, the effect of the oxidation state of the glass on the amount of foaming gas produced is hardly investigated in literature. Carbon in bubbles surrounded with oxidized molten glass, extracts oxygen from this glass. Inside the glass, part of the chemically dissolved oxygen can be converted into physically dissolved oxygen by redox reactions in the glass phase. Diffusion processes in the glass transfer physically and chemically dissolved oxygen to the bubble glass interface and this diffusion governs the evolution rate of gas (formation of CO) from carbon plus oxygen. The information derived from the qualitative and quantitative foaming gas identification experiments has been used to develop a model describing the transient bubble growth in foam glass. To study the effect of various physicochemical properties, e.g., glass viscosity, surface tension, glass melt composition, oxidation state and also the effect of process parameters, e.g., initial bubble size or heating rate on the bubble growth in foam glass, a first principles model has been developed. The model includes local redox equilibrium reactions of multiple polyvalent ions and physically dissolved oxygen in the glass and their effect on the concentration profiles of the diffusing species.

The validation of the foam glass model has shown, that the model, which assumes no gas loss to the environment, estimates the bubble growth of foam glass in the initial stages very well, but it strongly overestimates the final foam height. Several causes for the overestimation of the foam height at extended foaming times are proposed to be:

1. the loss of reaction gases through open pores before the start of the foaming,
2. the amount and distribution of foaming agent and
3. the exact foaming gas reactions.

Especially the identification of the redox reactions which take place and which are responsible for oxygen release from the glass are very important: Chemical reactions are modeled, delivering a specific amount of foaming gas, depending on the stoichiometry of the gas forming reactions. A theoretical calculation of the thermodynamic equilibrium between  $FeO$ ,  $Fe_2O_3$  and  $Fe_3O_4$  at 923 K using standard state pure substance Gibbs free energies indicates the presence of  $Fe_3O_4$  at considerable concentrations.

The effect of the heating rate on the initial real foam expansion rate is in good agreement comparing the model with observations in the initial stages of the foaming experiments. The parameter study on the two main process parameters, the initial bubble size (depending on the size of the glass powder particles) and the heating rate has shown, that

these parameters significantly influence the bubble growth rate. The choice of initial glass particle size, which directly influences the initial bubble size and shell thickness is thus significant for the modeled bubble growth rate, but not for the final modeled foam volume. Furthermore, it has been shown that the model is capable of respecting mutual chemical interaction and local thermodynamic equilibrium of the diffusing species in the glass shells in the foam glass. This can be transferred to other models describing, e.g., the growth or shrinkage of bubbles during fining of industrially glass melting processes. Despite the deviations between the modeled and experimental foam expansion rates, the model offers a beneficial tool to any foam glass producer to optimize the process and glass compositions.

## 6.3 Recommendations for future research

The results of the calculations with the thermodynamic model (IMCM), presented in chapter 3, and the assumed ideal mixture behavior between the single oxides and the structural compounds (compound approach), have shown, that future research is required to improve the model and its applicability to industrial problems. It is proposed for future research, to investigate in more detail the partitioning of the Gibbs free energy and melting enthalpy contribution of the structural compounds among the participating constitutional components in the liquid state in order to determine the mole fraction of the constitutional components in the melt at the melting temperature of the different structural compounds. Another aspect that should be studied in more detail is the incorporation of iron oxide in soda-lime-silica glasses at concentration levels around 3 wt.% on thermodynamic properties of these glasses or melts.

From the results of the experiments presented in chapter 4, future research on the reduction-oxidation reactions of iron oxide in glasses with increased iron oxide concentration levels ( $> 3$  wt.%) is recommended to identify the different reduction steps of iron oxide in the glass during foaming. For foam glass production this is especially important at temperatures between 923 and 1273 K. Also, the interaction between iron oxide and sulfur species and their effect on the foaming gas formation with a reduced foaming agent may be of importance. Depending on the oxidation state of the glass, sulfur can be incorporated in the glass at different oxidation states. Oxygen can thus also be chemically dissolved by sulphur species in the glass. An improved understanding of these redox reactions in the glass would also be beneficial to the bubble growth model.

To improve the bubble growth model, developed in chapter 5, further controlled foaming experiments should be performed to obtain an improved understanding of possible factors causing lower foaming volumes in practice compared to predictions with the model.



# Samenvatting

De productie van schuimglas uitgaande van vliegas, het afvalproduct van afvalverbrandingsinstallaties, is een veelbelovende technologie voor het creëren van commerciële waarde aan dit afvalproduct. Tijdens de verschillende processtappen die doorlopen worden bij de vliegasverwerking worden de aanwezige milieubelastende componenten zoals zware metalen (Pb, Cu, Zn, etc.), zouten en organische giftige stoffen (dioxinen en furanen) verwijderd uit het vliegas. Het resulterende schuimglas is een lichtgewicht materiaal bestaande uit een groot aantal homogeen verdeelde gasbellen die van elkaar gescheiden worden door dunne glasvliezen. De toepassing van schuimglas betreft voornamelijk warmte- en geluidsisolatie waarbij zeer strenge eisen gesteld worden aan warmtegeleidbaarheid, mechanische sterkte en weerstand tegen corrosie. Als bouw materiaal dient het schuimglas te voldoen aan de wettelijke eisen die opgelegd worden aan de duurzaamheid van het materiaal in het milieu. Voor schuimglas dat geproduceerd wordt uit commerciële glazen zijn deze eisen niet belemmerend, maar vanwege de aanwezigheid van de bovengenoemde milieubelastende componenten zijn speciale behandelingen noodzakelijk om schuimglas te produceren uit vliegas en in te kunnen zetten als wettelijk geaccepteerd bouw materiaal. De meest kritische eisen aan het schuimglas gelden op het gebied van uitloging van milieubelastende stoffen uit het glas naar de omgeving.

Het doel van de studie beschreven in dit proefschrift betreft het verkrijgen van fundamentele kennis omtrent de verschillende processtappen die benodigd zijn voor het omzetten van vliegas naar een hoogwaardig schuimglas. Een belangrijk aspect tijdens de studie is het ontwikkelen van rekenmodellen ter ondersteuning van het begrip van het totale schuimglas productie proces. Dit proces kan ruwweg opgedeeld worden in een viertal separate processtappen:

1. Ontgifting van het vliegas;
2. Afscheiding van de zich tijdens het ontgiften vormende zoutlaag;
3. Verglazing van het ontgifte and vliegas door versmelting;
4. Schuiming van het verglaasde en verpoederde vliegas door toevoeging van een reductor.

Het zodanig definiëren van de verschillende processtappen dat de producten van de deelprocessen optimaal (qua samenstelling en eigenschappen) op elkaar aansluiten is van groot belang bij dit project om het complexe proces van schuiming van voorbehandeld vliegas tot een succes te maken. De belangrijkste ontwikkelde rekenmodellen ter ondersteuning van

het schuimproces in zijn totaliteit betreffen een thermodynamisch model ter voorspelling van chemische activiteiten in multicomponent glazen en een model ter berekening van het tijdafhankelijk gedrag van schuimvorming.

Zowel zware metalen als giftige organische stoffen kunnen verwijderd worden van het vliegaskas door het chloreren van het vliegaskas in een gepakt bed dat doorstroomd wordt met bevochtigd HCl of  $\text{Cl}_2$  bij circa 1173 K. De zware metalen worden hierbij omgezet in vluchtige metaalchloriden en de giftige organische verbindingen worden afgebroken. De mate waarin deze milieubelastende componenten verwijderd worden door chlorering wordt aangetoond aan de hand van resultaten van thermodynamische berekeningen en gebruikmakend van resultaten van experimenten die beschreven staan in de literatuur. In de literatuur zijn waarden van 98.5 % (Zn), 99.5 % (Cu), 99.8 % (Cd en Pb) gerapporteerd als maat van verwijdering uit het vliegaskas. Naast het chloreren van vliegaskas in een gepakt bed kunnen zware metalen ook verwijderd worden door het vliegaskas te gloeien met vast  $\text{MgCl}_2$  waarbij tot 90 % van Pb, Zn, Cu en Cd verwijderd kan worden.

De ontstane relatief grote hoeveelheden metaalzouten na ontgifting van het vliegaskas kunnen vervolgens verwijderd worden door het behandelde vliegaskas vervolgens te verwarmen tot circa 1473 K. Experimenten laten zien dat bij deze temperatuur de zouten op de gevormde glassmelt drijven en zodanig eenvoudig verwijderd kunnen worden door middel van vloeistof-vloeistof scheiding. Na scheiding is een glas verkregen dat vrij is van milieubelastende componenten en dat vervolgens verder verwerkt kan worden tot een schuimglas.

Het bereiden van een homogene glassmelt dat gebruikt kan worden voor het produceren van schuimglas dient vervolgens als eerste verhit te worden tot circa 1673 K. Vanwege het hoge gehalte aan CaO in het glas kan tijdens afkoeling van de hete homogene smelt, en/of tijdens het schuimen van de glassmelt in een later stadium van het proces, kristallisatie optreden. De kristallen die zich vormen tijdens kristallisatie beïnvloeden de viscositeit van het glas resulterend in een schijnbare viscositeit die hoger is dan de intrinsieke glassmelt viscositeit. Daar de viscositeit een zeer belangrijke parameter is voor het schuimen van glas tot een hoogkwaliteit schuimglas is het toevoegen van additionele componenten aan het verglaasde vliegaskas ter onderdrukking van kristallisatie onontbeerlijk. Naast de invloed op viscositeit zorgen de kristallen tevens voor het openbreken van de glasvliezen rondom de gasbellen waardoor zowel de isolerende werking als de sterkte van het schuimglas afneemt. Om de neiging van en gevoeligheid tot kristallisatie van schuimglas te verminderen, dienen componenten toegevoegd te worden die een verlaging van de liquidus temperatuur van het glas tot gevolg hebben.

Voorspelling van het kristallisatiegedrag van glazen en de bepaling van het effect van toevoegingen aan het glas op de kristallisatie neiging behoeft de ontwikkeling van mathematische modellen die de chemische activiteit van glascomponenten bepaalt als functie van de temperatuur en de glassamenstelling: de chemische activiteit van een glascomponent is indicatief voor de kristallisatie neiging van het glas. In het huidige project is een zogenaamd 'ideal mixture compound model (IMCM)' ontwikkeld waarmee de chemische activiteit van afzonderlijke oxiden (bijvoorbeeld  $\text{Na}_2\text{O}$  of  $\text{SiO}_2$ ) en zogenaamde structurele componenten (bijvoorbeeld  $\text{Na}_2\text{O} \cdot \text{SiO}_2$  of  $\text{CaO} \cdot \text{SiO}_2$ ) bepaald kan worden. Het

IMCM beschouwt een glassmelt als een ideaal mengsel van de afzonderlijke oxiden en de structurele componenten. Het in dit project ontwikkelde model bepaalt de chemische activiteit van de glassmelt componenten door minimalisatie van de Gibbs vrije energie van het totale glassysteem met nevenvoorwaarde het behoud van elementen (i.e. Lagrange with undetermined multipliers). Deze methodiek maakt het mogelijk om de huidige chemische modellen ter bepaling van chemische activiteiten uit te breiden naar multi-component systemen. Vergelijk van experimentele en berekende waarden voor activiteiten van componenten in multi-component systemen (zoals bijvoorbeeld de Na<sub>2</sub>O activiteit in vlakglas) tonen een goede overeenkomst. Bijvoorbeeld, de maximale afwijking in Na<sub>2</sub>O activiteit in een vlakglassamenstelling bedraagt 24 % bij 1386 K.

Het IMCM is tevens gebruikt voor het berekenen van de activiteiten van de bovengenoemde afzonderlijke oxiden en zogenaamde structurele componenten in glazen die bereid zijn uit vliegias. Berekeningen hebben aangetoond dat het model de kristallisatie-eigenschap van ontgift en verglaasd vliegias goed kan afschatten op basis van een vergelijk van de berekende chemische activiteiten voor de verschillende oxidische componenten in het vliegias.

Tot slot is het IMCM toegepast om een gedeelte van de liquidus curve van het systeem Na<sub>2</sub>O en SiO<sub>2</sub> te bepalen. Na uitbreiding van het IMCM model met een zogenaamde modificatieparameter wordt de liquiduscurve gesimuleerd die in goede overeenstemming is met de curve die in de literatuur gerapporteerd is. Deze aanpassing is noodzakelijk om de verschillende referentietoestanden van de gebruikte/berekende activiteiten aan elkaar te koppelen. Vanwege een gebrek aan thermodynamische data kan geen goede voorspellingen gedaan worden voor liquidustemperaturen van multicomponentsystemen zoals glazen die geproduceerd worden uit vliegias. Het blijkt echter dat de modificatie aan het model die doorgevoerd is ter voorspelling van liquidustemperaturen voor het binaire systeem van Na<sub>2</sub>O en SiO<sub>2</sub> niet eenvoudig toepasbaar is voor multicomponent systemen. Kleine verschillen in thermodynamische data voor de afzonderlijke oxiden in glassystemen hebben relatief grote invloed op de berekende activiteiten en daarmee op de accuraatheid in voorspelling van de liquiduscurve. Hierdoor kunnen grote afwijkingen in berekende en actuele liquidustemperaturen optreden.

Het produceren van schuimglas uitgaande van het voorbehandelde vliegias behoeft fundamentele kennis omtrent de mechanismen die bepalend zijn voor de kwaliteit van het geproduceerde schuimglas. Voor schuiming van het bereide glas wordt aan het glas koolstof toegevoegd dat dienst doet als gasvormende component. Het koolstof reageert tijdens opwarmen van het mengsel van glas en koolstof voornamelijk tot CO, hetgeen aangetoond is aan de hand van een serie experimenten. De zich vormende gasbel zal groeien onder invloed van de productie van gas en indien de opgewekte druk in de bel de geïntroduceerde kracht door bij voorbeeld de oppervlaktespanning overschrijdt. De mate van gasproductie blijkt volgens experimenten in sterke mate af te hangen van de oxidatietoestand van het glas.

Voor beheersing en optimalisatie van de condities waaronder het schuimproces van glas, plaatsvindt is fundamentele kennis omtrent dit proces onontbeerlijk. Dit proefschrift

beschrijft een model dat de tijdsafhankelijke groei van bellen in schuimglas beschrijft als functie van glassmelteigenschappen en procesomstandigheden. Het model gaat uit van thermodynamisch evenwicht tussen de gasbelcomponenten en de polyvalente ionen in de glassmelt dat de bel omsluit. Experimentele validatie van het model toont aan dat het model zeer goed geschikt is om de belgroei in schuimglas af te schatten tijdens de initiele fase van het schuimingsproces. Het model overschat echter de uiteindelijke belgroei in het schuim en daarmee het totale schuimglasvolume. Het effect van zowel de initiele belgrootte en de opwarmsnelheid van het mengsel van glas en koolstof op de belgroei is gesimuleerd met het ontwikkelde model. Voor beide parameters blijkt er een grote impact te zijn op de belgroei. Ondanks de afwijkingen tussen de gemodelleerde en experimenteel bepaalde schuimsnelheden kan het model goed gebruikt worden ter optimalisatie van procescondities en glaseigenschappen voor de productie van schuimglas. Daarnaast heeft het model de potentie om, met enkele wijzigingen, de bestaande glasbellenmodellen te verbeteren zodat een betere beschrijving van ontgassing in industriële glasovens mogelijk gemaakt wordt.

In dit proefschrift is een methodiek voor de productie van hoogwaardig schuimglas uitgaande van vliegas van afvalverbrandingsinstallaties beschreven. De belangrijkste processtappen bij de schuimglasproductie zijn bepaald en beschreven aan de hand van zowel experimenten als resultaten van simulaties met de in het project ontwikkelde rekenmodellen. Op basis hiervan zijn praktische oplossingen voor de heersende problematiek aangebracht.



# Zusammenfassung

Die Herstellung von Schaumglas aus Flugaschen der Hausmüllverbrennung (HMV) ist ein vielversprechender Ansatz um den Wert dieser Abfallstoffe zu erhöhen. HMV Flugaschen beinhalten umweltschädliche Stoffe wie z. B. Schwermetalle, Salze und organische Giftstoffe und zeigen starke Zusammensetzungsunterschiede. Schaumglas hingegen ist ein Glaswerkstoff mit einem hohen Volumenanteil an kleinen, homogen verteilten und geschlossenen Gasblasen, die durch dünne Glaslamellen voneinander getrennt sind. Im Baubereich wird Schaumglas zur Wärme- und Schallisolation eingesetzt. Es ist ein Glas mit engen Anforderungen hinsichtlich Isolationsvermögen, mechanischer Beanspruchung und Korrosionswiderstand. Als Baustoff unterliegt Schaumglas jedoch den gesetzlichen Bedingungen hinsichtlich seiner Umweltverträglichkeit, die bei Einsatz von Standardglasrohstoffen bei der Herstellung unbedenklich ist. Beim Einsatz von Abfallgläsern oder Gläsern aus der HMV Flugascheverglasung kann dies jedoch zu Problemen führen. In diesem Zusammenhang ist das Eluieren von umweltschädlichen Stoffen wie z. B. Schwermetallen oder Salzen aus dem Glas in die Umwelt als besonders kritisch anzusehen.

Das Ziel dieser Arbeit ist die Entwicklung eines generellen Verständnisses der einzelnen Prozessschritte und der einbezogenen Physik und Chemie sowie von Simulationsmodellen, um HMV Flugaschen sicher in ein hochqualitatives Schaumglas zu transformieren. Der Produktionsprozess von Schaumglas aus HMV Flugaschen kann in vier Hauptschritte unterteilt werden:

- Entgiften der Flugaschen;
- Abtrennen der Salzphase;
- Glasherstellung durch Schmelzen der entgifteten Flugaschen;
- Schäumen des Glases.

Hierbei ist das Abstimmen der verschiedenen Prozessschritte aufeinander besonders wichtig, damit die Produkte der einzelnen Schritte als Ausgangsmaterial des nächsten Schrittes eingesetzt werden können. In dieser Arbeit wurde einerseits ein Simulationsmodell zur Berechnung von chemischen Aktivitäten in Multikomponentengläsern und andererseits ein Modell zur Berechnung des zeitabhängigen Blasenwachstums in Schaumglas entwickelt. Viele verfügbare Entgiftungsprozesse für HMV Flugaschen erzeugen ungiftige Endprodukte, die sich aber nicht unbedingt zur Schaumglasproduktion eignen. Die Chlorinierung von HMV Flugaschen mithilfe von HCl- oder Cl<sub>2</sub>- Gas in Festbett-Reaktoren bei 1173 K beseitigt effektiv die Schwermetalle (Pb, Cu, Zn, etc.) und die organischen Giftstoffe.

Die hauptsächlich auf der Oberfläche der Flugaschepartikel anwesenden Schwermetalle werden unterhalb des Schmelzbereichs der Flugasche in flüchtige Schwermetallchloride umgewandelt. Die Effektivität eines solchen Entgiftungsprozesses wird durch Diskussion thermodynamischer Berechnungen und experimentellen Ergebnissen aus der Literatur gezeigt. Literaturquellen berichten über Entfernungsraten von 98.5% für Zn, 99.5% für Cu, 99.8% für Cd, und 99.8% für Pb mittels Hydrochlorinierung (HCl). Daneben zeigt das Rösten der Flugaschen mit z. B. festem  $\text{MgCl}_2$  unterhalb des Schmelzbereichs der Flugaschen ebenfalls Entfernungsraten größer 90% für Pb, Zn, Cu und Cd. Die relativ großen Salzfraktionen in der Flugasche nach der Chlorinierung können durch eine flüssig-flüssig Trennung zwischen Glas- und Salzphase beseitigt werden. Dies kann durch Aufheizen der Schmelze auf Temperaturen um 1473 K erreicht werden. Im Rahmen dieser Arbeit durchgeführte Experimente haben gezeigt, dass bei diesen Temperaturen die Silikatphase komplett flüssig ist und dass sich eine Salzphase, die auf der silicatischen Schmelze schwimmt, bildet. Ein Glas, das als Rohstoff zur Schaumglasherstellung verwendet werden soll, muss homogen und frei von umweltschädlichen Stoffen sein, sowie eindeutige physikalisch-chemische Eigenschaften aufweisen (z.B. Viskositäs-Temperatur Verhalten, Oberflächenspannung oder Oxidationszustand). Um ein homogenes Glas aus den chlorinierten Flugaschen zu produzieren, das frei von verbliebenen Salzen ist, muss es nach der Salzabtrennung auf Temperaturen um 1673 K erhitzt werden.

Die Glasschmelze aus Flugaschen neigt aufgrund der z. B. hohen Kalziumoxyd Konzentrationen ( $\text{CaO} > 25$  gew.%) zur Kristallisation. Die Kristallisation läuft entweder während des Abkühlens vom Schmelzprozess oder während des Schäumungsprozesses ab, der gewöhnlich zwischen 923 and 1173 K stattfindet. Kristalle im Glas beeinflussen die wahrnehmbare Viskosität des Glases und somit das Blähverhalten. Die Kristalle beeinflussen aufgrund unterschiedlicher Ausdehnungskoeffizienten von Glas und Kristall zudem die strukturelle Integrität des Schaums. Diese Einflussfaktoren verursachen offene oder rissige Lamellen zwischen angrenzenden Blasen und dadurch ein reduziertes Isolationsvermögen. Um die Zusammensetzung und somit die Haupteigenschaften des Glases zu kontrollieren können der Flugasche Additive zugeführt werden, die unter anderem die Kristallisationsneigung reduzieren. Um die Herstellung von Schaumglas aus Flugascheschmelzen zu optimieren, wurde ein allgemeines und fundamentales Modell zur Berechnung der chemischen Aktivitäten der Glasschmelzkomponenten entwickelt. Das sogenannte IMC Modell (Ideal Mixture Compound Modell) oder 'Compound Modell', berechnet die chemischen Aktivitäten der individuellen Oxide (z. B.  $\text{Na}_2\text{O}$  oder  $\text{SiO}_2$ ) und strukturellen Einheiten (z. B.  $\text{Na}_2\text{O} \cdot \text{SiO}_2$  oder  $\text{CaO} \cdot \text{SiO}_2$ ) einer als ideale Mischung dieser Komponenten betrachteten Glasschmelze. Die Anwendung der Methode der Lagrange'schen Multiplikatoren als Minimierungsroutine, erlaubt das Erweitern und Verbessern bestehender Compound Modelle für binäre und ternäre Systeme hin zu Multikomponentensystemen. Der Vergleich zwischen berechneten und experimentellen Natriumoxid-Aktivitäten aus Literaturquellen zeigt sogar für klares Floatglas eine sehr gute Übereinstimmung. Die maximale Abweichung der Natriumoxid Aktivität zwischen berechneter und experimentell bestimmter Literaturwerte für klares Floatglas lag bei 24% (bei 1368 K). Des Weiteren wurden mit dem Modell die Aktivitäten einiger individueller Oxide und struktureller Einheiten in Schmelzen aus verglasten Flugaschen berechnet. Mithilfe des Modells kann die Kristallisationsneigung des Glases durch Vergleich der berechneten Aktivitäten abgeschätzt werden. Das

IMC Modell wurde ebenfalls mit guter Übereinstimmung verwendet, um Teile der Liquiduslinie im binären  $\text{Na}_2\text{O} \cdot \text{SiO}_2$  System zu berechnen. Hierzu ist die Verwendung eines Faktors notwendig, um die unterschiedlichen Referenzzustände der verwendeten Aktivitäten miteinander zu korrelieren. Aufgrund nicht vorhandener thermodynamischer Daten zeigten die Berechnungen der Liquidustemperaturen multikomponenter Gläser oder Gläser aus Flugascheschmelzen keine zufriedenstellenden Resultate. Es scheint, dass der Korrelationsfaktor, der im binären Natriumsilikat System zu guten Ergebnissen führt, nicht direkt auf Multikomponentensysteme transferiert werden kann. Kleine Änderungen in  $\Delta G$  Werten haben einen signifikanten Einfluß auf berechnete Aktivitätswerte und verursachen somit signifikante Unterschiede zwischen berechneten und experimentell bestimmten Liquidustemperaturen.

Um Schaumglas aus den entgifteten, verglasten und hinsichtlich der Zusammensetzung angepassten Flugaschen herzustellen, ist eine detaillierte Analyse des Blähprozesses und insbesondere der Blähgasreaktionen notwendig. Im Inneren der geschlossenen Blase des Schaumes reagiert ein reduziertes Blähmittel (z. B. Kohle) mit dem Sauerstoff aus dem Glas und bildet die Blähgase CO bzw.  $\text{CO}_2$ . Die Blase wächst, wenn der Druck in der Blase durch die Blähgasbildung steigt und die äußeren Kräfte durch z.B. die Oberflächenspannung des Glases, das die Blase umringt, übersteigt. Experimente mit Gläsern, die nur Eisen als polyvalentes Ion beinhalten, haben gezeigt, dass CO das vorherrschende Blähgas ist. Die Menge des während des Blähprozesses gebildeten CO-Gases hängt vom Oxidationszustand des Glases ab.

Zur quantitativen Beschreibung des Blähprozesses wurde ein Grundsatzmodell aufgestellt, das das zeitabhängige Blasenwachstum im Schaumglas als Funktion der physikalischen, chemischen und Prozessparameter beschreibt. Das Modell berücksichtigt auch das thermodynamische Gleichgewicht zwischen den polyvalenten Ionen und dem physikalisch gelösten Sauerstoff im Glas. Die Validierung des Modells in kontrollierten Blähexperimenten im Labor zeigt, dass das Modell zur Abschätzung des anfänglichen Blasenwachstums verwendet werden kann, jedoch wird das Endvolumen des Schaums stark überschätzt. Der Vergleich des modellierten Einflusses der Aufheizrate auf das zeitabhängige Blasenwachstum zeigt eine relativ gute Übereinstimmung mit der realen (experimentellen) anfänglichen Schaumexpansionsrate. Eine Parameterstudie über die anfängliche Blasengröße (die von der Größe der Glaspartikel abhängt) und die Heizrate zeigt, dass diese Parameter die Wachstumsrate der Blase signifikant beeinflussen. Trotz der Abweichungen zwischen berechneten und experimentellen Schaumexpansionsraten, kann das Modell aufgrund seiner fundamentalen Basis zur Optimierung der Prozesskonditionen und Glaseigenschaften zur Herstellung eines Schaumglases mit erforderlichen Eigenschaften verwendet werden. Zusätzlich dazu kann das Modell mit einigen Modifikationen einen ansehnlichen Beitrag zur Verbesserung existierender Modelle, die Läuterprozesse in Glasschmelzen beschreiben, beitragen.

In der vorliegenden Arbeit wurde ein Weg zur Entgiftung und Transformation von HMV Flugaschen in Schaumglas vorgestellt. Die bedeutensten Prozessschritte wurden identifiziert und mithilfe von Experimenten und Ergebnissen aus Modellen dieser Arbeit beschrieben. Auf dieser Basis wurden praktische Lösungen für die beschriebenen Probleme entwickelt und Vorschläge für weiterführende Untersuchungen präsentiert.



# Acknowledgments

As I present the culmination of my research, resulting in this thesis, I reflect on the fact that all learning is a collaborative process. I have much to be thankful for including my instructors, mentors, friends and family, on whom I could always rely on.

This project was funded by TNO in Eindhoven and I like to express my gratitude for their financial support.

To Prof. Ruud Beerkens, I express my gratitude for his initiative in this research and his patience, advice and concern throughout this project. I am very grateful to Prof. Alfons Buekens from the Vrije Universiteit Brussel for being my second promoter and for his advice, concern and vast experience covering fly ash. I am also very grateful to my copromoter, Dr. John van der Schaaf, for his support, trust understanding and encouragement in this project. I will never forget the hours we searched for the errors in the Matlab code and the Skat games with Katrin. Your continuous motivation helped me considerably. Thank you.

Gratitude is also expressed to my colleagues at TNO for their support using TNO equipment, the experimental support and the fruitful discussions. You always gave me the feeling of being one of you. I am grateful to the colleagues of SCR for their support and the good time we had. The beer-pizza-video evenings are in fond remembrance. I am also grateful to the promovendi/post-doc groep, with which I shared much. I want to thank Katrin for the great time we had sharing the office. I also want to thank Paul Laimböck for the very interesting discussions we had on glass and, redox and activity modeling. A very special thank you goes to Oscar for a profound friendship far beyond working together. When the worst came to the worst, you were always there for me. Thank you.

Thanks to all of you on the home front and sorry that my time spent with you was so limited in the last few years. Mark, I am very grateful to you. My best friend in good and bad times, you always had an open ear for me. Thank you.

Most of all, I want to thank my parents, Urs-Peter and Gretha Steiner. Without your love, trust, understanding, and continuous support, I would never have made it this far. You have always been there for me, Thank you.



# Curriculum Vitae

Arjen Steiner was born on march 20th 1971, in Düsseldorf, Germany. He obtained his university-entrance diploma in 1990 and studied Glass Ceramics and Building Materials at the RWTH Aachen (Germany), ENSCI Limoges (France) and Alfred University (USA). He graduated in 1997 on "Design, Construction, and Validation of a Laboratory Float Furnace; Initial Characterization of the Tin-Glass Interface using SIMS, XPS, EDAX and AFM" and started to work as project engineer in the Glass Technology Group of TNO in Eindhoven. In 1998 he started his PhD study at Eindhoven University of Technology, resulting in this thesis. From 2003 to 2006 he worked as the assistant of the plant manager for Saint-Gobain Glass's float glass plant in Cologne (Germany). Since March 2006 he works as a project manager for glass technology and research & development at DTEC Engineering & Consulting GmbH in Gelsenkirchen (Germany).